# Competing anisotropies in epitaxial exchange biased thin films and patterned nanostructures

Wei Zhang

A dissertation
submitted in partial fulfillment of the
requirements for the degree of

Doctor of Philosophy

University of Washington
2013

Reading Committee:
Kannan M. Krishnan, Chair
Xiaodong Xu
Jiangyu Li

Program Authorized to Offer Degree:
Materials Science & Engineering

University of Washington

**Abstract**

Competing anisotropies in epitaxial exchange biased thin films and patterned nanostructures

Wei Zhang

Chair of the Supervisory Committee:
Professor Kannan M. Krishnan
Materials Science & Engineering

Magnetization reversal properties in thin-films and patterned nanostructures are essential for various modern magnetic devices. The magnetization reversal is determined by the magnetic anisotropies of the system, which can come from different origins. Specifically, the exchange bias, also known as the exchange anisotropy, brings in a shift of the magnetic hysteresis loop which has been widely applied in magnetic recording technologies and magnetic sensors. In an exchange bias system, other types of magnetic anisotropies, such as the magnetocrystalline anisotropy or the shape anisotropy, can be present and interacts with the exchange anisotropy thus affecting the magnetic reversal cooperatively.

In order to study the competing magnetic anisotropies in the exchange bias system, we have developed approaches to grow epitaxial exchange-biased ferromagnetic-antiferromagnetic thin-film bilayers, which bring significant magnetocrystalline anisotropy into the exchange bias system. We studied the magnetization reversal of these bilayers using magneto-optic Kerr effect and anisotropic magnetoresistance, and investigated systematically the dependence of magnetic anisotropies on various sample parameters, including layer thickness, temperature, relative orientation, interfacial spin behavior,

and the antiferromagnetic bulk structure. To explain the samples' unique magnetic behaviors, we developed a quantitative model based on magnetic domain-wall nucleation and propagation process, and offered a consistent and integrated interpretation on the magnetic reversal properties.

To further incorporate the shape anisotropy into the exchange bias system, we developed a large-area, efficient epitaxial patterning process using nanoimprint lithography, which allows us to pattern epitaxial magnetic thin-film bilayer and multilayers into nanostructures. By combining the bilayer-resist template and Molybdenum liftoff, we are able to create high-quality, patterned structures with different sizes ranging from ~ 70 nm to ~ 5μm. The magnetization reversals, especially the domain-wall structures during the reversal, are subsequently studied by hysteresis loop measurements and direct imaging techniques. Finally, in addition to fundamental studies on the magnetic reversal, the nanoimprint processes developed for this thesis can also find great potential in relevant industries.

# ACKNOWLEDGEMENTS

First, I would like to thank Professor Kannan Krishnan for giving me the opportunity to join his group and work in the exciting field of nanomagnetism. His encouragement, support, and guidance have accompanied me throughout my Ph.D study. I also want to thank my committee members, Prof. Xiaodong Xu, Prof. Jiangyu Li, Prof. Peter Pauzauskie, and Prof. Marjorie Olmstead, for their time and insight, which helped to make this work complete.

For helpful technical guidance at the beginning of this project, I want to thank Dr. Dirk Weiss and Dr. Qingfeng Zhan; for help with measurements and technical advice, many thanks are owed to my collaborators, Dr. Mark Bowden, Dr. Deirdre Olynick, Prof. Thomas Eimüller, Dr. Sebastian Brück, and Prof. Mingzhong Wu.

My group colleagues have also given me tremendous help in the past five years. I want to express the same gratitude to many current and former group members, especially Dr. Matt Ferguson, Dr. Tianlong Wen, Yufeng Hou, Zheng Li, and Amit Khandhar, for their helpful suggestions and technical support.

Finally, my deepest appreciation belongs to my family. Without their unending support through the years, I would not have been able to go this far.

# TABLE OF CONTENTS

page

# Chapter 1

# ANISOTROPIES AND MAGNETIZATION REVERSAL

## *1.1 General introduction to magnetic anisotropy*

The dependence of the internal energy of a system on the directions of the spontaneous magnetization is termed magnetic anisotropy [1]. The physical origins and relevant theory of magnetic anisotropy can be found in many classic textbooks on magnetism [2]. It is an experimental fact that ferromagnetic single crystals exhibit ‘easy’ and ‘hard’ directions of the magnetization. This magnetic anisotropy is one of the most important properties of magnetic materials. Physically, the two main sources of the magnetic anisotropy are the magnetic dipolar interaction and the spin-orbit interaction. The dipolar interaction has a long range character and results in a contribution to the anisotropy that closely depends on the shape of the sample. The spin-orbit interaction couples the spin (magnetism) of the electron with its orbit (movement), where the latter can be influenced by the crystal lattice. This results in a total energy which depends on the orientation of the magnetization relative to the crystalline axes, and which reflects

the symmetry of the crystal. In anisotropic materials, the easy axis, determined by various factors, refers to the energetically favorable direction of the spontaneous magnetization. The total magnetization of a system will prefer to lie along the easy axis. Some common magnetic anisotropies include: 1. magnetocrystalline anisotropy due to crystallographic symmetry of the material and the spin-orbit coupling; 2. Shape anisotropy due to the shape of the object that is caused by the dipolar interaction; 3. surface/interface (exchange) anisotropy caused by exchange coupling and lowered symmetry at the surface/interface; 4. magnetoelastic anisotropy caused by the spin-orbit interaction and the mechanical stress in a strained system. The hysteresis loops, coercivity, saturation magnetization, magnetic remanence, and other important magnetic parameters are strongly dependent on the magnetic anisotropies. In the following subsections each of these anisotropy terms will be discussed in more detail.

*(1) Magnetocrystalline anisotropy*

Magnetocrystalline anisotropy is the energy cost per unit volume to realign the magnetization from one crystallographic direction to another. The spin-orbital interaction is the primary source of the magnetocrystalline anisotropy. The energy density of the magnetocrystalline anisotropy for a cubic crystal can be expressed as:

$$E_a = K_0 + K_1(\alpha_1^2\alpha_2^2+\alpha_2^2\alpha_3^2+\alpha_3^2\alpha_1^2) + K_2(\alpha_1^2\alpha_2^2\alpha_3^2) + \cdots\cdots, \quad (1.1)$$

where $K_0$, $K_1$, $K_2$... are the anisotropy constants, which are material dependent, and $\alpha_i$ are the directional cosines of the angle between the magnetization and the principle crystalline axes. The intrinsic crystalline anisotropy is usually not preserved in amorphous materials, as the crystal field rapidly averages to 'zero'

on a macroscopic scale. In a typical case, the magnetic anisotropy gives rise to a uniaxial anisotropy in orientation. The expression for the energy density for a uniaxial anisotropy is:

$$E_K = K_{u1}\sin^2\theta + K_{u2}\sin^4\theta + \cdots\cdots, \quad (1.2)$$

where $\theta$ is the angle between the easy axis, and the direction of the magnetization $M_S$, and $K_{u1}$, $K_{u2}$, ... are the uniaxial anisotropy constants. If higher order anisotropy constants are negligible in comparison with $K_{u1}$, the magnetocrystalline anisotropy energy can be re-written as:

$$E_K = K\sin^2\theta, \quad (1.3)$$

where $K$ is an effective uniaxial anisotropy constant. This expression is very useful for studying single-domain particle. It shows two local energy minima at each pole ($\theta$=0° and 180°) separated by an energy barrier $KV$ at $\theta$=90°, where $V$ is the volume of the single-domain particle.

*(2) Shape anisotropy*

The magnetic shape anisotropy, also called dipolar anisotropy, is caused by the dipolar interaction. This interaction is long range, therefore it depends on the shape of the specimen. A uniformly magnetized single-domain spherical particle has no shape anisotropy, since the demagnetizing factors are isotropic in all directions. However for an elongated particle, the demagnetizing field is smaller in the long direction but larger in the short one. This is because the induced poles at the surface of the sample are further apart. The shape anisotropy energy of a uniform magnetized ellipsoid can be written as:

$$E_{shape} = \frac{1}{2}\mu_0(N_x M_x^2 + N_y M_y^2 + N_z M_z^2), \quad (1.4)$$

where $M_x$, $M_y$, $M_z$ and $N_x$, $N_y$, $N_z$ are the components of the magnetization and of the demagnetization

factors to the *x*, *y* and *z* axes. If the ellipsoid has long axis along the *z* direction, the anisotropy energy is:

$$E_{\text{shape}} = \frac{1}{2}\mu_0 M_S^2 (N_z cos^2\theta + N_x sin^2\theta) \ , \tag{1.5}$$

where $M_S$ is the saturation magnetization, $N_z$ and $N_x$=$N_y$ are the demagnetization factors along the polar and the equatorial axes, respectively. Further, since $N_x + N_y + N_z = 1$, the shape anisotropy energy and the uniaxial magnetocrystalline anisotropy energy can be combined to first order as:

$$E_{\text{total}} = [\frac{1}{2}\mu_0 M_S^2 (N_x - N_z) + K] sin^2\theta \ , \tag{1.6}$$

this equation is very useful in analysis of single domain particles with elongated shape as it takes into consideration both uniaxial magnetocrystalline anisotropy and shape anisotropy.

*(3) Surface/interface anisotropy*

The atomic symmetry of the surface or interface is substantially different from the bulk, therefore, the magnetic anisotropy is different at the surface and interface. Surface anisotropy is caused by the breaking of symmetry and a reduction in the nearest neighbor coordination at the surface. For small spherical particles with diameter *d* the effective magnetic anisotropy can be expressed as:

$$K_{eff} = K_V + \frac{S}{V} K_S \, , \tag{1.7}$$

where $S=\pi d^2$, and $V=\pi d^3/6$ are the surface and the volume of the particle. It is easy to see that by decreasing the particle size, the magnetic contributions from the surface will eventually become more important than those from the bulk of the particle, leading to a domination of the surface anisotropy over magnetocrystalline anisotropy and shape anisotropy energies. A special case of surface/interface anisotropy is the exchange anisotropy (exchange bias) that results when an antiferromagnetic (AF) layer

is grown in contact with a ferromagnetic (F) layer. Its name comes from the origin of the interaction which lines up the spins in a magnetic system, which is called the exchange interaction. When spin magnetic moments of adjacent atoms *i* and *j* makes an angle $\phi_{ij}$, the exchange energy, $w_{ij}$, between the two moments can be expressed as $w_{ij} = -2JS^2\cos\phi_{ij}$, where *J* is the exchange integral and *S* is the total spin quantum number of each atom. Typically, a shift in the hysteresis loop of the ferromagnet away from the zero field axis is observed in such F/AF bilayers. According to Eq. (1.7), the effect of the exchange anisotropy becomes more significant as the F layer becomes thinner.

*(4) Magnetoelastic anisotropy*

Upon magnetization, a previously demagnetized crystal experiences a strain that can be measured as a function of the applied field along the principal crystallographic axes, an effect called 'magnetostriction'. An important effect related to the magnetostriction is the inverse magnetostrictive effect, which is further related to the effects of stress on the magnetization of a magnetic material. In the presence of external/internal stresses, the magnetization and stress will be coupled via the magnetostriction to induce preferred directions for the magnetization. This stress-induced uniaxial anisotropy is called magnetoelastic anisotropy. Such localized induced uniaxial anisotropy will have the effect of hindering the magnetization rotation and domain wall movement, and the applied field will need to overcome the magnetoelastic anisotropy energy. Quantitatively, the anisotropy is often described by:

$$E = -\frac{3}{2}\lambda\sigma cos^2\theta \quad , \tag{1.8}$$

where $\lambda$ is the magnetostriction constant (can be positive or negative) and $\sigma$ is the stress. The angle $\theta$

measures the direction of the magnetization relative to the direction of uniform stress.

In the next sections, the magnetic anisotropies that are relevant to this thesis work will be discussed in detail.

## *1.2 Effect of anisotropy symmetry on the magnetization reversal*

### *1.2.1 Cubic magnetocrystalline anisotropy of Fe thin films*

Epitaxial Fe films on MgO or GaAs single-crystal substrates continue to be of great interest from an application as well as fundamental point of view [3,4]. For example, the Fe/MgO/Fe multilayer structure is widely applied in magnetic tunneling junctions [5]. Moreover, the Fe/MgO(001) system is an excellent candidate to investigate the correlation between atomic structure and magnetism in low dimensional heterostructures [6,7]. There has been much effort put into the fabrication of high-quality epitaxial Fe films. Advances in thin-film deposition techniques have allowed such films of a few monolayers to be epitaxially deposited, yielding a single crystal with the crystallographic axes well defined over many millimeters. The highly-ordered thin film gives rise to significant magnetocrystalline anisotropy, which further results in unique magnetization reversal processes.

Bulk Fe has a body-centered cubic (BCC) structure and the magnetocrystalline anisotropy is also cubic [8]. The energy state when $M$ aligns along the different crystal axes can be calculated according to Eq. (1.1). For instance, the energy states for the three principle axes (small index) are determined to be:

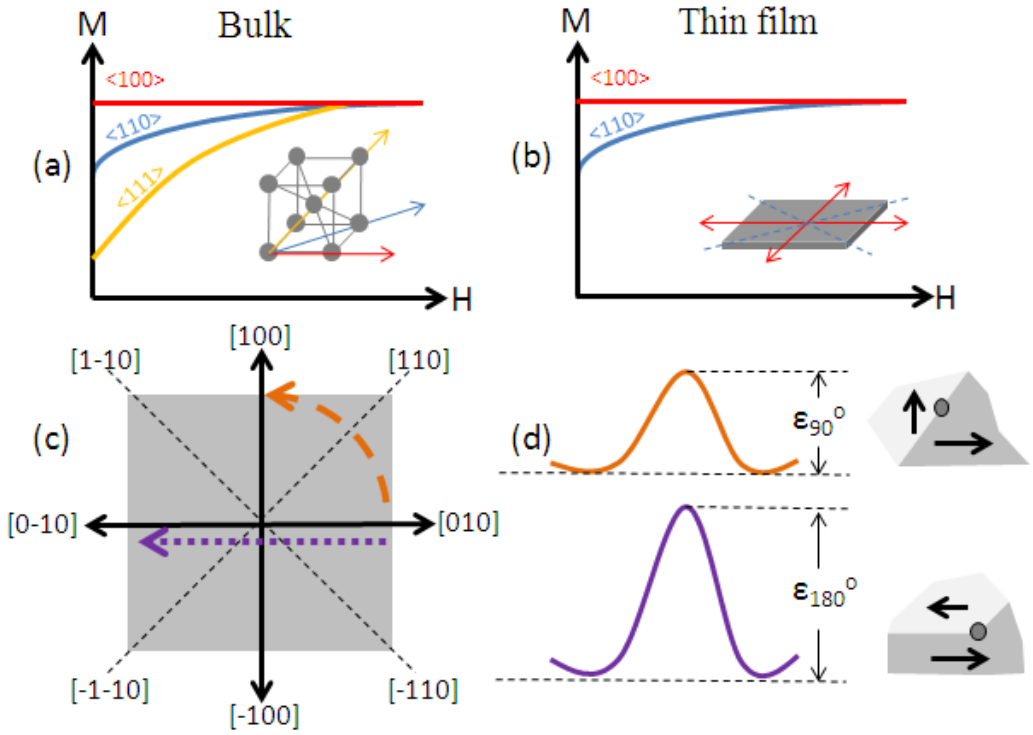


Figure 1.1: (a) Magnetizing curve along the principal axes for bulk Fe with a BCC structure. <100> are the easy and <111> are the hard directions. (b) Magnetizing curves for epitaxial Fe(001) thin films. (c) Top view of the anisotropy axes for epitaxial Fe(001) thin films, showing the easy axes (solid line) and hard axes (dash line). Dash arrows indicate the possible routes for magnetization reversal, either 90° or 180°. (d) The energy barrier associated with each type of reversal, 90° or 180°, caused by the pinning force of the defects in the film. The energy barrier for 180° reversal is always greater than the 90° reversal.

$E_{<100>} = K_0$, $E_{<110>} = K_0 + \frac{1}{4}K_1$, and $E_{<111>} = K_0 + \frac{1}{3}K_1$, (higher order anisotropy terms are neglected). As can be seen, $K_1$ accounts for the differences of the energy along different axes. In the case of Fe, the standard value is $K_1 = 4.8 \times 10^5$ erg/cm$^3$ [9]. Consequently, the magnetizing curve along different axes yields different results. Specifically, as indicated in Fig. 1.1(a), the <100> directions are the easiest axes for magnetization to align with but the <111> directions are the hardest. The <110> directions show an intermediate behavior. For epitaxial Fe thin films grown on MgO(001) substrate, and in the absence of any external field, the spins are confined to lie in the plane of the sample by shape anisotropy, and along the in-plane <100> crystallographic directions by magnetocrystalline anisotropy, Fig. 1.1(b). An

illustration of the easy ([100], [010], [-100], [0-10]) and hard ([110], [-110], [-1-10], [1-10]) axes for a single crystal thin film (viewed from the top) is shown in Fig. 1.1(c).

Upon the magnetization reversal by an applied field, a simple mechanism to consider is the coherent rotation of all the spins (a macro magnetization vector) from the positive to negative field direction. This mechanism was developed by Stoner and Wohlfarth (1948) [10] and then widely used by researchers afterwards for decades. If the $180^o$ coherent rotation applies to the single crystal Fe film, the magnetization must cross the hard axes (large energy barrier) at least two times during reversal, which would correspond to a very large switching field (coercivity) in the hysteresis loop. Actually, experiments by Cowburn *et al* [11] showed that the magnetic switching fields in these films are much smaller than that predicted by the coherent rotation protocol. Besides, by direct Kerr imaging, they revealed that the magnetization reversal mechanism is mainly magnetic domain wall (DW) nucleation and propagation along the different easy axes [12]. Specifically, respective domains along different easy axes can nucleate, grow and propagate across the whole film as the external magnetic field is applied, thus the magnetization does not have to cross any hard axes.

There are two types of magnetic switching observed: one is the $90^o$ reversal, i.e., from a certain easy axis to an adjacent axis (e.g, [010] → [100]); the other is the $180^o$ reversal, i.e., from one to the opposite easy axis (e.g, [010] → [0-10]). During the magnetic reversal, relevant magnetic domains tend to nucleate, grow and propagate due to the external driving force, i.e. external applied field. However, the nucleation and propagation are also hindered by an energy barrier, termed as the 'DW nucleation energy'. Only if the external field overcomes such energy barrier, the relevant domains can nucleate, grow and propagate, so the magnetization reversal occurs. Specifically, $\varepsilon_{90}{}^o$ is the domain wall nucleation energy for a $90^o$ reversal,

and so for $\varepsilon_{180}^{o}$. Both $\varepsilon_{90}^{o}$ and $\varepsilon_{180}^{o}$ are very small (~5 Oe in the form of effective field, $\varepsilon/M$, in CGS unit) [12], and are phenomenological parameters of dimension energy density. Physically, they correspond to the maximum pinning pressure that defects can exert on the initiation of a new domain wall, as illustrated in Fig. 1.1(d).

*Effects from a small uniaxial anisotropy*

If there are no additional anisotropies in the film, the four Fe easy axes are identical and have the same energy ground state. However, in reality, magnetic measurements on these films always indicate the existence of a small uniaxial anisotropy, $K_u$, apart from the dominant, fourfold magnetocrystalline anisotropy, $K_1$. This uniaxial component is a common feature for ferromagnetic films grown on various substrates and has been attributed to different origins, including surface dangling bonds [13], stepped substrate [14] and oblique-incidence deposition [15]. Consequently, the fourfold symmetry is broken and the energy ground state for [010] and [0-10] are lower than the other two easy axes, [100] and [-100]. This further results in significant changes on the magnetization reversal along different axes. Specifically, under an external field, $H$, the energy state of the four easy axes can be written as: $E_{[010]} = -K_u + MH\cos\phi$, $E_{[0\text{-}10]} = -K_u - MH\cos\phi$, $E_{[100]} = MH\sin\phi$, $E_{[\text{-}100]} = -MH\sin\phi$, where $\phi$ is the angle between the external field and the [010] axis and $M$ is the total magnetization. Following such analysis, the reversal should occur when the energy advantage in doing so is equal to the energy cost in nucleating and propagating a DW of the relevant type, $\varepsilon_{90}^{o}$ or $\varepsilon_{180}^{o}$. With this argument, the switching fields at each $\phi$ angle can be predicted [11] and the theory fits very well with experiments [16-19]. More details on this aspect will be

discussed in Chapter 3.

We also tested the theory by growing and measuring an epitaxial Fe thin film (10 nm) on MgO(001). Sample growth detail will be introduced in Chapter 2. With the collinear uniaxial anisotropy along [010], the magnetization reversal showed a one-step loop at [010] and [0-10] (Fig. 1.2(a)). However, it showed a

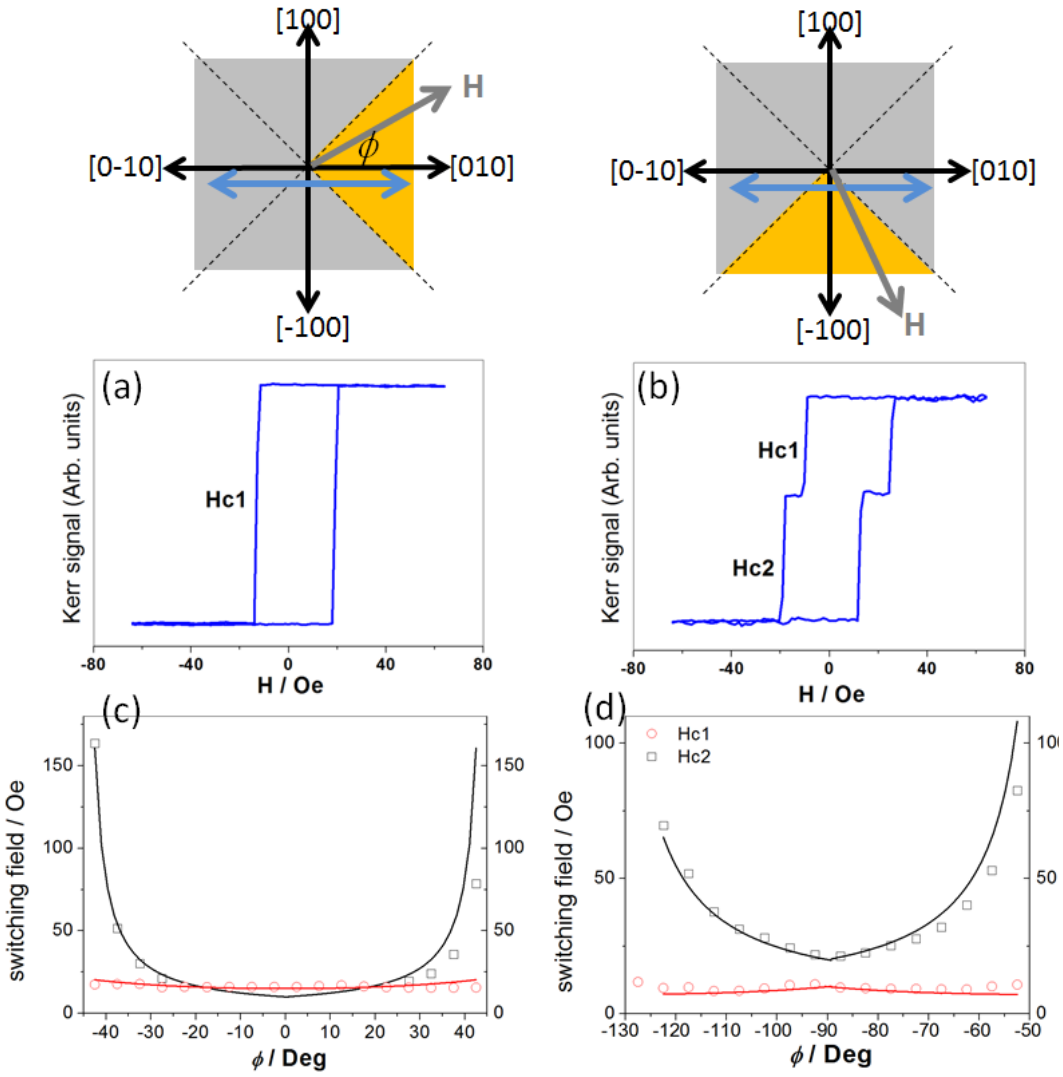


Figure 1.2: (a) Hysteresis loop measured for epitaxial Fe(15 nm) on MgO substrate, along the easy axis [010], which is also the direction of the uniaxial anisotropy. (b) Hysteresis loop measured along the easy axis [-100], displaying two-step feature. (c) Angle-dependent switching fields ($H_{c1}$, $H_{c2}$) at various angles close to [010], where $\phi$ = 0° indicate the [010] easy axis. (d) Angle-dependent switching fields ($H_{c1}$, $H_{c2}$) at various angles close to [-100], where $\phi$ = -90° indicate the [-100] easy axis. The angle-dependent data were fitted using the equations as reported in Ref. 12.

two-step loop along [100] and [-100] (Fig. 1.2(b)). Actually, the two-step behavior can be observed when measuring at most $\phi$ angles except for those close to the [010] and [0-10] directions. The angle-dependent switching fields were also plotted for the measuring angles close to [010] (Fig. 1.2(c)) and [-100] (Fig. 1.2(d)). As can be seen, the $\phi$-dependent reversal characteristics are essentially different for measuring angles close to [010] and [-100] easy axes, due to the symmetry breaking by the additional uniaxial anisotropy. Such uniaxial anisotropy has attracted much attention among researchers. The magnitude of this anisotropy is usually very small, on the order of 1% or less in the total magnetocrystalline anisotropy. The physical origin of this anisotropy can be stepped surface, dangling bonds, and non-normal incidence growth beam during deposition [12]. Various ways have been proposed to control such anisotropy, including oblique deposition, ion sputtering, and lithography patterning. [16-19].

### *1.2.2 Uniaxial shape anisotropy of nanowires*

The favored orientation for aligning the magnetization also depends on the shape of the magnetic object. A perfect spherical object has no shape anisotropy since all directions are identical. On the other hand, strong shape anisotropy comes into play when one dimension of the object overwhelms the others, for example, a long wire. For a planar nanowire (usually made by lithography), the magnetization lies in the plane and preferably along the long axis of the wire, even in the absence of an applied field. This can be easily visualized by considering the net magnetic charges accumulated on the surface for each scenario. As shown in Fig. 1.3(a), when the magnetization aligns along the wire, the positive and negative net charges only accumulate at each end and are well-separated. On the other hand, when the magnetization is

perpendicular, the magnetic charges accumulate along the whole length of the wire; additionally, the positive and negative charges are very close to each other which is energetically unfavorable. The energy difference for the two magnetizing configurations can be calculated via Eq. (1.6), once the dimension of the object is given. In summary, for a planar magnetic wire, the long axis is the easy axis for magnetization alignment. Magnetic measurement along this axis gives rise to a square hysteresis loop (easy axis behavior). In contrast, magnetizing perpendicular along the wire shows a slim magnetization curve with indiscernible hysteresis (hard axis behavior). The magnetic reversal is dominated by coherent rotation due to the fact that the external field acts as a torque perpendicular to the magnetization. Such a torque gradually drags the magnetization towards the external field orientation. The remnant magnetization (at $H = 0$) is zero, indicating the magnetization realigns along the wire direction as the field decreases to zero.

We also fabricated Fe planar nanowire arrays (300 nm in width) by nanoimprint lithography and measured the hysteresis loop along the two orientations. The sample fabrication details will be discussed in Chapter 4. Our experiments (Fig. 1.3(b)) showed good agreement with the theoretical predictions: a square loop with large coercivity, ~ 250 Oe, was observed when measuring along the wire arrays; a slim magnetization curve, with negligible coercivity but a large saturation field, was observed when measuring perpendicular to the wire arrays.

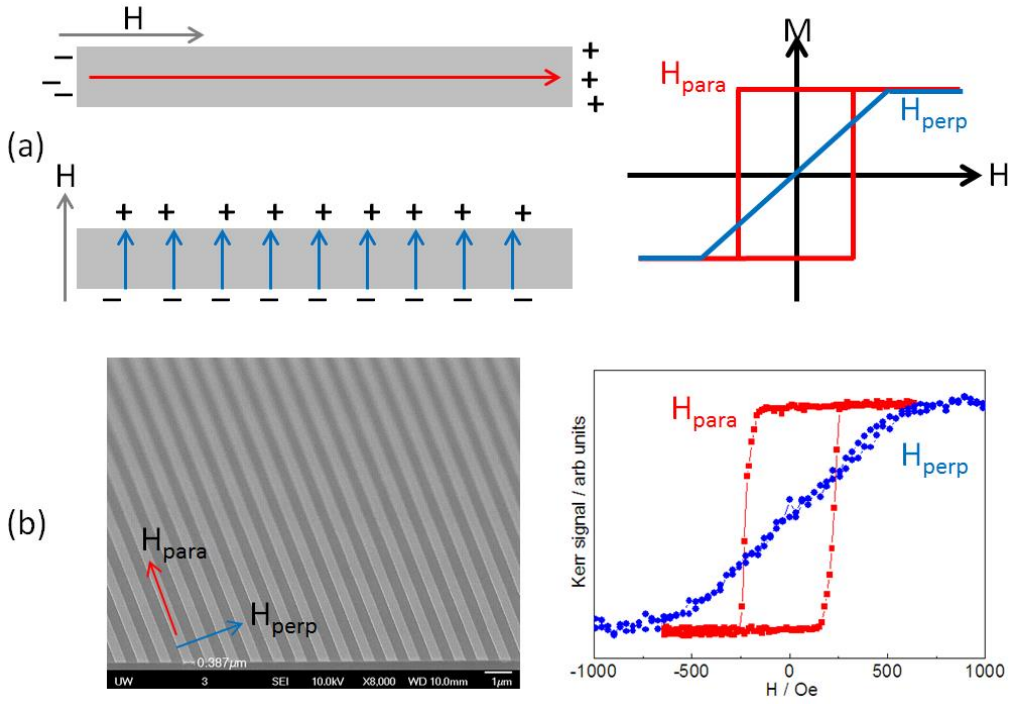


Figure 1.3: (a) Theory: due to the shape of the magnetic nanowire, magnetization reversal shows different behaviors when measuring parallel and perpendicular to the wire direction. (b) Experiments: scanning electron microscopy (SEM) image and the measured hysteresis loops, parallel and perpendicular to the wire, of the Fe nanowire arrays (300 nm in width) fabricated by nanoimprint lithography.

*DW detection*

Since the magnetization is constrained along the wire direction by the shape anisotropy, its reversal primarily occurs by nucleation of a perpendicular DW, followed by the propagation of such DW along the wire direction, as shown in Fig. 1.4. In this scenario, two opposite magnetic domains are separated by a 180$^{o}$ DW but remain magnetized along the wire direction. In a DW, the spin directions change rapidly within several nanometers thus the exchange energy is quite high. The cost of forming a DW is named DW energy. The magnitude of such DW energy density is on the order of several mJ/m$^2$. Technologically, the DW and its motion along the wire can be detected by direct imaging techniques [20], as well as

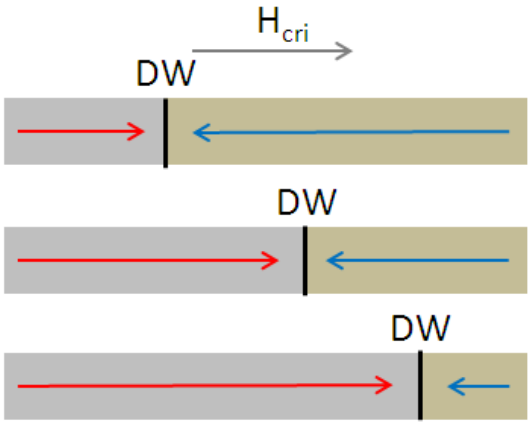


Figure 1.4: Illustration of the DW propagation along the magnetic nanowire under a critical driven field, $H_{cri}$.

magnetoresistance measurement of the DW intrinsic resistance [21]. Specifically, quantitative measurements of DW position in ferromagnetic nanostripes have been achieved using multilayers with giant or tunnelling magnetoresistances (GMR or TMR), in which the change of resistance depends on the relative magnetization orientation of the two ferromagnetic layers [22,23]. In materials with in-plane magnetization, the anisotropic magnetoresistance (AMR) is usually used to detect the presence of DWs, which can indicate whether or not the DW is present in between the contacts [24]. The AMR originates from the anisotropic spin-orbit coupling effect that results in a resistance maximum when the magnetization is aligned along the direction of the current, and a minimum when they are mutually orthogonal. More details on AMR and its application will be discussed in Chapter 3 and Chapter 5. For perpendicularly magnetized nanowires, extraordinary Hall effect (EHE) can be used, which points out the presence of a DW within a Hall cross [25]. Recently, it has also been shown that the contribution of magnons to the resistivity, i.e., the magnon magnetoresistance (MMR), allows for measuring the position of a DW in a FePt nanowire with perpendicular magnetization [26].

One of the interesting physical parameters related to the DW motion is the velocity of the DW when it propagates along the wire. To probe this velocity, an experiment using giant magnetoresistance (GMR) effect was done by Kasatani and co-workers [27,28], by growing a trilayer Fe/Au/NiFe nanowire with standard 4-probe connecting electrodes. Due to the GMR effect, the low and high resistance values can be observed when the Fe and NiFe magnetizations align parallel and antiparallel, respectively. Since the switching fields for Fe and NiFe are different, the change of resistance from low to high (and vice versa), observed in the normal *R-H* curve, indicates the magnetization reversal of each layer. In order to detect the DW velocity for the Fe layer, for example, the external field was set and held at the critical field for Fe reversal, and an oscilloscope (with GHz sampling rates) was used to resolve the time-dependent voltage change. In the experiment, the authors found the voltage changed (reflecting the Fe reversal) linearly within 1 μs upon a traveling distance of 413 μm. As a result, a DW velocity of ~ 500-1000 m/s was therefore derived.

*Internal structure of a DW*

A DW achieves a magnetization transition from one direction to the other in a relative short range, in tens of nm. How the spins make the transition determines the internal structure of a DW. With advanced imaging techniques and magnetic simulations, the internal structures of the DW were also investigated [29]. Two different types of internal structures, transverse and vortex, have been observed. In a transverse DW, Fig. 1.5(a), spins within the DW gradually rotate $180^{o}$ in the plane from left to the right. At the center of the DW, a perpendicular magnetization component is formed. This perpendicular component

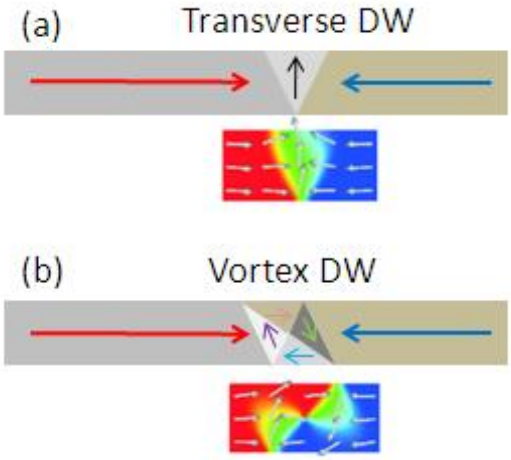


Figure 1.5: Illustration of (a) transverse and (b) vortex DW [29].

also indicates magnetic charges accumulated along the wire width at the local area, generating certain magnetostatic energy. In order to reduce such energy, a vortex DW is favored instead of the transverse configuration, Fig. 1.5(b). For the vortex DW, the local spins gradually rotate $360^{o}$ in the plane. Along the wire edges, the spins are aligned parallel to the wire direction, developing negligible magnetostatic energy. The formation of different DWs strongly depends on the intrinsic properties of the materials as well as the dimensions of the wire [29]. A simple diagram of the DW type on the wire dimensions (width, $W_b$ and thickness, $t_b$) is introduced in [29]. Generally speaking, transverse DWs (with net magnetic charges along the edges) are more often observed in narrow and thin planar wires, while vortex DWs (without net charges) are often encountered in wide and thick ones due to magnetostatic energy minimization. For a ferromagnetic long strip with weak magnetocrystalline anisotropy (e.g. polycrystalline NiFe wire), the transition from transverse to vortex DW occurs at ~13 nm thickness for 100 nm wire width.

*Pinning and driving the DW*

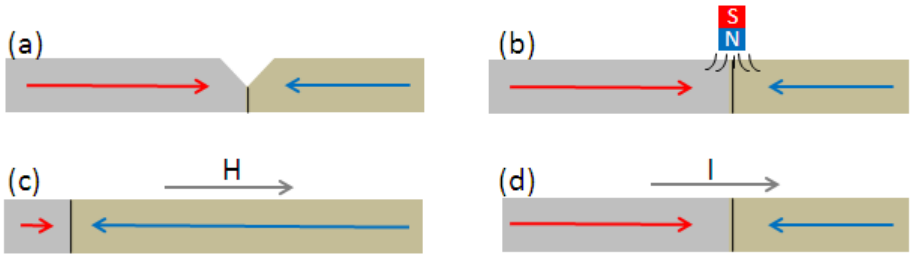


Figure 1.6: (a) DW pinning by notch (example can be found in Ref. 31). (b) DW pinning by magnetostatic interaction (example can be found in Ref. 32). (c) DW driven by magnetic field (example can be found in Ref. 33). (d) DW driven by current (example can be found in Ref. 34).

Manipulating the DW motion is not easy, as the DW propagates along the wire quite fast. In the past decades, researchers have been developing ways for both pinning and driving the DWs. Two effective ways for DW pinning are the 'pinning by notch' [30,31] and 'pinning by magnetostatic interaction' [32]. The first method requires a local modification on the shape of the wire, i.e., creating a notch during the sample fabrication process. Technically, this can be done by changing the lithography mask (photolithography) or design (e-beam lithography). Such a local 'defect' acts as an artificial pinning center for the DW during its movement, Fig. 1.6(a). The second method does not require any shape modification of the wire itself. The DW is pinned via the magnetostatic interaction between the DW and a nearby small magnetic entity. The small magnetic entity can be created also by lithography and acts as a magnetic dipole that generates a small local magnetic field. The DW can be trapped at the local field during its propagation, Fig. 1.6(b).

Artificial driving of the DW motion is the key to any future DW devices. The field-driven DW motion is the most common driving approach, however, it also shows certain speed limitations [33] which may hinder the performance of future 'super-computers' (with information processing speed in GHz level). Fortunately, researchers have found that the DW motion can be also controlled by an electric

current. Such current-driven DW motion has even better performance than the field-driven approach [34]. A real-space experiment on the current-driven DW motion can be found in [34].

### *1.2.3 Unidirectional exchange anisotropy of ferromagnetic / antiferromagnetic bilayers*

Discovered in 1956 by Meiklejohn and Bean [35], exchange bias (EB) refers to the unidirectional pinning of a ferromagnet by an adjacent antiferromagnet. The antiferromagnet, via the F/AF exchange coupling, gives rise to a unidirectional easy axis for ferromagnetic magnetization. Coupling of the F to the AF can significantly alter the magnetic behavior, e.g., the hysteresis process and the domain structure. The most prominent effect found in these F/AF bilayers is the shift of the hysteresis loop of the F layer. In the last several decades, there has been considerable interest in exchange bias [36-41].

Exotic properties have been revealed with the exchange bias including enhanced coercivity, asymmetric magnetic reversal and rotatable interfacial AF spins. The hysteresis loop shift can be useful to control the magnetization in devices such as a magnetic read head. The change in magnetic properties arises from an established order in the AF in the presence of a F while cooling the AF below its ordering temperature (Neel temperature, $T_N$). By itself, the AF can order in any one of its degenerate energy minima. When it is coupled to an F layer, however, it chooses the state that minimizes the energy due to the coupling to the F. Furthermore, the AF is only weakly coupled to external fields, so it retains a 'memory' of the F direction at the time when the AF order was set, even when the F magnetization is later rotated. This coupling is often thought of as a unidirectional anisotropy or as a fixed magnetic field acting at the interface, as indicated in Fig. 1.7.

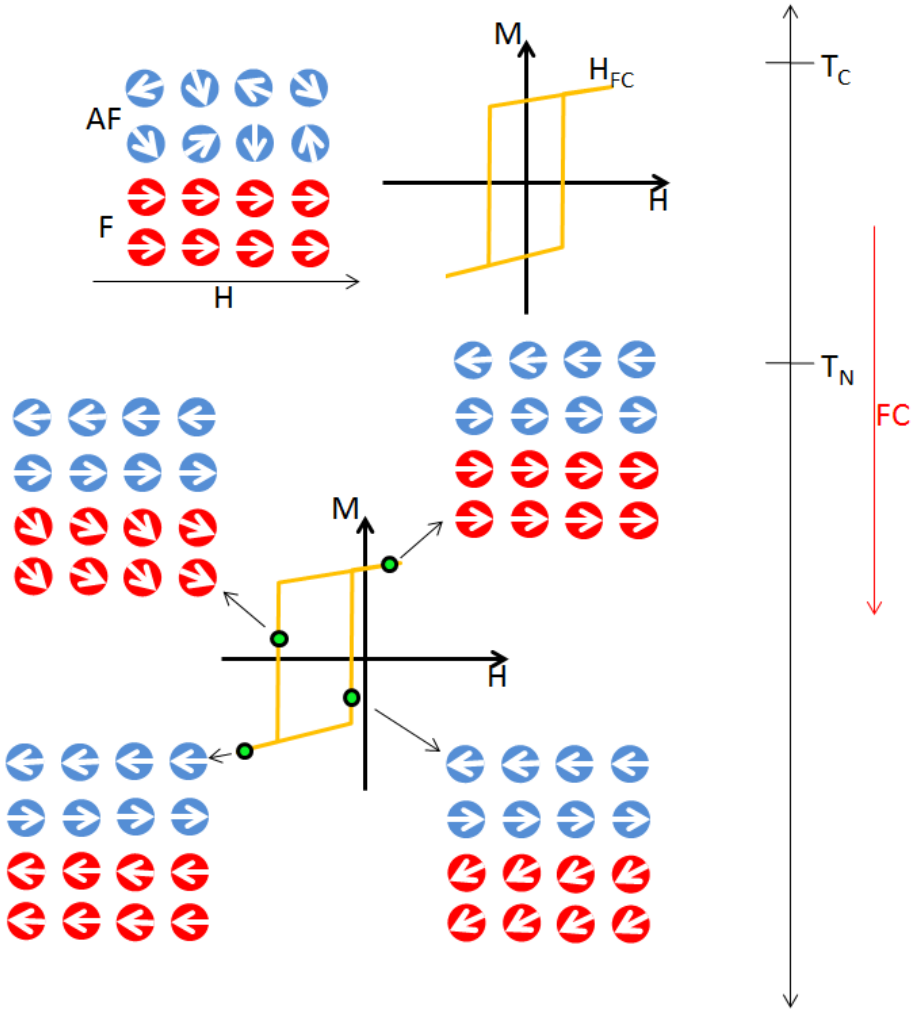


Figure 1.7: Conceptual illustration of the mechanism of exchange bias (after Meiklejohn and Bean). M is the magnetization, H is the externally applied magnetic field, T is the temperature, $T_C$ is the ordering (Curie) temperature of the ferromagnet (F), $T_N$ is the ordering (Neel) temperature of the antiferromagnet (AF), and $H_{FC}$ is the cooling field. At a temperature such that $T_N < T < T_C$, the F is ordered and the AF is disordered. Below $T_N$, the AF orders, which causes the exchange bias.

Although the first exchange bias was discovered in Co/CoO particles, exchange bias was extensively studied in layered thin films structures due to their potential applications. Typical F materials include Fe, Co, Ni, NiFe, FeCo, etc. Common AF materials have been the rocksalt-structure AF oxides like CoO, NiO, and the rocksalt-structure intermetallics like IrMn, FeMn, and some other nonmetallic materials like $FeF_2$. The samples are normally prepared by physical deposition, such as magnetron sputtering. Desirable

properties for an exchange bias material include a Neel temperature above room temperature, a large magnetocrystalline anisotropy and stable chemical structure. However, they are not a necessity for observing exchange bias. In the past decades, much work on exchange bias has studied polycrystalline thin film bilayers with weak magnetocrystalline anisotropy and disordered interface. The hysteresis loop shift was observed and studied, but fundamental properties of exchange bias were poorly revealed in these polycrystalline samples. Epitaxial growth, such as the work described in this thesis, has provided unique insights into these subjects.

### *1.2.4 Existing theories of Exchange bias*

We will discuss exchange bias in more detail since it is the main focus of this thesis. We first review the existing theories of the exchange bias.

#### *The ideal Meiklejohn-Beam model*

For the polycrystalline EB bilayers, the Stoner-Wohlfarth [10] model was commonly applied for interpretations of the observed exchange bias properties. This model is simple but has showed good agreement with many experiments. In this model [41], in order to account for the orientation of the magnetic moments, the minimum energy state is provided by analysis of the different contributing terms to the total magnetic energy: Zeeman term, anisotropy terms, and exchange coupling terms. This evaluation is performed by minimization of the total magnetic energy with respect to various parameters.

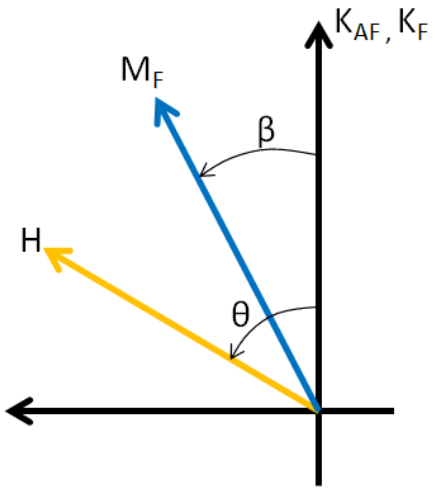


Figure 1.8: Schematic view of the angles and vectors used in the ideal Meiklejohn and Beam model. $K_{AF}$ and $K_F$ are the anisotropy of the AF layer and F layer, respectively. $\beta$ is the angle between magnetization $M_F$ of the F layer and the anisotropy direction. $H$ is the external magnetic field that can be applied at any direction $\theta$ with respect to the field cooling direction ($\theta = 0$).

It is assumed that all spins are confined in the film plane and that the response of the magnetization to an applied field is uniform. In other words, the spins coherently rotate during the variation of the external field. According to Fig. 1.8, the equation for the energy per unit area in the magnetic system can be written as:

$$E_{tot} = -\mu_0 H M_F t_F \cos(\theta - \beta) + K_F t_F \, sin^2(\beta) - J_{eb}\cos(\beta) \ , \tag{1.9}$$

where $J_{eb}$ is the interfacial exchange energy per unit area, and $M_F$ is the saturation magnetization of the ferromagnetic layer. $K_F$ and $t_F$ are the anisotropy and thickness of the F layer. $\beta$ is the angle between magnetization and $K_F$. By minimizing the total energy, two types of solutions are obtained. The switching fields $H_{c1}$ and $H_{c2}$ are extracted from the stability equation for $\beta=0$ and $\beta=\pi$:

$$H_{c1} = -\frac{2K_F t_F + J_{eb}}{\mu_0 M_F t_F} \ , \ H_{c2} = -\frac{2K_F t_F - J_{eb}}{\mu_0 M_F t_F} \ , \tag{1.10}$$

Using the expression above, the coercive field $H_c$ of the loop and the displacement $H_{eb}$ can be calculated according to:

$$H_c = \frac{-H_{c1}+H_{c2}}{2} \text{ and } H_{eb} = \frac{H_{c1}+H_{c2}}{2} \ , \tag{1.11}$$

which further gives:

$$H_c = \frac{2K_F}{\mu_0 M_F} \text{ and } H_{eb} = -\frac{J_{eb}}{\mu_0 M_F t_F} \ . \tag{1.12}$$

The $H_{eb}$ in the equation gives the expected characteristics of the hysteresis loop for an ideal case, especially the linear dependence on the interfacial energy $J_{eb}$ and the inverse dependence on the ferromagnetic layer thickness $t_F$. Therefore this equation serves as a guideline to which experimental values are compared. However, the values of $H_{eb}$ predicted from (1.12) are usually much higher than the experimentally obtained values. This is mainly due to the fact that many complexities of the magnetization reversal and detailed interfacial coupling configurations are neglected in this approach.

*Mauri model*

The model of Mauri *et al* [42] proposes that the AF spins develop a DW parallel to the interface. The motivation to introduce such a DW was to explore a possible reduction of the exchange bias field resulting from the Meiklejohn-Beam model. The Mauri model assumes single domain states for both F

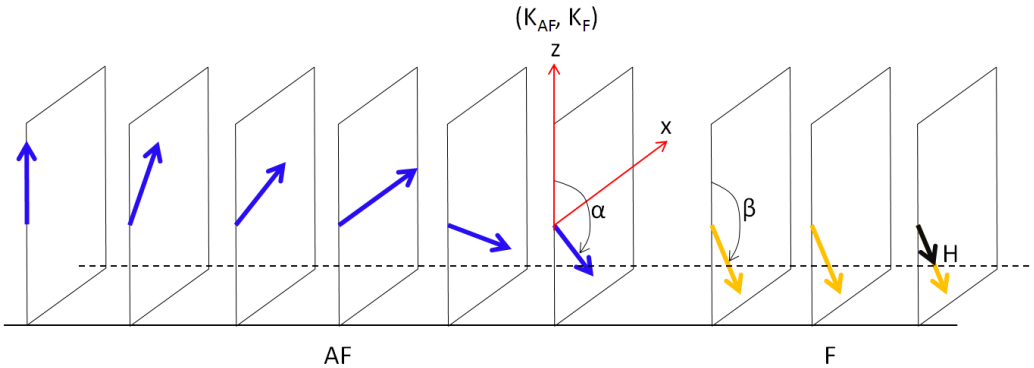


Figure 1.9: Illustration on the Mauri model for the interface of a thin ferromagnetic film on a antiferromagnetic substrate [42].

and AF layer and a uniaxial anisotropy for the AF layer. Schematically, as illustrated in Fig. 1.9, the F spins rotate coherently, when the applied magnetic field is swept as to measure the hysteresis loop. The first interfacial AF monolayer is oriented away from the F spins making an angle α with the field cooling direction and with the anisotropy axis of the AF layer. The next AF layers are oriented away from the interfacial AF spins as to form a domain wall parallel to the interface. (Note that only one sublattice is depicted in Fig. 1.9). Therefore the total magnetic energy can be written as:

$$E = -\mu_0 H M_F t_F \cos(\theta - \beta) + K_F t_F \, sin^2(\beta) - J_{eb} \cos(\beta - \alpha) - 2\sqrt{A_{AF} K_{AF}(1 - cos\alpha)}, \quad (1.13)$$

where the first term is the Zeeman energy, the second term is the anisotropy term of the F layer, the third term is the interfacial exchange energy, and the last term is the energy of the partial DW. Mauri *et al* [42] have calculated the magnetization curves by numerical minimization of the total magnetic energy and came up with the following expressions for the exchange bias field:

$$H_{eb} = \begin{cases} -J_{eb}/\mu_0 M_F t_F \,, & for\ J_{eb}/2\sqrt{A_{AF} K_{AF}} \ll 1 \\ -2\sqrt{A_{AF} K_{AF}}/\mu_0 M_F t_F \,, & for\ J_{eb}/2\sqrt{A_{AF} K_{AF}} \gg 1 \end{cases} \quad (1.14)$$

where $A_{AF}$ is the exchange stiffness and $K_{AF}$ is the AF anisotropy. In the strong coupling case ($J_{eb}/\sqrt{A_{AF} K_{AF}} \ll 1$), the expression is similar to the value given the Meiklejohn-Beam model. When the coupling is weak ($J_{eb}/\sqrt{A_{AF} K_{AF}} \gg 1$), the Mauri model gives rise to a reduced exchange bias field which is practically independent of the interfacial exchange energy, but depends on the parameter $\sqrt{A_{AF} K_{AF}}$ and the parameters of the F layer.

*Malozemoff random-field model*

Malozemoff proposed in 1987 a mechanism for the exchange bias assuming a random nature of exchange interactions at the F/AF interface [43,44,45]. Specifically, the chemical roughness or alloying at the interface that is present for any realistic bilayers causes lateral variations of the exchange field acting on the F and AF layers. The random field results in AF domains due to the energy minimization. The Malozemoff model is an approach from a mesoscopic scale for surface magnetism.

The idea of this model is illustrated in Fig. 1.10, where a DW is driven by an applied field, $H$. Assuming the interfacial energy of the two domains are different, i.e. $\sigma_1$ and $\sigma_2$ respectively, the exchange field can be then estimated by the equilibrium condition between the applied field pressure $2HM_Ft_F$ and the effective pressure from the interfacial energy $\Delta\sigma$:

$$H_{eb} = -\frac{\Delta\sigma}{2M_F t_F} \ , \tag{1.15}$$

where $M_F$ and $t_F$ are the magnetization and thickness of the F layer. For an ideally compensated interface, the exchange bias field is zero. For an ideally uncompensated interface, there is an interfacial energy difference $\Delta\sigma = 2J_i / a^2$, where $J_i$ is the exchange coupling constant across the interface, and $a$ is the lattice parameter of the AF layer. However, the resulting exchange bias $H_{eb} = J_i / a^2 M_F t_F$ is several orders of magnitude greater than the experimental observation. To address such a large discrepancy, the random field at the interface was proposed. Specifically, the roughness on the atomic scale of a compensated interface can lead to uncompensated spins. Each interface irregularity (e.g. a single mono-atomic 'bump') will give a local energy difference between domains whose sign depends on the particular location of the irregularity and whose magnitude is on the average $2zJ$, where $z$ is a number of order unity. For a random interface, the local unidirectional interface energy, $\sigma_l = \pm zJ / a^2$, will also be random and its average $\sigma$ in a region $L^2$ will go down statistically as $\sigma = \sigma_l / \sqrt{N}$, where $N = L^2 / a^2$ is the number of sites projected onto

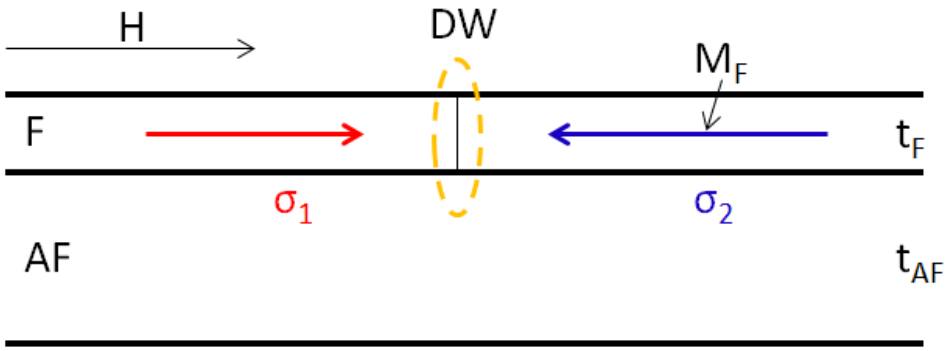


Figure 1.10: Schematic side view of a F/AF bilayer with a ferromagnetic wall driven by an applied field *H* [43].

the interface plane.

With the random field provided by the interface roughness, it is energetically favorable for the AF to break up into domains. By further analyzing the magnetic domains in the presence of random fields, a characteristic length $L$ of the frozen-in AF domains is obtained: $L \approx \pi\sqrt{A_{AF}K_{AF}}$. Therefore flipping the F orientation causes an energy change per unit area of $\Delta\sigma = 4zJ / \pi aL$, which further leads to the expression for the EB field [43]:

$$H_{eb} = \frac{2z\sqrt{A_{AF}K_{AF}}}{\pi^2 M_F t_F} \quad . \tag{1.16}$$

The EB fields estimated by the Malozemoff model are usually in good agreement with experimental values. The only difference between theory and experiment is that the AF domains can occur and vary in size and orientation after the very first magnetic reversal experimentally, however, they are assumed to develop during the field cooling procedure within the Malozemoff model.

*Domain-state model*

The domain-state model (DS) introduced by Nowak *et al* [46,47] is a microscopic model in which disorder is introduced via magnetic dilution at the interface as well as at the bulk of the AF layer. The AF layer is viewed as a diluted Ising antiferromagnet in an external magnetic field. In zero field, the system undergoes a phase transition from a disordered paramagnetic state to an ordered antiferromagnetic state at the Neel temperature. At low temperatures, the diluted AF layer develops a domain state phase. The formation of the AF domains originates from the statistical imbalance of the impurities of the two AF sublattices within any finite region. Such imbalance leads to a net magnetization which couples to the external field. The formation of a DW can be minimized if the DW passes through nonmagnetic defects at

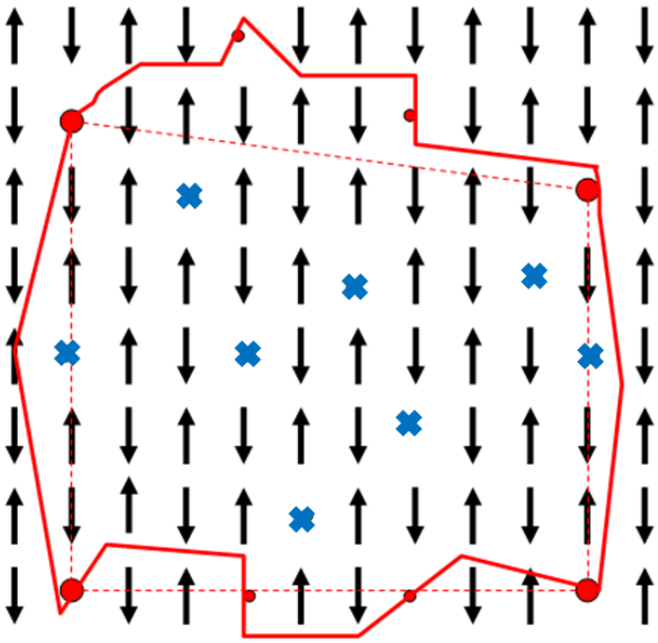

Figure 1.11: Illustration of the defects-mediated DW formation. When the defect concentration is very low (large dots), DW are not able to form since the formation of a DW (dashed line) would break the exchange interactions of many spin couples. This corresponds to the level of dilution which leads to small exchange bias field. As the defects concentration increases (small and large dots), it is energetically favorable to form a DW (solid line) that passing through these non-magnetic defects. This corresponds to the level of dilution where we get enhanced exchange bias field. However within the domain there are almost no defects. As the defects concentration further increase (dots and crosses), new defects can fill inside the domain. As a result, exchange bias field would decrease rapidly due to the reduced net magnetization of the AF domain that couples to the F layer.

a minimum cost of exchange energy. This is schematically illustrated in Fig. 1.11.

Based on the above idea, Nowak *et al* performed Monte Carlo simulation in a scenario of an F layer exchange coupled to a diluted AF film. Assuming that all spins in the F remain parallel during the reversal and some net magnetization of the interface layer of the AF remains constant during the reversal, the estimated EB field can be written as:

$$l\mu H_{eb} = J_{INT} m_{INT} \ , \tag{1.17}$$

where $l$ is the number of the F layers, $J_{INT}$ is the interface exchange constant and $m_{INT}$ is the interface magnetization of the AF per spin. For an ideal uncompensated interface ($m_{INT}$ =1) the exchange bias is too high, where for an ideally compensated interface the exchange bias is zero. Within the DS model, the interface magnetization $m_{INT}$ <1 is neither a constant nor a simple quantity. It is replaced by $m_{IDS}$, which is a measure of the irreversible domain state magnetization of the AF interface layer and is responsible for the EB field. By simulation of hysteresis loops we can obtain $m_{IDS}$ under different doping concentrations and thus get proper values of exchange bias field. Overall, the DS model is strongly supported by experimental observations where nonmagnetic impurities are added to the AF layer in a controllable fashion [48,49].

*Kim-Stamps approach*

The approach of Kim and Stamps [50,51] extends the planar DW (in the Mauri model) to the concept of a partial DW in the AF layer. Starting from the saturation state, the F spins aligned with the external field while the AF spins are collinear with the easy axis. As the field is reduced and reversed, the AF pins

the F layer by interfacial exchange coupling. When it is energetically more favorable to deform the AF, rather than breaking the interfacial coupling, a partial wall twists up as the F rotates. Ideally, the winding and unwinding of the partial DW is reversible. The value of the EB field is similar to the one given by the Mauri model. On the other hand, the coercivity is proposed to be related to the DW pinning at magnetic defects, providing an energy barrier for DW processes that controls the coercivity.

Kim and Stamps proposed that the defects in magnetic system can also be expressed as a kind of anisotropy, which does not have a simple description mathematically. For simplicity, Kim and Stamps first analyzed pointlike defects in the AF. Irreversible transitions are made possible by an energy barrier arising from magnetic impurities in the AF. The influence of a pointlike impurity at an arbitrary position in the AF is analyzed as a small local variation in the uniaxial anisotropy at some distance $x_d > 0$ from the interface,

$$K_u(x) = K_{u0}\{1 - \rho\delta[\frac{x - x_d}{\lambda}]\} \quad , \tag{1.18}$$

which represents a pointlike (delta function) reduction $\rho$ in the uniaxial anisotropy energy $K_u$ at a distance $x_d$ from the interface. $K_{u0}$ is the defect-free uniaxial anisotropy. The parameter $\lambda$ will be discussed later. The energy arising from deformations to the AF spin structure is given by:

$$E_{af}[\varphi(x)] = \int_0^\infty dx[A(\frac{\partial\varphi}{\partial x})^2 + K_u(x)\sin^2\varphi], \tag{1.19}$$

where $A$ is the exchange stiffness and $\varphi(x)$ represents the angle of the AF staggered magnetization relative to the easy axis. If $\rho$ is sufficiently small, the solution to the problem $\delta E/\delta\varphi = 0$ is valid to first order. Substituting this solution $\varphi^*(x)$ into Eq.(1.19) gives a modified form for the twist energy:

$$E_{af}(\varphi_0)/\sigma_w = \frac{1}{2}(1-\cos\varphi_0) - \frac{\frac{1}{4}\rho\sin^2\varphi_0}{[\cosh\left(\frac{x_d}{\lambda}\right)+\cos\varphi_0\sinh\left(\frac{x_d}{\lambda}\right)]^2}, \quad (1.20)$$

where $\varphi_0$ is the interface AF spin angle, $\lambda \equiv \sqrt{A/K_{u0}}$ is a characteristic length, and $\sigma \equiv 4\sqrt{AK_{u0}}$ is the energy of a $180^0$ DW. Depending on the position and density of the defects, a local minimum (or maximum) in the AF energy can appear, as indicated in Fig. 1.12. The minimum corresponds to the point at which the partial DW center coincides with the position of the defects. In other words, by centering the wall at $x_d$, the anisotropy energy cost is reduced. As such, the wall becomes pinned when $x_c = x_d$, in which $x_c$ is the center of the wall. In summary, the AF energy acquires, besides the DW energy, another term which depends on the concentration of the magnetic defects. These defects reduce the anisotropy locally and lead to an overall reduction of the AF energy (Fig. 1.12). This reduction of the AF energy leads to a local energy minimum for certain defect positions relative to the interface.

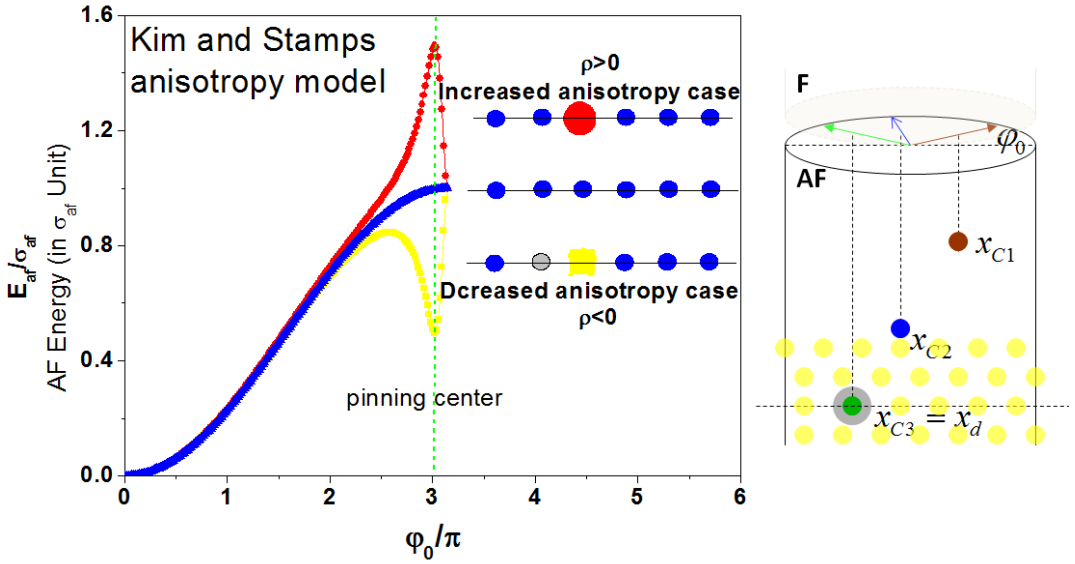


Figure 1.12: Angular dependence of the partial DW energy with point defects. The normalized AF energy, $E_{af}/\sigma_{af}$, is shown as a function of interface twist angle $\varphi_0$ for positive, negative, and zero impurity strengths $\rho$. Figure on the right shows the center of the partial DW, $x_{c3}$, coincides with the position of the defects, $x_d$. In this case, the local minimum of the AF energy is achieved [50].

*Spin-glass model*

In the Spin-glass (SG) model, a unique magnetic state is considered at the interface which is magnetically disordered behaving similar to a SG system [52]. Within this model, the AF layer is assumed to contain two types of AF states, i.e. one type has a large anisotropy with the direction ruled by the AF spins, and the other type with a weaker anisotropy which allows some AF spins to rotate with the F spins during reversal. The interfacial part of the AF is a frustrated region (spin-glass like) being responsible for the increased coercivity. The physical origins of the low anisotropy region can be chemical intermixing, deviations from stoichiometry, structural inhomogeneities, low coordination, etc. In addition, structural and magnetic roughness can also provide a weak AF interface region. The SG region can be visualized as a collection of spins which remains in a frozen disordered state even at low temperatures. Such partial random state can be introduced in the Meiklejohn-Beam model as an effective uniaxial anisotropy. The free energy can be written as:

$$E_{tot} = -\mu_0 H M_F t_F \cos(\theta - \beta) + K_F t_F \sin^2(\beta)$$

$$+K_{AF} t_{AF} \sin^2(\alpha) + K_{SG}^{eff} \sin^2(\beta - \gamma) - J_{eb}^{eff} \cos(\beta - \alpha) \ , \qquad (1.21)$$

where $K_{SG}^{eff}$ is an effective uniaxial SG anisotropy related to the frustrated AF spins, $J_{eb}^{eff}$ is the reduced interfacial exchange energy, and $\gamma$ is the average angle of the effective SG anisotropy. $K_{AF}$ is the anisotropy constant of AF layer. When the $K_{SG}^{eff}$ parameter is zero, the system behaves ideally as described by the Meiklejohn-Beam model. In the other case, when the interface is disordered we can relate the SG effective anisotropy to the available interfacial coupling energy as:

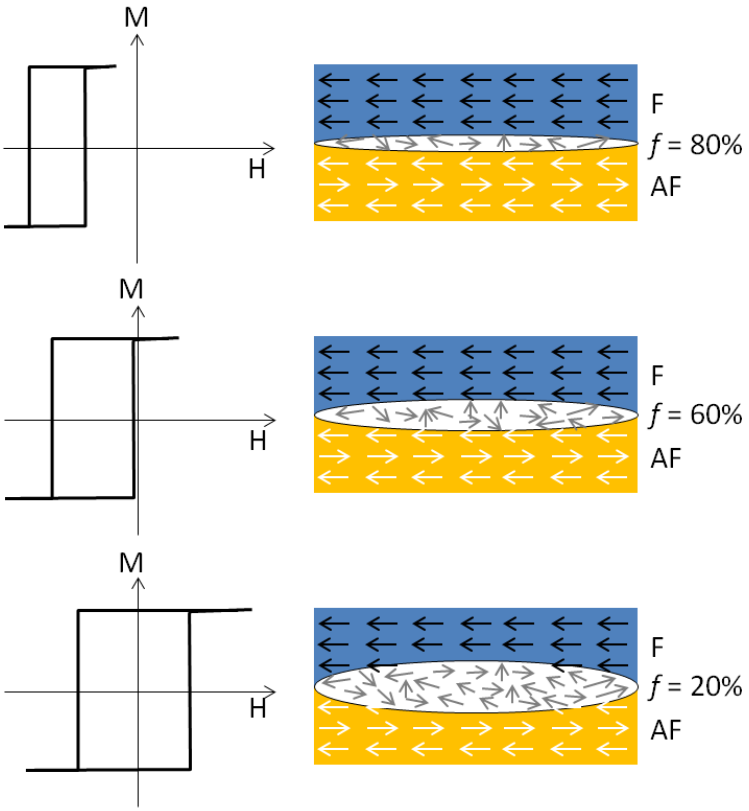


Figure 1.13: Schematic illustration of the effect of the conversion factor *f* on the hysteresis loop and exchange bias. Spin configurations of the bilayer structure is depicted in the right column [52].

$$K_{eff} = (1-f)J_{eb} \;\; and \;\; J_{eb}^{eff} = fJ_{eb} \quad , \tag{1.22}$$

where $J_{eb}$ is the total exchange energy and $f$ is a conversion factor describing the conversion of interfacial energy (in the form of effective field) into coercivity. Physically it also defines the fractional order at the interface. Specifically, $f$ = 1 indicates a perfect interface and $f$ = 0 indicates perfect disorder. Another important parameter with this model is the *R*-ratio, defining the strength of the AF layer:

$$R \equiv \frac{K_{AF}t_{AF}}{J_{eb}^{eff}} = \frac{K_{AF}t_{AF}}{fJ_{eb}} \quad . \tag{1.23}$$

The phase diagram for the EB field and coercivity as function of the *R*-ratio is often plotted to study the effect of *f*, which further allows us to compare directly the SG model and the Meiklejohn-Beam model. The above equations can be solved numerically however it does not provide a simple expression for EB

field. However, the EB field is directly proportional to $f$ and their relationship can be qualitative understood by the illustration in Fig. 1.13.

The SG model provides a visual pathway to understand the dual behaviors, i.e. rotatable and pinned mechanisms, of the interface AF spins. Recently, using element specific techniques such as x-ray magnetic dichroism (XMCD), both frozen and rotatable AF spins can be studied [53,54,55,56,57,58]. The main conclusion is that the frozen-in spins are responsible for the loop shift whereas the AF rotatable spins result in enhanced coercivity. These experiments provide strong and direct evidence to the basic assumptions and main conclusions of the SG model.

*Koon and Schulthess-Butler approach*

Koon [59] introduced a 'spin-flop' model and presented a particular issue of exchange bias with compensated F/AF interface. On the basis of a Heisenberg model, he calculated the interfacial energy density as a function of the angle between the F spins and the AF spins. The key result was the perpendicular coupling of F and AF spins, being the ground state configuration for a compensated interface (Fig. 1.14). In addition, Koon also showed that the magnetic moments in the AF exhibit canting relative to the AF bulk easy axis. The effect of this canting is that there will be a small net moment perpendicular to the AF easy axis. This moment will couple to the F moment, and leads to the exchange bias.

While the work of Koon is relevant in establishing the right interfacial magnetic structure, it actually fails to yield EB as properly pointed out later by Schulthess and Butler [60]. They did a more complete

calculation which allow for out-of-plane spins, and including dipole-dipole interactions. They found that a pure spin-flop coupling for Heisenberg spins, as well as the canted interface structure, does not give rise to exchange bias by itself. This spin-flop coupling can only account for the enhanced coercivity. Schulthess and Butler used a combination of spin-flop coupling and Malozemoff random field model to find realistic values for the exchange bias.

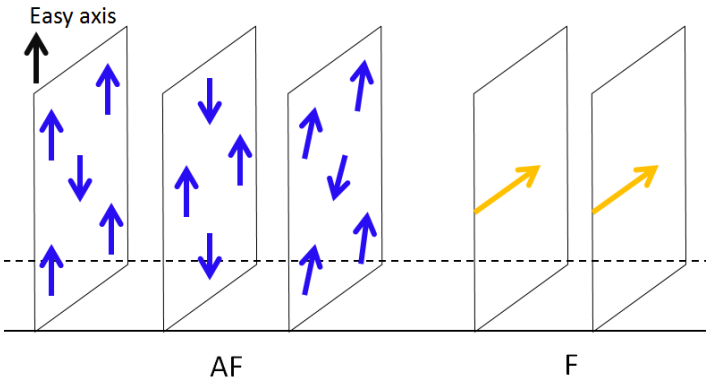


Figure 1.14: Illustration of the perpendicular F and AF magnetic interface configuration, with spin canting in the first AF layer [59].

*1.2.5 Epitaxial exchange biased ferromagnetic / antiferromagnetic bilayers*

Historically, experimental methods to study exchange bias were based on tools that measure the magnetic hysteresis loop of a sample, such as vibrating sample magnetometers (VSM) or superconducting quantum interference devices (SQUID). The exchange bias field and the coercivity can be directly obtained from hysteresis loops. In order to measure anisotropy directions, the samples were rotated in high fields and the torque was measured as a function of external field angle [61]. An alternative technique to address this question is using the ferromagnetic resonance (FMR) [62]. Recently, synchrotron methods exploiting x-rays, such as magnetic circular dichroism (XMCD), as well as neutrons,

such as neutron scattering and reflectivity, were also applied to measure element specific magnetic spin moments [53,54,63]. In contrast, magnetic force microscopy and Kerr microscopy directly reveal the domain behavior of exchange bias samples [64,65]. Last but not least, various other methods including Brillioun scattering [66], photoemission electrons [67] and Mossbauer [68], were also utilized to study exchange bias. However, despite extensive research, there are still many ongoing controversies in exchange bias such as the interface coupling, AF spin behaviors, and AF bulk effect. Such a situation is often referred to as the 'EB-lephant' [69].

One possibility for the controversial results for exchange bias is the variation in sample structure, geometry, and magnetization history used in different studies. As mentioned earlier, good structural quality and well-defined magnetocrystalline anisotropy are important parameters for desirable exchange bias properties. As a result, epitaxial exchange biased F/AF bilayers have attracted increasing attention in the past few years, and was believed to be the right direction for understanding the real physics of exchange bias [70]. Specifically, since the essential behavior of exchange bias critically depends on the atomic level chemical and spin structure at the interface between the F and AF components, epitaxial systems are favored in which the quality of the interface and the crystalline coherence are optimized. Additionally, the dependence of exchange bias on the spin configurations at the interfaces can be accomplished by selecting different crystallographic orientations. The role of interface roughness can also be understood from thin-film systems by changing the growth parameters and correlations between the interface structure and exchange bias can be made. With improved, epitaxial EB samples, a number of properties have been observed which provided a better understanding of the underlying physics of exchange bias. Some of the important properties are briefly introduced in the next paragraphs and

illustrated in Fig. 1.15.

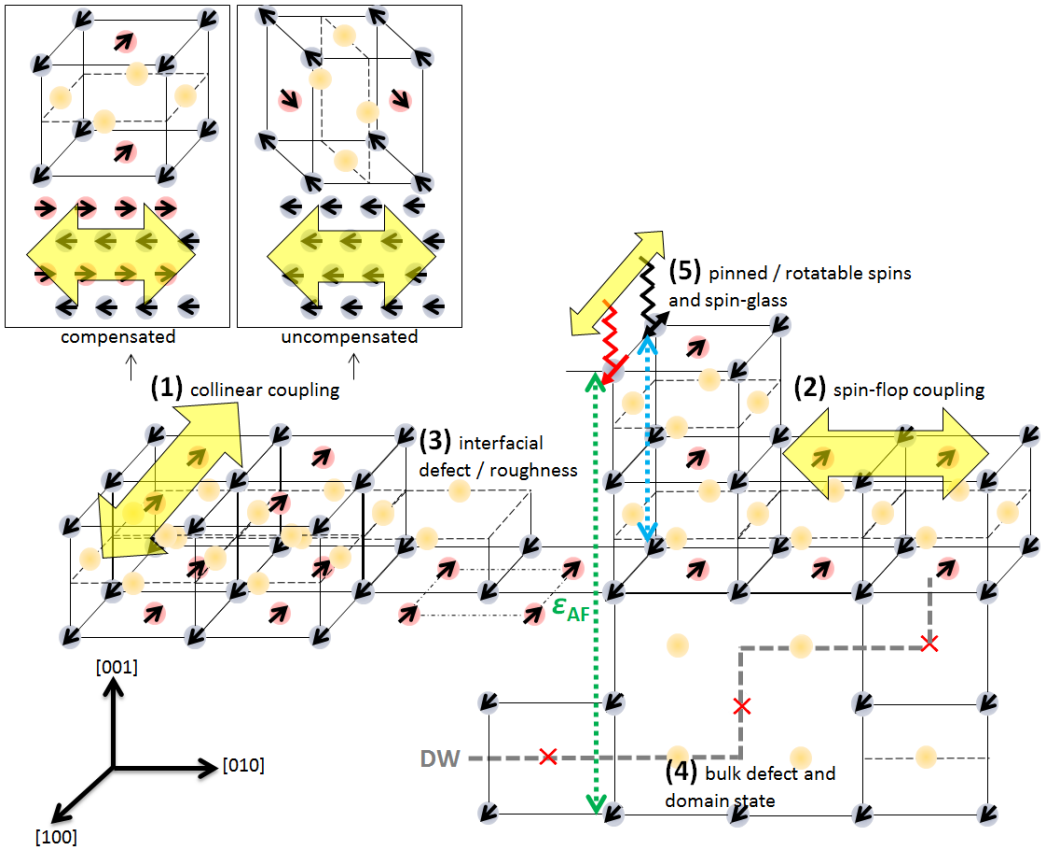


Figure 1.15: Various issues associated with epitaxial exchange biased bilayers: (1) compensated and uncompensated interfaces; (2) spin-flop coupling; (3) interfacial defect / roughness; (4) bulk defect and domain state; (5) pinned / rotatable spins and spin-glass. Double arrows indicate the F magnetization.

*(1) Compensated and uncompensated interfaces*

For an AF material below its $T_N$, the spins in each of the two sublattices point to its distinct anisotropy easy axis; furthermore, the exchange interaction make the adjacent spins antiparallel. In a well-ordered antiferromagnetic thin film, e.g., IrMn (rocksalt structure), the spin configurations are different viewed from different planes. For example, (001) plane gives rise to a compensated surface, with equal number of spins pointing along opposite directions. However, at the (010) plane, the spins all point

to one direction thus make it a perfect uncompensated surface. In the case of collinear coupling with an F layer, the uncompensated interface gives rise to a large unidirectional pinning and exchange bias. On the other hand, a perfect compensated interface should have no effect on exchange bias [71]. However, in reality, the interface defects and roughness can still give rise to an exchange bias field, according to a 'random field model' [43,44,45]. In epitaxial EB bilayers, one advantage is that the interface can be controlled by epitaxial growth of the AF material along different orientations [72,73], obtaining either a compensated or an uncompensated interface that further yields different magnetic properties [74,75].

*(2) Spin-flop coupling and induced uniaxial anisotropy*

The spin-flop coupling was first proposed only in theory and for a perfectly compensated F/AF interface. Such perpendicular coupling configuration is very sensitive to roughness as pointed by Koon in his early pioneering work [59]. He suggested that the introduction of roughness into his model resulted in the transition from perpendicular to collinear coupling. As a result, the issue of perpendicular coupling in F/AF bilayers may be only relevant in smooth single crystals rather than in polycrystalline films.

Owing to the application of epitaxial growth in the field of exchange bias, such spin-flop coupling has been experimentally revealed in several single crystal bilayers, such as $Fe/FeF_2$ [76], $Fe_3O_4/CoO$ [77,78], and Fe/MnPd [79]. Two important properties associated with the spin-flop coupling is the spin canting at the interface and the induced uniaxial anisotropy. The spin canting was thought to be partly responsible for the observed exchange bias. However, it is now believed that the exchange bias is more relevant to the local uncompensated regions, which are caused by defects, dislocations, grain boundaries,

and surface terraces across the interface. The spin-flop coupling only account for the induced uniaxial anisotropy, perpendicular to the field cooling direction. Such uniaxial anisotropy further gives rise to exotic magnetic properties including the stepped hysteresis measured along the bias direction. Undoubtedly, further exploration on the spin-flop coupling has to rely on epitaxial exchange biased thin film samples.

*(3) Interfacial defects and roughness*

Interfacial defects and roughness affect the film properties more significantly in epitaxial thin films. As mentioned earlier, such 'roughness' plays a key role in generating the exchange bias for a compensated interface. According to the Malozemoff model [43], the chemical roughness or alloying at the interface, which is present for any realistic bilayer system, causes lateral variations of the exchange field acting on the F and AF layers. This is especially important for epitaxial bilayers since these films are usually made at elevated temperatures, with a higher possibility of inter-diffusion among species. In addition, the roughness may also change the terminating atomic layers at local regions of the interface, which further modifies the nature of the coupling type at a microscopic level. For example, in case of IrMn, the terminating atom could be 'Mn' (parallel or antiparallel coupled with the F spins depending on the integer of the layers [80]), or 'Ir' (zero coupling with the F).

*(4) Bulk defect and domain state*

In polycrystalline bilayers, the bulk effect is not significant due to the lack of long-range order and the exchange bias is believed to be a pure interfacial phenomenon. In epitaxial thin-film bilayers, the long range magnetic ordering is maintained due to the good chemical structure; therefore the bulk AF spins may play a role in the interface exchange bias effect. According to the Mauri model [42], the F spins exert a torque on the AF spins during the magnetic reversal, causing a partial DW in the AF layer. In epitaxial bilayers, such partial DW can extend to a long distance in the bulk AF (over several tens of nanometers). The dependence of exchange bias on the partial DW can be studied by growing samples with different AF thickness below the intrinsic DW width. On the other hand, according to the Domain-state model [46], defects not only exist at the interface but also in the bulk of the film. These bulk defects can alter the interface behaviors by assisting the formation of AF domains near the interface. In epitaxial bilayers, dislocations and other types of defects are likely to form within the AF bulk due to the need for relaxing strains. Such relaxation allows the study of magnetic properties with the sample structural evolution. As a result, the epitaxial bilayers are ideal candidates for bulk-related EB studies.

*(5) Pinned and rotatable spins*

Experiments using synchrotron radiation revealed that certain numbers of interfacial AF spins are actually rotatable with the F spins during magnetization reversal, rather than pinned [57]. The ‘pinned’ and ‘rotatable’ behaviors depend on the strength of the AF anisotropy. In epitaxial thin films, the AF spins showed certain long range ordering within a characteristic length, $\varepsilon_{AF}$, also called the correlation length for AF ordering. Within the length of $\varepsilon_{AF}$, the spins have mutual ‘communication’ and they together

maintain an AF ordering. In thin films, if the thickness is greater than $\varepsilon_{AF}$, the AF anisotropy is strong and the interfacial spins are pinned to give rise to the loop shift. On the other hand, if the film thickness is smaller than $\varepsilon_{AF}$, there are not enough AF spins to maintain the AF anisotropy and the interfacial spins are rotatable with the F spins due to the strong F/AF exchange coupling. Theoretically, the previous introduced 'Spin-glass model' provides a phenomenological pathway to understand the pinned and rotatable behaviors and relevant properties [52]. Experimentally, epitaxial bilayers serve as ideal samples for studying such dual behaviors due to their large area of coherent spin behaviors.

*1.3 Competing anisotropies: state of the art and current challenges*

So far we have introduced the magnetocrystalline anisotropy, shape anisotropy and exchange anisotropy. The symmetry for each anisotropy can be different, e.g., the magnetocrystalline anisotropy of Fe and Ni are both cubic, the shape anisotropy for a wire is uniaxial, and the exchange anisotropy is unidirectional. Interplay between the different anisotropies in one system can significantly modify the magnetization reversal process. For example, in the epitaxial EB bilayers, the competing effects between magnetocrystalline anisotropy (cubic) and exchange anisotropy (unidirectional) result in stepped hysteresis loop [81] and asymmetric magnetic reversal [67]. However, limited by the stringent requirements for epitaxial growth, the magnetization reversal for epitaxial EB bilayers has not been systematically studied. Additionally, existing results [82] revealed that the magnetic reversal in these epitaxial bilayers occurs mainly via DW movement rather than coherent rotation of the magnetization. Thus, the well-established Stoner-Wohlfarth model seems not suitable anymore for hysteresis modeling.

Instead, a quantitative model that can represent the DW movement for the magnetic switching is relevant and desirable.

In addition, owing to the fast-developing nanotechnology, well-defined magnetic nanostructures can be fabricated using lithography technique, which further allows us to investigate the competing magnetic anisotropies. For example, in exchange-biased bilayer nanowire arrays, the magnetization reversal is dominated by competing exchange anisotropy (unidirectional) and shape anisotropy (uniaxial). Chung *et al* showed that in NiFe/FeMn EB nanowire arrays, the shift of the hysteresis loop changes non-monotonically with the orientation of the applied field with respect to the wire direction, and exhibits a maximum loop shift that exceeds the value that would be expected from the interface coupling alone [83]. Nevertheless, current lithography technology using polymer resist as template only allows us to deposit materials at ambient temperatures, as the polymers cannot maintain their structures at elevated temperatures. Therefore, polycrystalline EB nanowires have been extensively studied but not epitaxial ones, because of the technical limitations. For example, the competing effects between shape and magnetocrystalline anisotropy still remains unexploited.

So the remaining issues for competing magnetic anisotropies lie in: (1) the fabrication of epitaxial EB thin film bilayers and nanostructures; (2) the systematic investigation of the interplay among different anisotropies, including the combination of shape and magnetocrystalline anisotropies. In this thesis, we managed to solve the above two issues from both technical and scientific points of view, as will be discussed in the following chapters.

# Chapter 2

# EPITAXIAL EXCHANGE BIAS BILAYERS AND MULTILAYERS

Contents of this chapter have been partially published in Ref.[90]

## *2.1 Epitaxial thin film growth*

### *2.1.1 Mechanisms for thin film growth*

Thin film growth has been the key element over decades in the modern device technologies. Recently, controlled thin film growth at the atomic level has attracted much attention due to the increasing interest in surface science and nanotechnology. Work in this field has been motivated by the ever more stringent requirements on the quality of thin films needed for developing advanced microelectronic, optical and magnetic devices. Growth of thin film from atoms deposited from the gas phase is essentially a non-equilibrium phenomenon governed by a competition between kinetics and thermodynamics. It involves the adsorption of thin film atoms on the substrate surface, diffusion, aggregations, and development into film structure. All these processes are dependent upon the mobility of the deposited atoms on the surface, surface

energy of the substrate and film, and the substrate-film interface energy.

In the initial stages of thin film growth, the material deposited on the substrate can re-evaporate from the surface, nucleate into a cluster, and be consumed by existing clusters. Three modes of initial growth can be distinguished [84]. Specifically, island growth (Volmer – Weber) results in the formation of isolated islands on the surface. This occurs when the cohesive energy of the atoms within the film is greater than the cohesive energy between the film and atoms on the surface. Layer-by-Layer growth (Frank – van der Merwe) involves a deposition of one monolayer at a time and results in a very smooth epitaxial film. It occurs when the cohesive energy between the film and the surface atoms is greater than the cohesive energy of the film atoms. Island-layer growth (Stranski – Krastanov) is a mixed mode of the first two. It is an intermediary process characterized by both 2D layer and 3D island growth. Transition from the layer-by-layer to island-based growth occurs at a critical layer thickness, which is highly dependent on the chemical and physical properties, such as surface energies and lattice parameters of the substrate and film. Such layer-island growth is the most likely growth mode in our experiment, and will be discussed in detail.

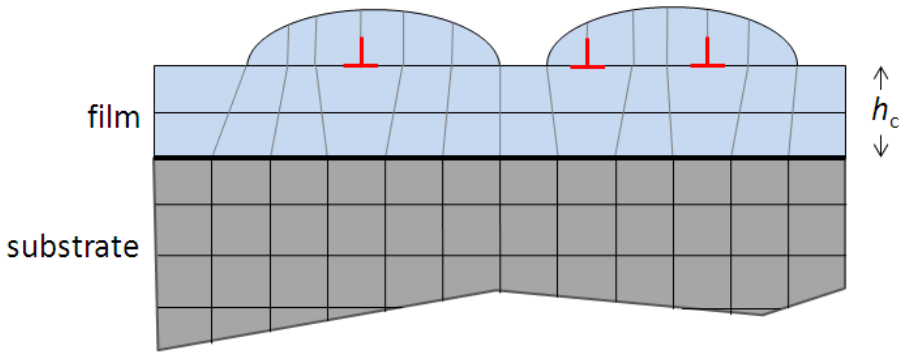


Figure 2.1: Layer-island growth showing the island formation after obtaining a critical thickness, $h_c$. Lines represent lattice planes with darker lines for the substrate lattice and lighter lines for the growing film. Edge dislocations are highlighted in red at the film/island interface.

In the layer-island growth, while initial film growth follows a layer-by-layer mechanism, non-trivial amounts of strain energy accumulate in the initially deposited layers, also known as the wetting layers. At a critical thickness, $h_c$, this strain induces a sign reversal in the chemical potential, leading to a switch in the growth mode. At this point it is energetically favorable to nucleate islands and further growth occurs by the island type mechanism. Since the formation of wetting layers occurs in a commensurate fashion at a crystal surface, there is often an associated misfit between the film and the substrate due to the different lattice parameters of each material. As the wetting layer thickens, the associated strain energy increases rapidly. In order to relieve the strain, island formation can occur in a dislocated fashion. In the dislocated islands, strain relief arises by forming interfacial misfit dislocations. The reduction in strain energy accommodated by introducing a dislocation is generally greater than the concomitant cost of increased surface energy associated with creating the clusters. The thickness of the wetting layer at which island nucleation initiates, i.e., $h_c$, is strongly dependent on the lattice mismatch between the film and substrate, with a greater mismatch leading to a smaller critical thickness. Values of $h_c$ can range from sub-monolayer coverage to up to several monolayers thick.

With increasing film thickness, the increased number of dislocations affects the epitaxy of the whole film. The lattice constant gradually relaxes, from a slightly distorted value (at the surface due to the mismatch), to the bulk value of the material as the film grows thicker. The increased dislocations also affect the magnetic properties. For example, the exchange bias field could be enhanced by domain formation in the antiferromagnet assisted by the dislocations [46].

Technically, substrate and deposition conditions will have an important effect in epitaxial growth. First, the single crystal substrate has a dominant influence on the oriented growth. A good lattice match

will help epitaxial growth, but it is neither a necessary nor a sufficient condition for the occurrence of epitaxy. Substrate temperature is another important issue for epitaxy. In some systems, there exists a certain temperature, called the epitaxial temperature, above which epitaxy is perfect and below which it is imperfect. Increasing temperature may improve epitaxy by providing the activation energy for adatoms to occupy the position of potential minima, as well as aiding the desorption of surface contaminants. Another issue is the deposition rate, which should be slow enough for the adatom to have sufficient time to jump to an equilibrium position of an ordered state by surface diffusion. Other factors such as surface electrostatic effects, contamination, and thin film thickness will also contribute to the epitaxy [85,86,87].

### *2.1.2 Method – ion beam sputtering*

#### *Thin film deposition*

Thin film deposition technology includes the process and tools by which thin film materials are transported to the substrate. Typical thin film deposition methods can be classified into physical deposition and chemical deposition. The major difference is physical deposition does not involve a chemical reaction, unlike chemical deposition. In this thesis, only physical deposition methods will be discussed. In the physical deposition process, the thin film materials are transported to the substrate by physical methods. A vacuum environment is necessary in this process, as the thin film materials have to be transported from source to substrate without too much collision with air molecules. The mean free path in a vacuum of $10^{-3}$ Torr is about 5 cm, and in $10^{-5}$ Torr vacuum is 5 m. Also, impurity gas is absorbing

and sticking on the substrate during the thin film deposition. For example, even at $10^{-5}$ Torr vacuum, the air molecules could also accumulate on the substrate with a rate of up to 2.4 monolayer (ML) per second [88]. Therefore, in general, higher purity thin films require higher vacuum conditions. Technically, atoms of thin film materials from the solid source can either be extracted by heating or collision by particles with high energy. The former method is called thermal evaporation. The latter is called sputtering.

Thermal evaporation includes general evaporation (using an electric resistance heater to melt the material), e-beam evaporation (using a high-energy beam from an electron gun to boil the material), and molecular beam epitaxy (MBE). Evaporation is a common method of thin film deposition. The source material evaporates in a vacuum, travels directly to the substrate, and condenses back to a solid state. MBE is a refined form of vacuum evaporation in which directed neutral thermal atomic and molecular beams impinge on a heated substrate under ultra-high vacuum (UHV) conditions. MBE is widely used in semiconductor industry, especially for preparing high quality films of III-V compounds (e.g. GaAs). The most important aspect of MBE is the deposition rate (typically < 1 Å/s) allows the film to grow epitaxially. The absence of carrier gases as well as the UHV result in the highest achievable purity of the grown films. The thermal evaporation methods were not used in this thesis work and readers are referred to [85] for more details.

Sputtering is a vacuum evaporation process which physically removes portions of a target material by bombarding the surface of the sputtering target with gaseous ions under high voltage acceleration, and deposits a thin, firmly bonded film onto the substrate. The process relies on a plasma, usually from a noble gas, such as Ar. Sputtering has proven to be a successful method of coating a variety of substrates with thin films of electrically conductive or non-conductive materials. Since the coating material is passed

into the vapor phase by a mechanical rather than a chemical or thermal process, virtually any material can be deposited. In sputtering, the composition of a sputtered film is the same as that of target, under the conditions that the temperature is not too high for the compensation of the higher-sputtering yield materials at the surface by volume diffusion form the bulk; the target does not decompose; and surface of the target does not change its chemical composition such as by oxidation; and the sticking coefficients for all the component elements on the substrate is the same. Sputter deposition also has an advantage over MBE due to its speed. The deposition rate is usually higher, resulting in lower impurity incorporation because fewer impurities are able to reach the surface of the substrate in the same amount of time. However, in some particular sputtering techniques, such as the ion beam sputtering (IBS), the deposition rate can be controlled by varying the source beam voltage. It is possible to achieve rather low sputtering rates, comparable to that of the MBE system. Sputtering is also categorized according to the physical mechanisms involved. Magnetron sputtering is one of the most frequently used methods. In this deposition process, after the chamber is evacuated, a continuous stream of working gas, typically Ar, is flowed into the deposition chamber. When the voltage between anode and cathode is sufficient, the dielectric working gas undergoes breakdown such that free ions and electrons are created. Sputtering sources are usually magnetrons that utilize strong electric and magnetic fields to trap electrons close to the surface of the magnetron, where the target is. The electrons follow helical paths around the magnetic field lines, undergoing more ionizing collisions with gaseous neutrals near the target surface. Magnetron sputtering is capable for deposition of various materials including both conductive (DC mode) and insulating (RF mode) materials. However, it is not suited for epitaxial growth due to its fast deposition rate and low vacuum. In contrast, the IBS is more appropriate for epitaxial thin film growth and will be

discussed below in detail.

*Ion beam sputtering*

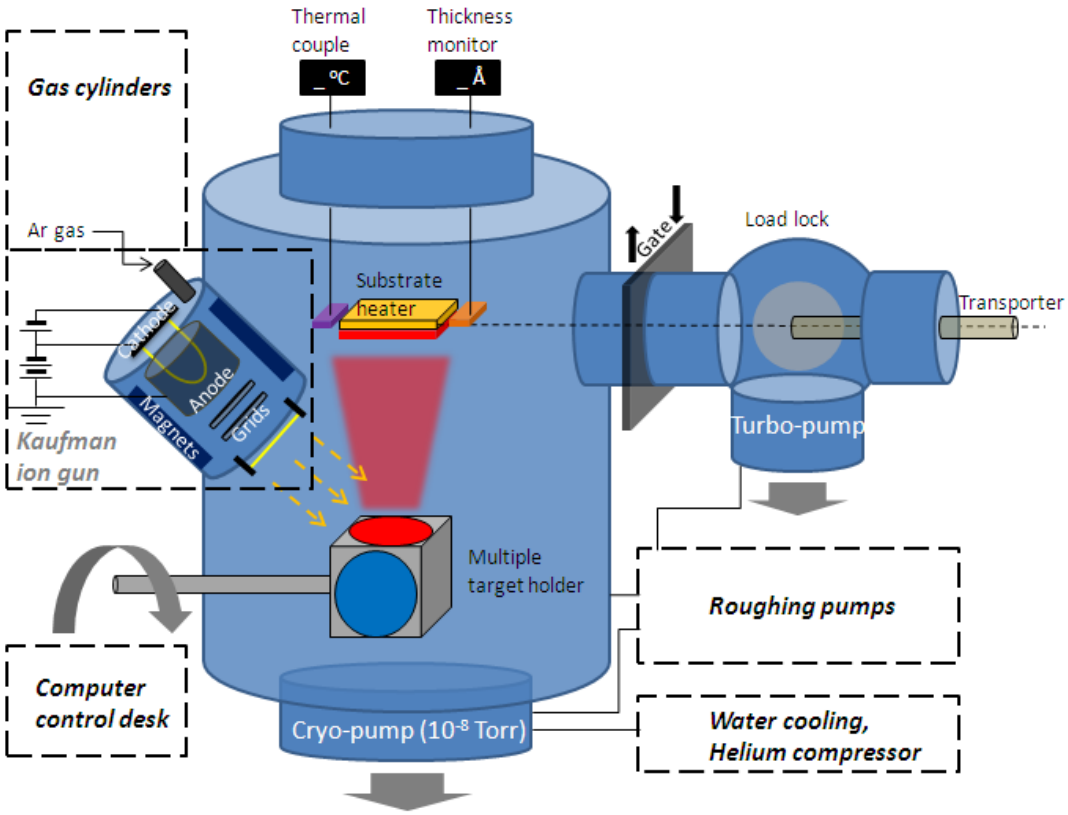


Figure 2.2: Schematic illustration of the ion-beam sputtering deposition system used in this work.

Our home-built IBS system provides simple and independent control of ion flux and ion energy by using a modified electron gun structure [89]. IBS is a method in which the target is external to the ion source. Figure 2.2 shows the ion-beam sputtering system used for all the deposition in this thesis. The key components are set up in the main vacuum chamber where the vacuum is kept at ~$10^{-8}$ Torr constantly, by a cryo-pump with a working temperature of 12 K. Such low temperature is maintained by a helium compressor following a water cooling cycle. This IBS system is equipped with a high intensity Kaufman

ion source. The discharge chamber (cathode and anode) and the ion optics (grids) are two major components of the ion source. The function of the discharge chamber is to generate ions. Specifically, Ar gas flow is introduced from a gas cylinder to the ion source in a controlled manner. Next, Ar ions are generated by collisions with electrons that are confined by a magnetic field as in a magnetron. The ions are extracted from the discharge chamber and accelerated toward a target by the electric field emanating from the grids. The IBS can also be used to deposit an insulating target, after neutralization of the ion beam. Neutralization of the ion beam is generally done by placing a hot filament in the path of the ion beam, by which the Ar ions are turned into neutralized Ar atoms. The target holder has a cubic shape and can hold up to four targets. Targets can be selected by simply rotating the external holder. The substrate is located at the top of the main vacuum chamber. The substrate may be heated during the deposition, up to 600$^{o}$C. A thermocouple is placed near the substrate holder for instant temperature reading. A thickness monitor is also positioned close to the substrate for monitoring the deposited thickness. Before and after each deposition, the substrate (sample) can be transported in-and-out the main chamber via a load lock system, by a magnetic transporter. The load lock helps maintain the high vacuum of the main chamber for a long time. A turbo-pump is incorporated with the load lock system and can achieve a vacuum of ~$10^{-4}$ Torr. Mechanical pumps are connected to the main chamber and load lock for pre-vacuuming, and also with the cryo-pump for regeneration purposes (pump out the absorbed gas in the cryo-pump during its standby mode).

As compared with thermal evaporation and magnetron sputtering, the IBS offers the following advantages. First, both IBS and magnetron sputtering have a significant advantage for deposition of multicomponent material. In the thermal evaporation method, it is difficult to control the composition of

different materials in the film because the composition is determined by vapor pressure of the compound. For the sputtering method, the composition of a sputtered film is mostly the same as that of the target. Even if the different elements have different sputtering yield, after a certain time, there will be deficiency of the higher sputtering yield compound. Thus the sputtering rate will reach equilibrium and deposit the same thin film composition as the target. Second, in the IBS ion source, the energy and flux of ions can be controlled independently. The deposition rate can be well controlled as low as 0.1Å/s while still forming a high energy beam, which can be used to grow high quality epitaxial films. Last but not least, IBS works at a relatively higher vacuum. The base pressure of the vacuum chamber is $10^{-8}$ Torr. The pressure during sputtering is typically $1.1\times10^{-4}$ Torr compared with $10^{-2}$ to $10^{-3}$ Torr used in magnetron sputtering. Therefore, less contamination from Ar gas is expected in IBS. In addition, the mean free path in IBS system during normal deposition is several meters at ~$10^{-4}$ Torr. The substrate and the target can be placed far enough (farther than in the magnetron sputtering system), which gives rise to a better film uniformity. The main drawback of IBS is the large amount of maintenance required to keep the ion source operating. The filaments have to be changed around every 10 hours of deposition time, due to the self-sputtering of the tungsten filament. The amount of this self-sputtering is tiny, thus it is not considered a source of contamination.

*Epitaxial exchange biased bilayers, Fe/MnPd and Fe/IrMn*

In the past few years, our lab has developed a series of recipes for growth of exchange biased Fe/MnPd bilayers on MgO(001) substrate using IBS [72,73]. The MnPd layer can be grown along

different crystallographic orientations, i.e., *c*-axis and *a*-axis normal to the film plane, which further gives rise to different interface characteristics, i.e., compensated and uncompensated (Fig. 1.15). Recently, we have also developed a recipe for growing epitaxial Fe/IrMn (*c*-axis) bilayers on MgO(001) substrate [90]. Specifically, the substrate was first pre-annealed at 500 °C for 1.5 hour and held at 145 °C for deposition of both Fe and IrMn layers. The Fe and IrMn layers were deposited under a deposition rate of ~2-3 Å/s. No post-annealing is required. The sample is then *in-situ* cooled to room temperature. A protection layer, 5nm Ta, was subsequently deposited before removing the sample from the chamber. The detailed recipes for fabrication of Fe/MnPd and Fe/IrMn samples are summarized in Table 2.1.

*Epitaxial relationship*

*Fe/IrMn*

In the epitaxial growth of MgO(001)/Fe(001)/IrMn(001), the Fe(001) planes grow on the MgO but rotate 45$^{o}$ with respect to MgO(001) so that the lattice mismatch is minimized, according to the lattice

| *Sample* | *Orientations* | $T_{\text{deposit}}$ | $T_{\text{anneal}}$ (1 h) |
|---|---|---|---|
| Fe/MnPd (*a*-axis) | MgO(001)/Fe(001)/MnPd(100) | 400$^{o}$C | 250$^{o}$C |
| Fe/MnPd (c-axis) | MgO(001)/Fe(001)/MnPd(001) | 90-120$^{o}$C | N/A |
| Fe/IrMn (*c*-axis) | MgO(001)/Fe(001)/IrMn(001) | 145$^{o}$C | N/A |

Table 2.1: IBS deposition recipes for epitaxial exchange biased Fe/MnPd and Fe/IrMn bilayers. The deposition temperature ($T_{\text{deposit}}$) and annealing temperature ($T_{\text{anneal}}$) are indicated. Annealing time is 1 hour in all cases.

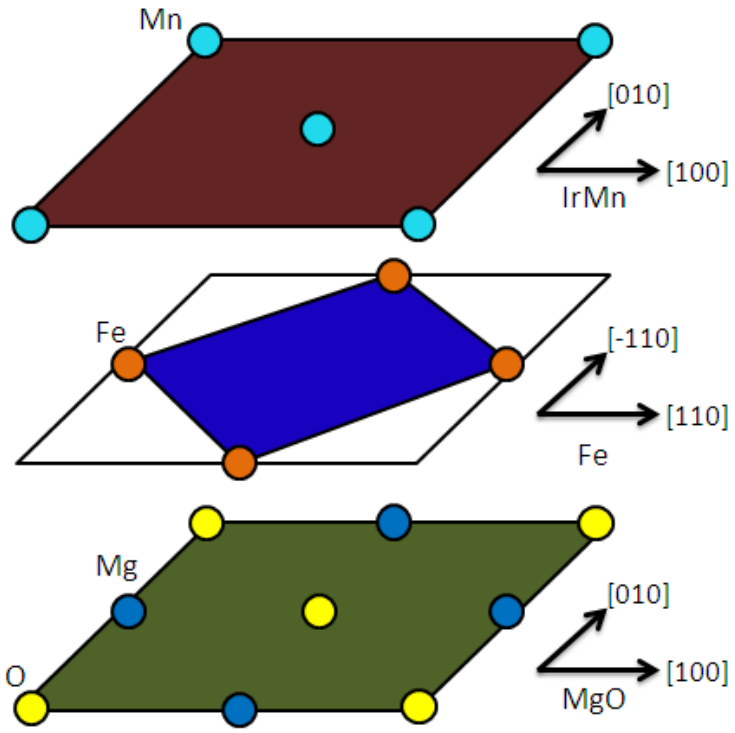


Figure 2.3: Epitaxial growth of Fe/IrMn bilayers is developed in this thesis. The epitaxial relationship of (001) textured Fe/IrMn bilayers grown on MgO(001) substrate is indicated, with the lattice parameters: $a_{MgO}$ = 4.20 Å, $a_{Fe}$ = 2.86 Å, and $a_{IrMn}$ = 3.8 Å. Similar discussions on Fe/MnPd can be found in [72,73].

constant of MgO, $a_{MgO}$ = 4.20 Å, and Fe, $a_{Fe}$ = 2.86 Å, Fig. 2.3. Specifically, the distance between two nearest Mg ions in the MgO is $4.20 \times \frac{\sqrt{2}}{2}$ = 2.97 Å, comparable to $a_{Fe}$ = 2.86 Å. Such a distance has a 4% mismatch with $a_{Fe}$, and if epitaxially grown following the 45$^o$ rotation, the Fe lattice would be slightly expanded. IrMn(001) has a lattice constant $a_{IrMn}$ = 3.8 Å. The IrMn(001) planes would rotate another 45$^o$ with respect to Fe(001) during its epitaxial growth, as the distance between two nearest Mn ions, $3.8 \times \frac{\sqrt{2}}{2}$ = 2.69 Å, is also comparable to $a_{Fe}$ = 2.86 Å. Still, the IrMn lattice would experience a slight lattice expansion and the mismatch is 6% with respect to Fe. As a result, our predicted epitaxial relationship for the Fe/IrMn bilayer is: MgO(001)[100] // Fe(001)[110] // IrMn(001)[100].

*Fe/MnPd*

In the epitaxial growth of MgO(001) / Fe(001) / MnPd(001) and MgO(001) / Fe(001) / MnPd(100), the Fe layer growth is the same with the Fe/IrMn growth as discussed above, i.e. Fe(001) planes grow on the MgO but rotate 45$^{o}$ with respect to MgO(001). For *c*-axis MnPd growth, MnPd(001) has a lattice constant $a_{\mathrm{MnPd}}$ = 4.07 Å. The MnPd(001) planes would rotate 45$^{o}$ with respect to Fe(001) during its epitaxial growth, as the distance between two nearest Mn ions, $4.07 \times \frac{\sqrt{2}}{2}$ = 2.88 Å, is almost the same with $a_{\mathrm{Fe}}$ = 2.86 Å. The lattice mismatch in this case is less than 1%. On the other hand, for *a*-axis MnPd growth, MnPd(100) has a lattice constant $a_{\mathrm{MnPd}}$ = 3.96 Å. The MnPd(100) planes still favor the 45$^{o}$ rotation with respect to Fe(001) during its epitaxial growth. The distance between two nearest Mn ions, $3.96 \times \frac{\sqrt{2}}{2}$ = 2.80 Å. The lattice mismatch in this case is 2%. In the a-axis growth, the thin-film lattice (3.96 Å) is distorted with respect to the bulk lattice, ~3.52 Å. Such distortion is likely due to the biaxial strain in the film to accommodate the epitaxial growth on the Fe/MgO [72,73].

*2.2 Structural characterizations*

*2.2.1 X-ray diffraction*

X-ray diffraction (XRD) is the result of x-rays encountering regularly spaced obstacles (atoms or ions) with spacing on the order of the ray wavelength. XRD is a versatile, non-destructive technique that reveals detailed information regarding crystallographic structure, thin film layer thickness and interface

roughness. X-rays are electromagnetic radiation generated by either x-ray tubes or synchrotron radiation. In an x-ray tube, which is the primary x-ray source used in laboratory x-ray instruments, they are generated when a focused electron beam accelerated across a high voltage field bombards a stationary or rotating solid target. A hole in an inner shell, normally K shell, is generated by ejecting the electron. The hole in the K shell is filled by an electron from an outer shell, normally L shell. The difference in energy is emitted as a characteristic x-ray quantum. Common targets used in x-ray tubes include Cu and Mo, which emits 8 keV and 14 keV x-rays with corresponding wavelengths of 1.54 Å and 0.8 Å, respectively. Because the wavelength of x-rays is comparable to the size of atoms, they are ideally suited for probing the structural arrangement of atoms and molecules in a wide range of materials.

### *2.2.2 X-ray $\theta - 2\theta$ scan (out-of-plane)*

In a $\theta - 2\theta$ scan, scattered waves from different atoms can interfere with each other and the resultant intensity distribution forms the diffraction pattern. If the atoms are arranged in a periodic fashion, as in crystals, the diffracted waves will consist of sharp interference maxima (peaks) with the same symmetry as in the distribution of atoms. The positions and the intensities of the peaks are used for identifying the underlying structure (or phase) of the material. For a given set of lattice planes (hkl) with an inter-plane distance of $d_{hkl}$, the condition for a diffraction peak to occur can be simply written as:

$$n\lambda = 2d_{hkl}\sin\theta, \tag{2.1}$$

also known as Bragg's law, in which $n$ is the order of wavelengths; $\lambda$ is the wavelength of the incident beam (~1.54Å for Cu target); $d_{hkl}$ is the spacing of planes; and $\theta$ is the angle of the incident beam. Figure

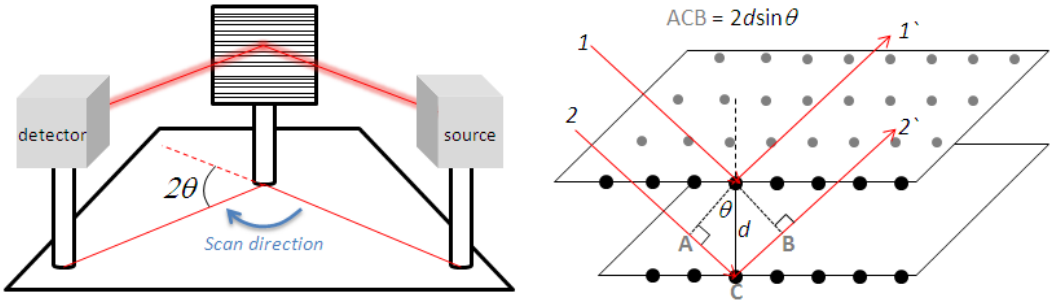


Figure 2.4: XRD '$\theta - 2\theta$ scan' geometry and the Bragg's law. 1(1`) and 2(2`) are two parallel incident beams.

2.4 is an illustration of the '$\theta - 2\theta$ scan' configuration and the Bragg's law. The detector is always at the angle of $2\theta$ with respect to the incident beam.

The $\theta - 2\theta$ scans were performed on our exchange biased samples. The equipment used in our experiment is Rigaku 12.5 kW rotating anode x-ray diffraction system using Cu $K_\alpha$. The samples being tested here are: Fe(15 nm)/IrMn(8 nm)/Ta cap(5 nm), Fe(10 nm)/c-axis MnPd(45 nm)/Ta cap(5 nm) and Fe(10 nm)/a-axis MnPd(45 nm)/Ta cap(5 nm). The diffraction patterns are shown in Fig. 2.5.

For IrMn (Fig. 2.5(a)), the highest peak observed at 43.1° comes from the substrate, i.e., MgO(002), and is verified by Bragg's law using $a_{MgO}$ = 4.20 Å. Specifically, we have $2a_{MgO}\sin\theta_{MgO}$= 2×1.54 Å thus $\theta_{MgO}$ = 21.5° and $2\theta_{MgO}$ = 43°. The peak at 65° is well known to come from Fe(002). The only peak left, at ~48°, is likely attributed to IrMn since $2a_{IrMn}\sin\theta_{IrMn}$ = 2×1.54 Å, therefore $\theta_{IrMn}$ = 23.9° ($2\theta_{IrMn}$ = 47.8°). In order to further verify our conclusion, we checked the PDF card for IrMn (PDF#: 290687) and compared the standard spectrum with our data. The only relevant peak corresponding to our result is the reported (200) peak at 48.130°. As a result, a clear (002) texture normal to the film plane is thus confirmed in our Fe/IrMn bilayer sample.

For MnPd (Fig. 2.5(b)), the highest peak is still the MgO(002) peak coming from the substrate. The

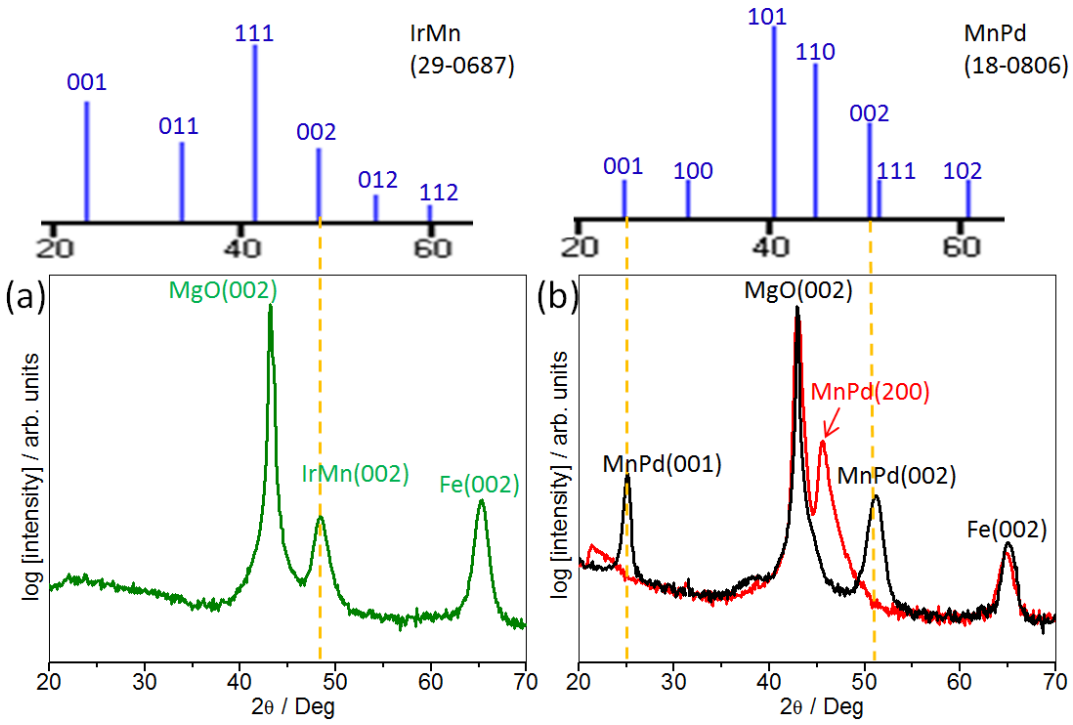


Figure 2.5: XRD $\theta - 2\theta$ diffraction patterns for (a) epitaxial Fe(15 nm)/IrMn(8 nm) bilayer, and (b) epitaxial Fe(10 nm)/c-axis MnPd(45 nm) and Fe(10 nm)/a-axis MnPd(45 nm) bilayers. Photo-captured images of the electronic PDF card for both structures (IrMn and MnPd) are also indicated on top of their XRD patterns.

Fe(002) peak at 65° is also well observed for both *c*- and *a*-axis MnPd. For *c*-axis MnPd, two relevant peaks are observed at $2\theta_{MnPd}$ ~25° and 52°, corresponding to the MnPd(001) and MnPd(002) peaks respectively, according to the relevant PDF card for MnPd (PDF#: 180806). For *a*-axis sample, the only relevant peak is the one observed at $2\theta_{MnPd}$ ~46°, corresponding to the MnPd(200). The MnPd(100) peak is not observed due to the missing of the chemical ordering [72,73].

We also fabricated a series samples with fixed Fe thickness (15 nm) but different IrMn thickness (0 – 14 nm). Their XRD patterns are indicated in Fig. 2.6, all showing a (002) texture along the normal direction. It is also noted that the IrMn peak is not significant for samples with IrMn thickness less than 8 nm. This can be explained by the considerable dislocations reducing the epitaxy in the thin films, due to the Fe and IrMn lattice mismatch.

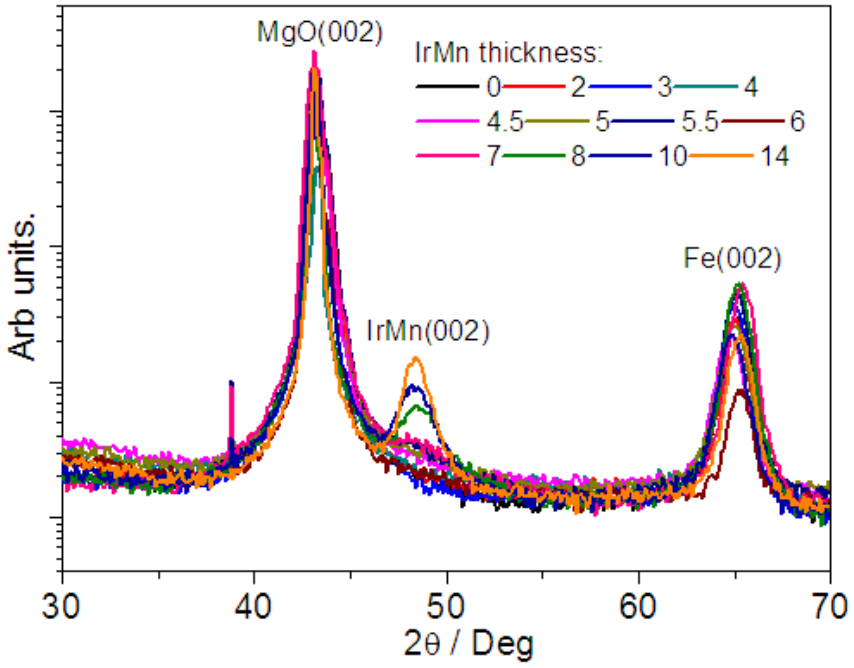


Figure 2.6: XRD $\theta - 2\theta$ diffraction pattern of epitaxial Fe(15 nm)/IrMn($t$ nm) bilayer samples with $t$ = 0, 2, 3, 4, 4.5, 5, 5.5, 6, 7, 8, 10, 14.

### *2.2.3 X-ray $\Phi$ scan (in-plane)*

Texture measurement ($\Phi$ *scan*), also called pole figure, is used to determine the epitaxy of a thin film sample by scanning certain crystallographic orientations in the film plane. In such scan mode, the $\theta$ is first set for a certain crystallographic orientation according to Bragg's law, and the sample is then rotated and scanned in the plane (Fig. 2.7). If the thin film is epitaxially grown, one crystallographic orientation can only be detected at certain $\Phi$ positions. The number of positions depends on the symmetry of the crystal structure, and the intensity is proportional to the probability of finding such a crystal plane normal to the reflection. In addition, $\Phi$ scan is also helpful in finding the orientation distribution of crystalline grains in a textured sample. A textured state of a material (typically in the form of thin films) is

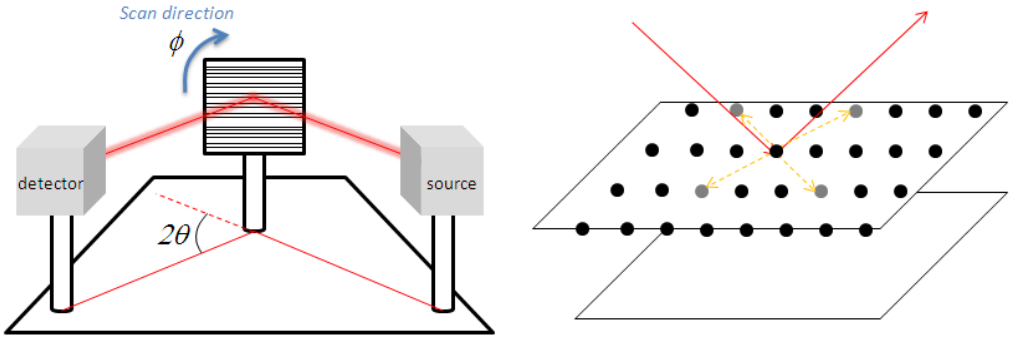


Figure 2.7: XRD '$\Phi$ scan' geometry. The sample rotates in the plane and the intensity is proportional to the probability of finding a certain crystal plane.

an intermediate state between a completely randomly oriented polycrystalline powder and a completely oriented single crystal. A texture measurement is often plotted in polar coordinates consisting of the tilt and rotation angles with respect to a given crystallographic orientation.

In order to confirm the epitaxy, in-plane $\Phi$ scans were performed on our Fe/IrMn samples using a four circle XRD at the PNNL through a user proposal program. In our scan, we followed the (110) plane group for all the three layers including the substrate. As indicated in Fig. 2.8, all three layers display four

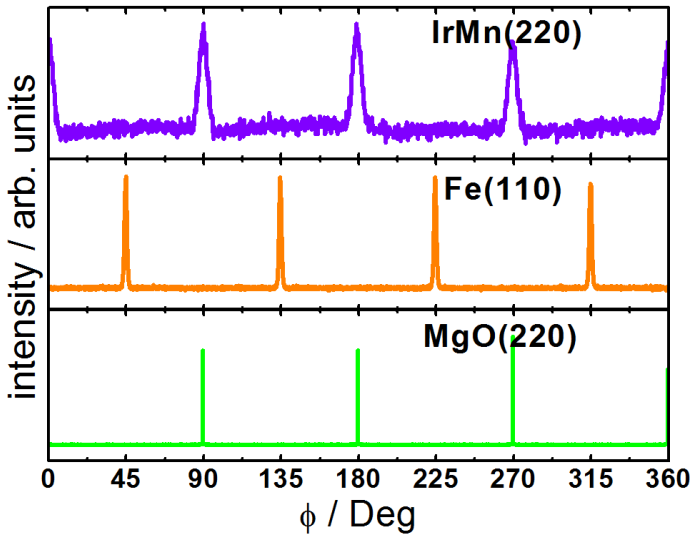


Figure 2.8: XRD $\Phi$ diffraction pattern of epitaxial Fe(15 nm)/IrMn(8 nm) bilayer sample. The (110) plane group was followed for each layer during the scan experiment.

peaks indicating their fourfold symmetry. High intensities were observed for MgO(220) at $\Phi$ = 0°, 90°, 180°, and 270°. Taking MgO as reference, the high intensities for Fe(110) were observed at 45°, 135°, 225°, and 315°, confirming the 45° rotation of the same plane group for Fe and therefore the epitaxial growth of Fe on MgO. Similarly, taking Fe as reference, the high intensities for IrMn(220) were observed at 0°, 90°, 180°, and 270°, showing that the same plane group for IrMn rotated another 45° with respect to Fe. Under the fourfold symmetry, one can also consider the IrMn lattice rotated back 45° and became collinear with the MgO. In summary, the sharp peaks observed at the well-defined angles for both Fe and IrMn unambiguously indicated the epitaxial growth for both layers, under the predicted epitaxial relationship: MgO(001)[100] || Fe(001)[110] || IrMn(001)[100].

*2.2.4 Rocking curve*

In reality, the surface for an as-deposited film cannot be perfectly flat. Microscopically, there are certain grains with their normal axes tilted slightly, giving rise to the observable roughness. In the $\theta - 2\theta$ scan, a certain $\theta$ angle points to a certain *d*-spacing in the lattice. However, due to the tilting of some of the grains, in Fig. 2.9, the diffraction relationship can be satisfied for those grains only if the sample plane rotates a bit so that the grain normal axis collinear with the incident beam normal axis. The sample tilting angle is called $\omega$, and such a scan is named a 'rocking curve' scan, or $\omega$ scan. In an $\omega$ scan, the $\theta$ is fixed for a certain *d*-spacing and a sharp single peak can be observed at $\omega$ = 0 (most grains are not tilted), decaying rapidly as $\omega$ deviates from 0. The width of the peak can be used as a gauge of the quality of the film, and a sharper peak corresponds to a better crystal quality.

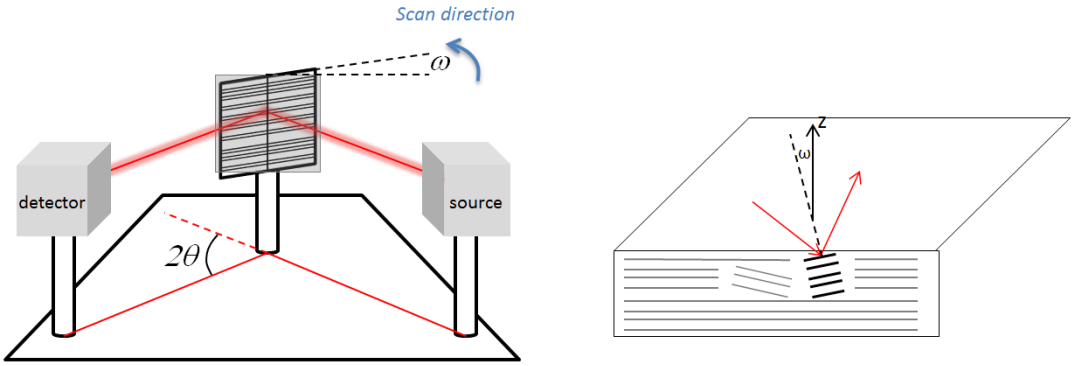


Figure 2.9: XRD '$\omega$ scan' geometry. The sample is tilted slightly at $\omega$ to satisfy the Bragg's law for a certain tilted grain.

## *2.3 Magnetic characterizations*

Typical magnetic measurements include DC hysteresis $M(H)$, AC susceptibility, and temperature dependent magnetization, $M(T)$, which offers characterization for general magnetic properties including saturation magnetization, coercivity, remanence and critical temperatures. The relevant magnetic measurements in this thesis include vibration sample magnetometer (VSM), magneto-optic Kerr effect (MOKE), and magnetotransport measurements, such as anisotropic magnetoresistance (AMR).

### *2.3.1 Vibrating sample magnetometer*

VSM is the most common method for measuring hysteresis loop based on the Faraday's induction law, which states that a changing magnetic flux will produce an electric voltage in a closed loop. Such an electric voltage can be measured and further correlated to the changing magnetic field. During the VSM

measurement, a uniform field is generated by a set of electromagnets, and the sample is placed in the field, inducing a magnetic moment. Driven by a motor, the sample vibrates in sinusoidal motion, inducing a sinusoidal electrical signal that can be read by a pickup coil. The electric signal has the same frequency as the vibration and its amplitude will be proportional to the magnetic moment, vibration amplitude, and the relative position with respect to the pickup coil. A typical thin-film sample for VSM measurement is in a dimension of 5 mm × 5 mm. The Lake Shore Model 7300 commercial VSM equipment (UW) can measure the room temperature magnetic moment of such a sample over a range that extends from $10^{-5}$ emu to $10^{4}$ emu.

### *2.3.2 Magneto-optic Kerr effect*

The magneto-optical Kerr effect (MOKE), also called the surface magneto-optical Kerr effect (SMOKE), is a technique that can be used to study the magnetism of thin films, or the surface magnetism of bulk samples. It is based on the phenomenon that linearly polarized light obtains a rotation in the polarization axis upon reflection from a surface with finite magnetization [91]. Microscopically, the electric field of the light is coupled with the spin of electrons. Macroscopically, an electron feels the Lorentz force in a magnetic field, so the dielectric constant and the reflectivity are changed. When the incident light is linearly polarized, after interaction with the sample, the reflected light can be elliptically polarized. The rotation of polarization is known to be proportional to the magnetization of the sample therefore the magnetization can be detected via measuring the Kerr rotation.

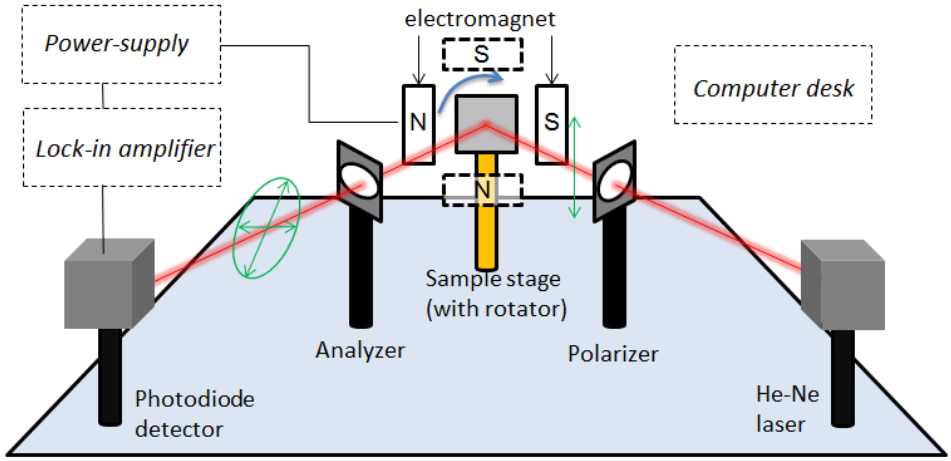


Figure 2.10: MOKE setup. Sample can rotate in the plane.

In our experimental MOKE setup (Fig. 2.10), a polarized He-Ne laser beam is used as the light source, and a set of electromagnets is used to generate the magnetic field, up to 2000 Oe. Linearly polarized light is first generated by a polarizer before shooting on the sample. Change of the polarization of the reflected light is detected by a second polarizer (analyzer) and a photodiode detector with a lock-in amplifier. A 360$^{o}$ rotator is equipped with the sample stage. As a result, the magnetic field can be applied in the sample plane, but at different orientations with respect to the anisotropy easy axis of the sample. A typical hysteresis loop measured by MOKE is plotted with the Kerr signals, i.e. Kerr rotation and Kerr elasticity, as a function of the applied magnetic field. Information about magnetic reversal (e.g. switching field and its distribution) can be obtained from such signals as they resemble the '*M-H*' curves of the sample. However, an absolute determination of the sample magnetization requires the use of other magnetometers such as a VSM. Finally, it is worth noting that MOKE can also be applied as a scanning microscopy for magnetic domain imaging, with a resolution down to micrometers [92].

In the MOKE measurement, three different modes, i.e., polar, longitudinal, and transverse, are used

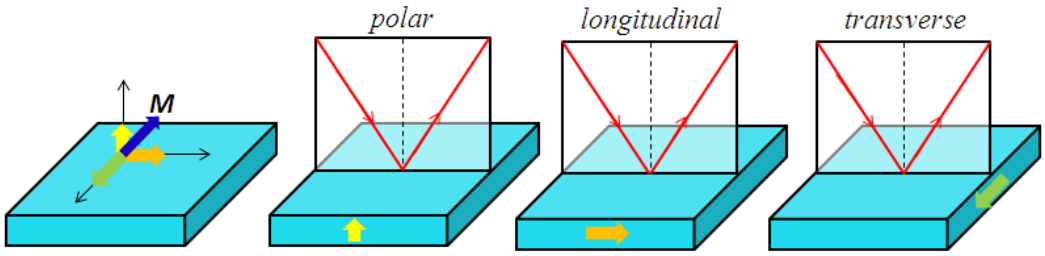


Figure 2.11: Illustration of MOKE measurement modes to detect the 3D magnetization components. Polar mode measures the component perpendicular to the sample plane; longitudinal mode measures the component in the sample plane and parallel to the light beam plane; transverse mode measures the component in the sample plane but perpendicular to the light beam plane.

to measure different components of a 3D magnetization, as indicated in Fig. 2.11. Specifically, polar mode measures the component perpendicular to the sample plane, therefore it is often used for samples with perpendicular magnetic anisotropy such as Co/Pt multilayers [93]; longitudinal mode measures the component in the sample plane and parallel to the light beam plane; transverse mode measures the component in the sample plane but perpendicular to the light beam plane. These two modes are widely applied in most thin film samples as the magnetization normally lies in the plane due to the shape anisotropy. In our MOKE setup (UW), the transition from longitudinal to transverse measuring geometry is achieved by simply rotating the magnet-couple, without changing the setup of the laser-detector system. Specifically, the field axis of the magnet-couple is parallel and perpendicular to the optical stage for longitudinal and transverse geometry, respectively. In summary, with the three different measuring modes, MOKE measurement provides a convenient way to map the 3D magnetization of a sample.

### *2.3.3 Anisotropic magnetoresistance*

Anisotropic magnetoresistance is one of the magnetotransport measurements, using the so-called

magnetoresistance, which is the tendency of a material to change the value of its electrical resistance when an external magnetic field is applied to it. Specifically, AMR is the property of a material that describes the dependence of electrical resistance on the angle between the direction of electric current and orientation of magnetic field. The effect was discovered by William Thomson in 1857 and has been called the 'orientation' effect. In general, the electrical resistance or resistivity is at its maximum when the axes of magnetization orientation and the current flow are parallel and is at its minimum when the magnetization is orthogonal to the axis of current flow. The angular dependence of the resistivity for the AMR effect can be described by the following:

$$\rho(\theta) = \rho_{\perp} + \delta\rho\cos^2\theta, \tag{2.2}$$

where $\delta\rho$ is the resistivity difference between the parallel and perpendicular resistivity [94]. The magnitude of the effect depends upon the material and is usually expressed as a ratio of the resistance or resistivity change. The physical origin of the AMR effect is associated with the angular dependence of the electronic scattering processes that are the origin of electrical resistance. Spin-orbit interactions have been suggested as a mechanism for enhancing spin-flip scattering. These interactions, combined with different scattering probabilities parallel and perpendicular to the magnetization, lead to the observed anisotropic resistance behavior. In this thesis, the AMR measurements are performed using the 4-probe method (I+, I–, V+, V–) by a commercial Quantum Design physical property measurement system (PPMS), as shown in Fig. 2.12. The electrical connections are set up by a wire bonder. We used a special AMR sample holder with an in-plane rotator so that the magnetic field can be applied at different orientations in the plane to make the measurements.

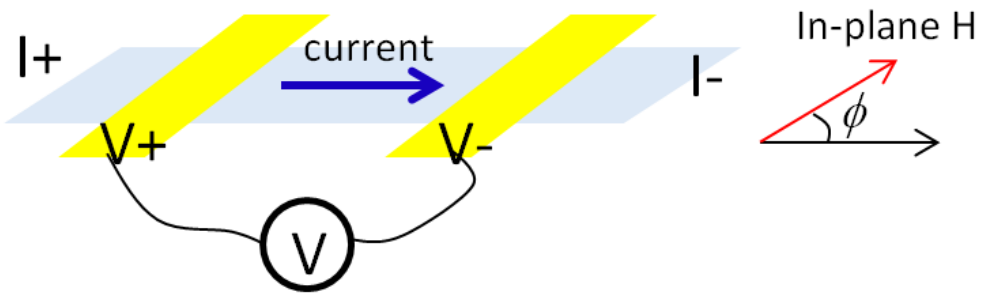


Figure 2.12: Illustration of AMR measurement by the 4-probe setup. Magnetic field can be applied at different angles in the sample plane.

*2.4 Magnetization reversal in epitaxial EB bilayers*

*2.4.1 Competing magnetocrystalline and exchange anisotropy*

The magnetic properties of epitaxial exchange biased Fe/IrMn bilayers on MgO(001) were studied using the above measurements. Two representative samples with different IrMn thicknesses, i.e., $S_{4.5}$: Fe(10 nm)IrMn(4.5 nm)/(Ta 3nm), and $S_8$: Fe(10 nm)IrMn(8 nm)/(Ta 3nm), illustrate the relevant physics. For the sample fabrication, the substrates were pre-annealed at 500 $^{o}$C for 1.5 hour and held at 130 $^{o}$C for the deposition of Fe and IrMn layers. A permanent magnet with a magnetic field ~300 Oe was positioned along the Fe[100] direction during growth. Due to epitaxial growth of Fe on MgO, and the exchange bias from Fe/IrMn interface, the magnetic properties of the sample are expected to be controlled by both magnetocrystalline and exchange anisotropies, and $S_8$ should have stronger exchange anisotropy than $S_{4.5}$. Additionally, there may be a collinear uniaxial anisotropy induced by the exchange bias. The anisotropy configuration for the sample is illustrated in Fig. 2.13.

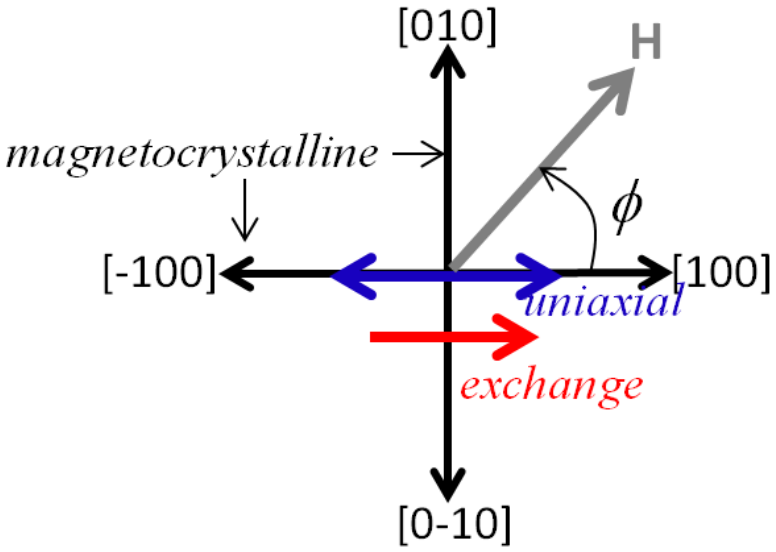


Figure 2.13: Illustration of the easy axes originated from different anisotropies (magnetocrystalline, exchange and uniaxial) with the different symmetries, in the epitaxial Fe/IrMn samples.

Magnetic properties were characterized at room temperature by combined measurements of the longitudinal (||) and transverse ($\perp$) MOKE for different field orientation, $\phi$, which is defined as the angle between the external applied field and the field cooling direction, with $\phi$ increasing in the anti-clockwise direction from $0^o$ to $360^o$. Both normal and stepped hysteresis loops with sharp magnetization transitions were observed. Different magnetic reversal processes were found for $S_{4.5}$ and $S_8$ and are compared in Fig. 2.14. At $|\phi| < 40^o$, the magnetic transitions for $S_{4.5}$ in the descending branch occur in two-steps, at, namely, $H_{c1}$ and $H_{c2}$, with $H_{c1} > H_{c2}$ ($10^o < |\phi| < 40^o$), Fig. 2.14(b). The transverse MOKE loop revealed that the first step is an intermediate state in which Fe spins are oriented along the [010] axis for $10^o < \phi < 40^o$, and along the [0-10] axis for $-40^o < \phi < -10^o$, when the magnetization switches from the [100] to [-100] directions. The magnetic transition displays a single step at $H_{c1}$, with $H_{c1} < H_{c2}$, at $|\phi| < 10^o$, Fig. 2.14(a). For the ascending branch, however, the magnetization switches smoothly from [-100] to [100] direction without resting at any intermediate state. The magnetization reversal for $S_8$ in the descending branch is the

same process as $S_{4.5}$.

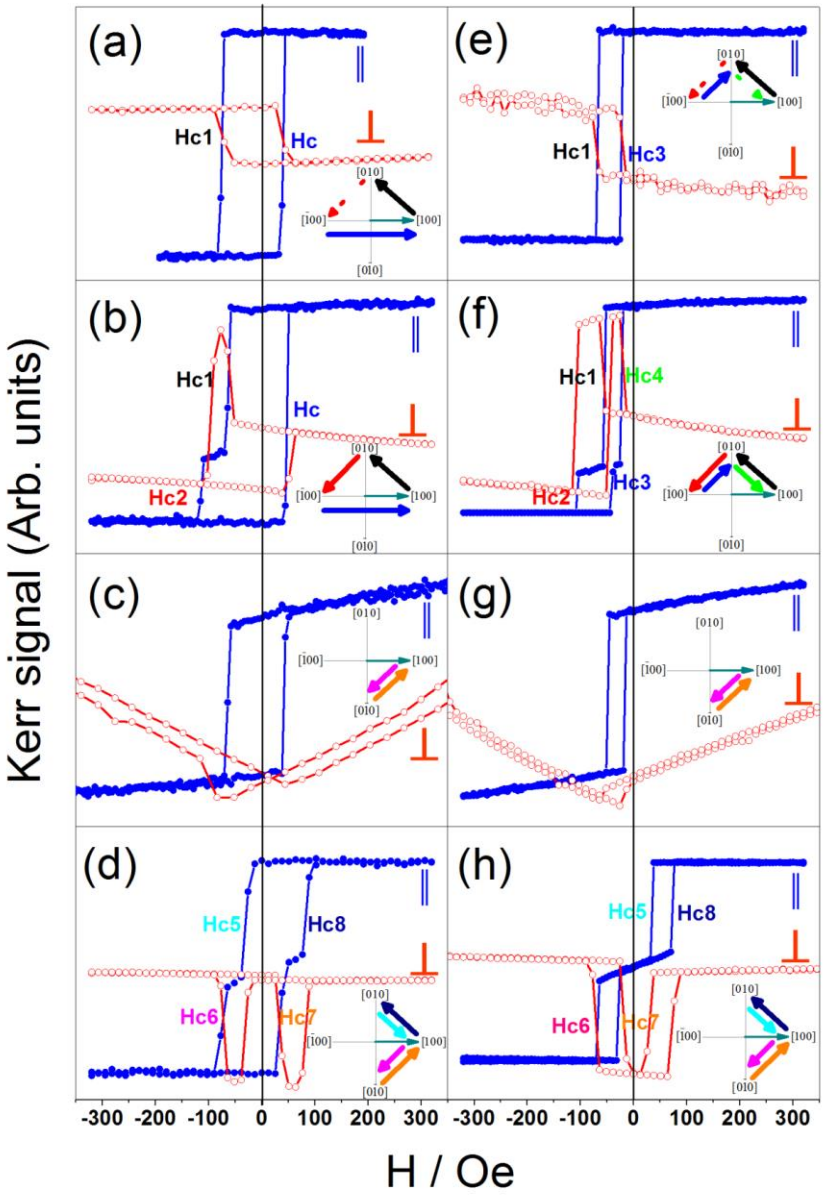


Figure 2.14: Longitudinal (||) and transverse (⊥) MOKE loops measured at various field orientations at $\phi$=2.5°, $\phi$=22.5°, $\phi$=–42.5°, and $\phi$=-87.5° for $S_{4.5}$ (a-d) and $S_8$ (e-h). Inset figures illustrate the magnetization reversal process corresponding to the hysteresis loop. The switching fields in each main figure are shown by the arrows with corresponding colors in the inset figure. Dashed arrow indicates the switching field that is not displayed during the two successive magnetic transitions. The asymmetry (hysteresis) in transverse (⊥) signals in (a) and (b), at $\phi$=2.5°, is due to the slight misalignment between MOKE laser beam plane and the magnetic field.

However, for the ascending branch, the direct 180° magnetic switching cannot be observed but is

replaced by a two-step reversal (Fig. 2.14(f)), i.e., the magnetic transitions take place at $H_{c3}$ and $H_{c4}$, with $H_{c3} < H_{c4}$ ($15^o < |\phi| < 40^o$). It should be noted that $H_{c3}$ and $H_{c4}$ belong to the same semicircle as $H_{c1}$ and $H_{c2}$, as revealed by the transverse MOKE signals. For $|\phi| < 15^o$, only a one-step reversal (at $H_{c3}$) can be observed (Fig. 2.14(e)), implying $H_{c3} > H_{c4}$ at such angular range. The second reversal occurs instantaneously after the first reversal at $H_{c3}$.

For the field applied around the Fe hard axes, i.e., $40^o < |\phi| < 50^o$, hysteresis loops with only one irreversible transition on both branches are observed for both samples (Fig. 2.14(c) and (g)). Double-shifted loops with two-stage magnetic transitions occurring on both branches (referred as $H_{c5}$, $H_{c6}$ for the descending branch and $H_{c7}$, $H_{c8}$ for the ascending branch) were observed for both samples at $50^o < |\phi| < 130^o$, far away from the bias direction (Fig. 2.14(d) and (h)). The transverse MOKE loops show the intermediate state for the ascending and descending branches lie on the same axis given by the bias, i.e., the [100] direction, and the switching route is [0-10] → [100] → [010] for decreasing field and the reverse route for increasing field.

*2.4.2 Modified 'Effective-field model'*

As discussed above, the hysteresis loops measured at various angles reflect, to a certain degree, the competing effect of magnetocrystalline and exchange anisotropies. However, no quantitative relationship has been established between the anisotropies and the switching fields. In the study of exchange biased Fe/$MnF_2$, Arenholz *et al* proposed an 'effective field model' that correlated the magnetic switching fields in the stepped hysteresis loop with the magnetic anisotropies by a series of angular dependent

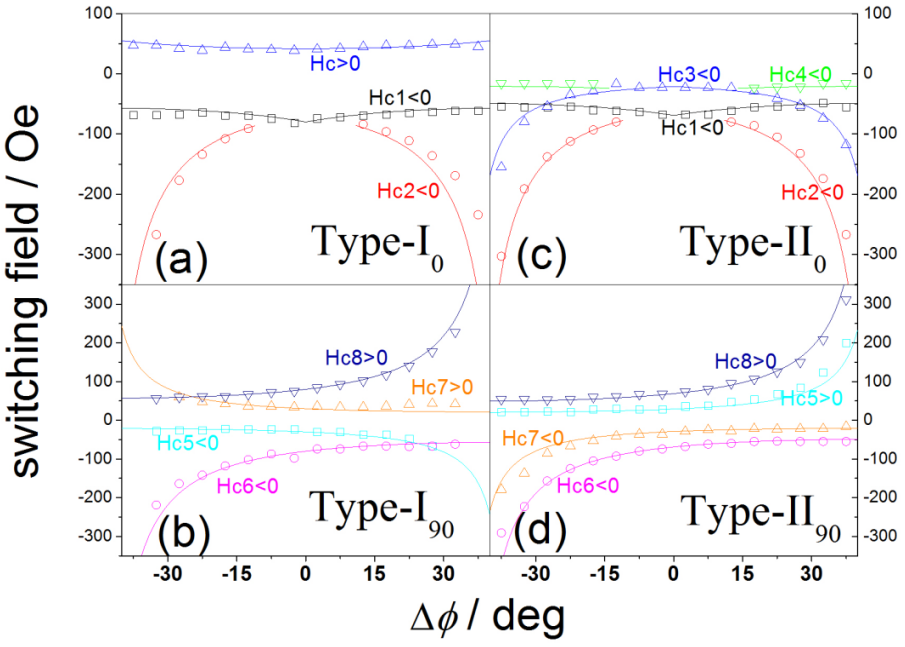


Figure 2.15: Field orientation dependence of the experimentally observed switching fields (symbols) and the corresponding theoretical fittings (curves) for $S_{4.5}$ and $S_8$. $S_{4.5}$ exhibits the type-$I_0$ (a), and type-$I_{90}$ (b) angular dependent behaviors with the characterizing switching fields $H_{c1}<0$, $H_{c2}<0$, $H_c>0$ at $\phi_{\parallel}$, and $H_{c5}<0$, $H_{c6}<0$, $H_{c7}>0$, $H_{c8}>0$ at $\phi_{\perp}$. $S_8$ exhibits the type-$II_0$ (c), and type-$II_{90}$ (d) angular dependent behaviors with the characterizing switching fields $H_{c1}<0$, $H_{c2}<0$, $H_{c3}<0$, $H_{c4}<0$ at $\phi_{\parallel}$, and $H_{c5}>0$, $H_{c6}<0$, $H_{c7}<0$, $H_{c8}>0$ at $\phi_{\perp}$.

measurements [95]. This model considers the effective field from the exchange bias, $H_X$ (unidirectional), and from the Fe magnetocrystalline anisotropy, $H_A$ (fourfold). We applied the basic idea of this model, including the induced uniaxial anisotropy, $H_U$, for a complete analysis. Physically, the existence of such additional uniaxial anisotropy has been confirmed by various measurements (see Fig. 1.2). Our model, considering the uniaxial anisotropy, is referred to as the modified 'effective field model' in the following discussions [96].

Experimentally, the angular dependent switching fields for $S_{4.5}$ and $S_8$ are summarized in Figure 2.15. The data is presented in two different field regions, (1) $\phi_{\parallel}$, for the field orientation $\phi = \phi_0 + \Delta\phi$ with $\phi_0 = 0^o$ and $-40^o < \Delta\phi < 40^o$, i.e., close to the bias direction; (2) $\phi_{\perp}$, for the field orientation $\phi = \phi_0 + \Delta\phi$ with $\phi_0$

= -90° and -40° <$\Delta\phi$< 40°, i.e., close to perpendicular to the bias direction. According to our modified 'effective field model', the effective field for magnetization reversal, $H_{eff}$, is considered to come from four different contributions rather than three as it was originally proposed, i.e., the external magnetic field, $H_{ext}$, the exchange field, $H_X$, the EB induced uniaxial anisotropy field, $H_U$, and the cubic anisotropy field, $H_A$, which is aligned with the Fe easy axis. Notably, both $H_A$ and $H_U$ depend on the projection of the ferromagnetic magnetization onto the Fe easy axis. The switching fields can be derived by comparing the effective fields at the initial and final Fe easy axes involved in the magnetic transition [97]. The theoretical switching fields for 90° magnetic transitions are obtained as:

$$H_{c1}= - (H_X + H_A + H_U) / (\cos\Delta\phi + \sin\Delta\phi), \quad (2.3a)$$

$$H_{c2}= - (H_X + H_A - H_U) / (\cos\Delta\phi - \sin\Delta\phi), \quad (2.3b)$$

$$H_{c3} = - (H_X - H_U - H_A) / (\cos\Delta\phi - \sin\Delta\phi), \quad (2.3c)$$

$$H_{c4} = - (H_X + H_U - H_A) / (\cos\Delta\phi + \sin\Delta\phi), \quad (2.3d)$$

$$H_{c5} = - (H_A - H_U - H_X) / (\cos\Delta\phi - \sin\Delta\phi), \quad (2.3e)$$

$$H_{c6} = - (H_A + H_U + H_X) / (\cos\Delta\phi + \sin\Delta\phi), \quad (2.3f)$$

$$H_{c7} = (H_A - H_U - H_X) / (\cos\Delta\phi + \sin\Delta\phi), \quad (2.3g)$$

$$H_{c8} = (H_A + H_U + H_X) / (\cos\Delta\phi - \sin\Delta\phi). \quad (2.3h)$$

For 180° magnetic switching from the [-100] to [100] axes,

$$H_c = (H_A - H_X + H_U) / \cos\Delta\phi. \quad (2.3i)$$

As can be seen in both Fig. 2.14 and 2.15, within $\phi_{\parallel}$, the characterizing switching fields of $S_{4.5}$ satisfy $H_{c1}$<0, $H_{c2}$<0, but $H_c$>0. A relationship between the effective fields $H_A$>$H_X$-$H_U$ can therefore be predicted according to the above equations. Similarly, the switching fields of $S_8$ show $H_{c1}$<0, $H_{c2}$ <0, $H_{c3}$ <0, and $H_{c4}$

<0, which indicates that $H_X > H_A \pm H_U$. Within $\phi_\perp$, the switching fields for $S_{4.5}$ satisfy $H_{c5}$, $H_{c6} < 0$ and $H_{c7}$, $H_{c8} > 0$, thus $H_A > H_X + H_U$. However, the switching fields for $S_8$ satisfy $H_{c6}$, $H_{c7} < 0$ and $H_{c5}$, $H_{c8} > 0$, which indicates $H_X > H_A - H_U$. Here, we label the angular dependent switching fields for $S_{4.5}$ as type-$I_0$ ($\phi_\parallel$) and type-$I_{90}$ ($\phi_\perp$) behavior (Fig. 2.15(a-b)), and for $S_8$ as type-$II_0$ ($\phi_\parallel$) and type-$II_{90}$ ($\phi_\perp$) behavior (Fig. 2.15(c-d)). Each type of angular dependent behavior has its distinct characteristic switching fields and effective field relationships, as summarized in Table 2.2. Notably, in the original 'effective field model' which excludes $H_U$, the effective field relationships regresses to two simple formulas, i.e., $H_A > H_X$ for Type-$I_{0,90}$ and $H_A < H_X$ for Type-$II_{0,90}$.

Using Eq. (2.3a-i), the angular dependence of the switching fields for $S_{4.5}$ and $S_8$ can be well fitted. Our fitting gave the anisotropy fields: $H_A$= 55 Oe, $H_X$ = 19 Oe, $H_U$ = 6 Oe for $S_{4.5}$; and $H_A$= 20 Oe, $H_X$ = 45 Oe, $H_U$ = 4 Oe for $S_8$. Using the relation $J_{ex} = H_X M_{Fe} t_{Fe}$ and the magnetization for bulk Fe, $M_{Fe}$ = 1700 emu/cm$^3$, and thickness, $t_{Fe}$ = 10 nm, the effective interface energy, $J_{ex}^{eff}$, between Fe and IrMn is obtained as 0.032 erg/cm$^2$ for $S_{4.5}$ and 0.077 erg/cm$^2$ for $S_8$. According the spin-glass model for EB (Chapter 1), this $J_{ex}^{eff}$ can be expressed by $f \times J_{ex}$, where $f$ is the conversion factor ($0 < f < 1$) and $J_{ex}$ is the maximum exchange energy (exchange constant). Value of $f$ depends on the disordered SG spins at

| range | Type | Characterizing switching fields | Effective fields relationship (mEFM) | Effective fields relationship (EFM) |
|---|---|---|---|---|
| $\phi_\parallel$ | Type-$I_0$ | $H_{c1}, H_{c2} < 0, H_c > 0$ | $H_A > H_X - H_U$ | $H_A > H_X$ |
| | Type-$II_0$ | $H_{c1}, H_{c2}, H_{c3}, H_{c4} < 0$ | $H_X > H_A \pm H_U$ | $H_X > H_A$ |
| $\phi_\perp$ | Type-$I_{90}$ | $H_{c5}, H_{c6} < 0, H_{c7}, H_{c8} > 0$ | $H_A > H_X + H_U$ | $H_A > H_X$ |
| | Type-$II_{90}$ | $H_{c6}, H_{c7} < 0, H_{c5}, H_{c8} > 0$ | $H_X > H_A - H_U$ | $H_X > H_A$ |

Table 2.2: Summary of the characterizing switching fields and the effective-field relationship of the different types of angular dependent behaviors for modified effective field model (mEFM) and (effective field model) EFM.

the interface which further depends on the AF layer thickness (Fig. 1.13). A thinner AF layer usually has more significant SG phase due to the weak AF anisotropy (smaller *f*), therefore further gives rise to a smaller $J_{ex}^{eff}$.

In the original 'effective field model', the Type-$I_0$ (Type-$II_0$) angular dependent behavior is predicted to show up simultaneously with Type-$I_{90}$ (Type-$II_{90}$) according to the effective field relationships. This is not a problem in the reported Fe/$MnF_2$ systems, where $H_A$ is significantly larger than $H_X$. However, as we have demonstrated, taking into account $H_U$ discriminates the critical conditions for the type-$I_0$ and type-$I_{90}$ angular dependent behaviors, as well as for type-$II_0$ and type-$II_{90}$. By comparing those critical conditions, we predict theoretically that the observation of type-$II_0$ should simultaneously lead to the observation of type-$II_{90}$, since $H_X > H_A - H_U \subset H_X > (H_A \pm H_U)$; however, the observation of type-$I_0$ does not necessarily lead

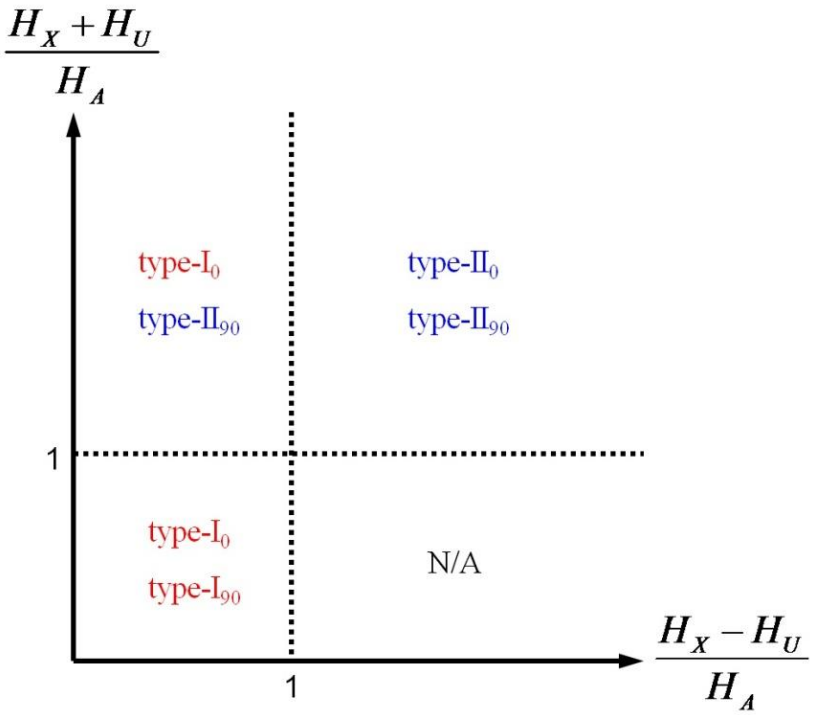


Figure 2.16: Phase diagram showing the relationship between different types of angular dependent behaviors with the relative magnitudes of the effective anisotropy fields.

to the observation of type-$I_{90}$, because $H_A > H_U + H_X \not\subset H_A > H_X - H_U$. In other words, it is possible to observe the combination of both type-$I_0$ and type-$II_{90}$ when the relationship $H_U + H_X > H_A > H_X - H_U$ is satisfied. This critical effect of $H_U$ is particularly significant when $H_A$ and $H_X$ are of comparable magnitude. A phase diagram shows the different sets of angular dependent behavior is varied with the ratio $(H_X - H_U)/H_A$ and $(H_X + H_U)/H_A$, as plotted in Fig. 2.16. In the original model, only two sets of angular dependence, i.e., type-$I_{0,90}$ and type-$II_{0,90,}$ are predicted to appear on either side of the critical point of $H_X = H_A$. The induced $H_U$ in our model results in the new combination (type-$I_0$, type-$II_{90}$) where $H_U + H_X > H_A > H_X - H_U$ is satisfied.

In summary, to unravel the ongoing puzzles of exchange bias as introduced in Chapter 1, we developed recipes for depositing epitaxial Fe/IrMn and Fe/MnPd bilayers using ion beam sputtering. We also performed structural characterizations on the samples and revealed the details of their epitaxy relationships. These thin-film bilayers, with optimized crystalline coherence and well defined interface structure, serve as ideal candidates for EB related studies. Using different growing temperatures, the AF compensation can be controlled by selectively growing *c*-axis MnPd (spin-compensated) or *a*-axis MnPd (spin-uncompensated) on top of Fe/MgO. In addition, series of samples can be grown with varying F and AF layer thicknesses without altering their epitaxy property. The content covered in this chapter laid the material foundation to the subsequent work of this thesis.

We also characterized the basic magnetic reversal properties of the thin-film bilayers. By applying the external field along different orientations to the anisotropy axis, we measured the angular-dependent magnetic reversal at room temperature and found unique, stepped hysteresis loops along certain angles. These preliminary results indicate competing effects of different magnetic anisotropies on the magnetic

reversal. A phenomenological ‘effective-field model’ was also used to give a tentative interpretation on the angular dependence of the reversal fields. Nevertheless, the detailed reversal mechanisms (rotation or DW process) are still unclear for these samples, as well as their dependence upon various parameters such as F and AF thicknesses, temperature, misalignment, and AF bulk properties. Systematic work is required to address the above issues, as will be discussed in the next Chapter.

# Chapter 3

# 'DOMAIN WALL NUCLEATION MODEL' FOR EXCHANGE BIAS

Contents of this chapter have been partially published in Ref.[90], [98], [101], [108], [124]

## *3.1 Model development and key parameters*

In Chapter 2, we used the 'effective field model' to tentatively give a quantitative interpretation on the magnetization reversal of our sample with competing anisotropies. However, the 'effective fields' used in the analysis, particularly $H_A$, does not have a clear physical origin. In other words, the effective fields are inferred rather than defined, and the mechanism for magnetization reversal has not been deliberated. In practice, similar stepped hysteresis loops are even observed in Fe/MgO(001) thin films and attributed to the DW nucleation and propagation along different Fe easy axes [16-19]. Such DW behaviors were also verified by direct magnetic imaging [82]; as a result, it is reasonable to consider DW motion as the reversal mechanism for our epitaxial Fe/IrMn and Fe/MnPd bilayers [98].

Let's consider an epitaxial Fe/IrMn bilayer system with competing magnetocrystalline ($K_1$), exchange ($K_{eb}$) and an induced uniaxial ($K_u$) anisotropy, where both $K_{eb}$ and $K_u$ are superimposed along

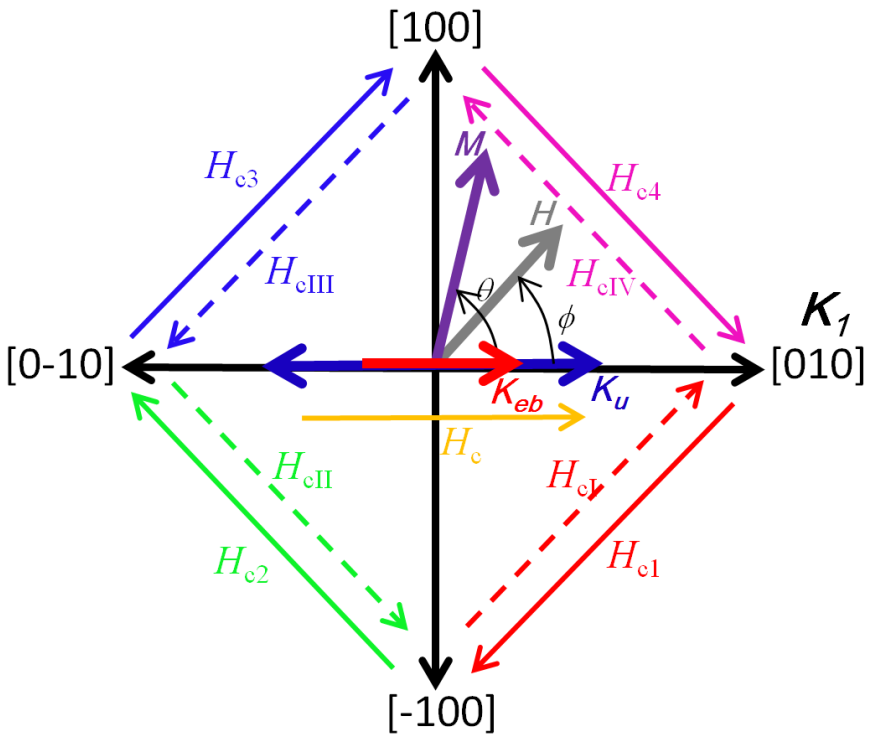


Figure 3.1: Geometry of the magnetic anisotropies and definition of the various switching fields between different Fe easy axes.

the Fe[010] easy axis, Fig. 3.1. The significant $K_1$ favors magnetization reversal via DW motion along the fourfold Fe easy axes, which must overcome the intrinsic energy barriers, i.e. DW nucleation energies: $\varepsilon_{90}{}^{o}$ and $\varepsilon_{180}{}^{o}$. On the other hand, the unidirectional ($K_{eb}$) and uniaxial ($K_u$) anisotropies break the fourfold symmetry of $K_1$; thus the actual switching fields ($H_{c1}$, $H_{c2}$, $H_{c3}$, $H_{c4}$, $H_{cI}$, $H_{cII}$, $H_{cIII}$, $H_{cIV}$), indicated in Fig. 3.1, are altered and depend on $\varepsilon$, $K_{eb}$ and $K_u$. Specifically, the total energy for the Fe/IrMn bilayer can be rewritten as:

$$E = \frac{K_1}{4}\sin^2 2\theta - K_u \cos^2\theta - K_{eb}\cos\theta - MH\cos(\phi - \theta), \qquad (3.1)$$

where $\theta$ is the angle between the magnetization $M$ and the EB direction. Therefore, the energies of single domain states at these four Fe easy axes are:

$$E_{[010]} = -K_{eb} - K_u - MH\cos\phi, \quad (3.2a)$$

$$E_{[100]} = -MH\sin\phi, \quad (3.2a)$$

$$E_{[0\text{-}10]} = K_{eb} - K_u + MH\cos\phi, \quad (3.2c)$$

$$E_{[\text{-}100]} = MH\sin\phi. \quad (3.2d)$$

Reversal can occur when the energy advantage equals the energy cost in nucleating and propagating a DW of the relevant type, $\varepsilon_{90}{}^{o}$ and $\varepsilon_{180}{}^{o}$. As a result, the various switching fields can be derived as a function of the key parameters of the sample, i.e., $\varepsilon_{90}{}^{o}$ or $\varepsilon_{180}{}^{o}$, $K_{eb}$ and $K_u$. Specifically:

$H_{c1}$ is the switching field from [010] to [-100] easy axis. The energy at the initial direction of magnetization is $E_i^{[010]} = K_u + K_{eb} + MH_{ext}\cos\phi$, and at the final direction is $E_f^{[-100]} = -MH_{ext}\sin\phi$. The magnetic transition occurs at $H_{c1}$ when $E_f^{[010]} - E_i^{[-100]} = \varepsilon_{90}{}^{o}$. Therefore,

$$H_{c1} = -(\varepsilon_{90}{}^{o} + K_{eb} + K_u) / M(\cos\phi + \sin\phi). \quad (3.3a)$$

$H_{c2}$ is the switching field from [-100] to [0-10] easy axis. The energy at the initial direction is $E_i^{[-100]} = -MH_{ext}\sin\phi$, at the final direction is $E_f^{[0-10]} = K_u - K_{eb} - MH_{ext}\cos\phi$. The magnetic transition occurs at $H_{c2}$ when $E_f^{[-100]} - E_i^{[0-10]} = \varepsilon_{90}{}^{o}$. Therefore,

$$H_{c2} = -(\varepsilon_{90}{}^{o} + K_{eb} - K_u) / M(\cos\phi - \sin\phi). \quad (3.3b)$$

$H_{c3}$ is the switching field from [0-10] to [100] easy axis. The energy at the initial direction is $E_i^{[0-10]} = K_u - K_{eb} - MH_{ext}\cos\phi$, at the final direction is $E_f^{[100]} = MH_{ext}\sin\phi$. The magnetic transition occurs at $H_{c3}$ when $E_f^{[0-10]} - E_i^{[100]} = \varepsilon_{90}{}^{o}$. Therefore,

$$H_{c3} = (\varepsilon_{90}{}^{o} - K_{eb} + K_u) / M(\cos\phi + \sin\phi). \quad (3.3c)$$

$H_{c4}$ is the switching field from [100] to [010] easy axis. The energy at the initial direction is $E_i^{[100]} =$

$MH_{ext}\sin\phi$, at the final direction is $E_f^{[010]} = K_u + K_{eb} + MH_{ext}\cos\phi$. The magnetic transition occurs at $H_{c4}$ when $E_f^{[100]} - E_i^{[010]} = \varepsilon_{90^o}$. Therefore,

$$H_{c4} = (\varepsilon_{90^o} - K_{eb} - K_u) / M(\cos\phi - \sin\phi). \quad (3.3d)$$

$H_{cI}$ is the switching field from [-100] to [010] easy axis. The energy at the initial direction is $E_i^{[-100]} = -MH_{ext}\sin\phi$, at the final direction is $E_f^{[010]} = K_u + K_{eb} + MH_{ext}\cos\phi$. The magnetic transition occurs at $H_{cI}$ when $E_f^{[-100]} - E_i^{[010]} = \varepsilon_{90^o}$. Therefore,

$$H_{cI} = (\varepsilon_{90^o} - K_{eb} - K_u) / M(\cos\phi + \sin\phi). \quad (3.3e)$$

Note that $H_{cI}$ is different from $H_{c1}$ simply because that the $K_{eb}$ and $K_u$ break the fourfold symmetry of the Fe magnetocrystalline anisotropy.

$H_{cII}$ is the switching field from [0-10] to [-100] easy axis. The energy at the initial direction is $E_i^{[0-10]} = K_u - K_{eb} - MH_{ext}\cos\phi$, at the final direction is $E_f^{[-100]} = -MH_{ext}\sin\phi$. The magnetic transition occurs at $H_{cII}$ when $E_f^{[0-10]} - E_i^{[-100]} = \varepsilon_{90^o}$. Therefore,

$$H_{cII} = (\varepsilon_{90^o} - K_{eb} + K_u) / M(\cos\phi - \sin\phi). \quad (3.3f)$$

$H_{cIII}$ is the switching field from [100] to [0-10] easy axis. The energy at the initial direction is $E_i^{[100]} = MH_{ext}\sin\phi$, at the final direction is $E_f^{[0-10]} = K_u - K_{eb} - MH_{ext}\cos\phi$. The magnetic transition occurs at $H_{cIII}$ when $E_f^{[100]} - E_i^{[0-10]} = \varepsilon_{90^o}$. Therefore,

$$H_{cIII} = -(\varepsilon_{90^o} + K_{eb} - K_u) / M(\cos\phi + \sin\phi). \quad (3.3g)$$

$H_{cIV}$ is the switching field from [010] to [100] easy axis. The energy at the initial direction is $E_i^{[010]} = K_u + K_{eb} + MH_{ext}\cos\phi$, at the final direction is $E_f^{[100]} = MH_{ext}\sin\phi$. The magnetic transition occurs at $H_{cIV}$ when $E_f^{[010]} - E_i^{[100]} = \varepsilon_{90^o}$. Therefore,

$$H_{cIV} = -(\varepsilon_{90^o} + K_{eb} + K_u) / M(\cos\phi - \sin\phi). \quad (3.3h)$$

$H_c$ is the switching field from [0-10] to [010] easy axis. The energy at the initial direction is $E_i^{[0-10]} = K_u - K_{eb} - MH_{ext}\cos\phi$, at the final direction is $E_f^{[010]} = K_u + K_{eb} + MH_{ext}\cos\phi$. $H_c$ is the 180° magnetic transition, which occurs when $E_f^{[010]} - E_i^{[0-10]} = \varepsilon_{180^o}$. Therefore,

$$H_c = (\varepsilon_{180^o} - 2K_{eb}) / 2M\cos\phi . \quad (3.3i)$$

In summary, the predicted equations for the switching fields, based on the DW nucleation and propagation mechanism, are written as:

$$H_{c1} = -(\varepsilon_{90^o} + K_{eb} + K_u) / M(\cos\phi + \sin\phi), \quad (3.3a)$$

$$H_{c2} = -(\varepsilon_{90^o} + K_{eb} - K_u) / M(\cos\phi - \sin\phi), \quad (3.3b)$$

$$H_{c3} = (\varepsilon_{90^o} - K_{eb} + K_u) / M(\cos\phi + \sin\phi), \quad (3.3c)$$

$$H_{c4} = (\varepsilon_{90^o} - K_{eb} - K_u) / M(\cos\phi - \sin\phi), \quad (3.3d)$$

$$H_{cI} = (\varepsilon_{90^o} - K_{eb} - K_u) / M(\cos\phi + \sin\phi), \quad (3.3e)$$

$$H_{cII} = (\varepsilon_{90^o} - K_{eb} + K_u) / M(\cos\phi - \sin\phi), \quad (3.3f)$$

$$H_{cIII} = -(\varepsilon_{90^o} + K_{eb} - K_u) / M(\cos\phi + \sin\phi), \quad (3.3g)$$

$$H_{cIV} = -(\varepsilon_{90^o} + K_{eb} + K_u) / M(\cos\phi - \sin\phi), \quad (3.3h)$$

$$H_c = (\varepsilon_{180^o} - 2K_{eb}) / 2M\cos\phi , \quad (3.3i)$$

In the model discussed above, the key anisotropy parameters – $\varepsilon_{90^o}$, $K_{eb}$, $K_u$ – determine the DW nucleation and propagation process; $\varepsilon_{90^o}$ gives the energy barrier for a DW to nucleate and propagate along the Fe easy axis. In EB samples, this energy barrier is attributed to the pinning pressure caused by defects in the film; however, it can also be influenced by the F/AF coupling as will be discussed later in this chapter. The latter two parameters, $K_{eb}$ and $K_u$ respectively, are unidirectional and uniaxial anisotropies induced by the exchange bias.

*3.2 Magnetic properties of epitaxial EB bilayers*

Magnetic reversal of the epitaxial Fe/IrMn bilayers were first studied by angular dependent MOKE and AMR at room temperature. The switching fields determined by MOKE and AMR yield the same results in our experiment, thus these two techniques are considered equivalent methods for detecting magnetic reversal. Since our MOKE system does not have a low temperature measurement setup, we used the AMR for probing magnetic reversal at a wide range of temperatures from 10 to 300 K. Values for $\varepsilon_{90}{}^{o}$, $K_{eb}$, and $K_u$, as well as their evolutions with film parameters (F, AF thickness, field cooling, and temperature, etc) were determined and interpreted by the DW nucleation model, which further allowed the magnetization reversal processes and interfacial spin behaviors to be examined for these epitaxial EB films.

*3.2.1 Pinned and rotatable AF spins (AF layer dependence)*

*Magnetic reversal characteristics*

A series of Fe/IrMn bilayers with different IrMn layer thicknesses were grown and studied. The substrates were pre-annealed at 500°C for 1.5 h and held at 145°C for deposition. A permanent magnet generating a field of ~ 300 Oe was positioned along the Fe[010] direction during growth. Samples with the structure of MgO/Fe(15nm)/IrMn($t_{IrMn}$)/Ta(3nm, cap) were deposited with $t_{IrMn}$=0, 2, 3, 4, 4.5, 5, 5.5, 6,

8, 10, 14 nm. The anisotropy geometry and the magnetic switching routes were the same as illustrated in Fig. 3.1. The EB gives rise to $K_{eb}$ and a collinear uniaxial anisotropy, $K_u$, along the field cooling direction. Various switching routes between the Fe easy axes were observed using longitudinal (||) and transverse ($\perp$) MOKE loops, which were obtained at different $\phi$: the angle between the external applied field, $H_{ext}$, and the field cooling direction.

For samples with $t_{IrMn} \leq 4$ nm, the IrMn is too thin to establish a clear EB. Square loops (Fig. 3.2(a)) and double-sided two-step loops (Fig. 3.2(b) and 3.2(c)) were observed due to a weak $K_u$ superimposed on the fourfold magnetocrystalline anisotropy. The transverse MOKE signals revealed the magnetization reversal in the descending and ascending branches of the double-sided two-step loops are in opposite semicircles. The angular dependent behavior (Fig. 3.3(a)) looks symmetrical about $H$($y$-axis) = 0, $\phi$ ($x$-axis) = $0^o$ and $90^o$ due to the weak EB and is similar to Fe/MgO(001) films (Fig. 1.2).

For $t_{IrMn}$ = 5 nm sample, the loop measured at $\phi = 0^o$ starts to shift to the negative direction (Fig. 3.2(d)). The loop was asymmetric near $\phi = 0^o$ and showed a two-step transition in the descending branch, while a single step was observed in the ascending branch, Fig. 3.2(e). Perpendicular to the bias, for $45^o < \phi < 135^o$, two kinds of double-sided two-step loops were observed. When $\phi$ is far from $90^o$, the magnetization reversal for descending and ascending branches still occur at opposite semicircles; however, when $\phi$ is close to $90^o$, the magnetic switching routes for both branches are mediated via the same Fe easy axis determined by the bias (Fig. 3.2(f)). The $\phi$-dependent switching fields shows a clear asymmetry about $\phi = 90^o$ (Fig. 3.3(b)), suggesting the enhanced EB introduces an asymmetry in anisotropy about $\phi = 90^o$.

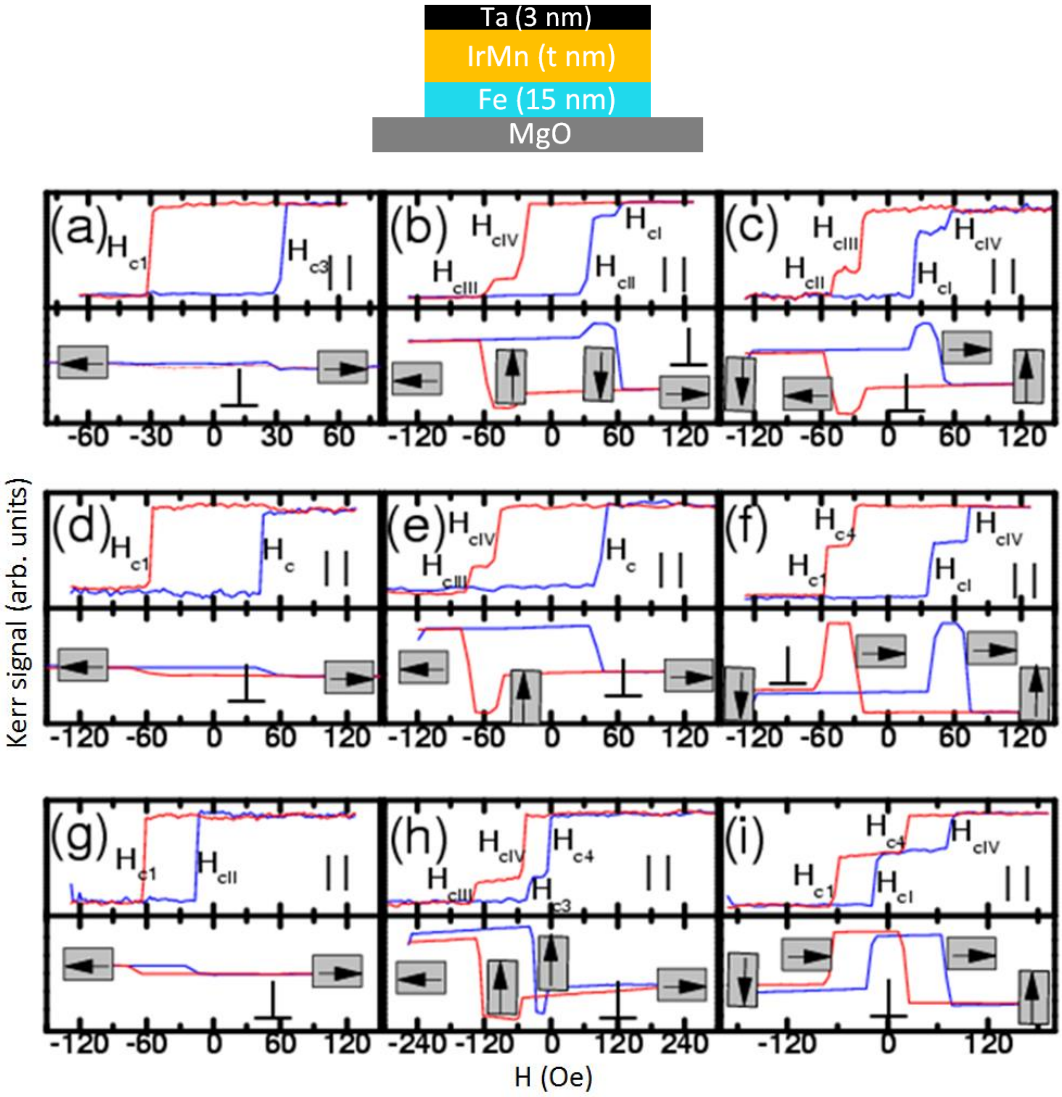


Figure 3.2: Illustration of the sample structure (top) and the longitudinal (||) and transverse (⊥) MOKE loops measured at various field orientations for three samples with different $t_{IrMn}$. Results for 4 nm $t_{IrMn}$ sample at (a) $\phi = 0^o$ (square loop), (b) $\phi = -30^o$ (double-side two-step loop, opposite semicircles), and (c) $\phi = 70^o$ (double-side two-step loop, opposite semicircles). Results for 5 nm $t_{IrMn}$ sample at (d) $\phi = 0^o$, (e) $\phi = -15^o$ (asymmetrically shaped loop), and (f) $\phi = 85^o$ (double-side two-step loop, same semicircle). Results for 6 nm $t_{IrMn}$ sample at (g) $\phi = 0^o$, (h) $\phi = -27.5^o$ (double-side two-step loop, same semicircle), and (i) $\phi = 82.5^o$ (double-side two-step loop, same semicircle). The orientation of Fe spins in the switching processes is represented by the arrows enclosed in a rectangle.

Finally, as $t_{IrMn}$ increases to 6 nm, the loop at $\phi = 0°$ is completely shifted to the negative field regime (Fig. 3.2(g)). Within $-45^o < \phi < 45^o$, a different type of double-sided two-step loop was observed at $\phi$ away from $0^o$ (Fig. 3.2(h)), with the magnetization reversal for both branches mediated via the same

Fe easy axis. Between $45^o$ and $135^o$, all magnetization reversals are mediated via the same Fe easy axis superimposed by the bias, as shown in Fig. 3.2(i). In the $\phi$–dependent behavior, the symmetry about $\phi$ = $90^o$ is completely broken. For bilayers with $t_{IrMn}$> 6 nm, the magnetization reversal characteristics are identical to the 6 nm $t_{IrMn}$ sample.

*Angular dependence interpreted by the 'DW nucleation model'*

We can use the DW nucleation model to interpret the angular dependence of the switching fields. For samples with $t_{IrMn} \leq 4$ nm, the data shows excellent agreement with the model for $K_{eb} = 0$ (Fig. 3.3(a)) due to the weak EB. It should be noted that, according to the reversal mechanism of two successive $90^o$ magnetic transitions [18], the switching fields for the square loop are fitted to $H_{c1}$ and $H_{c3}$ ($90^o$ DW process), rather than $H_c$, ($180^o$ DW process). This is because the $90^o$ DW process is energetically more favorable (occurring at smaller field) than the $180^o$ one (occurring at larger field). The absence of the second step ($H_{c2}$ or $H_{c4}$) from the hysteresis loop is simply because that $H_{c1} < H_{c2}$ and $H_{c3} > H_{c4}$. Therefore the second step takes place instantaneously after the first step. The one-step (Fig. 3.2(a)) and two-step (Fig. 3.2(b)) routes, for example in the case $-45^o < \phi < 0^o$, correspond to $H_{clII} > H_{clV}$ ($H_{cI} < H_{cII}$) and $H_{clII} < H_{clV}$ ($H_{cI} > H_{cII}$) for decreasing (increasing) field, respectively. On the other hand, for samples with $t_{IrMn}$ = 5 nm a non-zero $K_{eb}$ must be used (Fig. 3.3(b)). For $-45^o < \phi < 45^o$, a direct $180^o$ DW nucleation and propagation becomes energetically favorable instead of the two successive $90^o$ DW process. Actually, the $180^o$ DW process and the successive $90^o$ DW process can be distinguished just from the angular ($\phi$) dependence of the relevant switching field.

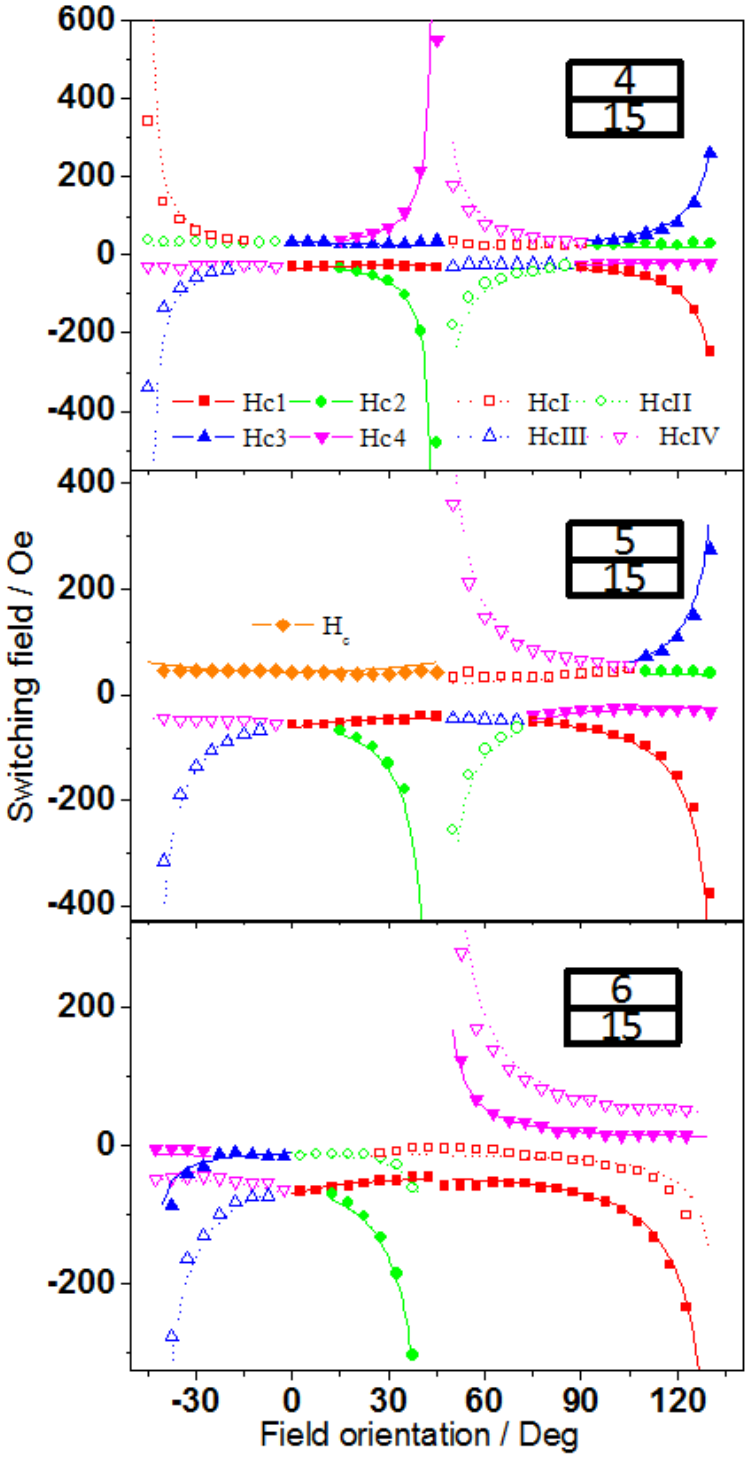


Figure 3.3: Typical field orientation dependence of the experimentally observed switching fields (symbols) and the corresponding theoretical fitting results (curves) for Fe/IrMn bilayers with (a) $t_{IrMn}$ = 4 nm, (b) $t_{IrMn}$ = 5 nm, and (c) $t_{IrMn}$ = 6 nm. The switching fields, represented by different symbols and curves, correspond to the magnetic transitions between different initial and final Fe easy axes orientations as defined in Fig. 3.1.

According to Eq. (3.3), the 180° DW process gives rise to a local minimum around $\phi = 0^{o}$ ($\frac{1}{cos\phi}$ dependence), however, the 90° DW process gives rise to a local maximum around $\phi = 0^{o}$ ($\frac{1}{cos\phi \pm sin\phi}$ dependence). For $70^{o} < \phi < 110^{o}$, the magnetization reversal occurs along the same semicircle for descending ($H_{c1}$, $H_{c4}$) and ascending ($H_{cI}$, $H_{cIV}$) branches. Hysteresis loops revealed that $H_{c4} < 0$, $H_{cI} > 0$ at $\phi = 90^{o}$. As $t_{IrMn}$ increased to 6 nm, the $\phi$-dependent behavior was further modified (Fig. 3.3(c)). Double-side, two-step loops were observed at $25^{o} < |\phi| < 45^{o}$. The critical angle separating one-step to two-step reversal is different for descending and ascending branches. For example within $-45^{o} < \phi < 0^{o}$, the critical angle is -5° and -25° for descending and ascending branch, respectively. Note that in this sample, $H_{c4} > 0$, $H_{cI} < 0$ at $\phi = 90^{o}$.

*AF thickness dependence*

Similar analyses on all other samples were performed and the fitted parameters (in the form of effective fields) are plotted in Fig. 3.4. Notably, the value for $\varepsilon_{90^{o}}/M$ becomes much greater than that in the single Fe films (~ 5Oe), which indicates, apart from the defects in the Fe layer, the F/AF interface contributes to the energy barrier for DW nucleation and propagation. Specifically, for $t_{IrMn} \leq 4$ nm, $K_{eb}/M = 0$ and $\varepsilon_{90^{o}}/M$ displays a gradual enhancement with $t_{IrMn}$. For 4 nm < $t_{IrMn}$ < 6 nm, $K_{eb}/M$ rapidly increases, while $\varepsilon_{90^{o}}/M$ decreases after peaking at 4.5 nm. In comparison, the induced $K_u$ is very small for all values of $t_{IrMn}$. Finally, since the 180° DW process is only observed in one sample ($t_{IrMn}$ = 5 nm), it is impossible to plot such thickness dependence for $\varepsilon_{180^{o}}/M$.

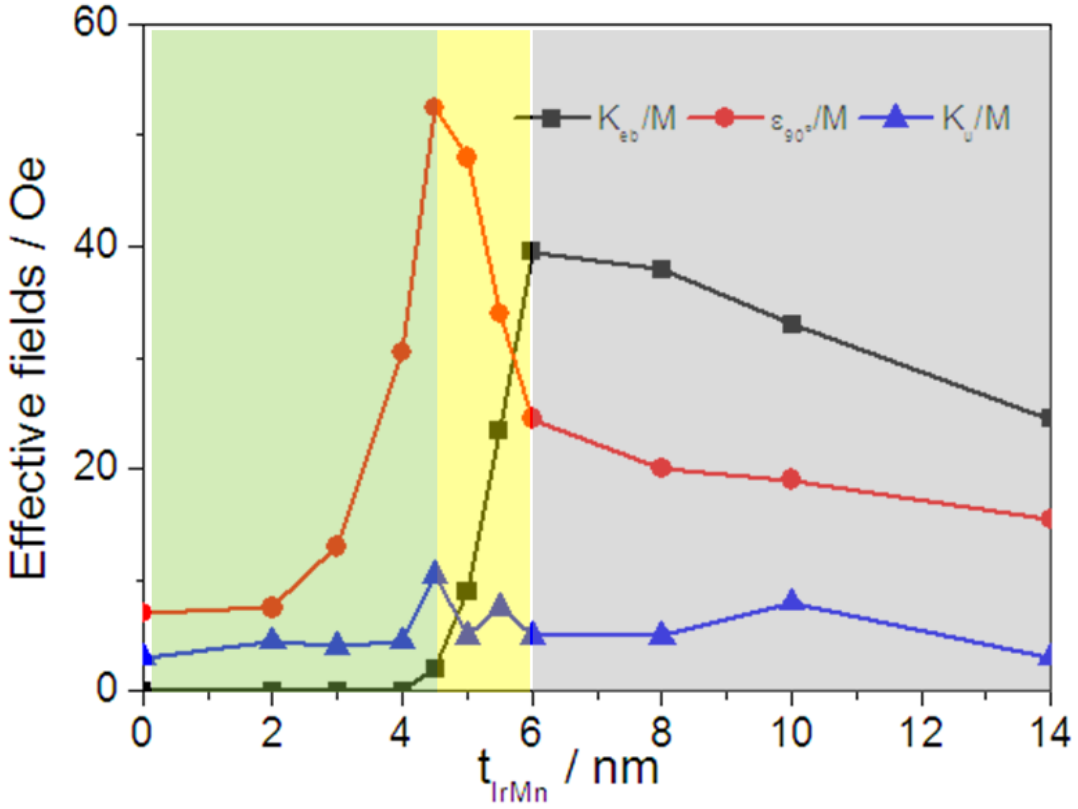


Figure 3.4: IrMn thickness dependence of $\varepsilon_{90}{}^{o}$, $K_{eb}$, and $K_u$ (in the form of effective fields) derived by the fittings from Fig. 3.3 for the series of Fe/IrMn bilayers.

*Pinned and rotatable AF spins*

In the studies of epitaxial Fe/MgO system [16-19], $\varepsilon_{90}{}^{o}$ is believed an intrinsic parameter of Fe, whose magnitude is determined by the pinning pressure from defects against the nucleation of a new DW. Here, the $t_{AF}$ dependence of $\varepsilon_{90}{}^{o}$ in our result indicates that such parameter is also contributed by spins in the AF layer. Earlier works using Synchrotron radiation have revealed a 'rotatable' behavior, in addition to the 'pinned' behavior, of the AF spins close to the F/AF interface [57,58,99]. Specifically, the pinned spins (along the field cooling direction) give rise to the unidirectional anisotropy and thus the loop shifts. But the rotatable ones would just reverse with the F spins during magnetic reversal, and provide no

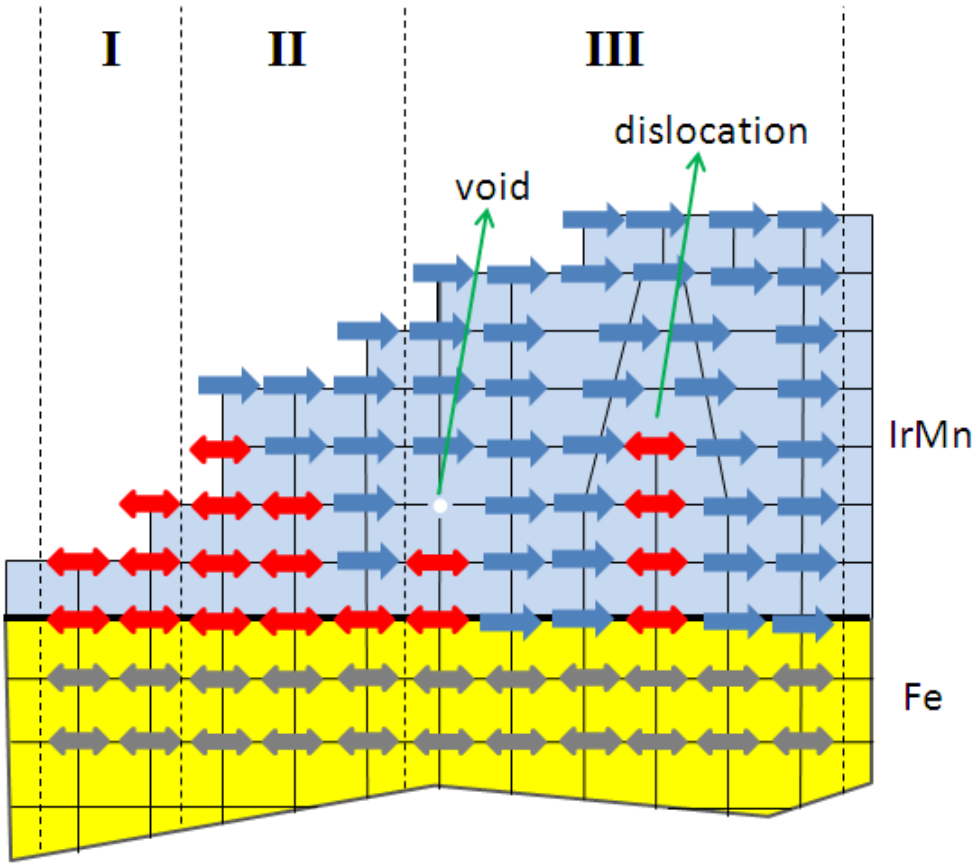


Figure 3.5: Illustration of the physical origin, i.e. pinned (→) and rotatable (↔) AF spins, of the $t_{AF}$ dependence of $K_{eb}$ and $\varepsilon_{90}{}^{o}$. I: AF spins are all rotatable (↔) due to the strong F/AF coupling and the weak AF anisotropy at thin $t_{AF}$. Increasing the $t_{AF}$ only enhances $\varepsilon_{90}{}^{o}$. II: Competing region for the rotatable and pinned (→) spins at intermediate $t_{AF}$. Certain spins are pinned and gives rise to $K_{eb}$. III: Saturation region for exchange bias where ideally all spins are pinned to give rise to $K_{eb}$. Rotatable spins exist at the interface only because the defects in the film that break the AF ordering.

unidirectional anisotropy but only an enhanced coercivity. Such rotatable characteristic can be revealed by element specific measurements [57,58]. For example, by using x-ray magnetic reflectivity [57], the spin behaviors of Mn and Fe in an epitaxial Fe/MnPd bilayer were investigated. The field hysteresis of the antiferromagnetic Mn moments exhibits almost the same behavior with the ferromagnetic Fe moments, indicating that certain Mn moments are strongly coupled to the Fe ones during the magnetic reversal. Further experiments also revealed the distinct depth profiles of the pinned and rotatable spins. In the case of Fe/MnPd, the rotatable Mn moments are found only in a narrow region of 4 Å width directly below the

interface. The pinned Mn moments, on the other hand, occur in a much wider region of 13 Å in width with the maximum of the pinned moment distribution ~ 2 Å below the maximum for the rotatable ones. In our sample, the 'coercivity' is essentially the DW nucleation energy, $\varepsilon_{90}{}^{o}$ and $\varepsilon_{180}{}^{o}$, as they both physically reflect the pinning pressure against the magnetic reversal (DW process in our case). Therefore, the enhanced values of $\varepsilon_{90}{}^{o}$ in our EB bilayers (Fig. 3.4) are straightforwardly attributed to the rotatable AF spins.

We then focus on understanding the non-monotonic behavior of the $t_{AF}$ dependence. As demonstrated in Fig. 3.5, for $t_{IrMn} \leq 4$ nm (Region I), the AF anisotropy is too weak to establish a bias – AF spins at the interface only reverse with the F spins due to the strong exchange coupling, and contribute to the enhanced 'coercivity', i.e. $\varepsilon_{90}{}^{o}$. Further increasing the AF thickness enhances $\varepsilon_{90}{}^{o}$ until $t_{IrMn}$ = 4.5 nm, while some AF spins start to get pinned and provide a non-zero $K_{eb}$ (Region II) – this is the competing region for the pinned and rotatable spins, where both AF components increase as $t_{IrMn}$ increases. The total number of pinned and rotatable spins reaches saturation at a certain $t_{IrMn}$ value (4.5 nm in our case). Further increase in $t_{IrMn}$ only results in more AF spins being pinned and less of them being rotatable; thus an increase in $K_{eb}$, but a decrease in $\varepsilon_{90}{}^{o}$, can be observed for 4.5 nm $\leq t_{IrMn} \leq$ 6 nm. Above 6 nm (Region III), the exchange bias field reaches saturation because $t_{IrMn}$ exceeds the AF correlation length, $\varepsilon_{AF}$. This correlation length is sometimes also understood as the AF DW width, thus is determined by the exchange stiffness and the AF anisotropy. AF spins within such a length maintain their mutual interactions. At Region III, all the AF spins should be pinned and give rise to EB. However, due to inevitable defects in the film (voids, dislocations, etc), long range AF ordering can be broken; therefore the spins below the defects are rotatable and still contribute to $\varepsilon_{90}{}^{o}$ (although $t_{IrMn}$ is greater than $\varepsilon_{AF}$). In consequence, both $K_{eb}$

and $\varepsilon_{90}{}^{o}$ reach saturation at 6 nm and maintain a finite value even with further increases in $t_{IrMn}$. The maximum exchange field is $H_{eb}{}^{m} = K_{eb}{}^{m}/M$ = 40 Oe at $t_{IrMn}$ = 6 nm. Using the relation $J_{ex} = H_{eb}{}^{m}M_{Fe}t_{Fe}$, and the magnetization for bulk Fe, $M_{Fe}$ = 1700 emu/cm$^3$, and $t_{Fe}$ = 15 nm, the interfacial exchange energy, $J_{ex}$, between Fe and IrMn is obtained as 0.102 erg/cm$^2$. The critical thickness of the IrMn layer for observing EB, $t_{cri}$, is ~ 4.5 nm from the data. According to the generalized Meiklejohn and Bean model [100], the AF anisotropy, $K_{AF} = \frac{J_{ex}}{2\sqrt{2}t_{cri}}$, is obtained as $0.8\times10^5$ erg/cm$^3$. For $t_{IrMn}$ > 6 nm, slight decrease of both $\varepsilon_{90}{}^{o}$ and $K_{eb}$ can be observed.

*3.2.2 Interfacial effect of anisotropies (F layer dependence)*

Two series of Fe/IrMn EB samples (A and B) were grown with the structure of MgO/Fe($t_{Fe}$)/IrMn($t_{IrMn}$)/Ta(3nm cap). Series A has a fixed $t_{IrMn}$ = 4.5 nm (EB not saturated), and different $t_{Fe}$ = 10 nm ($A_{10}$), 30 nm ($A_{30}$), 50 nm ($A_{50}$), and 70 nm ($A_{70}$); series B has fixed $t_{IrMn}$ = 8 nm (EB saturated), and different $t_{Fe}$ = 10 nm ($B_{10}$), 30 nm ($B_{30}$), 50 nm ($B_{50}$), and 70 nm ($B_{70}$). The exchange bias direction was set parallel to the Fe[010] easy axis. Angular dependent magnetization reversal was studied by MOKE at room temperature. The DW nucleation model was then applied to obtain the sample parameters, $\varepsilon_{90}{}^{o}$, $K_{eb}$, and $K_u$, via curve fitting. The dependence of $\varepsilon_{90}{}^{o}$, $K_{eb}$, and $K_u$ on the F layer thickness is plotted for A and B series in Fig. 3.6(a) and (b), respectively. They all roughly follow a '$1/t_{Fe}$' dependence, as indicated by the fittings, confirming that $\varepsilon_{90}{}^{o}$, $K_{eb}$, and $K_u$ all have contributions from the interface. The '$1/t_{Fe}$' behavior for exchange bias, $K_{eb}$, and the induced $K_u$ is straightforward as both arise from the F/AF interface coupling: according to the phenomenological equation, the exchange bias field is

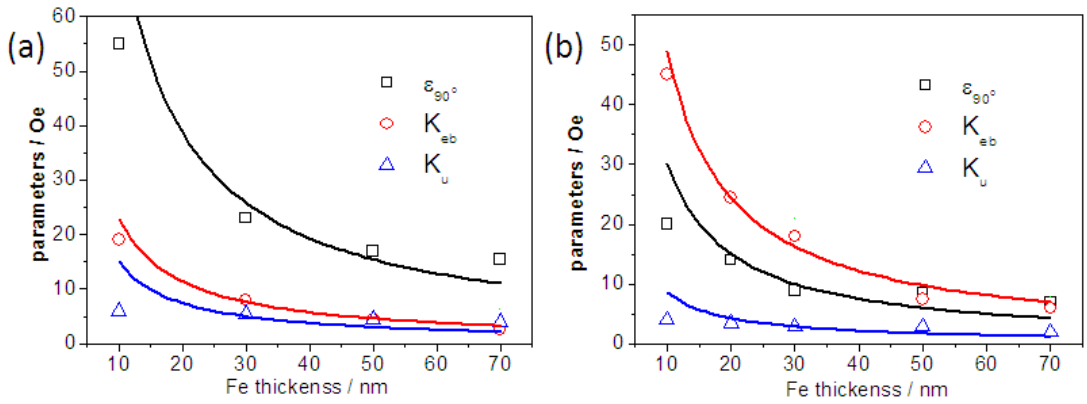


Figure 3.6: Fe thickness dependence of $\varepsilon_{90}{}^{o}$, $K_{eb}$, and $K_u$ (in the form of effective fields) derived by angular fittings for (a) A series of Fe/IrMn(4.5 nm) bilayers; and (b) B series of Fe/IrMn(8 nm) bilayers. Solid lines are curve fittings by the $1/t_{Fe}$ behavior.

written as $H_{eb} = J_{ex}/M_{Fe}t_{Fe}$, where $J_{ex}$ is the interfacial exchange energy. The '$1/t_{Fe}$' behavior for the DW nucleation energy, $\varepsilon_{90}{}^{o}$, reflects such behavior of the rotatable AF spins at the interface.

### *3.2.3 Freezing effect of the pinned AF spins (temperature dependence)*

Using anisotropic magnetoresistance measurement, we measured the angular dependence of magnetization reversal over a wide temperature range (10-300K) in a Quantum Design's physical property measurement system (PPMS) with an in-plane rotator [101]. The AMR measurement is advantageous over other magnetometry in studying the magnetization reversal; in particular, it is more sensitive to the distribution of magnetization during the reversal process [102,103]. The AMR originates from the anisotropic spin-orbit coupling effect that results in a resistance maximum when the magnetization is aligned along the direction of the current, and a minimum when they are mutually orthogonal. So the critical fields at which the MR switches from a high to a low value (or vice versa)

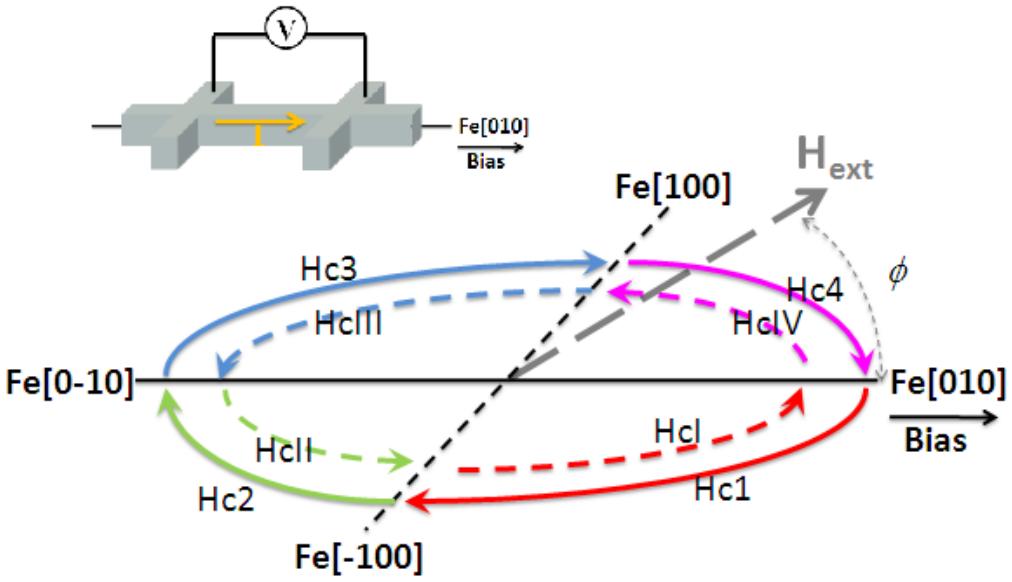


Figure 3.7: Geometry of the AMR experimental setup with the relative orientation of the bias, DC current, external magnetic field, $H_{ext}$, and the various switching fields between different Fe easy axes.

corresponds to the switching fields of magnetic reversal. However, the AMR cannot distinguish the magnetizations parallel or antiparallel to the current (both give rise to high resistance). As a result, only the 90$^{o}$ DW processes can be defected.

Epitaxial Fe(10nm)/IrMn(4.2nm) bilayers in the shape of a Hall bar were deposited through a shadow mask on MgO(001) substrates (Fig. 3.7). A Ta layer (5 nm) was used as a capping layer. A permanent magnet generating a field of ~300 Oe was applied along the Fe[010] easy axis throughout the sample deposition and cooling process (to RT) to define the EB direction. The AMR measurement was performed using the PPMS with a horizontal rotator. Since the AMR signals are quite small (Fig. 3.8), the conventional 4-probe technique was applied with a DC current flowing along the bias direction; see Fig. 3.7. Such small AMR signals may not be detected if the 2-probe method is used. The sample was first field-cooled from 300 to 10 K under a 5 KOe field parallel to the bias. Subsequently, the angle-dependent

AMR data was acquired at 10 K, and at temperature steps of 20 K from 20 to 300 K. Specifically, at each temperature, MR signals versus the applied field $H_{ext}$, $R(H)$, were measured at different $\phi$, defined as the angle between $H_{ext}$ and the Fe[010] easy axis (Fig. 3.7).

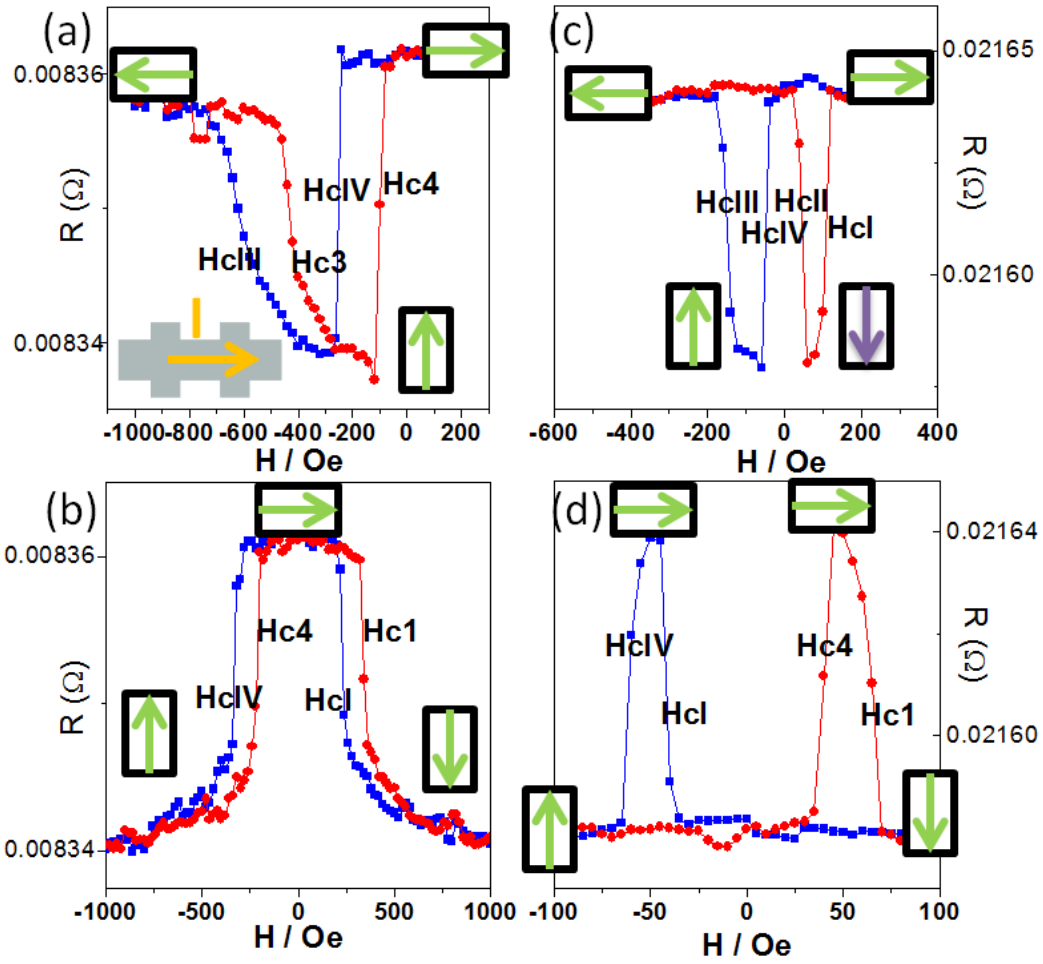


Figure 3.8: Angle-dependent $R(H)$ signals at (a) $\phi$ = -30° and (b) $\phi$ = -90° at 10 K; and at (c) $\phi$ = -30° and (d) $\phi$ = -90° at 300 K. The orientation of Fe spins in the switching processes is represented by the arrows enclosed in a rectangle.

The AMR originates from the anisotropic spin-orbit coupling effect that results in a resistance maximum when the magnetization is aligned along the direction of the current flow and a minimum when they are mutually orthogonal. The critical field, $H_{crit}$, at which the MR switches from high to low resistance (or vice versa) indicates the 90° DW nucleation process. Previously we showed the

magnetization reversals are achieved via nucleation of either 90° or 180° DWs with propagation along the different Fe easy axes, and the switching fields are referred as $H_{c1}$ to $H_{c4}$ (clockwise), $H_{cI}$ to $H_{cIV}$ (counterclockwise); see Fig. 3.7. Note again that AMR is only sensitive to 90° magnetization reversals and the 180° magnetization reversal via DW nucleation cannot be probed because there is no resistance change from parallel to antiparallel configuration of magnetization with respect to the current.

The $R(H)$ signals at 10 K at various representative $\phi$ (Fig. 3.8(a)-(b)) show the two-step magnetic reversal by two successive 90° DW nucleations. At $\phi$ = -30° [Fig. 3.8(a)], for the decreasing field process, the magnetization was originally saturated along Fe[010], which is parallel to the current direction and displays a high resistance state. Upon the first switching, the magnetization reverses abruptly at $H_{cIV}$ to the intermediate state in which the Fe spins are oriented along Fe[100], perpendicular to the initial and final remnant axes. In this case, the magnetization is perpendicular to the current leading to a low resistance state. During the second switching, it reverses smoothly to Fe[0-10] at $H_{cII}$ and displays a high resistance state. It is worth noting that the reversal mechanism in each step is likely different. In the first step, the magnetization reverses via a sharp irreversible transition, indicating that the reversal is governed by nucleation and propagation of magnetic domains; in the second one, smooth, reversible transition is observed, indicating that the magnetization rotation is likely the relevant process. The magnetization reversals for the increasing field follow the same semicircle with the decreasing field, marked by the switching fields, $H_{c3}$ and $H_{c4}$, according to our DW nucleation model. Perpendicular to the bias, $\phi$ = -90° [Fig. 3.8(b)], the reversal process for decreasing and increasing field is symmetric with respect to $H$=0 (*x-axis*), and only the sharp, irreversible transitions are observed. The intermediate states for $\phi$ = -90° are mediated by Fe spins oriented along the bias direction, i.e. Fe[010], parallel to the current. As a result, the

high resistance state is observed at the intermediate states. For comparison, $R(H)$ signals at 300 K and at the same $\phi$ are shown in Fig. 3.8(c)-(d). Here, only the sharp, irreversible transitions are obtained (at all $\phi$). Certain magnetization reversals are marked by different switching fields as compared to the data at 10 K. This is due to the different semicircles involved during the switching along decreasing and increasing fields, respectively, according to our model. Specifically, the magnetization reversal route for decreasing and increasing field lies in opposite semicircles for $\phi$ = -30°, and lies in the same semicircle for $\phi$ = -90°.

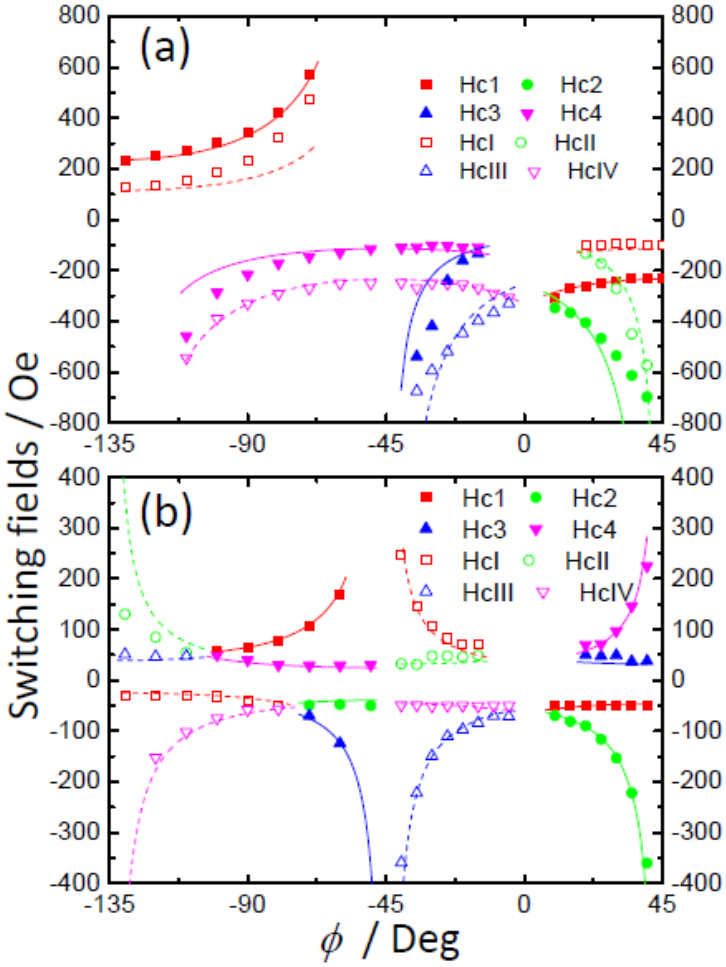


Figure 3.9: Angular dependence of the experimentally observed switching fields (symbols) and the corresponding theoretical fitting results (curves), at (a) 10 K and at (b) 300 K. The switching fields, represented by different symbols and curves, correspond to the magnetic transitions between different initial and final Fe easy axes orientations (Fig. 3.1).

The $\phi$- dependence of the switching fields at 10 K and 300 K is summarized in Fig. 3.9, and subsequently interpreted by the DW nucleation model, with $\varepsilon_{90}{}^{o}$, $K_{eb}$, and $K_u$. The results of the fitting for the data at 10 K shows relatively good agreement with the fitting parameters $K_{eb}/M$=206 Oe, $\varepsilon_{90}{}^{o}/M$=85 Oe, and $K_u/M$=40 Oe. Overall, the angular-dependent behavior is well reproduced by the DW nucleation model. However, slight deviations exist for the switching fields $H_{c2}$, $H_{c3}$, $H_{cII}$, $H_{cIII}$ at -45° < $\phi$ <45°, and $H_{cI}$ and $H_{c4}$ at -135°< $\phi$ <-45°. This is likely due to the change of reversal mechanism at such a low temperature. Taking a look back at the $R(H)$ signals, smooth, reversible transitions rather than sharp ones were observed at these corresponding $\phi$ for these switching fields, indicating that the magnetization reversal was mainly achieved via coherent rotation rather than DW nucleation. Therefore it is reasonable to observe the slight deviations since our model is completely based on DW nucleation and propagation. For the data at 300 K, all the switching fields can be well reproduced under the single DW nucleation model, with the fitting parameters $K_{eb}/M$=10 Oe, $\varepsilon_{90}{}^{o}/M$=50 Oe, and $K_u/M$=5 Oe. Compared with the values at 10 K, both $K_{eb}/M$ and $K_u/M$ got significantly reduced; however, $\varepsilon_{90}{}^{o}/M$ only got slightly decreased, from 85 Oe to 50 Oe. The temperature dependence of these parameters are further exploited by similar angular dependent measurement and analysis at each temperature from 20 K to 300 K, in steps of 20 K. Actually, the angular dependence of each switching field can be well reproduced by the DW nucleation model for any $T$ > 20 K (indicating an exclusive, DW-type reversal mechanism). The coherent rotation is only observed for $T \leq$ 20K and only for certain switching fields. For 200 K < $T$ < RT, the magnetization reversal close to the bias occurred via one-step (180°) DW process, thus not accessible by AMR measurements. The derived parameters $K_{eb}/M$, $\varepsilon_{90}{}^{o}/M$, and $K_u/M$ for 10 K < $T$ < 200 K are summarized in Fig. 3.10. The bias field, $K_{eb}/M$, decreases linearly with increasing temperature. The

uniaxial anisotropy field, $K_u/M$, also shows similar linear dependence, confirming the bias induced nature of $K_u$. For some Fe based EB systems, it is possible to induce a perpendicular coupling at the F/AF interface. A non-linear temperature dependence of EB due to this perpendicular coupling has been reported and a negative $K_u$ was also indicated [79]. But in our Fe/IrMn system, linear temperature dependence is observed and is in good agreement with the Malozemoff model for EB that considers a parallel F and AF coupling. The all-positive $K_u$ values determined from our fitting also show no evidence of any perpendicular coupling even at low temperatures. Finally, the 90° DW nucleation energy, $\varepsilon_{90}{}^{o}/M$, does not show significant temperature dependence compared with $K_{eb}$ and $K_u$, indicating weak temperature dependence of the rotatable AF spins at the F/AF interface.

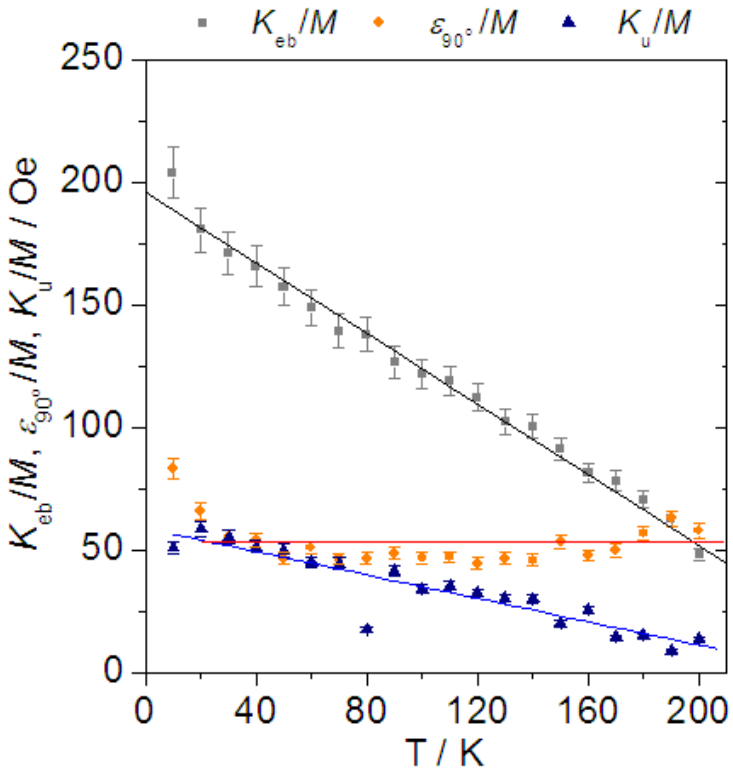


Figure 3.10: Temperature dependence of the parameters $\varepsilon_{90°}/M$, $K_{eb}/M$, and $K_u/M$, given by the fitting for the angular dependent switching fields. Linear lines are guides to eye.

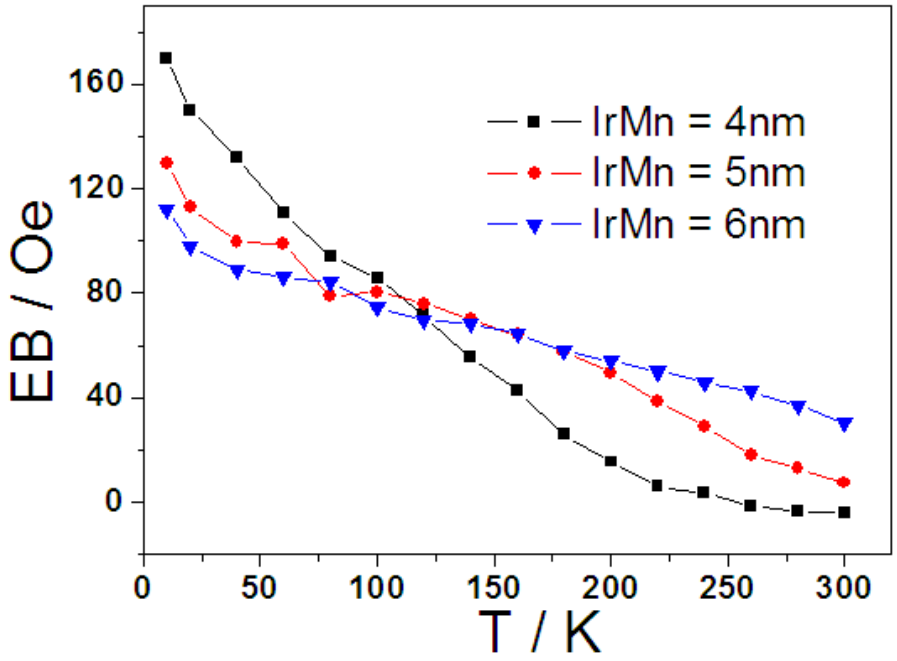


Figure 3.11: Temperature dependence of exchange bias for three samples with the IrMn thickness of 4, 5, 6 nm.

The IrMn layer thickness also affects the exchange bias behavior as a function of temperature, as shown in Fig. 3.11. The samples have a structure of Fe(15nm)IrMn($t_{IrMn}$) where $t_{IrMn}$ = 4, 5, 6 nm. At room temperature, 300 K, EB increases with increasing $t_{IrMn}$. The EB field for 4 nm samples is almost zero but for 6 nm sample is ~30 Oe. However, when the samples were cooled (under field 1T) to low temperature, 10 K, an inverse relationship between EB and $t_{IrMn}$ was observed; specifically, the 4 nm sample showed the largest EB field and the 6 nm one showed the smallest. It should be noted that although approximately the same value of $H_{eb}$ were found at ~100 K for the three samples (Fig. 3.11), the situations at the interface are still different. This will be explained in more details below.

The differences in the temperature dependence (Fig. 3.11) are directly correlated to the IrMn domain behavior explained by the Malozemoff theory [43]. In the samples with thin AF layer, good long range AF ordering were not well established so the characteristic length, $L$, of frozen-in AF domains are quite small,

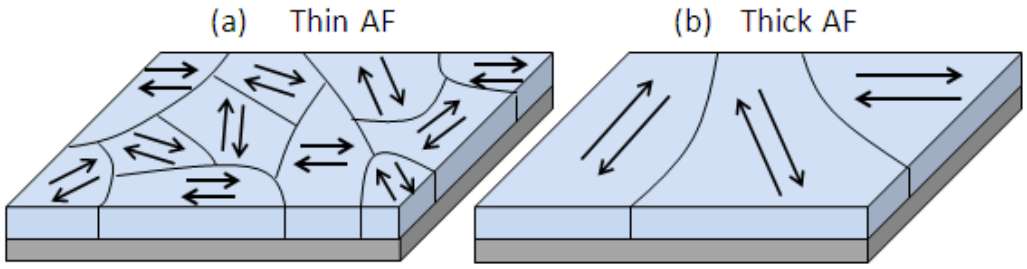


Figure 3.12: (a) Samples with a thin AF layer form small grains with lower blocking temperature but higher exchange bias at low T (easier to be polarized by field cooling). (b) Samples with a thick AF layer form larger grains with higher blocking temperature but weaker exchange bias at low T (harder to be polarized by the field cooling), based on the Malozemoff theory.

which further leads to low blocking temperatures, Fig. 3.12(a). In other words, these small grains are not 'set', or only partially set at room temperature, resulting in low EB fields. In contrast, larger AF domains (both laterally and longitudinally) with higher blocking temperatures (>RT) can form in thicker samples (Fig. 3.12(b)), therefore displaying greater EB. However, when these samples were cooled to low temperatures under a large field, all the grains, large and small, were set to give rise to the EB. According to the Malozemoff model, the interfacial effective coupling that governs the EB is inversely proportional to the characteristic length of AF domains, i.e. $J_{eb} \propto L^{-1}$. As a result, samples with smaller grains (smaller $L$) have a greater EB field at low temperatures.

The grain size in the IrMn films evolves from small to large as the thickness gradually increases. For a grain with certain size, $L$, the maximum EB field (at 0 K) and the blocking temperatures can be written as $H_{eb}^{max}(L)$ and $T_B(L)$. According to Malozemoff theory, the temperature dependent EB field for such a grain can be written as: $H_{eb}(T) = H_{eb}^{max}(L) \times (1 - \frac{T}{T_B(L)})^{\alpha(L)}$, where $\alpha(L)$ represents the coupling between the AF grains; if the grains are decoupled, $\alpha(L)$=1. For a film with certain grain size distribution, the EB field can be rewritten as: $H_{eb}(T) = \sum_{L_1}^{L_2} H_{eb}^{max}(L)(1 - \frac{T}{T_B(L)})^{\alpha(L)}$. In thin AF samples with small grains,

$H_{eb}^{max}$ is large however they are not easily set unless cooled to low temperatures. In thick AF samples, $H_{eb}^{max}$ is small but they are set at room temperature and give rise to EB. Regarding the $\alpha(L)$, the thin samples always show a better linearity with temperature than the thick samples, due to the weaker inter-coupling of the smaller grains.

### *3.2.4 Misalignment of anisotropies (field-cooling dependence)*

Previous experiments only dealt with collinear cubic and exchange anisotropies, where the unidirectional EB easy axis sits along one of the Fe cubic easy axis. However, the interfacial exchange coupling effects depend on the strength of competing anisotropies [104] as well as their relative orientation [105], that together lead to a complex phase diagram of different reversal behavior. The relative importance of the anisotropies involved can be selectively enhanced either intrinsically by interfacial frustration [106] or extrinsically via special field cooling (FC) procedures [107]. The induced $K_u$ are also affected which further complicates the system. Both the magnitude and orientation of the $K_u$ can be different from the collinear case and are usually hard to predict. In this section, we describe the magnetization reversal of epitaxial Fe/IrMn bilayers with both collinear and non-collinear anisotropy configurations, which reveals the importance of the misalignment between cubic anisotropy and the direction of the applied field during the FC procedure [108]. For simplicity, the induced $K_u$ is not included in the discussion here but definitely deserve future investigations.

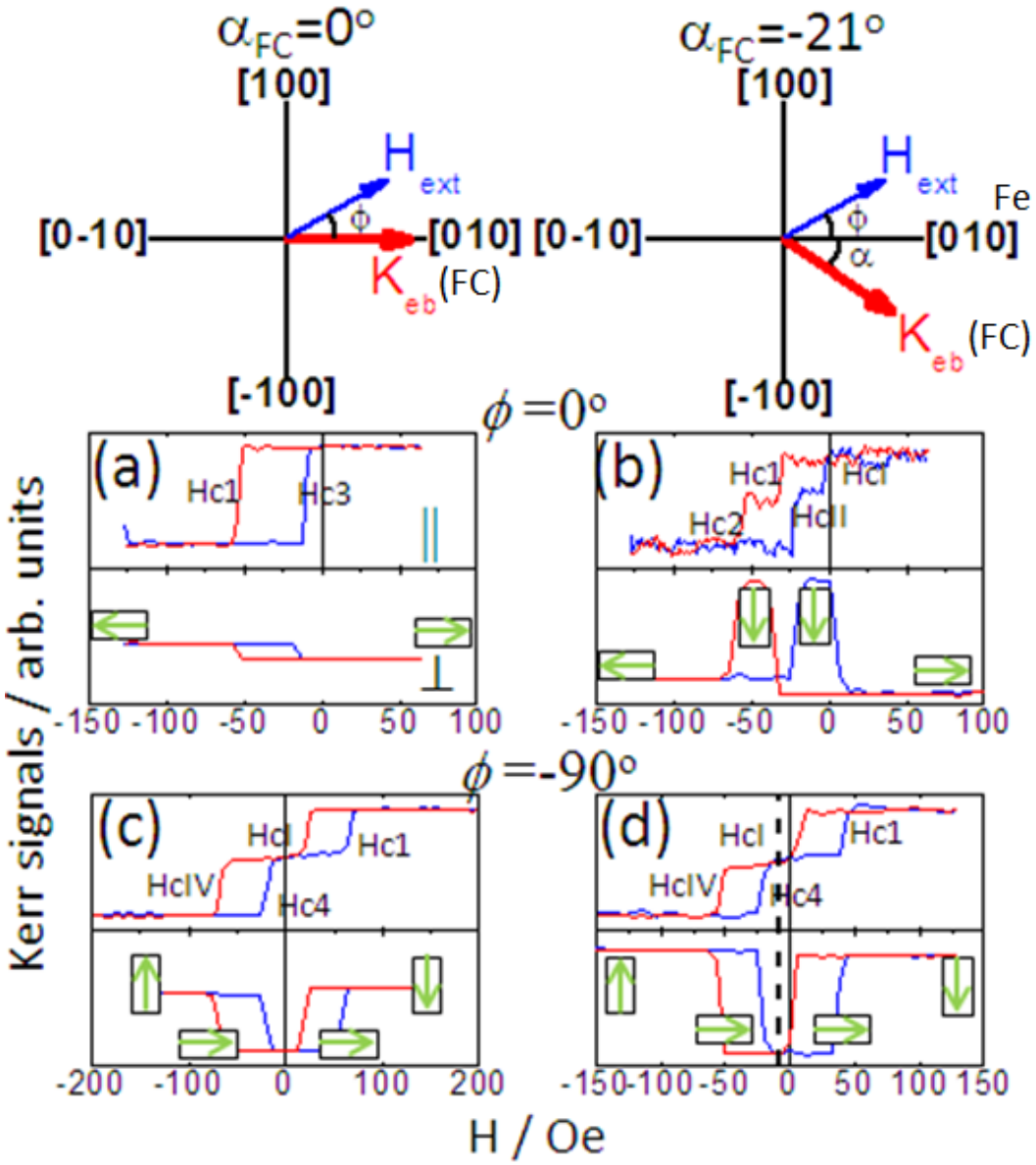


Figure 3.13: Longitudinal (||) and transverse (⊥) MOKE loops measured (a-b) at $\phi$ = 0° and (c-d) at $\phi$ = -90°, with different anisotropy configurations, schematically shown on top, including collinear ($\alpha_{FC}$ =0°) and non-collinear ($\alpha_{FC}$ = -21° ) cases. The orientation of Fe spins in the switching processes is represented by the arrows enclosed in a box.

Epitaxial Fe(15 nm)/IrMn(10 nm) bilayers were chosen for the relevant study due to the negligible $K_u$ in such a EB system (Fig. 3.4). A permanent magnet generating a field of ~300 Oe was employed to define the EB direction during sample growth. The field direction of the magnet was misaligned by an angle $\alpha_{FC}$ with respect to the Fe[010] easy axis. Two different anisotropy configurations were set by using

$\alpha_{FC}$ = 0° (collinear) and $\alpha_{FC}$ = -21° (non-collinear). Angular dependent MOKE measurements were performed *ex situ* at RT to study the reversal of both in-plane magnetization components, i.e., longitudinal (||) and transverse ($\perp$) components at different $\phi$, defined as the angle between the external applied field, $H_{ext}$, and the Fe[010] easy axis. The switching fields are still defined as $H_{c1}$ to $H_{c4}$ (clockwise), and $H_{cI}$ to $H_{cIV}$ (counterclockwise), respectively, as illustrated in Fig. 3.1.

Figure 3.13 compares the in-plane magnetization hysteresis loops at Fe[010] ($\phi$ = 0°) and Fe[-100] ($\phi$ = -90°) for the collinear ($\alpha_{FC}$ = 0°) and non-collinear ($\alpha_{FC}$ = -21°) coupling configurations, respectively. In the collinear configuration, for $\phi$ = 0°, we observed biased loops with one-step magnetization reversal for both descending and ascending branches of the hysteresis loop [Fig. 3.13(a)]. In contrast, the non-collinear case – due to the broken cubic symmetry by the EB – showed biased loops with two-step magnetic switching for both branches [Fig. 3.13(b)]. The intermediate state indicates magnetization reversal along Fe[-100]. For $\phi$ = -90°, double-shifted loops with two-step switching were observed for both configurations, Fig. 3.13(c) and (d). The intermediate states for both branches are mediated via the same Fe[010] easy axis. The hysteresis loop also exhibits a shift along the field axis for the non-collinear anisotropy configuration, marked with a vertical dashed line in Fig. 3.13(d). This shift corresponds to the $K_{eb}$ component (projection) along the [-100] direction caused by the artificial misalignment.

An asymmetric magnetization reversal behavior is found for the non-collinear coupled bilayer. The left and right panels of Fig. 3.14 show the hysteresis loops acquired close to Fe[010] at corresponding negative and positive $\phi$ values, respectively. For positive $\phi$ ($0° \leq \phi < 45°$), transverse MOKE signal revealed that the magnetization reversal for descending and ascending branches always occurred in two steps and in the same bottom semicircle as revealed, with the intermediate states mediated by Fe[-100].

The magnetic switching occurs via $H_{c1}$ and $H_{c2}$ for the descending branch and the reverse processes, $H_{cII}$ and $H_{cI}$, for the ascending branch. For $-15° \leq \phi < 0°$, $H_{ext}$ lies between the Fe[010] and the EB direction. Due to a strong $K_{eb}$, the magnetization reversal still occurs in the bottom semicircle, similar to that for positive $\phi$. This is different from the collinear configuration where the magnetization reversal is accommodated by the top semicircle right after $H_{ext}$ passes Fe[010]. For $-45° < \phi \leq -25^{o}$ ($H_{ext}$ applied past the EB), the magnetization reversal was accommodated by the top semicircle for descending branch ($H_{cIV}$ and $H_{cIII}$); however, it still occurs in the bottom semicircle for the ascending branch ($H_{cII}$ and $H_{cI}$). In other words, the magnetization reversal involves two opposite semicircles (top and bottom), and the intermediate states are mediated by Fe[100] and Fe[-100] for the descending and ascending branches, respectively. This is also significantly different from the collinear configuration where magnetization reversal involves only the top semicircle for all negative $\phi$. It should be noted that for the ascending branch, the second switching at $H_{cI}$ is not observed when $H_{cI} < H_{cII}$, for example at $\phi = -35^{o}$ (Fig. 3.14). The magnetization reversal of the non-collinear coupled sample for the corresponding positive and negative values of $\phi$, shows significant asymmetry compared to the collinear sample. For the latter, the magnetization reversal is symmetric about $\phi = 0°$ and only involves one semicircle for each $\phi$.

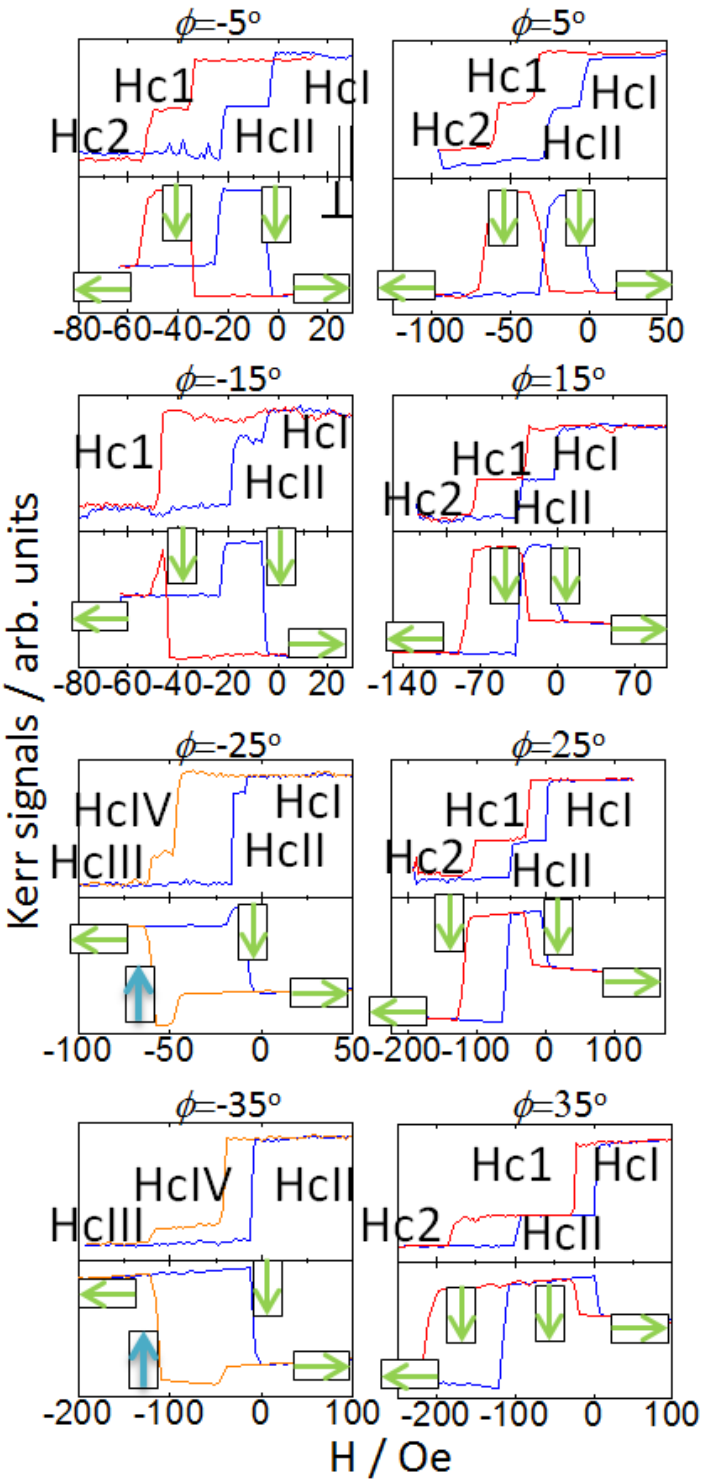


Figure 3.14: Longitudinal (∥) and transverse (⊥) MOKE loops measured at selective field angles for the non-collinear anisotropy configuration ($\alpha_{FC}$ = -21°). The orientation of Fe spins in the switching processes is represented by the arrows enclosed in a box.

Next, we propose a generalized DW nucleation model to interpret the $\phi$–dependence of the switching fields. In the original DW nucleation model, we included a small induced uniaxial anisotropy, $K_u$, collinear with $K_{eb}$. However, fitting for the $\phi$–dependence indicated that this induced $K_u$ is negligible, and thus excluded in our generalized DW nucleation model. For the non-collinear case as we reported here, $K_{eb}$ is decomposed into two components, $K_{eb(\parallel)} = K_{eb}\cos\alpha_{FC}$, and $K_{eb(\perp)} = K_{eb}\sin\alpha_{FC}$, lying along the two orthogonal cubic easy axes. The two orthogonal $K_{eb}$ components act as effective fields superimposed onto the cubic Fe easy axes. Similarly, the theoretical switching fields for 90° magnetic transitions are obtained as:

$$H_{c1} = -\frac{\varepsilon_{90^o} + K_{eb}(\cos\alpha_{FC} + \sin\alpha_{FC})}{M(\cos\phi + \sin\phi)}, \tag{3.4a}$$

$$H_{c2} = -\frac{\varepsilon_{90^o} + K_{eb}(\cos\alpha_{FC} - \sin\alpha_{FC})}{M(\cos\phi - \sin\phi)}, \tag{3.4b}$$

$$H_{c3} = \frac{\varepsilon_{90^o} - K_{eb}(\cos\alpha_{FC} + \sin\alpha_{FC})}{M(\cos\phi + \sin\phi)}, \tag{3.4c}$$

$$H_{c4} = \frac{\varepsilon_{90^o} - K_{eb}(\cos\alpha_{FC} - \sin\alpha_{FC})}{M(\cos\phi - \sin\phi)}, \tag{3.4d}$$

$$H_{cI} = \frac{\varepsilon_{90^o} - K_{eb}(\cos\alpha_{FC} + \sin\alpha_{FC})}{M(\cos\phi + \sin\phi)}, \tag{3.4e}$$

$$H_{cII} = \frac{\varepsilon_{90^o} - K_{eb}(\cos\alpha_{FC} - \sin\alpha_{FC})}{M(\cos\phi - \sin\phi)}, \tag{3.4f}$$

$$H_{cIII} = -\frac{\varepsilon_{90^o} + K_{eb}(\cos\alpha_{FC} + \sin\alpha_{FC})}{M(\cos\phi + \sin\phi)}, \tag{3.4g}$$

$$H_{cIV} = -\frac{\varepsilon_{90^o} + K_{eb}(\cos\alpha_{FC} - \sin\alpha_{FC})}{M(\cos\phi - \sin\phi)}. \tag{3.4h}$$

We applied these equations and fit for the angular dependent switching fields. The $\phi$–dependence

close to Fe[010] and Fe[-100] are summarized in Fig. 3.15(a) and (b), respectively. All the switching fields fit nicely with fitting parameters $K_{eb}/M$ = 31 Oe, $\varepsilon_{90}{}^{o}/M$ =14.5 Oe, and $\alpha_{FC}$= -21°. Such values of $K_{eb}/M$ and $\varepsilon_{90}{}^{o}/M$ are only slightly different from the values in the collinear case ($K_{eb}/M$ = 33 Oe and $\varepsilon_{90}{}^{o}/M$ =18 Oe) with the same F/AF structure. Because $K_{eb}$ and $\varepsilon_{90}{}^{o}$ are both AF dependent, this slight difference of the fitted values for the two configurations is likely just caused by the AF misalignment. In Fig. 3.15(a), the symmetry about $\phi$ = 0° is broken. For the descending branch, the magnetization reversal via the top semicircle ($H_{cIII}$ and $H_{cIV}$) was suppressed by the non-collinear EB. The magnetization reversal via the bottom semicircle ($H_{c1}$ and $H_{c2}$) became largely favorable. The transition of the magnetization reversal from the bottom to the top semicircle occurred at $\phi$ ~ -15°, not at $\alpha_{FC}$ = -21° as one would intuitively expect, [Fig. 3.15(a)]. This is also consistent with our model using the above fitting parameters. Physically, the transition angle is dependent on $\alpha_{FC}$ as well as the relative strength of $K_{eb}$ and $\varepsilon_{90}$°. For the ascending branch, the magnetization reversal via the top semicircle ($H_{c3}$ and $H_{c4}$) is completely prohibited; only the reversal via the bottom semicircle ($H_{cI}$ and $H_{cII}$) is possible. The strong preference of the magnetization reversal along the bottom semicircle is attributed to the enhanced Fe[-100] easy axis by the $K_{eb(\perp)}$ component. In Fig. 3.15(b), the four characterizing switching fields, $H_{c1}$, $H_{c4}$, $H_{cI}$, $H_{cIV}$, are all shifted downwards due to the $K_{eb(\perp)}$. As can be seen, our generalized DW nucleation model reproduces the switching fields very well over the entire angular range, by simply taking into account the misalignment angle, $\alpha_{FC}$= -21°.

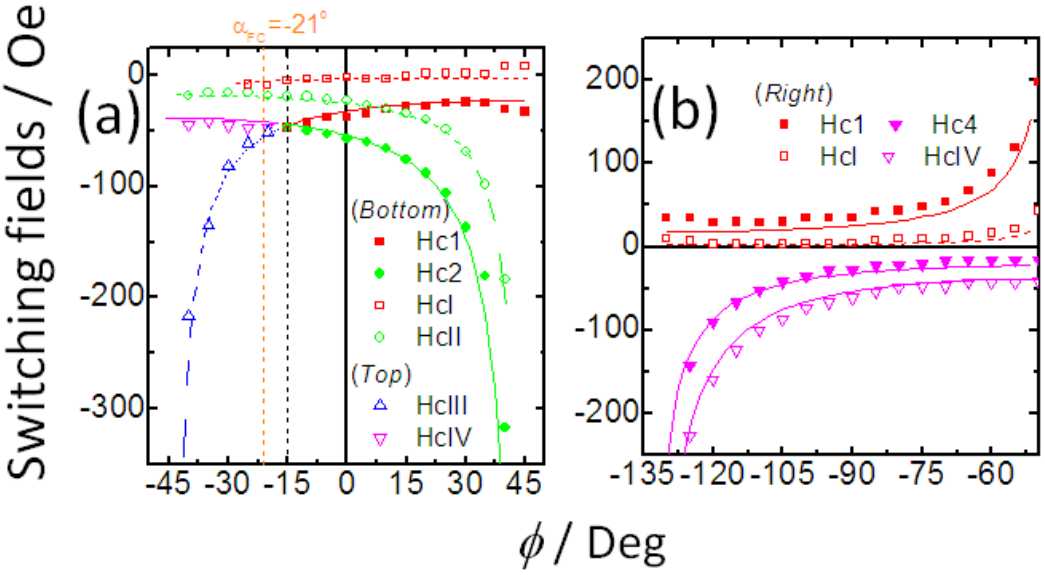


Figure 3.15: Angular dependence of the experimentally observed switching fields (symbols) and the corresponding theoretical fitting results (curves) for the non-collinear coupled bilayer. The switching fields, represented by different symbols and curves, correspond to the magnetic transitions between different initial and final Fe easy axes orientations. The semicircles followed by the switching fields during the reversal are also indicated.

### *3.3 Spin reorientation transition and thermal hysteresis of epitaxial Fe/MnPd*

In previous sections of this chapter, we have systematically discussed the magnetic reversal properties of EB bilayers under a typical system, i.e. Fe/IrMn. The induced $K_u$ in the Fe/IrMn system is parallel to $K_{eb}$ due to the collinear interface coupling. In this section we turn to another system, i.e. Fe/MnPd, which exhibits a perpendicular induced $K_u$ due to the spin-flop coupling at the interface. We will discuss the magnetic reversal of epitaxial Fe/MnPd bilayers and focus on a unique property of such system, i.e. spin reorientation transition (SRT).

Although most EB bilayers exhibit collinear coupling (like Fe/IrMn), Koon argued that an orthogonal arrangement, i.e. spin-flop coupling, of the F and AF spins should be a natural consequence

for a compensated AF surface, since it minimizes the frustration of exchange coupling from the two AF sublattices [59]. The result of spin-flop coupling is an effective uniaxial anisotropy perpendicular to the field cooling direction [60,76,77,78]. Such spin-flop coupling is usually found in epitaxial EB samples, where the F magnetocrystalline anisotropy is also strong, and with the possibly of a higher order symmetry such as fourfold (e.g. Fe/MgO(001)). As a result, the magnetic reversal is thus determined by the competing anisotropies induced from both interface and crystalline origins. An in-plane SRT, denoting the change of the coupling type (collinear to spin-flop and vice versa), may also occur due to the different behaviors of the competing anisotropies as a function of temperature, film thickness, or the strength of exchange coupling [109,110,111].

Due to the competing effect of interface anisotropies ($K_{eb}$ and $K_u$) and the Fe magnetocrystalline anisotropy, our Fe/*a*-axis MnPd bilayers also exhibit the SRT effect that is driven by both the MnPd thickness and temperature [79]. To systematically characterize such SRT, we studied the magnetic reversal of the Fe/MnPd bilayer over a wide range of temperatures, using VSM and AMR which are equivalent methods for detecting field-driven magnetic reversals, by measuring magnetic switching from $M(H)$ and $r(H)$ curves, respectively. We used AMR as much as possible to probe the magnetic reversal characteristics due to its better sensitivity on the magnetization distribution. The sample is epitaxial Fe(15 nm)/*a*-axis MnPd (40 nm)/Ta cap(5 nm) in the shape of a 1 mm wide stripe on MgO(001) deposited under a shadow mask. For electrical measurement, the Au contact pads, ~ 70 nm thick, were subsequently deposited (Fig. 3.16). A conventional 4-probe geometry was used for the AMR measurement, with the DC current, I, applied along Fe[010] easy direction. An in-plane rotator was used to achieve different $\phi$, of the in-plane magnetic field with respect to [010].

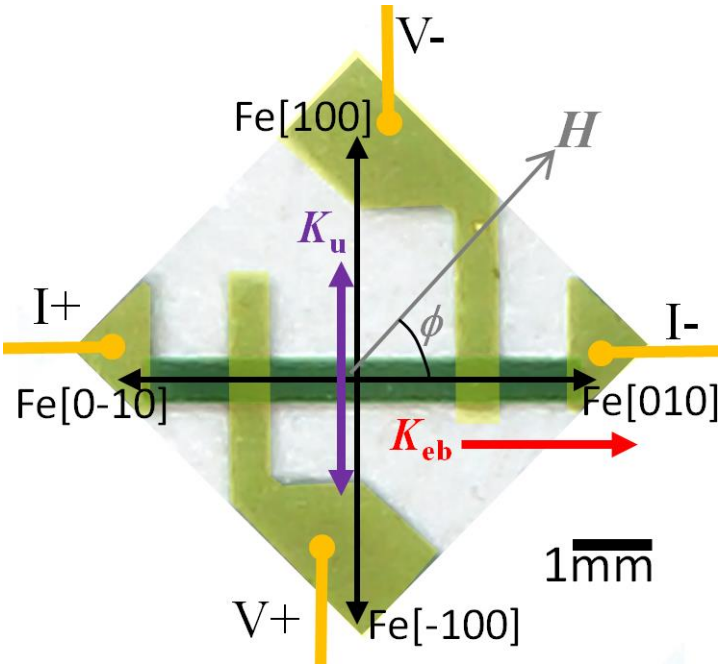


Figure 3.16: Photograph of the Fe(15 nm)/MnPd(40 nm) sample (center stripe) and electrical contacts for AMR measurement. The relative orientations of the magnetic anisotropies, external field, *H*, and the applied current, *I*, are indicated.

*Temperature dependent magnetic reversal*

In the Fe/MnPd bilayer, the induced $K_u$ reorients from parallel to perpendicular orientation with respect to the $K_{eb}$ (Fig. 3.16) once it is field-cooled below $T_B$ ~ 95K, of the *a*-axis MnPd [79]. At 300K, the small coercivity, ~ 7 Oe, of the hysteresis loop (Fig. 3.17(a)) indicates the small reversal barrier of the Fe layer alone. After FC to 10K at $H_{FC}$ = 2kOe along [010], $K_{eb}$ and $K_u$ are both established and a two-step, shifted loop was observed along [010]. The intermediate states at $H_1$ and $H_3$ indicates the magnetization aligned along $K_u$, i.e. [100] and/or [-100]. The shift field, $H_s$, is determined from the center shift of the two sub-loops (Fig. 3.17(a)), i.e. $H_s = (H_1 - H_2 - H_3 + H_4)/4$, which is further related to $K_u$ via $K_u = M_s H_s$, where $M_s$ is the saturation magnetization. $H_{eb}$ is determined by the center shift of the entire loop, i.e. $H_{eb}$ =

$|(H_1 + H_2 + H_3 + H_4)/4|$. Figure 3.17(b) shows the corresponding AMR curve at 10K. The critical fields at which the MR switches from a high to a low value (or vice versa) corresponds exactly to the switching fields observed in the hysteresis loop (Fig. 3.17(a)). In this sense, $M(H)$ and $r(H)$ are equivalent methods for measuring the magnetic reversal, but the latter can be readily probed, with the capability of applying the field along different directions by using the special sample rotator with the resistivity option of PPMS.

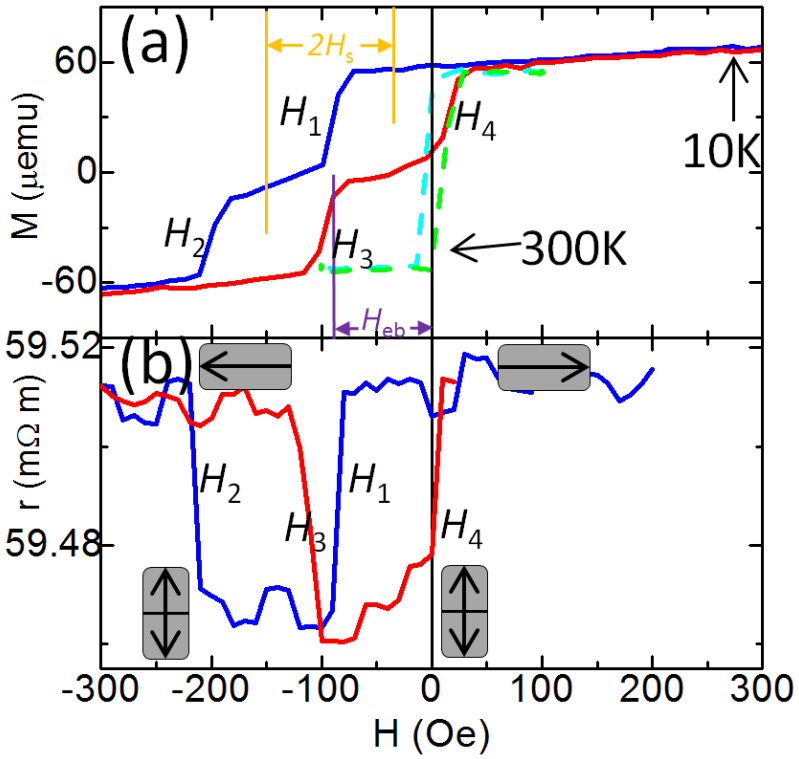


Figure 3.17: $M(H)$ curves measured along [010] at 300K (dashed) and 10K (solid) after FC from 300K at $H_{FC}$ = 2kOe. (c) Corresponding $r(H)$ curve measured along [010] at 10K after the same cooling process. The orientations of the Fe spins are represented by arrows enclosed in a rectangle.

$r(H)$ curves were first measured at the two perpendicular Fe easy directions, i.e. [010] ($\phi$ = 0°) and [100] ($\phi$ = 90°) respectively, after initial FC from 300K to 10K at $H_{FC}$ = 2kOe parallel to [010]. Training effect was removed by large field (2kOe) cycling prior to measurements. The training effect refers to the dramatic change of the hysteresis loop when sweeping consecutively the applied magnetic field of a EB

sample. In a typical case, the switching field along the descending branch decreases from an initial value to an equilibrium value after consecutive measurements, though the switching field along the ascending branch is not sensitive to the field cycling and can either increase or decrease at a small amount. Such effect is related to the unstable state of the AF layer and/or F/AF interface prepared by field cooling procedure, however, it is not yet well established what mechanisms are dominantly contributing to this effect [112,113,114].

At 10K, the establishment of EB upon different $H_{FC}$ was first examined. To our surprise, almost the same magnitude of $H_{eb}$ and $H_s$ were induced at any value of a positive $H_{FC}$, including $H_{FC}$ = 0 but approached from a finite positive field (dashed curve in Fig. 3.18(a)). Such a FC-independent effect implies that the remanence of Fe magnetization, stabilized along the cubic easy axis by the anisotropy barrier, is sufficient to induce both EB and spin-flop coupling once cooled below $T_B$. Such superficial need for the $H_{FC}$ used for the EB is a unique feature of epitaxial samples due to their strong magnetocrystalline anisotropy. For the measurement along [100] (Fig. 3.18(e)), the positive ([100]) and negative ([-100]) saturations both give rise to low resistance states. The observation of the intermediate, high resistance state indicates that the magnetization is aligned along [010], given by the $K_{eb}$ during the reversal, for both descending and ascending branches. In other words, reversals on both branches take place within the right semicircle that encloses the bias direction (inset Fig. 3.18(e)). In practice, this is the other criterion for judging an exchange biased sample. Samples should be considered 'biased' as long as such an intermediate state is observed when measuring perpendicular to the bias. The magnitude of such unidirectional anisotropy, in the form of an effective field, $K_{eb}/M_s$, can be estimated by the separation of the two subloops, $K_{eb}/M_s = (H_5-H_6-H_7+H_8)/4$, and can be a different value from the $H_{eb}$ obtained along the

bias direction.

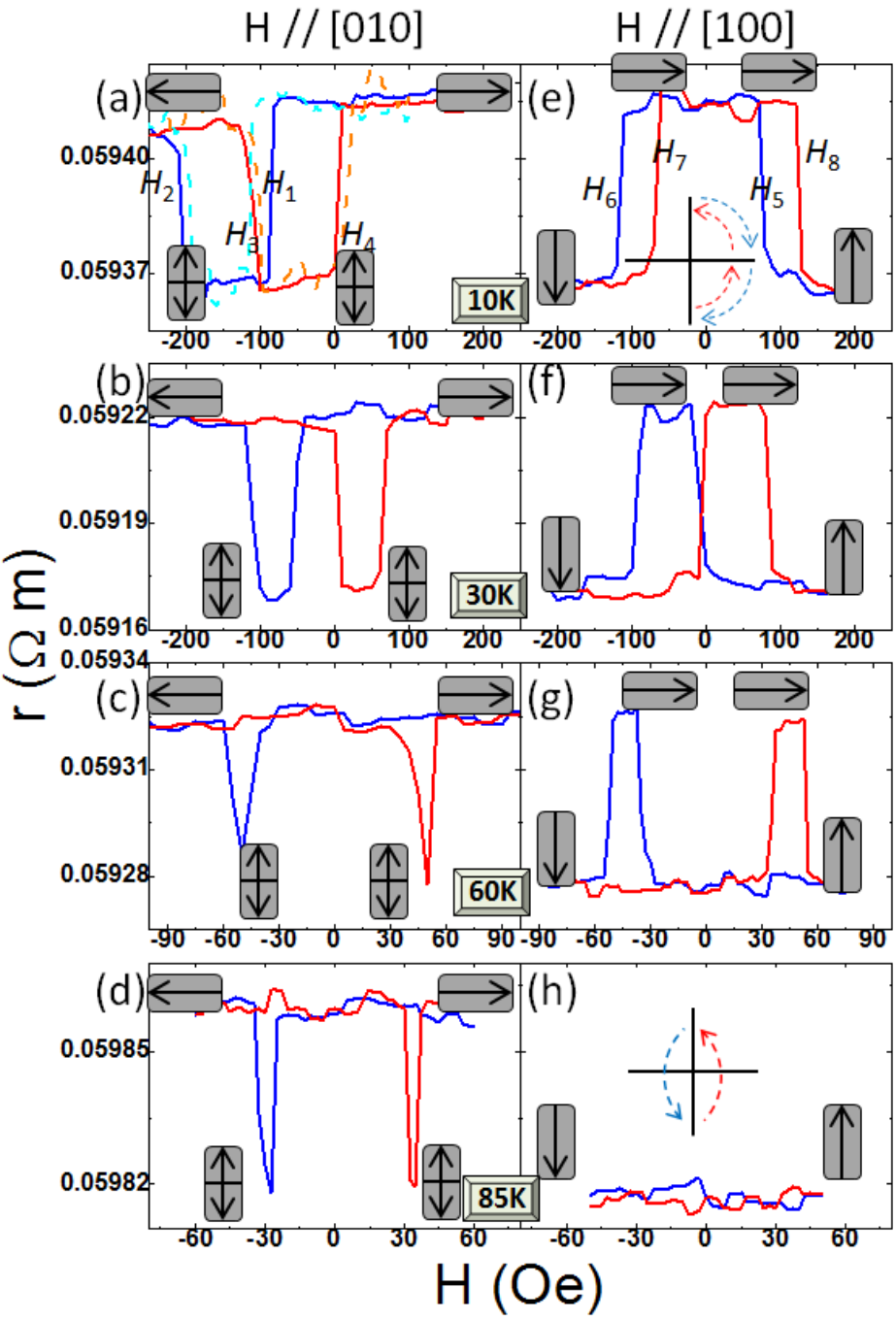


Figure 3.18: $r(H)$ curves measured along [010] at selective temperatures at (a) 10K, (b) 30K, (c) 60K, and (d) 85K, and along [100] at the same temperatures at (e) 10K, (f) 30K, (g) 60K, and (h) 85K, after the initial FC from 300K to 10K at $H_{FC}$ = 2kOe. Dotted curve in (a) shows the $r(H)$ measured along [010] at 10K after the initial cooling from 300K to 10K at $H_{FC}$ = 0 (but approached from a positive field). The orientations of the Fe spins are represented by arrows enclosed in a rectangle.

Similar $r(H)$ curves were measured at different temperatures up to 100K in steps of 5K during

warming up (Fig. 3.18). $r(H)$ along [010] (left panel of Fig. 3.18) helps to determine $H_{eb}$ and $K_u/M_s$, while $r(H)$ along [100] (right panel of Fig. 3.18), allows to determine $K_{eb}/M_s$. At 60K, $r(H)$ along [010] (Fig. 3.18(c)) is symmetrical around $H = 0$ ($H_{eb} = 0$); but the intermediate high resistance states can be still observed along [100] (Fig. 3.18(g)), indicating a finite $K_{eb}$. In other words, a unidirectional anisotropy is still present even if there is no observable EB field. At 85 K, the intermediate state exists along [010] (Fig. 3.18(d)) but not along [100] (Fig. 3.18(h)), indicating a finite $K_u$ but a zero $K_{eb}$. The constant low resistance state along [100] (Fig. 3.18(h)) indicates a direct magnetic reversal from [100] to [-100] and vice versa.

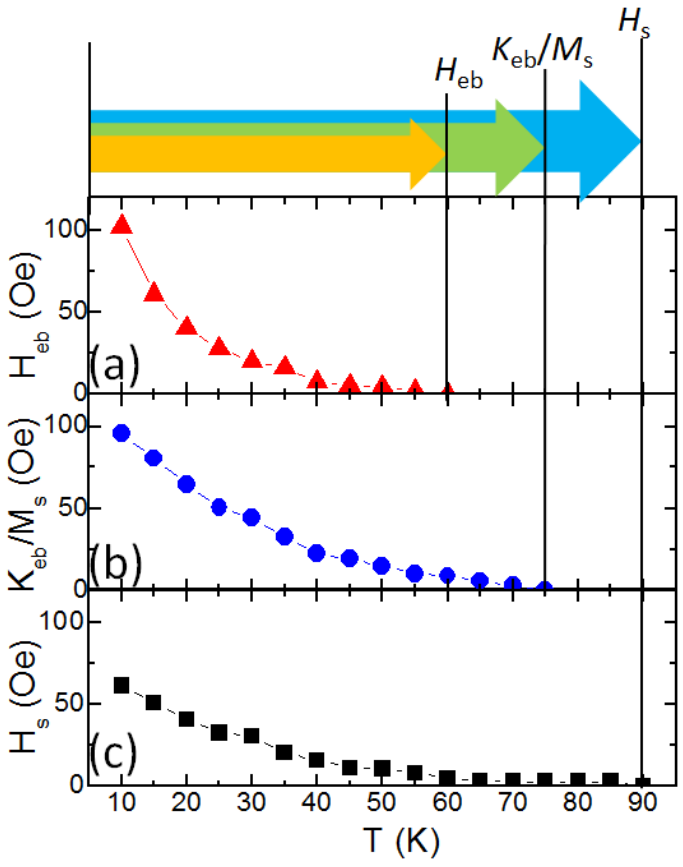


Figure 3.19: Temperature dependence of (a) loop shift, $H_{eb}$, (b) unidirectional anisotropy, $K_{eb}/M_s$, and (c) uniaxial anisotropy, $K_u$ , in the form of the shift field $H_s$ via $K_u = H_s M_s$.

Following the above discussions, the temperature dependence of $H_{eb}$, $H_s$, and $K_{eb}/M_s$ can be obtained from $r(H)$ along [010] and [100] (Fig. 3.19). We found that the onset temperatures of the three parameters are different. The curve shift, $H_{eb}$, vanishes to zero at 60K (Fig. 3.19(a)), but the intermediate state (symbolizing the presence of $K_u$) can be persistently observed until 90K (Fig. 3.19(c)). On the other hand, $r(H)$ data along [100] showed that the unidirectional anisotropy field, $K_{eb}/M_s$, derived from the reversal asymmetry, can persist up to 75K (Fig. 3.19(b)). Such discrepancies in the onset temperatures are attributed to the different interface origins of $H_{eb}$, $H_s$, and $K_{eb}/M_s$. Specifically, $K_u$, being the direct result of the spin-flop coupling, persists up to $T_B$ of the MnPd layer, ~ 95K. However, both $H_{eb}$ and $K_{eb}/M_s$ originate from the unidirectional biasing thus independent to the intrinsic coupling mechanism. Such biasing must be connected to some uncompensated characteristics at the interface [43,78], otherwise reversal pinning is unachievable if a perfectly compensated interface is present [115]. The difference in the temperature onset for $K_{eb}/M_s$ and $H_{eb}$ is unclear and certainly deserve further investigation. We propose an explanation by considering the rotatable behavior of the uncompensated AF spins. It is widely accepted [116] that the vanishing temperature of the loop shift is not necessarily the magnetic ordering temperature, i.e. Néel temperature, of the AF. The loop shift vanishes when the AF anisotropy, even though it exists, is too weak to pin the AF spins along the FC direction. Therefore, the AF spins rotate with the F spins during the magnetic reversal (no loop shift) when measured along the bias direction ([010] in our case). However, the AF spins are held in place by the AF anisotropy when zero torque is exerted by the F moments. In this sense, when the sample is measured perpendicular to the bias ([100] in our case), the interface AF spins, although rotating with the F moments, would still favor the alignment along the bias direction ([010]) during the intermediate state of reversal (causing the asymmetry). This is somewhat

similar to the observation by Ohldag *et al* [117] that the AF spins can be held in place due to the exchange coupling with the F moment, yet the anisotropy direction is still determined by the AF lattice. To conclude, both the loop shift and the asymmetry are manifestations of the unidirectional bias effect. The true 'blocking' of the EB in this sample should be at 75K, where all the unidirectional characteristics vanish completely. In summary, by studying the temperature dependent magnetic reversal, we argue that the existence of EB should be characterized by two features in the magnetic reversal, i.e. the conventional loop shift observed along the bias direction and the reversal asymmetry measured perpendicular to the bias. We also found different temperature behaviors of the spin-flop coupling, the loop shift, and the reversal asymmetry. The SRT occurs at $T$ ~ 95 K however the EB characteristics varnish at a lower temperature ~ 75 K.

The different interface origins of the EB-induced anisotropies further enable the independent manipulation of $H_{eb}$ and $H_s$ by controlled FC experiments. At any temperatures below $T_B$, resetting the cooling field does not affect $K_u$ because the intrinsic spin-flop coupling is frozen-in. However, $H_{eb}$ is sensitive to the local pinning environment, which can be altered (at least partially) by resetting the cooling field even below $T_B$. Figure 3.20 illustrates such a re-cooling process at four different $T_{int}$ = 15K, 20K, 25K, and 30K. The sample is initially cooled from 300K to 10K at $H_{FC}$ = 2kOe along [010] and then heated up to $T_{int}$, at which an $r(H)$ curve is measured (left panel in Fig. 3.20). Second, without altering the direction of $H_{FC}$, the strength of $H_{FC}$ is fixed at a select value that stabilizes the magnetization along $K_u$ (low resistance state), taking advantage of the intrinsic SRT. We point out that different $H_{FC}$ are used for different $T_{int}$. Next, the sample is cooled back to 10K under this new $H_{FC}$ and the $r(H)$ curve is measured again (right panel in Fig. 3.20). When compared to the initial $r(H)$ at 10K (Fig. 3.18(a)), all the new $r(H)$

curves show a reduced $H_{eb}$ and a slightly enhanced $H_s$. For $T_{int}$ = 30K, $r(H)$ measured after this particular re-cooling process is almost symmetrical with $H$ = 0 (Fig. 3.20(h)), implying the erasing of $H_{eb}$ along [010].

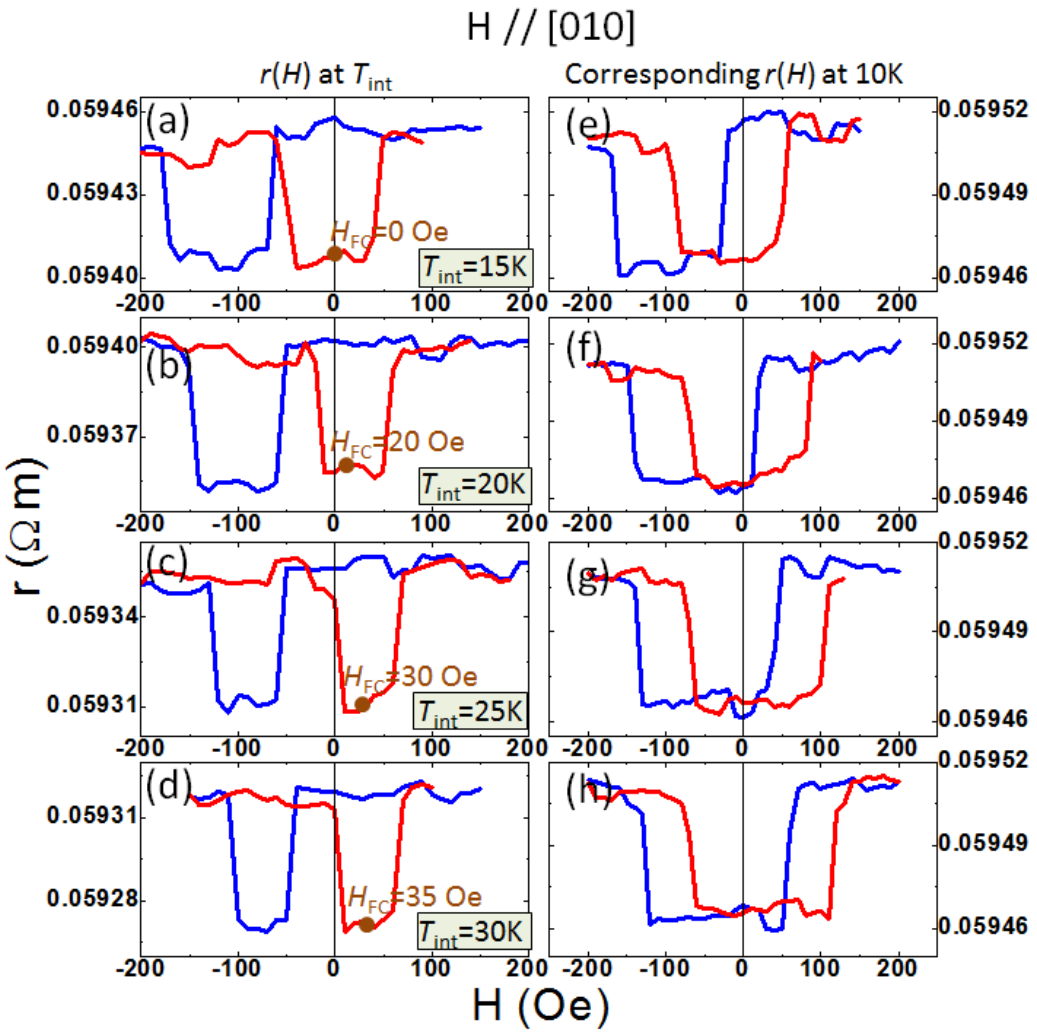


Figure 3.20: $r(H)$ curves measured along [010] at selective $T_{int}$ (left panel), (a) 15K, (b) 20K, (c) 25K, and (d) 30K after initial FC from 300K to 10K at $H_{FC}$ = 2kOe, and their corresponding $r(H)$ curves measured at 10K (e-h) after the re-cooling process from $T_{int}$ under the new $H_{FC}$ (value indicated in each figure of the left panel).

The underlying mechanism for such independent manipulation of $H_{eb}$ is the redistribution of the pinning directions from primarily [010] to [100] and [-100] through the above re-cooling process. It relies on two facts: (1) the local pinning effects have lower thermal stabilities therefore can be reset at $T_{int}$ ($<T_B$);

(2) the resultant $K_{eb}$ can be efficiently set/reset just by the remanence of the F magnetization without using appreciable $H_{FC}$. Here, the direction of $H_{FC}$ is kept unchanged along [010] during re-cooling from $T_{int}$ to 10K, thus almost equal amount of pinning is expected to be induced along [100] and [-100] without changing the symmetry of the system. Such increased pinning along both ends of $K_u$ leads to the slight enhancement of $H_s$. As a result, using this controlled re-cooling processes, we can tune the value of $H_{eb}$ at low temperatures from its maximum to zero while keeping the value of $H_s$ and the symmetry of the system nearly unchanged. Such re-cooling process can give rise to different thermal hysteresis behaviors as will be discussed later in this section.

*Angular dependent magnetic reversal*

We also performed angular dependent measurements to examine the reversal mechanism of the sample. $r(H)$ curves measured at 10 K and at selective external field angle, $\phi$, are illustrated in Fig. 3.21. The AMR signals are again quite small, but can be readily observed taking advantage of the 4-probe method. The AMR ratios are on the order of 0.1%. Sharp reversals are observed at each angle, implying a DW type switching characteristic. The angular dependent switching fields are further plotted in Fig. 3.22. The DW nucleation model is used for fitting the angular dependence, with the fitting parameters, $K_{eb}/M$ = 100 Oe, $\varepsilon_{90^o}/M$ =25 Oe, and $K_u/M$ = -25 Oe. The negative value of $K_u$ indicates its perpendicular orientation to the $K_{eb}$.

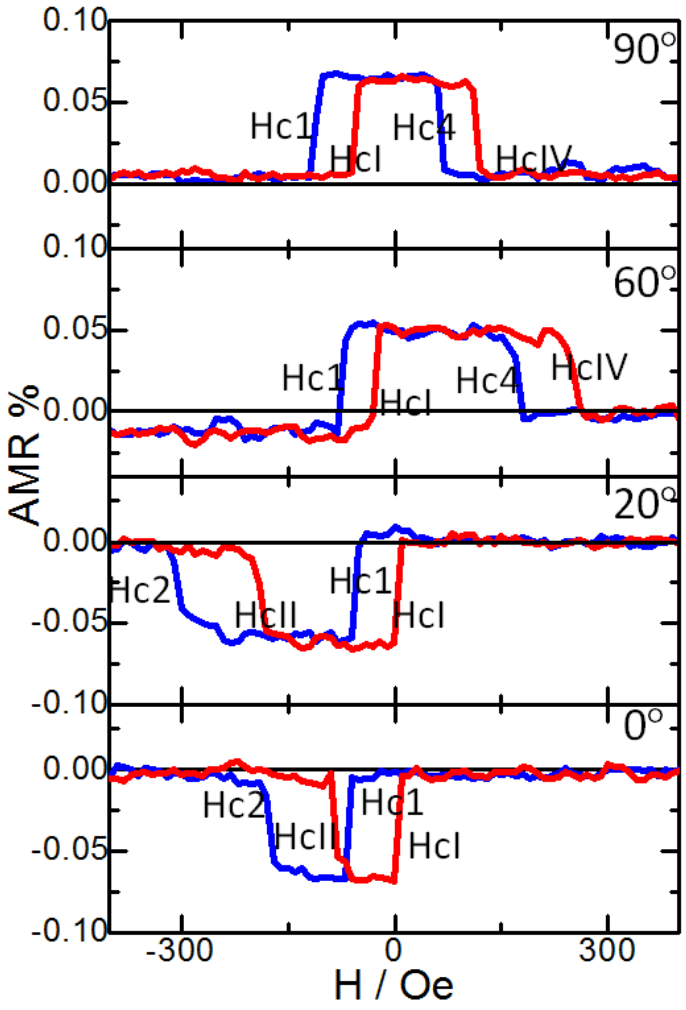


Figure 3.21: $r(H)$ curves measured at 10 K and at selective external field angles, $\phi = 0^{o}$, $20^{o}$, $60^{o}$, $90^{o}$.

*Thermal hysteresis*

Thermal hysteresis is a unique feature of the EB bilayers exhibiting the SRT effect. It states that the magnetization can switch, from the reoriented state (RS) to the aligned state (AS) and vice versa, driven by temperature instead of the external field. Such an effect has been proposed only in theory and has not been experimentally observed so far [118]. The ultimate driving forces for this temperature-driven

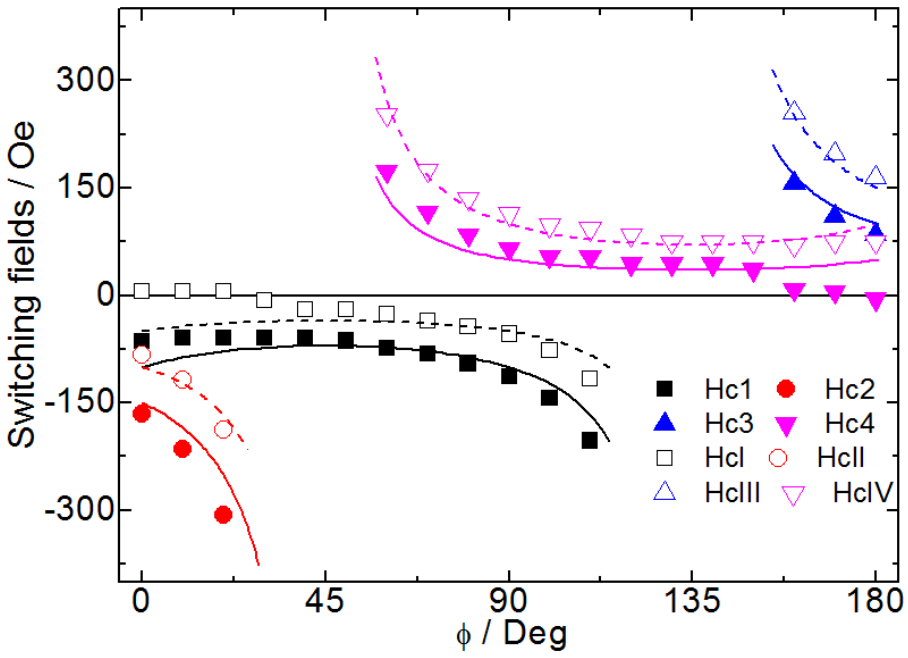


Figure 3.22: Angular dependent switching fields at 10 K and the relevant fittings using the DW nucleation model. $H_{c1\text{-}4,I\text{-}IV}$ are defined the same as in Fig. 3.1.

reversal are the competing magnetic energies in the system, including the interface exchange energy (intrinsic sample property) and the Zeeman energy (set by a constant external field). Two types of thermal behavior, denoted as I and II, have been reported in distinct cases under low and high Zeeman energies, respectively [118]. For example, starting from the RS, i.e. [100] (Fig. 3.16), the magnetization first switches to the AS([010]) upon heating under a constant external field along [010], and then reverses back to the RS upon cooling (type I) forming a thermal loop, or holds irreversibly at the AS upon cooling to the initial temperature (type II). The type II behavior is observed when larger values of the external field are used to inhibit the transition back to the RS at low temperatures. This behavior is of potential interest for magnetoelectronic applications in that a switch from an initial magnetic state to another final state is produced upon one temperature cycle.

We studied such thermal hysteresis in our Fe/MnPd EB bilayers. First, the hysteresis loop is

measured at 10K (Fig. 3.23(a), middle panel) after FC from 300K at $H_{FC}$ = 2kOe along [010]. Second, without changing the direction of $H_{FC}$, its strength is fixed at a select value, $H_m$, that aligns the magnetization along the perpendicular RS in the ascending branch. Such $H_m$ is indicated, in the middle panel of Fig. 3.23(a), by a solid dot on top of the loop. In previous theoretical work [118], a small, positive $H_m$ is usually good enough to stabilize the RS at low temperatures owing to the strong, induced perpendicular $K_u$. However in our sample, a strong $K_{eb}$, in addition to $K_u$, is also induced which is virtually equivalent to an effective field along [010]. Hence, negative values of $H_m$, that partly cancels the $K_{eb}$, need to be used to initialize the RS at 10K in our case. With the field being fixed at $H_m$, a thermal hysteresis curve, $M(T)$, is then measured on heating the sample to 300K (ascending) and cooling it back to 10K (descending).

Figure 3.23(b)-(f) show different $M(T)$ curves at selective $H_m$. $M(T)$ at $H_m$ = -10Oe (Fig. 3.23(b)) exhibits a typical thermal hysteresis behavior. Starting from the RS, a transition to the AS ([010]) is induced in the heating curve at $T_1$, by the effective field along the same direction given by the sum, $H_{eb}(T)$ + $H_m$. The magnetization stays at [010] over a certain temperature range that even exceeds the $T_B$, after which the magnetization along AS is continuously held by the Fe anisotropy against the negative $H_m$. When temperature further increases, the Fe coercivity eventually becomes smaller than the applied, negative $H_m$, so the magnetization switches to the opposite-AS ([0-10]) at $T_2$. During the cooling curve, a new exchange bias along [0-10] is established by the F remnant magnetization along the same direction. Therefore, a positively-shifted, stepped hysteresis loop is observed when cooled back to 10K (lower panel in Fig. 3.23(a)).

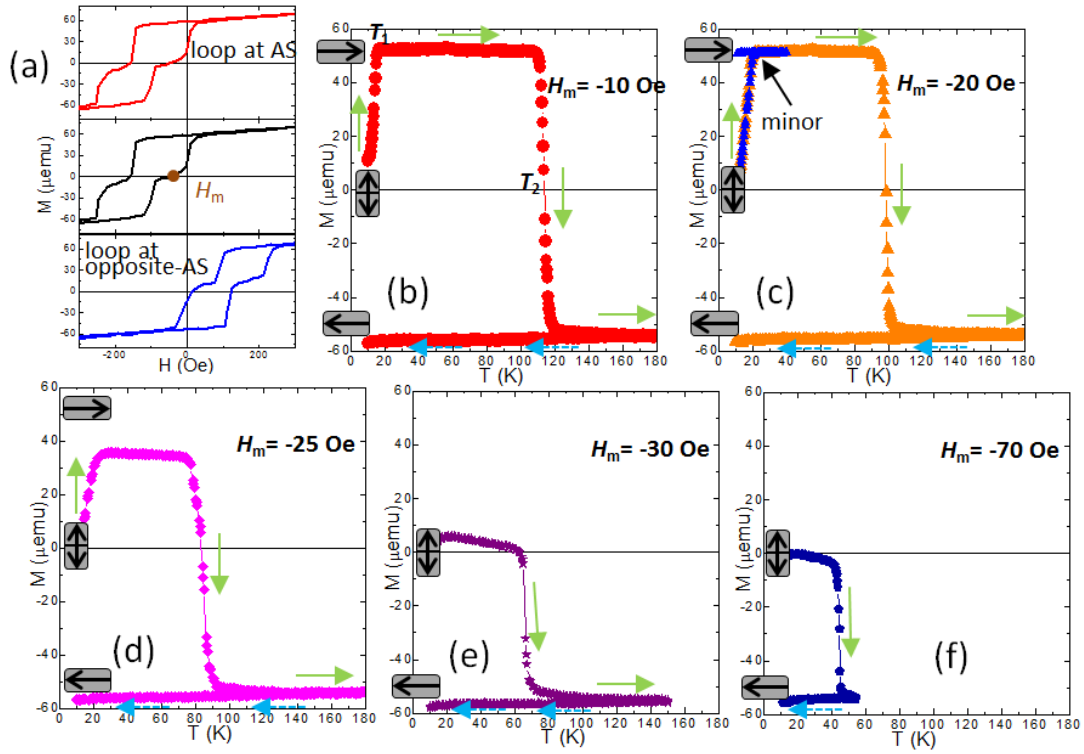


Figure 3.23: (a) $M(H)$ curves measured at 10 K for initial state (middle panel), AS (upper panel) and opposite-AS (lower panel). The field used to stabilize the RS, $H_m$, is also indicated in the initial loop. $M(T)$ curves measured at selective $H_m$, (b) -10 Oe, (c) -20 Oe, (d) -25 Oe, (e) -30 Oe, and (f) -70 Oe, all starting from the RS. The minor curve for $H_m$ = -20 Oe is also indicated. In each $M(T)$ curve, the orientation of Fe spins is represented by an arrow enclosed in a rectangle. The solid and dashed arrows indicate the heating and cooling branches, respectively.

Similar thermal behavior with two transitions at $T_1$ and $T_2$ can be observed for -30 Oe < $H_m$ $\leqslant$ -10 Oe. In all these cases, the magnetization begins from the initial RS, goes through an intermediate AS([010]) and finally ends up at the opposite-AS ([0-10]) during a complete thermal cycle. Notably, the magnetization can return to AS ([010]) if subject to a minor thermal hysteresis, i.e. heating and measuring from 10K to any $T$ between $T_1$ and $T_2$, and cooling back to 10K. This is experimentally illustrated by the minor curve at $H_m$ = -20 Oe (Fig. 3.23(c)). Subsequently, the hysteresis loop measured at 10K shows the conventional negative bias (upper panel in Fig. 3.23(a)). Actually, such minor $M(T)$ curve is exactly the type II thermal hysteresis as discussed in [118].

Both the RS (stabilized by $K_u$) and the loop shift (induced by $K_{eb}$) originate at the interface and point to certain exchange energies, which are proportional to the thermal average value of the AF spins at the interface. Since the interface exchange energy vanishes at sufficiently high temperature, a transition in the heating branch is certain to occur. However, whether the magnetization transitions to [010] or to [0-10] depends on the effective field, $H_{eb}(T)$ + $H_m$. For example, larger negative values of $H_m$ ($\leqslant$ -30 Oe) actually favors [0-10] instead of [010] for the initial transition from RS and maintains such a state for the rest of the thermal cycle (Fig. 3.23(e) and (f)).

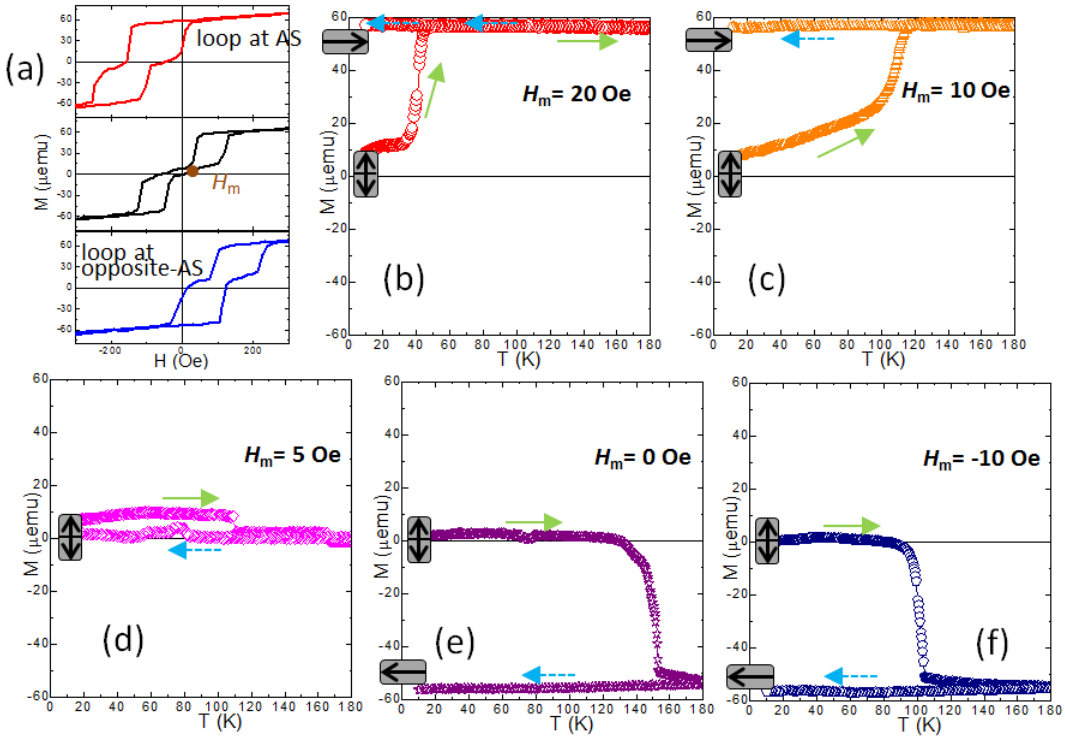


Figure 3.24: (a) $M(H)$ curves measured at 10 K for initial state after the re-cooling process from 30K to 10K at $H_{FC}$ = 40 Oe (middle panel), AS (upper panel) and opposite-AS (lower panel). The field used to stabilize the RS, $H_m$, is also indicated in the initial loop. $M(T)$ curves measured at selective $H_m$, (b) 20 Oe, (c) 10 Oe, (d) 5 Oe, (e) 0 Oe, and (f) -10 Oe, all starting from the RS. In each $M(T)$ curve, the orientation of Fe spins is represented by an arrow enclosed in a rectangle. The solid and dashed arrows indicate the heating and cooling branches, respectively.

We then studied the thermal hysteresis after 'erasing' the $K_{eb}$ along [010] by the re-cooling process. After the initial FC from 300K to 10K at $H_{FC}$=2kOe along [010], the sample is heated to $T_{int}$ = 30K and

subsequently cooled back to 10K, at a reduced $H_{FC}$ = 40Oe (still along [010]) that reorients the Fe magnetization along $K_u$. The hysteresis loop at 10K after the re-cooling exhibits nearly no loop shift ($H_{eb}$ ~ 0), as shown by the middle panel in Fig. 3.24(a). Next, $M(T)$ curves were measured at selective $H_m$ (Fig. 3.24(b)-(f)). Without the exchange bias, the transition is simply driven by $H_m$ alone, and thus favors AS ([010]) and opposite-AS ([0-10]) when positive and negative $H_m$ are used, respectively. Specifically, when a positive $H_m$ is applied, it not only drives the transition from RS to AS, but also maintains such a state during the cooling curve (Fig. 3.24(b) and (c)). Similarly, the negative $H_m$ drives the transition from RS to opposite-AS and maintains such a state during the cooling curve (Fig. 3.24(f)). As a result, the observed curves are primarily type II with only one transition observed over the whole temperature cycle.

We note that the measurement at exactly zero $H_m$ (Fig. 3.24(e)) also exhibits a transition to opposite-AS([0-10]), which may be due to the imperfect erasing of the $H_{eb}$ during the re-cooling experiment (negative effective field). This small residue of $H_{eb}$ can be balanced by applying a comparable $H_m$ with opposite sign, so as to completely get rid of the effective pinning field along the [010] direction. On top of this assumption, if this $H_m$ is also smaller than the Fe coercivity up to 300K, the switching to other states above $T_B$ can be prevented as well. In reality, we observed such a situation at $H_m$ = 5 Oe (Fig. 3.24(d)), where the magnetization favors transitions along neither [010] nor [0-10], but preferably stays along the RS over the whole temperature cycle. As a result, when the $K_{eb}$ along [010] is properly balanced, the RS is stabilized by the perpendicular $K_u$ up to $T_B$, and then by the Fe reversal barrier, i.e. 7 Oe (> $H_m$) at 300K, up to the maximum temperature (300K) used in the measurement.

In summary, we showed experimental evidence for the thermal hysteresis in EB bilayers exhibiting SRT. On the heating branch, we observed two distinct transitions, below and above $T_B$, that are driven

primarily by the interface exchange energy and the Zeeman energy, respectively. The first transition is determined by the effective field along AS, and can favor two opposite directions (AS and opposite-AS) at different effective fields. The second transition is driven by the competition between the external field and the reversal barrier of the ferromagnet. On the cooling curve, the new exchange bias established by the F remnant magnetization can prohibit the transition back to the RS at low temperatures. However, once the bias is erased (by the re-cooling experiment), the transitions are determined primarily by the external field, i.e., the transition simply favors AS and opposite-AS when positive and negative fields are used, respectively. Moreover, if the external field is sufficiently small, i.e. less than the reversal barrier, the magnetization is constantly stabilized along the RS over the whole temperature cycle.

*3.4 Antiferromagnetic bulk effect in epitaxial EB multilayers*

Although EB is an interface-originated effect, many recent studies indicated that the AF bulk spins play important roles in defining the EB phenomenon [119-122]. Due to the long spin correlation length in epitaxial samples, the bulk effect of the AF can be studied by working on EB multilayered heterostructures [123]. We have also conducted relevant investigations on the bulk effects in the spin-flop coupled Fe/MnPd system [124].

We first reveal the role of bulk AF structures using a series of Fe/MnPd bilayer samples with varying AF thickness. We then studied the effective change in the internal AF spin configuration and its role in EB by F reversal using well-behaved, epitaxially grown multilayer samples, i.e., Fe(F1)/MnPd(AF1)/Fe(F2)/IrMn(AF2). In this multilayer structure, AF1 is *a*-axis MnPd that has a

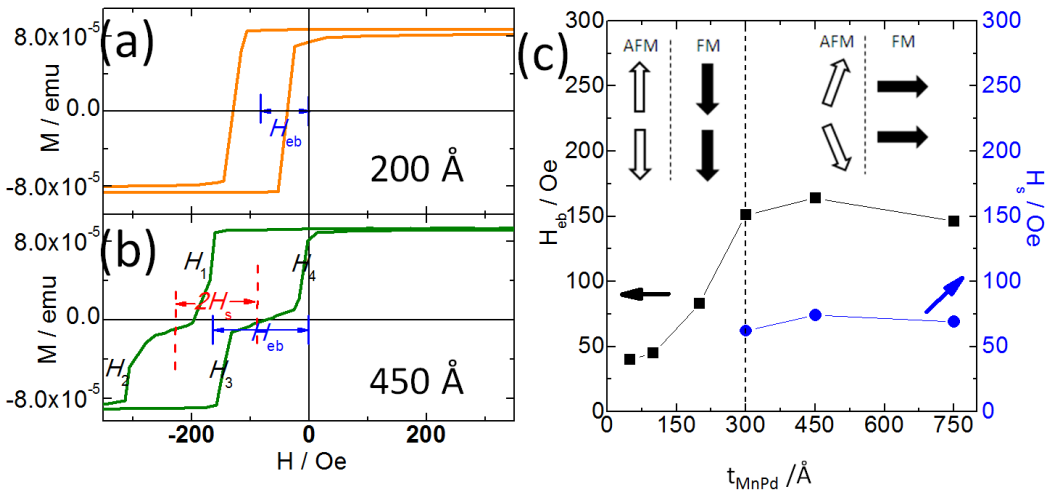


Figure 3.25: (a) Hysteresis loop of Fe/MnPd (t = 200 Å) at 20K. The one-step loop indicates the collinear F/AF coupling at the interface. (b) Hysteresis loop of Fe/MnPd (t = 450 Å) at 20K. The two-step loop indicates the spin-flop coupling at the interface. The determination of the shift field, $H_s = (H_1-H_2-H_3+H_4)/4$, and the EB field (center shift of entire loop), $H_{eb}$ are illustrated. (c) Thickness dependence of $H_s$ and $H_{eb}$ of Fe/MnPd bilayer samples measured at 20K. Interface coupling transitions from parallel to spin-flop at $t_{sat}$ ~ 300 Å. [124]

blocking temperature, $T_B^{MnPd}$, ~ 90K. AF2 is IrMn with $T_B^{IrMn}$ > RT, which is used to provide a strong pinning on F2. This enables us to define the AF1 bulk spin arrangement at RT by field-cooling F1 and F2 in parallel (P) or antiparallel (AP) configurations. Observations of how the F magnetization history in the F2/AF2 couple affects the EB of F1/AF1 couple provides direct evidence for the specific role played by the bulk AF spins, as a function of thickness, and how they rearrange during the magnetization switching of the individual F layers on either side of the AF1.

Epitaxial bilayers and multilayers were fabricated on MgO(001) substrate by ion beam sputtering following our earlier works [72,73,79]. Bilayer samples have a $Fe_{(100\ Å)}$/*a*-axis $MnPd_{(t\ Å)}$ structure with *t* = 50, 100, 200, 300, 450, 750 Å. Two multilayer samples have a $Fe_{(100\ Å)}$/*a*-axis $MnPd_{(s\ Å)}$/$Fe_{(100\ Å)}$/$IrMn_{(80\ Å)}$ stacking sequence with *s* = 350 Å and 700 Å. Finally, all samples were protected by a 50 Å Ta capping layer. The multilayer sample structure is referred to as F1/AF1/F2/AF2 in all subsequent discussions. All samples were grown at 120°C in the presence of an in-plane magnetic field, $H_{growth}$ = 300 Oe, along the

Fe[100] easy direction to induce an exchange anisotropy only at the F2/AF2 interface. As a result, the F2 layer is pinned and exhibits a loop shift at RT. Since the magnetizations of F1 and F2 switch at different fields, the effects of F2 magnetization reversal on the EB of the F1/AF1 couple through the AF1 bulk spin rearrangement can be readily detected. *M-H* curves were measured using a Quantum Design physical property measurement system over a wide temperature range from 10 to 300 K.

The bilayer samples were cooled from 300 to 20 K under a cooling field, $H_{cool}$ = 1 KOe parallel to $H_{growth}$ and subsequently measured at 20 K. We first used a large magnetic field of 1 KOe and cycled > 10 times to minimize the training effect of all layers. When $t$ < 300 Å, a conventional biased loop can be observed and the $H_{eb}$ was determined by the center-shift of the loop, Fig. 3.25(a). For samples with $t \geq$ 300 Å, a stepped loop can be observed indicating the low temperature in-plane spin reorientation, Fig. 3.25(b). The shift field, $H_s$, was determined from the center shift of the two sub-loops (Fig. 3.25(b)), i.e., $H_s = (H_1-H_2-H_3+H_4)/4$, which is further related to a perpendicular $K_u$ via $K_u = M_sH_s$. $H_{eb}$ was determined by the center shift of the entire loop. The thickness dependence of $H_{eb}$ and $H_s$ are summarized in Fig. 3.25(c). $H_{eb}$ reached saturation at $t_{sat}$ = 300 Å, which is also the critical thickness for the onset of $H_s$. The $t_{sat}$ is also understood as the maximum depth of the AF spins in the bulk that can affect the interfacial coupling. It is very likely that such a length should be comparable to, but not bigger than the longitudinal dimension, $\delta$, of stable AF domains. Such large domain size is anticipated in epitaxial samples due to the well-defined chemical ordering. The longitudinal lattice constant for *a*-axis MnPd is ~3.94 Å, so the width of a stable MnPd domain ($\delta$ ~ 300 Å) contains ~76 atomic monolayers. This large $\delta$ in MnPd is unique whereas much smaller values are usually observed in other AFs. However, when the AF layer thickness > $\delta$, no additional anisotropy energy is generated with increasing AF thickness and the EB is

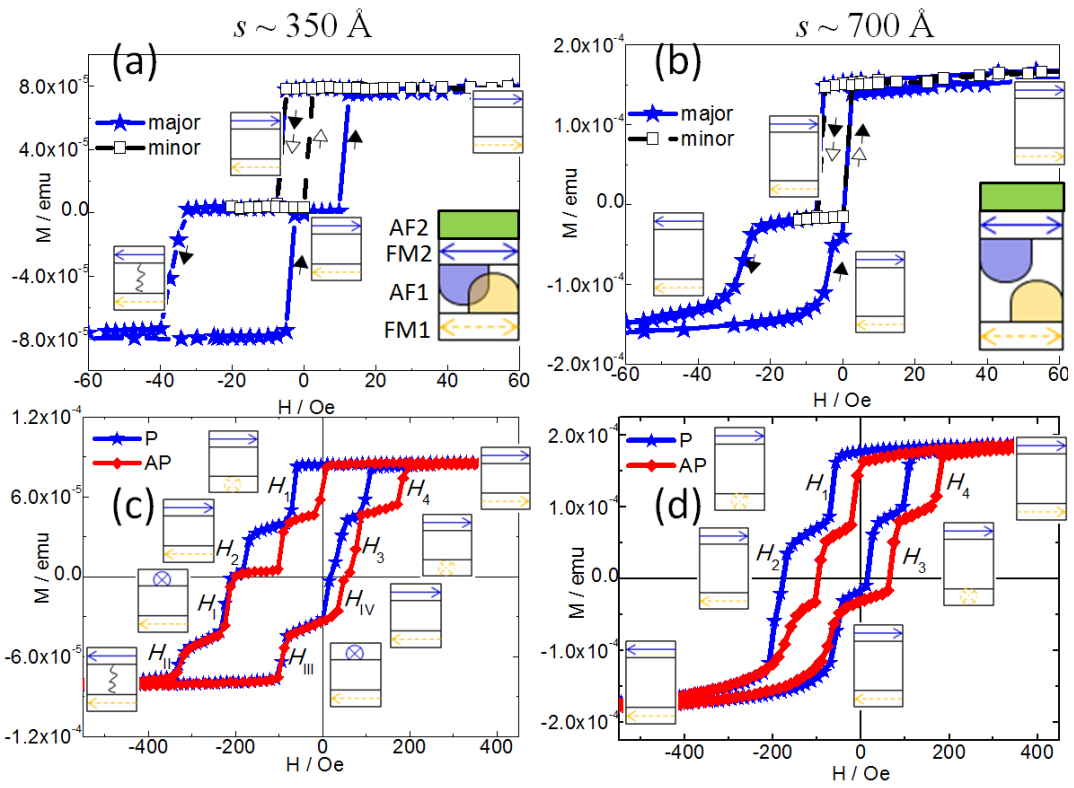


Figure 3.26: RT major and minor loops of (a) thin (s ~ 350 Å) and (b) thick (s ~ 700 Å) multilayer samples. Hysteresis loops measured at 20 K under parallel (P) and antiparallel (AP) cooling from RT of (c) thin (s ~ 350 Å) and (d) thick (s ~ 700 Å) multilayer sample. Magnetization configuration of F1 (dashed arrow) and F2 (solid arrow) are illustrated in an enclosed box for each magnetic switching. [124]

saturated.

In the F1/AF1/F2/AF2 multilayer sample with $s$ = 350 Å, the MnPd (AF1) thickness is just enough to support a single, fully developed AF domain. Figure 3.26(a) shows the RT hysteresis curve for the $s$ = 350 Å sample measured along $H_{growth}$ after minimizing the training effect. The solid curve reflects the magnetization switching of the entire structure, containing two magnetization hysteresis sub-loops. Due to additional pinning in the F2 layer, the upper and lower sub-loops should correspond to F1 and F2, respectively. The solid F1 sub-loops reflect the F1/AF1 coupling with the F2 magnetization experiencing a complete switching process, from being first aligned parallel to $H_{growth}$ to the opposite direction and then back to align with $H_{growth}$. In the same figure, the dashed lines correspond to the magnetization minor

loops for F1 without F2 layer switching. In simple terms, the solid and dashed F1 loops compare the F1/AF1 exchange bias with and without a complete F2 switching process. Notably, without switching of F2, the ascending branch of the F1 loop shifts leftward. For the other multilayer sample, $s \sim 700\text{Å} > 2\delta$, Fig. 3.26(b), the effect of F2 magnetization history is much less pronounced and almost indiscernible, indicating that the ascending branches of F1 are not affected by the F2 switching. These observations provide direct evidence that a non-recoverable change in the AF1 can occur during F2 magnetization switching, i.e., the bulk AF1 spin structure is affected by the F2 magnetization configuration. When $s$ is comparable to $\delta$, the AF1 spin rotation driven by the switching of F1 and F2 overlap each other, which makes it possible to overcome the energy barrier of the spin configuration built by their initial state and partially unlock the exchange bias of F1 after switching F2 back and forth. However, when $s > 2\delta$, AF1 spins, from both interfaces to their respective bulk parts rotate independently; therefore, the switching of F2 has no effect on F1.

The effect of F reversal on the AF bulk spin structure was further investigated by field-cooling the thin multilayer sample to $T < T_B^{MnPd}$ with F1 and F2 parallel or antiparallel to each other. At $T < T_B^{MnPd}$, due to the spin-flop exchange coupling, shifted and stepped hysteresis loops can be simultaneously observed, Fig. 3.26(c). For parallel cooling, $H_{cool}$ = + 20 Oe was applied at RT and the sample was subsequently cooled to 20 K and measured (solid curve). Exchange bias and spin reorientation behavior were observed for both F1 and F2 sub-loops. $H_s^{F1} = (H_1\text{-}H_2\text{-}H_3\text{+}H_4)/4 = 42$ Oe and $H_{eb}^{F1} = -34$ Oe are obtained for F1; and $H_s^{F2} = (H_I\text{-}H_{II}\text{-}H_{III}\text{+}H_{IV})/4 = 50$ Oe and $H_{eb}^{F2} = -174$ Oe are obtained for F2. Note that $|H_{eb}^{F2}| >> |H_{eb}^{F1}|$ due to the contribution from both AF1/F2 and F2/AF2 interfacial couplings. In the F1 sub-loop, the field difference between the two sequential steps in the descending branch, i.e. $|H_1 - H_2|$

~ 108 Oe, is greater than that for ascending branch $|H_3 - H_4| \sim 61$ Oe. This is attributed to the propagation effect of the exchange bias that shifted $H_2$ leftward due to the parallel cooling of F2 along the $H_{growth}$. Physically, it is harder to fully reverse F1 to $-H_{growth}$ with F2 cooled along $H_{growth}$.

For antiparallel cooling, $H_{cool}$ is -18 Oe, approached from a large positive field, to reverse only F1; the whole structure is subsequently cooled to 20 K and measured (dashed curve). The F2 sub-loop looks almost the same with the parallel cooling configuration; however, the F1 sub-loop shifts to the positive field direction. Thus, $H_s^{F1} = 44$ Oe and $H_{eb}^{F1} = 36$ Oe are obtained from the F1 sub-loop. Similarly, $H_{IV}$, also shifts towards the positive field direction due to the EB propagation effect. Physically, F1 is now pinned along $-H_{growth}$ which makes it harder for F2 to reverse back to $H_{growth}$. On the other hand, the F1 sub-loop is symmetric with respect to its center in the antiparallel case, i.e. $|H_1 - H_2| \sim 96$ Oe, and $|H_3 - H_4| \sim 103$ Oe.

Figure 3.26(d) compares the hysteresis loops for the other multilayer sample in the two field-cooling configurations. F1 spin reorientation can be clearly observed, as indicated by the stepped F1 sub-loop. However, such behavior is missing for the F2 layer, which indicates that the spin-flop coupling was not maintained throughout the MnPd layer. For this sample with $s$ (700 Å) > $2\delta$, during sample growth the bulk AF stabilizes at least two separated, fully-developed domains, located at the F1/AF1 and AF1/F2 interfaces, respectively. Therefore, the spin-flop coupling established at the F1/AF1 interface can only propagate within its respective domain but is stopped at any domain wall. From Fig. 2(d), $H_s^{F1} = 46$ Oe and $H_{eb}^{F1} = -28$ Oe, for the parallel cooling configuration, and $H_s^{F1} = 45$ Oe and $H_{eb}^{F1} = 30$ Oe, for the antiparallel case, were obtained.

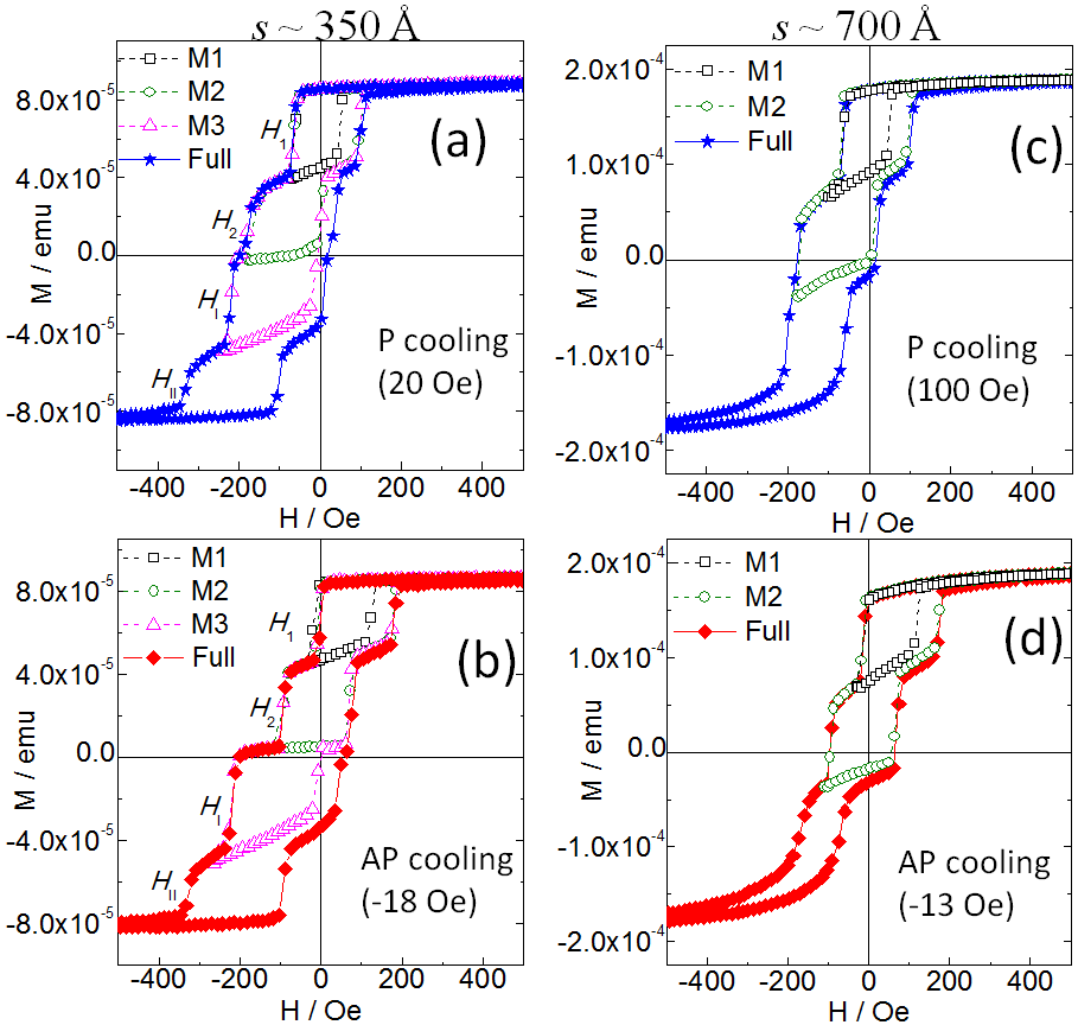


Figure 3.27: Complete hysteresis (solid) and minor loops (open) measured at 20K for (a) parallel cooling and (b) antiparallel cooling of the thin multilayer sample. Complete hysteresis (solid) and minor loops (open) measured at 20K for (c) parallel cooling and (d) antiparallel cooling of the thick multilayer sample. [124]

Minor loops at each distinct reversal step for the descending branch were further studied to reveal spin-flop coupling and the effect of the bulk AF structure, Fig. 3.27. Samples were first cycled under large magnetic field (1 KOe) to minimize training effects. As discussed earlier, $H_1$ points to the spin reorientation of F1, in which the magnetization is along Fe[010], perpendicular to $H_{growth}$. The associated minor loop, $M_1$, is irreversible for both cooling configuration (Fig. 3.27(a) and (b)), showing that magnetic switching is mainly via DW nucleation and propagation. The second minor loop, $M_2$, represents

the complete F1 hysteresis sub-loop with F2 kept fixed along $H_{growth}$. For parallel cooling, for F1, the switching field shifts leftward upon reversal back from negative field direction to the reoriented state, Fe[010], when compared to the sub-loop for the full hysteresis (solid). However, for antiparallel cooling, $M_2$ show almost indiscernible difference with the full hysteresis sub-loop. The result indicated that the internal AF1 domain structure depends on the cooling process as well as the reversal history. In the parallel configuration, non-recoverable change in the AF1 occurs at $H_{II}$ when both F1 and F2 were reversed from their original cooled stable states. In such circumstances, when a F domain is reversed, the adjacent AF spin structure is exposed to a magnetic torque whose magnitude is given by the strength of the F/AF exchange coupling. A strong torque exerted from both F1 and F2 when combined positively is able to alter the internal AF1 spin structure. In the antiparallel case, however, AF1 is subjected to one torque (by F2) and to another torque (by F1) in the descending and ascending branches. A single torque exerted on the AF at any one time is not strong enough to bring about non-recoverable changes in the AF. In addition, the antiparallel cooling mode forced the formation of at least two antiparallel AF domains in the bulk, one at each F interface. Thus this torque exerted on the AF, from either F1 or F2, was absorbed within each respective AF domain, and any long-range spin effects are not able to propagate across the domain wall. As a result, the spin states of F1 and F2 are not able to influence each other through the bulk AF spins. This is an elegant experimental demonstration of the effect of F reversal on bulk AF spin structure.

It is worth noting that the perpendicular reoriented state causes no effect on the AF bulk spin structure, as revealed by minor loop $M_3$. Specifically, F2 switched to the reoriented state at $H_I$ and then irreversibly switched back to $H_{growth}$; but the F1 sub-loop in $M_3$ showed indiscernible difference compared

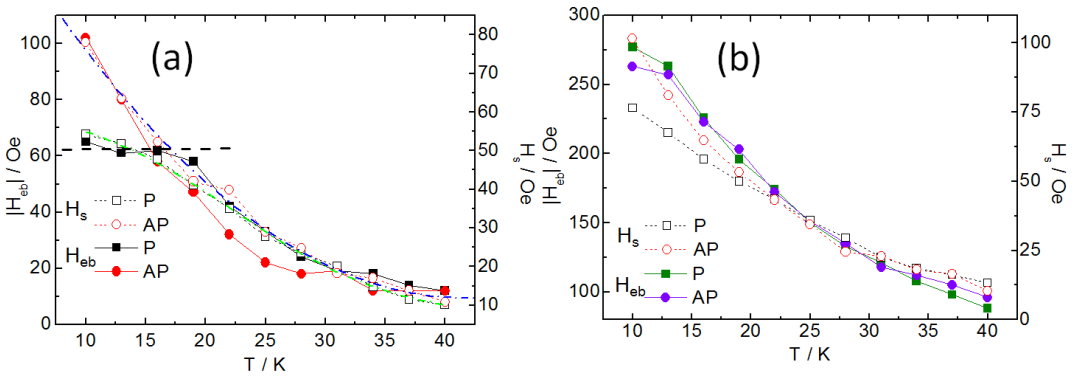


Figure 3.28: Data for the thin multilayer sample (s ~ 350Å). (a) Temperature dependence of $|H_{eb}|$ (solid) and $H_s$ (open) under parallel (square) and antiparallel (circle) cooling process of F1. Two lines (in dash dot) are guide to the eye. (b) Temperature dependence of $|H_{eb}|$ (solid) and $H_s$ (open) under parallel (square) and antiparallel (circle) cooling process of F2. [124]

with $M_2$. It is likely because the spin-flop coupling only gives rise to an effective uniaxial anisotropy, which reorients the F magnetization by DW nucleation and propagation. The DW movement along the intermediate reoriented state effectively introduces a lower torque on the AF and has only a small effect on the bulk domain structures that control the EB. Similar measurements were conducted for the sample with $s$ = 700 Å, under parallel (Fig. 3.27(c)) and antiparallel (Fig. 3.27(d)) cooling mode. In both cooling modes, the minor loop $M_2$ is indiscernible from the full hysteresis sub-loop, which indicates that the AF spins at the F1/AF1 and AF1/F2 interfaces, including their respective inner parts, do not communicate due to the thick AF layer.

Further temperature dependent measurements indicate that the spin reorientation and exchange bias can be simultaneously observed up to ~50K. $|H_{eb}(T)|$ and $H_s(T)$ for F1 of the thin multilayer sample ($s$ = 350Å) under both cooling modes are summarized in Fig. 3.28(a). $H_s$ showed the same temperature behavior as $|H_{eb}|$. The strong correlation in the temperature dependence of $H_s$ and $H_{eb}$ confirms that the spin-flop coupling is attributable for the exchange bias. For antiparallel cooling, both $|H_{eb}|$ and $H_s$ decay with temperature from 10 to 40 K. However, for parallel cooling, $|H_{eb}|$ and $H_s$ are suppressed and

maintained a constant value at low temperatures from 10 to 20 K.

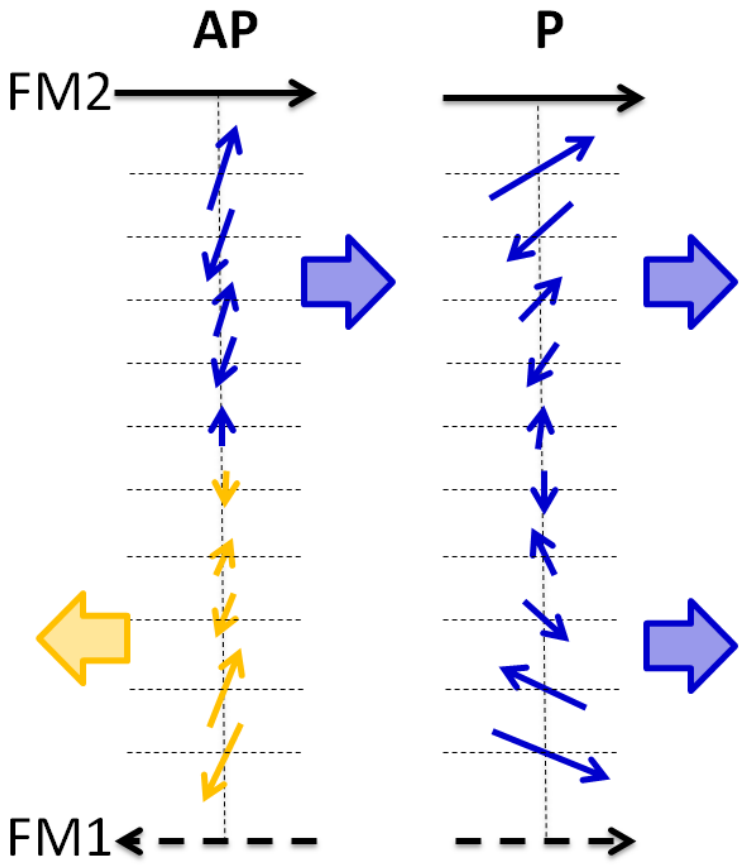


Figure 3.29: Schematic illustration of a qualitative model, showing the possible AF domain formation and spin canting for the two cooling modes. Block arrows indicate the preferred canting directions at different regions in the AF.

To interpret our observations, we propose a qualitative model based on spin-flop coupling (Fig. 3.29). Such model does not rely on complex AF spin structures, but is based on simple assumptions, i.e. possible AF domain formation and the interfacial spin canting at different depths within the AF. An antiparallel configuration of F1 and F2 can mutually drag the AF spins to the perpendicular direction (large rotating angles) thus favoring the perpendicular spin-flop coupling and leading to a greater $H_s$; besides, it also assists the formation of opposite frozen-in domains and associated DWs in the AF bulk. Uncompensated AF moments can be enhanced by the DW passing through the defects or dislocations in the films, thus

increase the $H_{eb}$ according to the domain state model. On the contrary, parallel cooled F1 and F2, both along $H_{growth}$, will favor the competing parallel spin coupling with small rotating angles throughout the AF bulk; this parallel configuration also decreases the possibility for AF domain wall formation. As a result, both $|H_{eb}|$ and $H_s$ are suppressed when compared with the antiparallel cooling configuration at low temperatures. Our model qualitatively explains the differences for parallel and antiparallel cooling configurations. Besides, it also sheds light on tuning the spin-flop coupling via extrinsic, field cooling approach in epitaxial samples.

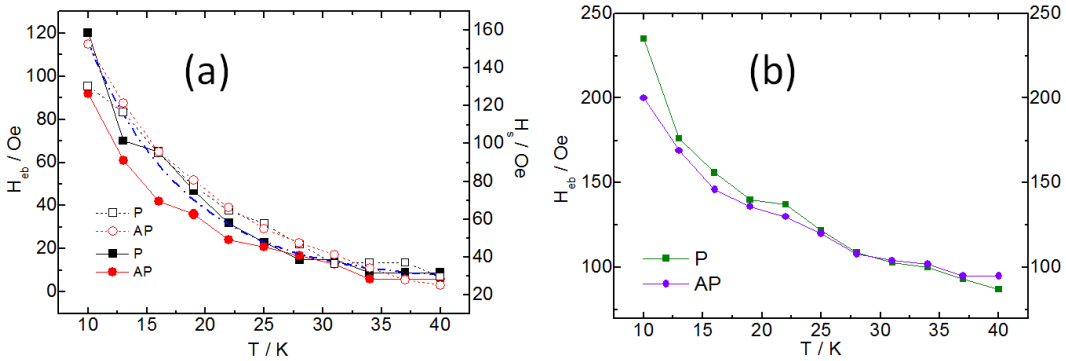


Figure 3.30: Data for the thicker multilayer sample (s ~ 700Å). (a) Temperature dependence of $|H_{eb}|$ (solid) and $H_s$ (open) under parallel (square) and antiparallel (circle) cooling process of F1. (b) Temperature dependence of $|H_{eb}|$ under parallel (square) and antiparallel (circle) cooling process of F2.

Similar effect has been observed at the AF1/F2 interface. As shown, in Fig. 3.28(b), a gap of $H_s$ at 10 ~ 20 K was found between the parallel and antiparallel cooling mode. $|H_{eb}|$ decreases with temperature and almost overlaps each other for parallel and antiparallel cooling configurations, due to the much stronger pinning of F2 by the AF2 from the other interface. Finally, we note that measurements for the thick multilayer sample showed almost overlapped behavior of $|H_{eb}|$ and $H_s$ of F1 and $|H_{eb}|$ of F2 (Fig. 3.30), confirming the non-interacting interfaces on the two sides of thick AF.

In conclusion, we have revealed the role of bulk AF structures on exchange bias with spin

reorientation transitions in epitaxial bilayers and multilayers. A large correlation length of the order of ~ 300 Å for the epitaxial antiferromagnet, MnPd, was confirmed. Using such multilayered sandwich structures, the effect of F magnetization history on bulk AF spins is elegantly investigated at both the saturated (final) and spin-reoriented (intermediate) F states. The saturated F state, achieved by magnetization rotation, is considered the relevant process for the effective AF bulk modification due to the exertion of a larger spin torque, unlike the spin-reoriented state that only involves ferromagnetic DW movement.

# Chapter 4

## DEVELOPING EPITAXIAL PATTERNING FOR MAGNETIC NANOSTRUCTURES

Contents of this chapter have been partially published in Ref.[147], [154], [155], [157]

In the last chapter, we have shown that the competing anisotropies play a dominant role in the magnetic reversal of epitaxial EB samples. We also demonstrated that the unidirectional anisotropy, in terms of both magnitude and orientation, can be modified by varying layer thicknesses, temperatures, and field cooling processes. However, the induced uniaxial anisotropy seems to have less flexibility. Although its magnitude is modified upon different layer thicknesses and temperatures, its orientation is quite rigid, lying either parallel (e.g: Fe/IrMn), or perpendicular (e.g: Fe/MnPd) with the field cooling direction (unidirectional anisotropy). Besides, its magnitude is usually quite small and sometimes even ignorable.

From a scientific point of view, in order to amplify the possible effect of the uniaxial anisotropy, one opportunity is to take advantage of the shape anisotropy of a magnetic object. This can be done by making magnetic nanostructures with significantly enlarged shape anisotropies. The direction of the shape anisotropy can be also controlled, independent of the unidirectional anisotropy thus offering more flexibility. From a technological point of view, in modern nano-devices, the shape of the thin-film

non-trivially affects the magnetic properties and needs to be taken into consideration [125]. As a result, it would be very interesting and desirable to study the competing effect of anisotropies including the shape anisotropy of the nanostructures. Technically, a combination of the nano-shape with more macro-scale magnetic thin film properties is desirable. In order to obtain well-defined nanostructures and maintain the thin-film properties as much as possible, lithography techniques, including photolithography, e-beam lithography and nanoimprint lithography, are applied in this work.

*Photolithography*

Photolithography, or optical lithography, is a photon-based process widely used in micro-fabrications to selectively remove parts of a thin film or bulk substrate [126]. This process uses UV light to transfer a geometric pattern from a photomask to a light-sensitive chemical photoresist, also called the 'resist', deposited on the substrate. Key steps in photolithography process involve cleaning/preparation, photoresist application, exposure/developing, etching and photoresist removal. Advantages for photolithography including high-speed, high-throughput, and low cost. However, the feature size is constrained by the light wavelength, limiting photolithography to the creation of micrometer scale patterns.

*E-beam lithography*

Electron beam (e-beam) lithography passes a beam of electrons in a patterned fashion across a

surface covered with resist [127], analogous to ‘exposing’ the resist, and then exposed or non-exposed regions of the resist are selectively removed, or ‘developed’. The purpose, as with photolithography, is to create very small structures in the resist that are subsequently transferred to the substrate material. E-beam lithography was developed for manufacturing integrated circuits and is now used for creating nano-scale architectures. By using electrons, one can create features down to the nanometer range, giving e-beam lithography an advantage over traditional photolithography. However, the time required to expose an entire silicon wafer or glass substrate is greater than with photolithography, limiting the throughput of processing using e-beam lithography.

*Nanoimprint lithography*

Nanoimprint lithography (NIL) is the newest method for fabricating nanometer scale patterns. NIL is a simple nanolithography process featuring low cost, high throughput and high resolution. Patterns are created by mechanical deformation of imprint resist by a template (stamp), eliminating any wavelength limitations of feature size. The imprint resist is typically a monomer or polymer formulation that is cured by heat (thermal NIL) or UV light (UV NIL) during the imprinting (Fig. 4.1). Adhesion between the resist and the stamp is controlled to allow proper release of the stamp after imprinting. The term ‘Nanoimprint Lithography’ appeared in the scientific literature first in 1996 [128], although hot embossing (now taken as a synonym of NIL) of thermoplastics had been in the patent literature for a few years previous. After that, different variations and implementations of NIL have been developed [129,130]. Recently, nanoimprint lithography was added to the International Technology Roadmap for Semiconductors (ITRS)

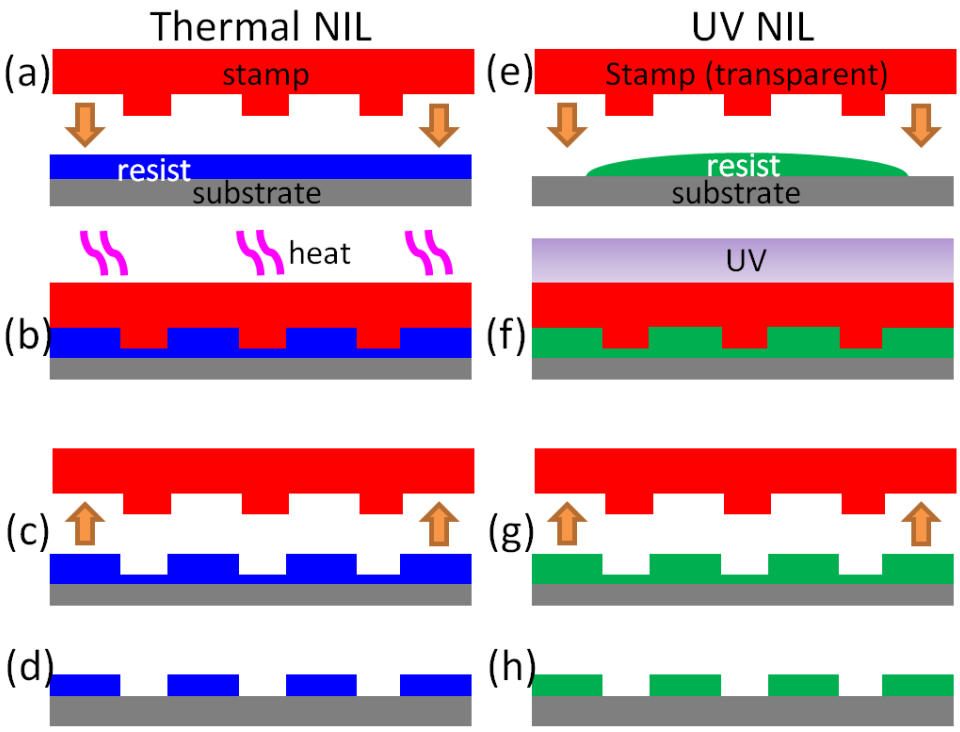


Figure 4.1: Illustration of thermal NIL (a-d) and UV NIL (e-h) processes. (a) Resist is spin coated on substrate, (b) stamp is applied and the sample stack is heated to elevated temperature for imprinting, (c) stamp is released and the resist copies the feature of the stamp, (d) resist residue is removed by etching to expose the substrate for subsequent processing. (e) Resist is dispensed on substrate, (b) stamp is applied and the sample stack is subjected to UV light for imprinting, (c) stamp is released and the resist copies the feature of the stamp, (d) resist residue is removed by etching to expose the substrate for subsequent processing.

for the 32 and 22 nm nodes.

A key benefit of nanoimprint lithography is its simplicity. The single greatest cost associated with chip fabrication is the optical lithography tools needed to print the circuit patterns. Optical lithography requires high powered lasers and a number of precision ground lens elements to achieve nanometer scale resolution. There is no need for complex optics or high-energy radiation sources with a nanoimprint tool. There is no need for finely tailored photoresists designed for both resolution and sensitivity at a given wavelength. The simplified requirements of the technology lead to its low cost.

Imprint lithography is inherently a three-dimensional patterning process. Imprint stamps can be

fabricated with multiple layers of topography stacked vertically. Resulting imprints replicate both layers with a single imprint step, which allows chip manufactures to reduce chip fabrication costs and improve product throughput. As mentioned above, the imprint material does not need to be finely tuned for high resolution and sensitivity. A broader range of materials [129,130] with varying properties are available for use with imprint lithography. The increased material variability gives chemists the freedom to design new functional materials rather than sacrificial etch resistant polymers. For example, functional materials such as ferroelectric polymers and molecular magnets may be imprinted directly to form a layer in a chip with no need for pattern transfer [131,132]. The successful implementation of a functional imprint material would result in significant cost reductions and increased throughput by eliminating many chip fabrication processing steps.

For our research and applications, we have developed several different patterning techniques, including an epitaxial patterning technique for making polycrystalline and epitaxial magnetic nanostructures on single crystal substrates, focusing primarily on nanoimprint lithography, as will be discussed below.

### *4.1 Epitaxial patterning via nanoimprint lithography*

#### *4.1.1 General nanoimprint process*

In the general NIL process, the substrate, such as a Si wafer, is first cleaned in a Barrel etcher using oxygen plasma. This treatment cleans the organic dirt off the wafer and makes the surface hydrophilic.

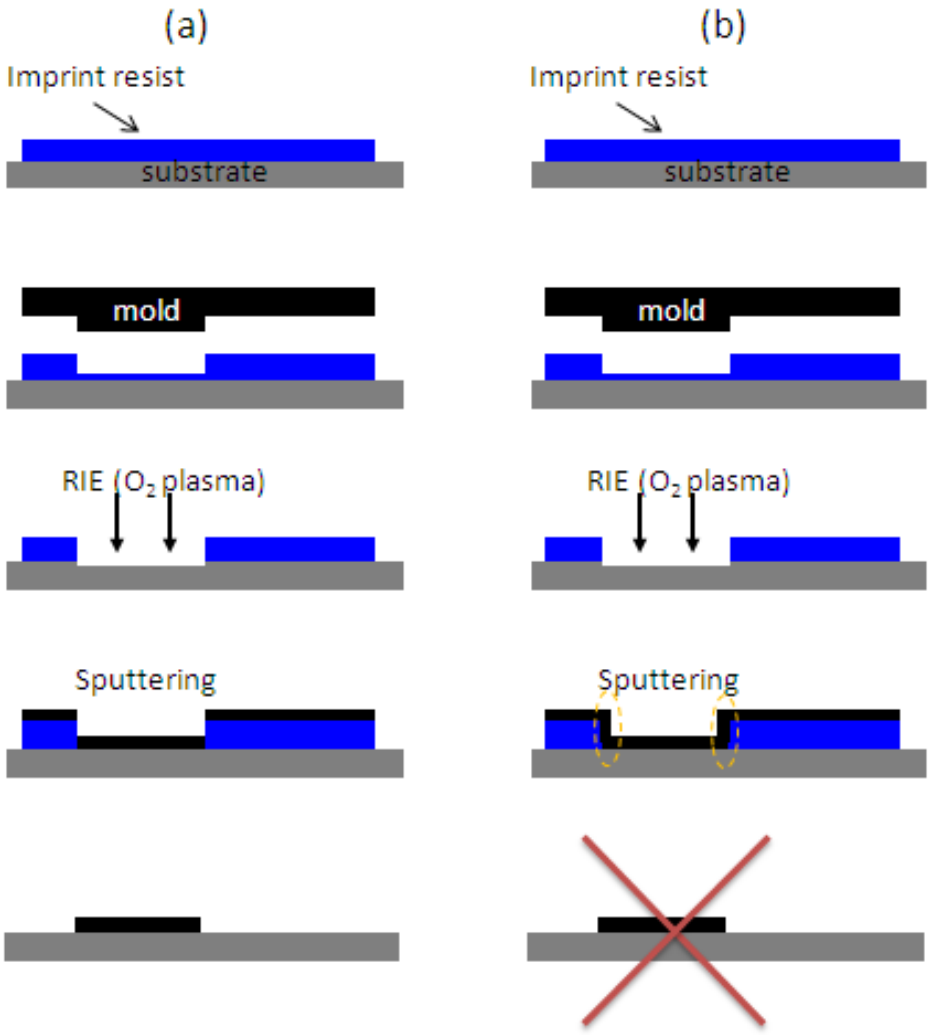


Figure 4.2: (a) NIL process for fabrication of metal nanostructures (ideal case). (b) In real processing, the metal deposited along the resist sidewalls may prevent a good lift-off.

Next, any visible dust particles are blown off using a nitrogen gun before covering the substrate in the resist. The substrate is coated in the imprint resist (NXR series) by using a spinner, creating a layer ~ 100 nm thick. The thickness is determined by the spinning speed and is verified with the Profilometer by simple scratching tests. Next, a hard stamp, made from Si or quartz, with nanostructures previously patterned on the surface, is carefully placed on top of the coated wafer and then the stack is sent to the thermal nanoimprinter (Nanonex NXB-100) for processing. The imprinting process and all the imprinting

recipes developed for this thesis are summarized in Appendix 2 and 3. After imprinting, the stamp and substrate continue to stick to each other, requiring the use of a razor blade to separate them by tickling the side (demolding). The demolding step should be done very carefully so as to avoid any damage to the expensive stamp.

*4.1.2 Bilayer nanoimprint process*

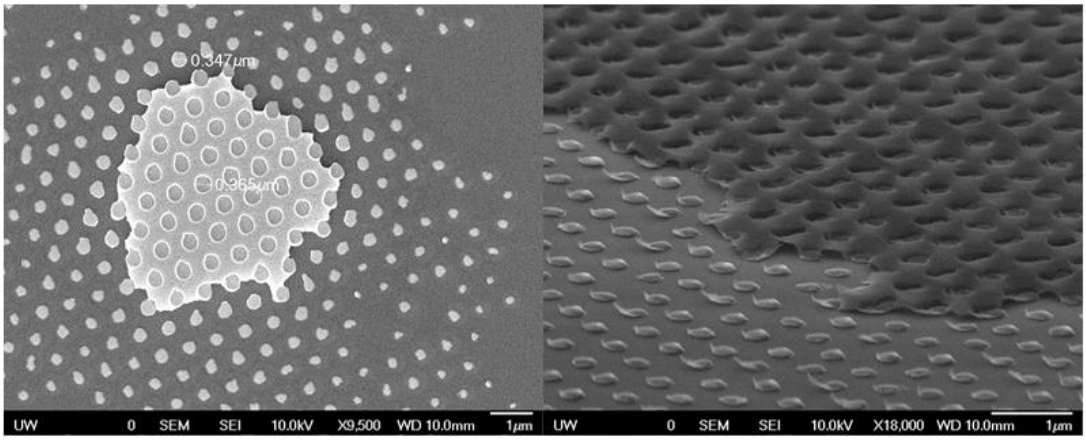


Figure 4.3: Scanning electron microcopy images showing the examples of incomplete lift-off results, caused by the sidewall depositions.

As a patterned resist is not the desired final product, a 'deposition-liftoff' process follows, converting the resist patterns to magnetic patterns. Normally, the patterned substrate first goes through a reactive ion etching (RIE) process, removing a specific amount of the resist and expose the patterned area on the substrate. Magnetic materials are then evaporated or deposited in vacuum onto the resist template and finally the substrate is ultrasonicated in a selective etchant to remove the resist, leaving only magnetic patterns on the substrate. The whole process, including the NIL, is illustrated in Fig. 4.2(a). Experimentally, we found that the metal deposited on top of the resist structures as well as the sidewalls. The latter usually prevented a good lift-off, as illustrated by Fig. 4.2(b), and also indicated by SEM

images as shown in Fig. 4.3.

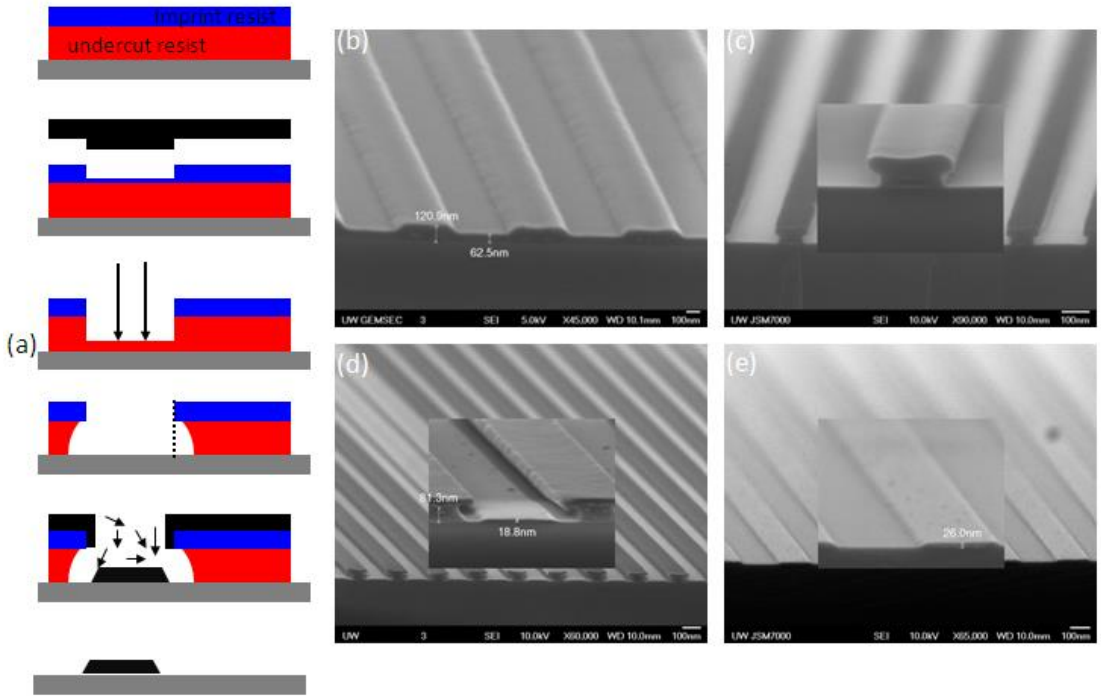


Figure 4.4: (a) Illustration of the bi-layer resist NIL process and SEM images of (a) as-imprinted wafer, in which the pattern is created only on the imprint resist by NIL; (b) undercut profile, obtained after RIE and a selective wet-etching of the under resist; (c) magnetic materials are subsequently deposited on the pattern template; note that the trenches exist for lift-off; (d) good lift-off, and subsequently high quality magnetic nanostructures on the substrate.

In order to achieve good lift-off and high-quality patterning, we developed a bilayer-resist process. An additional undercut resist layer is added before the imprint resist layer, followed by the normal imprint process. During the RIE etching step, we choose to etch not only the first layer residue but also certain amount of the second layer. Then, we use a selective etchant to etch only the second layer under a controlled manner so that an 'undercut' profile can be created. Due to this undercut, after the metallization, there are trenches (along the side of the resist) for the etchant to travel through, creating a cleaner liftoff, resulting in high quality metal patterns. Illustration of the process and related SEM images are indicated in Fig. 4.4, in which the fabrication of nanowire arrays was used as an example. Under the same recipe,

we also fabricated nanodot arrays, as indicated in Fig. 4.5.

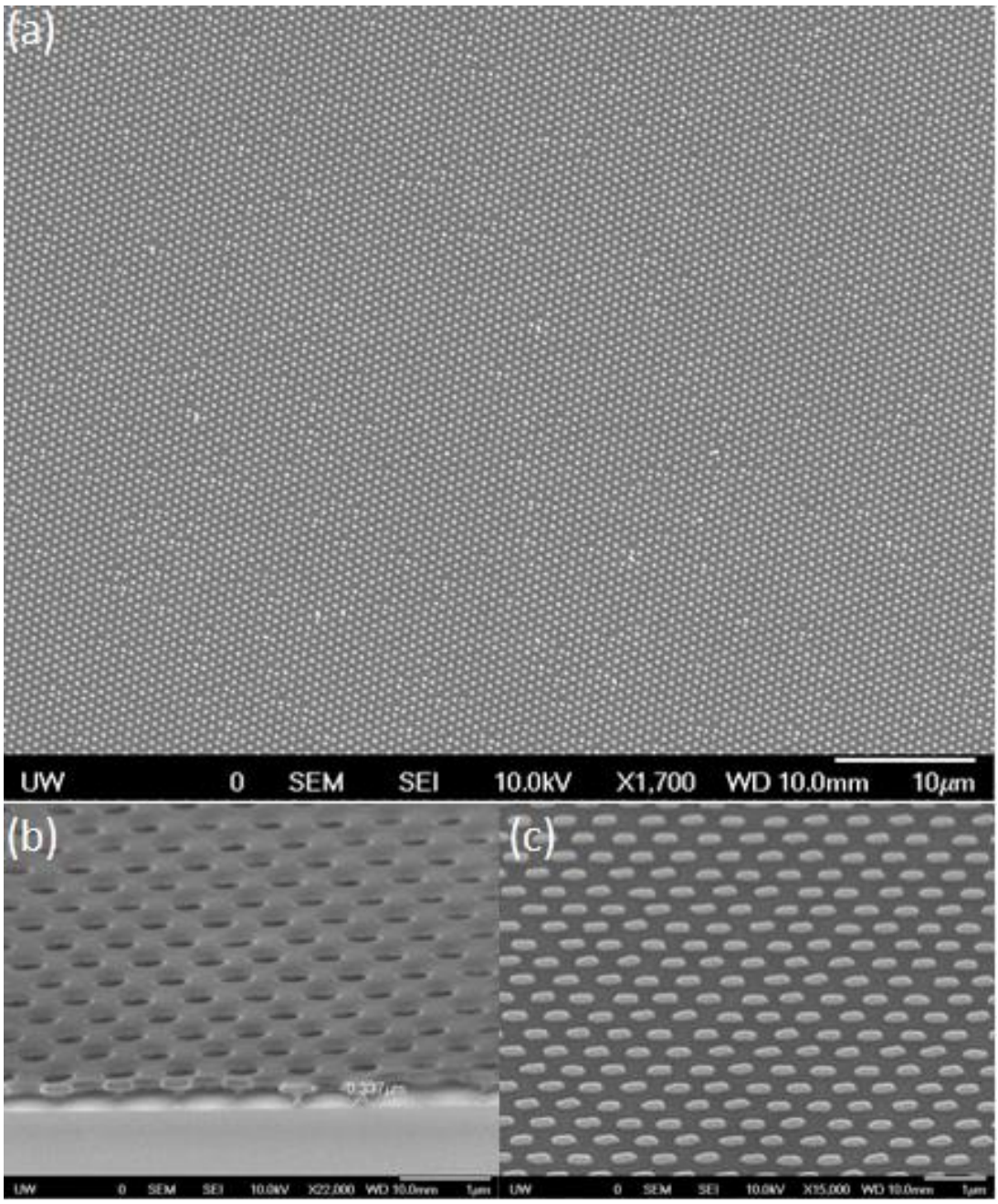


Figure 4.5: SEM images showing the (a) large area homogenous array of nanodots are fabricated using NIL, (b) undercut resist profile using the bilayer recipe for improving the lift-off, and (c) high quality nanodots with well-defined shape and clean edges.

*4.1.3 Mask-transferred nanoimprint process for epitaxial patterning*

The process introduced above is good for patterning polycrystalline magnetic thin-films. With the same or similar process, polycrystalline magnetic nanostructures have been fabricated and their properties have been studied. Interested readers are referred to several good review articles for more information [133-136]. However, patterned structures from epitaxial, single-crystalline films make it possible to study more technologically important properties, not easily accessible in their polycrystalline counterparts, such as magnetocrystalline anisotropy, magneto-elastic coupling, and surface/interface spin structures [137,138,139]. Particularly, it allows us to study the competing anisotropies (including shape anisotropy) and their effect on the magnetic reversal, which are directly relevant to this thesis. As a result, a reliable epitaxial patterning process is quite necessary. However, direct fabrication of such patterned elements over sufficiently large areas is not straightforward. Conventional method using ion-milling/etching of the

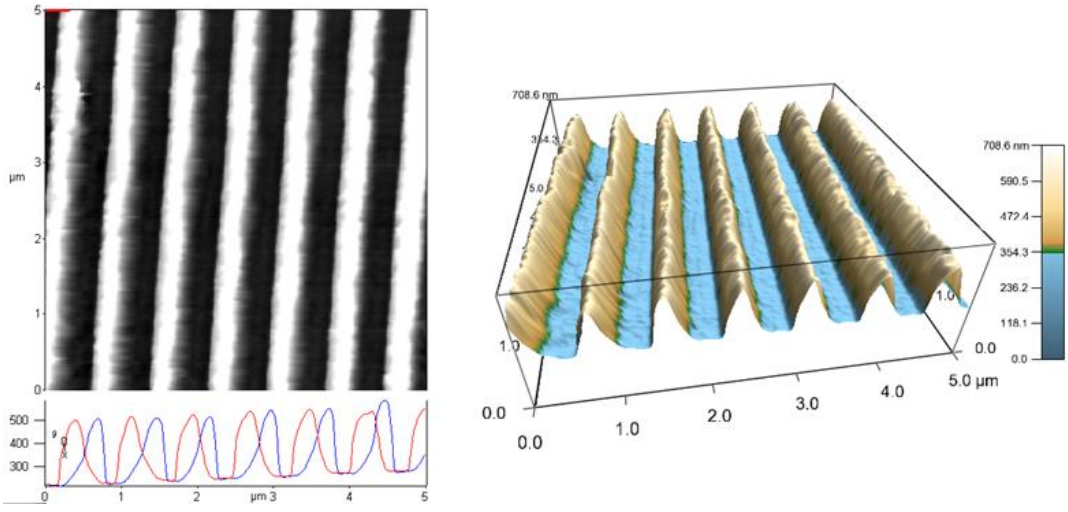


Figure 4.6: AFM 2D and 3D images showing the topography of a ETFE soft stamp with nanowire features, as replicated from a Si master stamp. The traces of the AFM line-scan along descending and ascending steps are indicated below the 2D image.

pre-deposited metal films (under lithography mask) brings significant side-effects due to the undesirable Ar-ion injection [140,141]. In this thesis, we have developed a new epitaxial patterning process using nanoimprint lithography that eliminates all sub-sequent metal-etching steps in the conventional methods.

*Defect-free nanoimprint*

Epitaxial magnetic structures are more sensitive to defects than polycrystalline samples. In lithography processes, induced shape defects act as local nucleation centers for magnetic domains and as pinning centers for domain wall movements. In order to investigate the intrinsic magnetization behaviors in epitaxial samples, high-quality, defect-free patterning is desired. Nevertheless, the conventional imprinting process uses Si or quartz stamps, which typically induce a significant numbers of unfavorable defects in the form of pinholes (on micro- to milli-meter scale), to the as-imprinted wafer. To solve this issue, we developed a recipe for imprinting using a soft plastic stamp material, ethylene tetrafluoroethylene (ETFE) [142,143]. An ETFE stamp can be fabricated via direct embossing with a Si master stamp, Fig. 4.6. The ETFE stamp is transparent, flexible, and homogeneous, as indicated by the photograph, Fig. 4.7(a). The use of the ETFE stamps makes it possible for large-area fabrication of homogeneous magnetic nanostructures. As a comparison, we first demonstrated the imprinting result by a traditional Si stamp. As shown in Fig. 4.7(b), even tiny defects in between the stamp and wafer will lead to a visibly large unimprintable area, because of the rigidness of both wafer and stamp. As a result, unpredictable but significant defects in the form of pinholes and thin strips were observed. These defects will be transferred to the final sample, following deposition and lift-off. Additionally, the defects get more

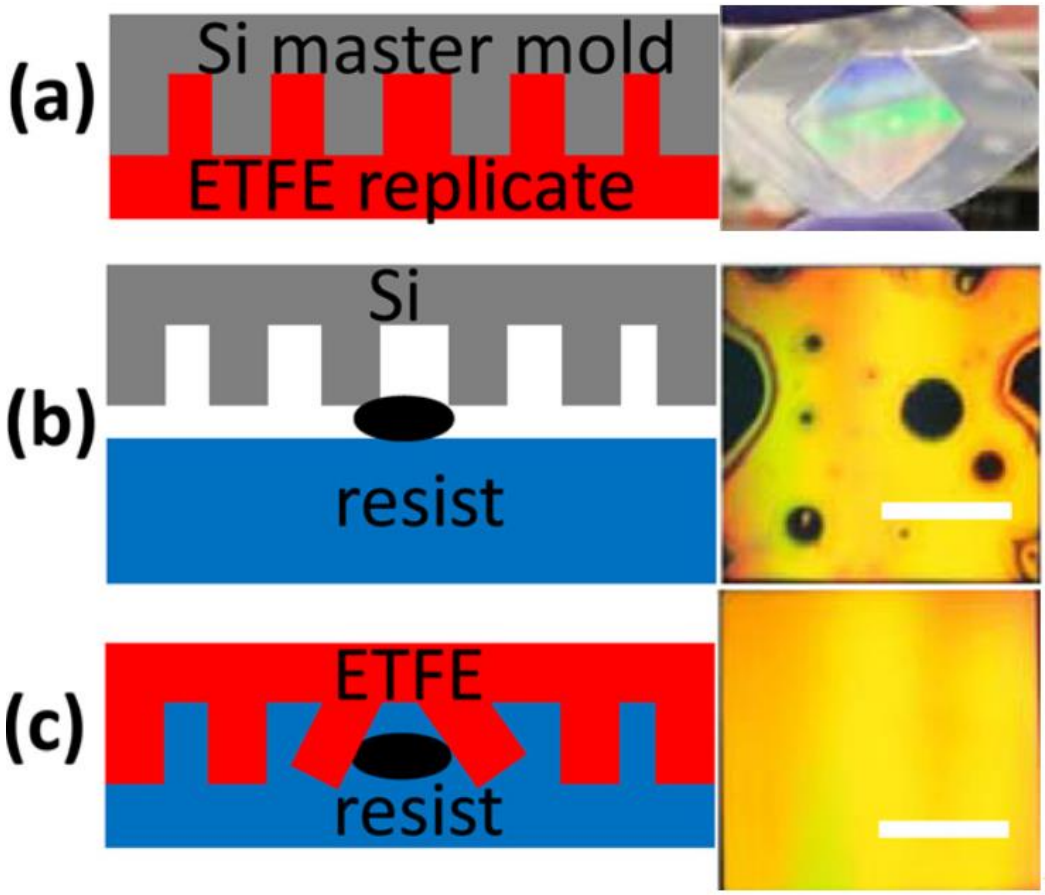


Figure 4.7: (a) Flexible ETFE replica fabricated by a Si master stamp; (b) wafer imprint with a Si stamp; (c) wafer imprint with ETFE stamp (scale bar: 5 mm).

substantial with time as the stamp is used again and again. These disadvantages limit the scalability of the stamping process. However, when using the flexible ETFE soft stamp, local defects are tolerated. After imprinting, the flexibility of the ETFE stamp makes the demolding process easier. Defect-free imprints can be achieved on the whole stamp area (Fig. 4.7(c)), ideal for epitaxial patterning purposes.

*Mask-transferred nanoimprint*

Conventional nanoimprint (or in a more general sense, all lithography techniques) is not built for

direct patterning of epitaxial films, because the polymeric resists are not compatible with the high temperatures required for the substrate cleaning and film growth. Instead, using a metallic, high-temperature-sustainable mask material, such as Molybdenum, this issue can be avoided [144]. Therefore, we developed a mask-transferred nanoimprint process with an additional step: converting the resist template to Mo metallic mask before subsequent deposition and lift-off. Furthermore, our process takes into consideration the appropriate lateral profile (undercut) of the metallic mask, making it possible for high-quality patterning of epitaxial magnetic materials.

Figure 4.8(a)–(f) shows a schematic of our process for obtaining a Mo mask with the right undercut profile, and the subsequent clean lift-off for epitaxial film structures. A bilayer of polymeric undercut resist and thermal imprint resist is thermally imprinted with an appropriate stamp. A brief anisotropic de-scum etch step removes the residue of the imprint resist and a certain amount of the undercut resist, figure 4.8(a). The undercut resist is then wet etched appropriately to develop a wedge-shaped resist profile. Since the wet-etch proceeds in a nearly isotropic manner, the etched resist profile therefore can be approximated by a circle, with the center located at the start point of the etch, figure 4.8(b). The following attributes are crucial for the success of our process, which is totally controllable by this two-step etch procedure: the start point of the wet-etch must be close to the top surface of the undercut resist layer and the radius of the circle defining the etching front, determined by the etch time, must be almost equal to the distance between the etch start point and the substrate. These are the key factors to obtain the wedge-shaped profiles. The Mo layer is then deposited, figure 4.8(c), followed by the polymer-resist lift-off. The wedge shaped resist produces an undercut profile of the Mo mask, figure 4.8(d). Epitaxial material is then deposited at high temperature onto the Mo template, figure 4.8(e), followed by the Mo

lift-off in the $H_2O_2$ solution, to complete the process. Due to the Mo undercut, very clean lift-off can be obtained and high quality epitaxial patterned structures can be produced.

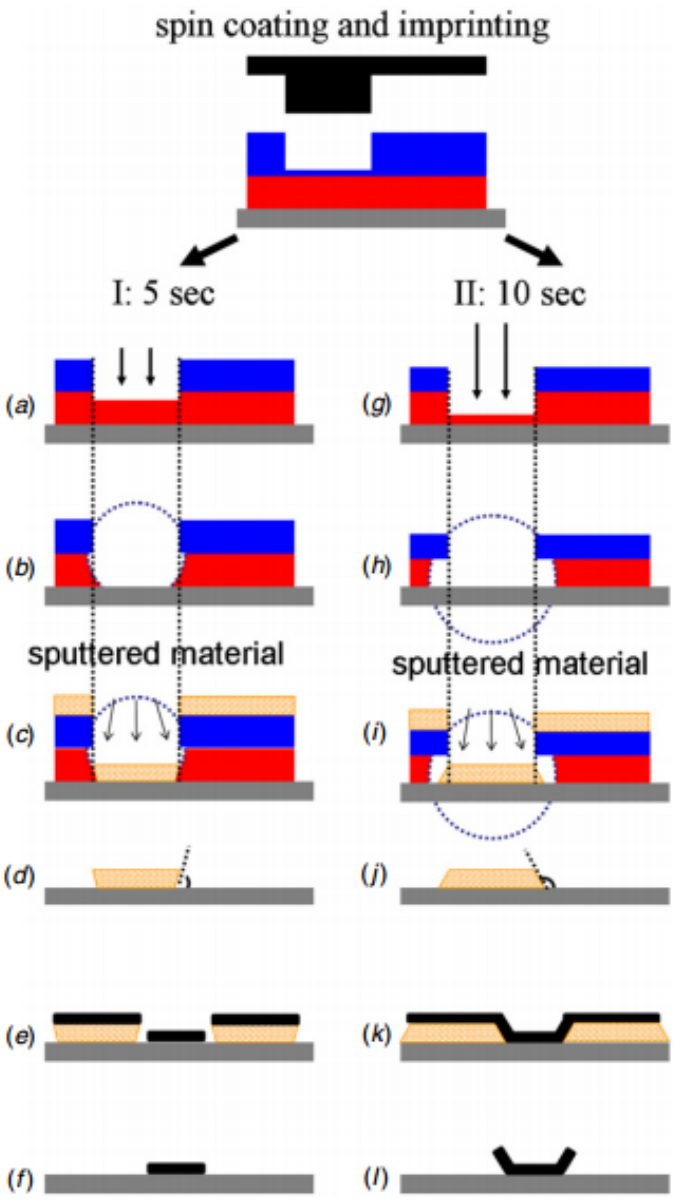


Figure 4.8: Illustration of our NIL process for epitaxial magnetic patterning with a short dry-etch step (a)–(f) and a conventional process with a longer dry-etch step (g-l). The circles in (b) and (h) show the edge of isotropic removal of the polymeric sacrificial resist layer during developing. Blue: thermal imprint resist; red: polymeric undercut resist; orange: Mo hard mask; black: magnetic multilayer film; gray: substrate.

The duration of the de-scum etch step in Fig. 4.8(a) is the key to obtain the desired wedge-shaped polymer resist profile. We demonstrate this in Fig. 4.8(g)-(l) for a de-scum etch duration increased by a

factor 2. This process creates a conventional undercut in the polymer bilayers; however, it does not create the desired undercut in the Mo mask. The process described by Suzuki *et al* [144], which uses an even longer anisotropic de-scum etch to remove the entire undercut resist layer underneath the imprinted area, is similar to this process. In brief, the start point of the wet-etch is moved downward, deep into the undercut resist layer by the longer anisotropic de-scum etch. After the wet-etch, as revealed by the circle, a conventional bilayer resist undercut is created, Fig. 4.8(h). Subsequently, the Mo layer is deposited (Fig. 4.8(i)), followed by the resist liftoff to complete the mask transfer (Fig. 4.8(j)). Epitaxial material is then deposited at high temperature onto the Mo template (Fig. 4.8(k)) and the Mo layer is finally removed in the $H_2O_2$ solution. Since the Mo mask does not have an undercut profile, the liftoff process often requires brief ultrasonication [144]. As a consequence, only very thin epitaxial films, usually less than 50 nm, can be deposited without the creation of rough edges in the patterned structures, as illustrated in Fig. 4.8(l).

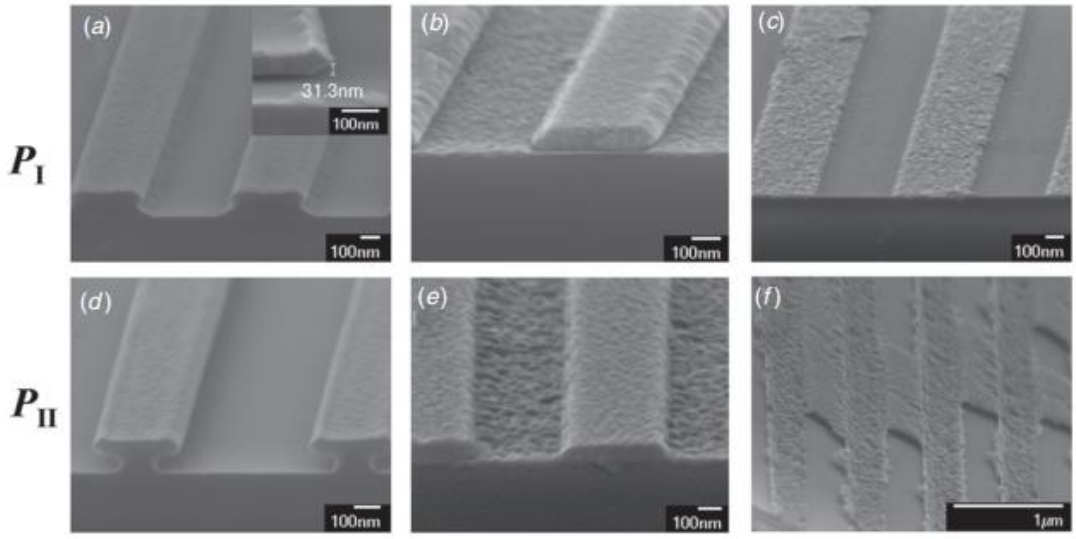


Figure 4.9: SEM images showing our NIL process on sample $P_I$ with (a) wedge-shaped polymer bilayer, inset: Mo mask with undercut; (b) magnetic materials deposited onto the Mo mask with undercut, and (c) successful lift-off; and the conventional NIL process on sample $P_{II}$ with (d) polymer undercut profile; (e) magnetic materials deposited onto the Mo mask without undercut, and (f) poor liftoff.

To explore the effects of the dry etch time on the undercut profile, two samples were created and etched for 5 and 10 s, creating samples $P_I$ and $P_{II}$, respectively (Fig. 4.9). Under SEM analysis, $P_{\mathrm{I}}$ exhibited the wedge-shaped polymer-resist profile (Fig. 4.9(a)), while $P_{\mathrm{II}}$ displayed a conventional undercut, as seen in Fig. 4.9(d). The different resist profiles significantly affected the cross sectional profiles of the deposited Mo structures. In this case, only sample $P_I$ gave the desired undercut profile (Fig 4.9(a), inset). Due to this undercut profile, the magnetic material deposited on top of the Mo mask does not connect with those at the bottom, allowing for cleaner liftoff and resulting in high-quality metallic wires (Fig. 4.9(b) and (c)). For sample $P_{\mathrm{II}}$ without the Mo undercut profile, the magnetic materials formed a continuous layer on the Mo masks, as shown in Fig. 4.9(e). The following liftoff is less efficient than with the $P_I$ style undercut. The sample requires ultrasonication but may still leave Mo residue and non-continuous metallic wires on the substrate. When using single crystialline MgO as a substrate, the same wedge-shaped resist patterns can be created, resulting in defect-free nanowires with the $P_I$ undercut style (Fig. 4.10).

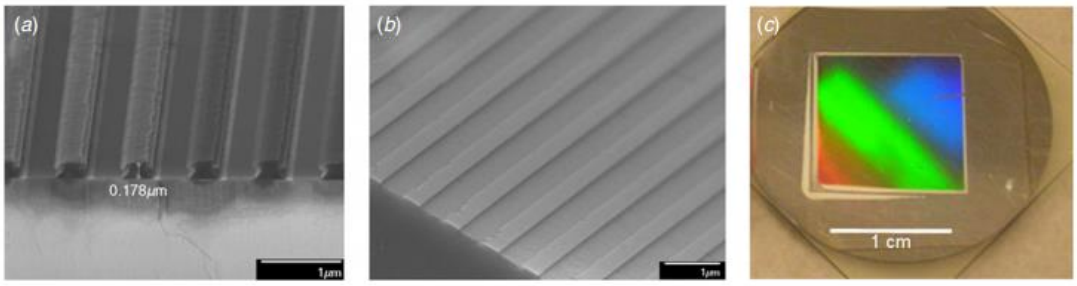


Figure 4.10: (a) Wedge-shaped polymer bilayer resist on the MgO substrate; (b) high resolution epitaxial wire arrays on MgO and (c) photographic picture of large area imprinted polymer wire arrays (after Mo deposition).

Also of interest are epitaxial nanodot arrays created through the same resist method. To create these epitaxial nanodot arrays, the Mo mask must have holes, which come from pillars in the resist template.

For effective liftoff, these bilayer resist pillars must also be wedge shaped (Fig. 4.11(a)). The pillars are not as robust as the wires, and subsequently, many disappear after imprinting with a Si hard stamp. By using an ETFE soft stamp, one can robustly create large areas of pillar arrays (Fig. 4.11(b)). Figure 4.11(b) and (c) contain SEM images of the pillars before and after Mo deposition, while Fig. 4.11(d) displays the Mo mask in anti-dot (hole) arrays after the resist lift-off.

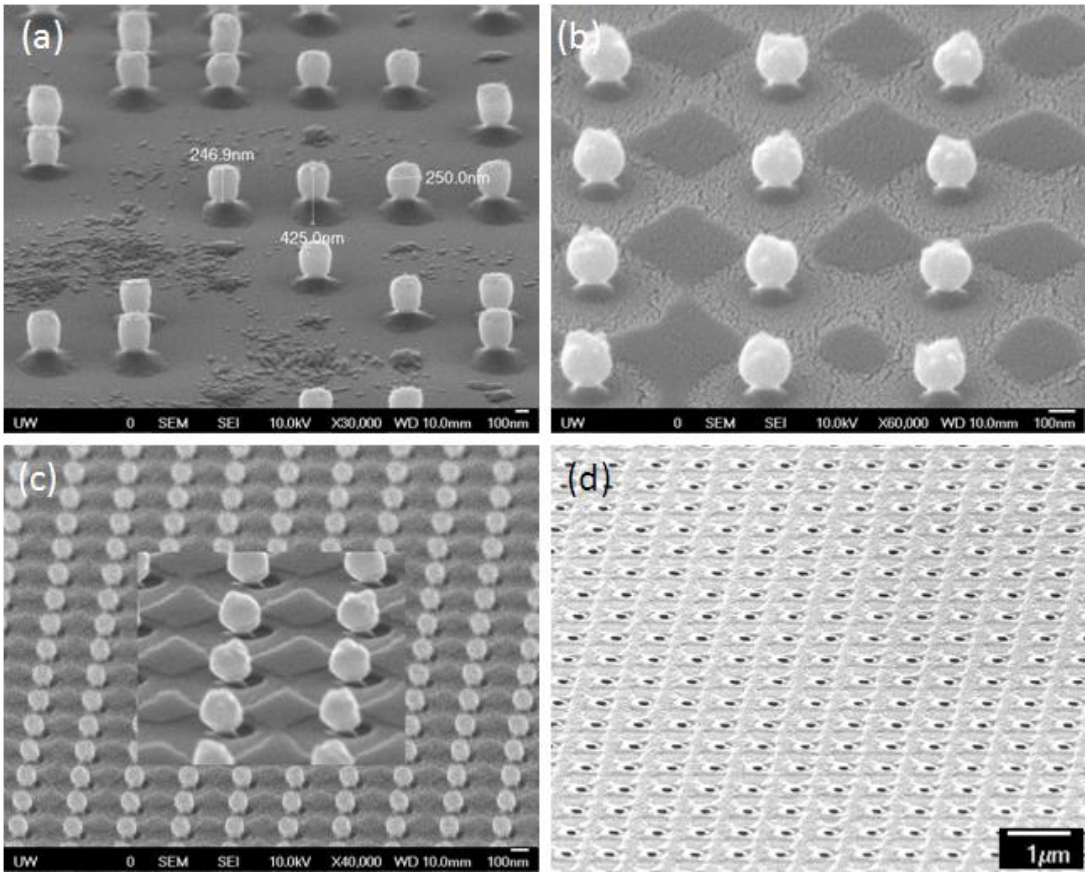


Figure 4.11: (a) Bilayer resist pillars with the wedge-shaped profile created by Si stamp, after relevant etching and development. (b) Large area resist pillars can be obtained when using ETFE stamp. (c) Mo layer deposited on the resist pillars. (d) Resist lift-off. Mo mask in hole arrays is left on the substrate.

The patterned nanostructures underwent XRD analysis to confirm the epitaxial structure. Figure 4.12 contains the XRD $\theta$–$2\theta$ scan, Φ–scan, and the rocking curve for an epitaxial Fe nanowire (300 nm) arrays on MgO substrate. In the $\theta$–$2\theta$ scan, the observation of a single Fe(002) peak indicated a good

out-of-plane (002) texture. The in-plane Φ-scan showed the four distinct peaks of Fe and MgO, as well as a 45° rotation of the Fe lattice with respect to that of the MgO, which are consistent with their epitaxial relationship. The rocking curve indicated a lattice misalignment of less than 2° along the film normal orientation. These results confirmed the epitaxy nature of the Fe nanowires. Figure 4.13 displays the *θ–2θ* scan for *c*- and *a*-axis Fe/MnPd bilayer nanowire (300 nm) arrays on MgO substrates. The different normal orientations were confirmed by the corresponding XRD peaks.

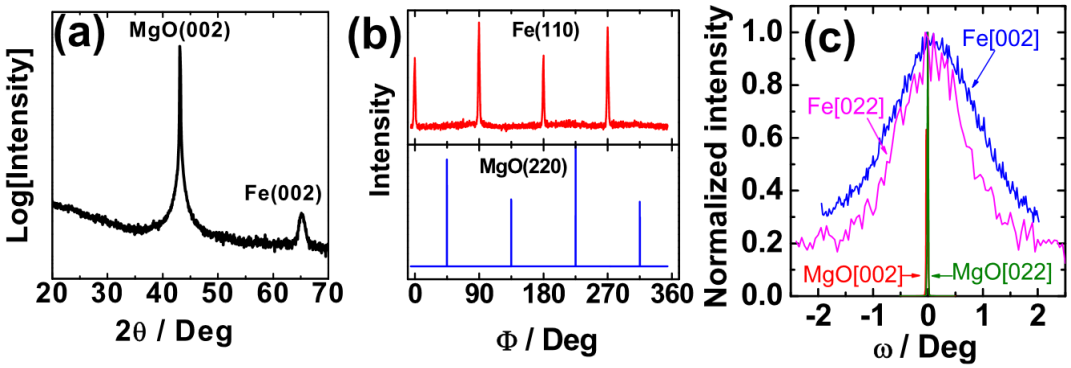


Figure 4.12: XRD characterizations for an epitaxial Fe nanowire (300 nm) arrays on MgO substrate. (a) *θ–2θ* scan indicating the (002) texture along the normal direction; (b) Φ–scan showing the 45° rotation of the in-plane lattice (epitaxy); and (c) rocking curve showing the small, ~ 2°, misalignment of the surface grains.

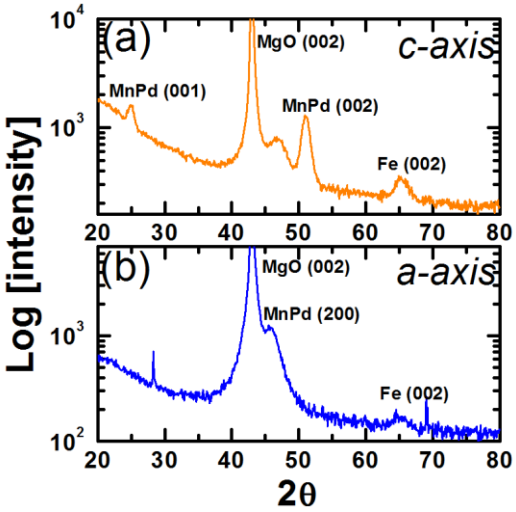


Figure 4.13: XRD *θ–2θ* scans of *c*-axis and *a*-axis Fe/MnPd bilayer metallic wire (300 nm) arrays on MgO substrates.

*4.1.4 Lithographic nanoparticles and release*

We have also explored utilizing nanoimprint lithography to efficiently fabricate free-standing 0D nanodots. Synthetic nanoparticles with possible magnetic, optical or bio-functional properties have been widely exploited in various biological and biomedical applications such as magnetic resonance imaging, magnetic particle imaging and drug delivery [145]. These nanoparticles are frequently fabricated by 'bottom-up' chemical routes, enabling mass production, but lacking precise and independent control of the particle shape, size, structure, and composition. In contrast, direct fabrication of synthetic nanoparticles by 'top-down' physical routes is a promising alternative approach. For example, Hu *et al* recently developed a novel approach using nanoimprint lithography, lift-off, and release to fabricate water-stable multifunctional magnetic nanoparticles [146]. These synthetic antiferromagnetic (SAF) nanoparticles (NPs) have a number of advantages, including high moment, monodisperse size, and zero remanence over a wide range of nanoparticle size - from tens of nanometers to micrometers. However, there are still several critical limitations associated with the original fabrication and release procedures, including functionalization and transferring to aqueous solution. First, due to the large size and low solubility of the SAFs, particle functionalization after release in water results in poor coatings. Coating before release (on-wafer) is easier and more desirable as in our process. Second, conventional NIL release methods use a sacrificial layer, either metal or polymer, that requires wet etching of such sacrificial layer and transferring product (SAFs) from the etchant to water. This makes it impossible to functionally coat the NPs before release, as the etchant, typically a caustic (pH~12) ammonia-$CuSO_4$ solution [146], will destroy any biological coatings (DNA, protein, etc). Additionally, the deposition and ion-milling of a Ta

protection layer, with the long deposition cycles, unstable ion milling rates, and possible release failure makes the process more complicated and unsuitable for functionalized NP fabrication.

To overcome these limitations associated with conventional imprinting fabrication, we have developed an improved process that avoids the need for a sacrificial layer. We fabricated disc-shaped SAF nanoparticles with a diameter of ~300 nm directly on Si wafer and released them via a dry etching procedure to avoid the previously described issues associated with the sacrificial layer [147]. While this thesis has not sought to functionally coat the particles, the new processing technique can potentially enable robust and facile coating before particle release, as the nanoparticles are released directly to water without any etchant transfer. Using an ETFE stamp (replicated from a master Si stamp) and the bilayer

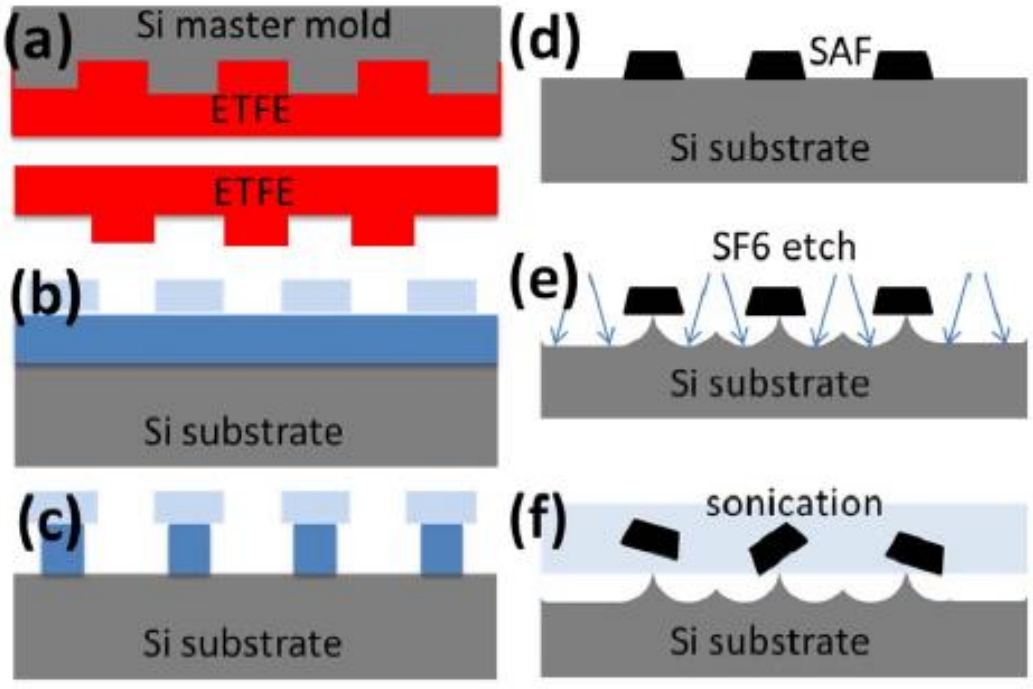


Figure 4.14: Fabrication steps for the preparation of SAF arrays and nanoparticles. (a) ETFE stamp is replicated from a master Si stamp, (b) bilayer resist is spin coated and the top layer is imprinted, (c) undercut profile is property developed by wet etching, (d) SAF particles are deposited, followed by the resist stripping, (e) Si substrate is etched so that the SAFs are barely attached on Si, (f) SAFs are released, by ultrasonicating the Si chip in solution.

resist lift-off, defect-free imprints and high-quality nanoparticles were created over the whole stamp size (> $1 \times 1$ cm$^2$). The ETFE replicas can be continuously fabricated from a single Si stamp and one ETFE stamp lasts for more than twenty imprints. Accordingly, the lifetime of the Si master stamp is significantly increased. As a process demonstration, we have fabricated high moment Fe/Ta multilayer SAF nanoparticles. Metallic Fe was chosen for its high saturation magnetization and lower toxicity, compared to other magnetic metals such as Co and Ni.

Figure 4.14 illustrates the complete fabrication procedure. The first step is fabrication of the ETFE stamp from the Si master stamp, Fig.4.14(a). A sheet of ETFE (DuPont 'Tefzel') is cleaned by sonication in acetone and then isopropyl alcohol (IPA) for 5 min in each, blow-dried, and placed onto a clean Si wafer. The Si master stamp (350 nm holes in a hexagonal lattice, from Lightsmyth Technologies) is placed onto the ETFE sheet and then embossed using a Nanonex NX-B100 compact thermal nanoimprinter at 250°C and 450 psi for 1 min. Next, the bilayer resist, made of an undercut resist LOR 1A (MicroChem) and an imprint resist NXR-1025 (Nanonex), is spin-coated on to a Si wafer. The coated wafer is then thermally imprinted by the ETFE stamp as demonstrated in Fig. 4.14(b). Demolding is easily achieved by peeling off the ETFE sheet. This process can be scaled to produce a flexible ETFE stamp (~350 nm pillars in a hexagonal lattice) with a usable area equal to that of the master Si stamp. The imprinted sample is then etched with anisotropic oxygen-plasma reactive ion etching to remove the imprint resist residue, followed by a selective wet-etch on LOR 1A to develop an undercut profile (Fig. 4.14(c)). Fe/Ta multilayers are deposited on to the patterned resist template via the ion-beam sputtering system, creating a stack of $Ta_{10nm}/(Fe(t_{Fe})/Ta_{0.6nm})_x/Fe(t_{Fe})/Ta_{10nm}$. The resist is stripped after the multilayers are deposited (Fig. 4.14(d)). To create a series of samples for measurement, we fabricated

samples with different Fe thickness, $t_{Fe}$ and repeat cycle, *x*, of the $(Fe/Ta)_x$ multilayer. At this point in the fabrication process, the disc-shaped SAF nanoparticles remain attached to the substrate (Fig. 4.14(d)). Next, we etch the substrate by anisotropic $SF_6$+$O_2$ mixed gas plasma RIE, which has a high etch selectivity to Si. This etches the Si substrate into patterned cone-shaped structures with one SAF nanoparticle loosely attached on each cone (Fig. 4.14(e)) via the Van der Waals force. The SAF nanoparticles are finally released from the substrate by centrifuging the chip in water (Fig. 4.14(f)). We followed the fabrication process via SEM and figure 4.15 contains those images.

Figure 4.15(a) contains a SEM profile of the bilayer resist on a Si substrate after the ETFE imprinting and undercut development. Figure 4.15(b) shows the as-fabricated SAF on the Si substrate after metal deposition and resist lift-off. In this case, the diameter of the disc-shaped SAF is ~300 nm. As highlighted in Fig. 4.15(c-d), the anisotropic $SF_6$+$O_2$ mixed gas plasma RIE selectively etches the Si substrate into a cone, leaving behind the nanoparticles attached to the tip. We found that the ideal etch recipe for liftoff is 100 Watts for 30 s; however, over-etching with a slightly longer etch time (~50 s) will not affect the SAF nanoparticles. With centrifugation, the SAF particles are completely released from the original wafer (Fig. 4.15(e)) to solution (Fig. 4.15(f)). For a closer structural investigation, we analyzed the particles via TEM (Fig. 4.16). As expected, the diameter and thickness of the wedge-shaped nanoparticle are ~300 nm and ~50 nm, respectively. These images also indicate that the shape and dimension of a particle remains unchanged during processing. However, significant over-etching may damage the SAF nanoparticles and we are currently completing a detailed study concerning this aspect of fabrication.

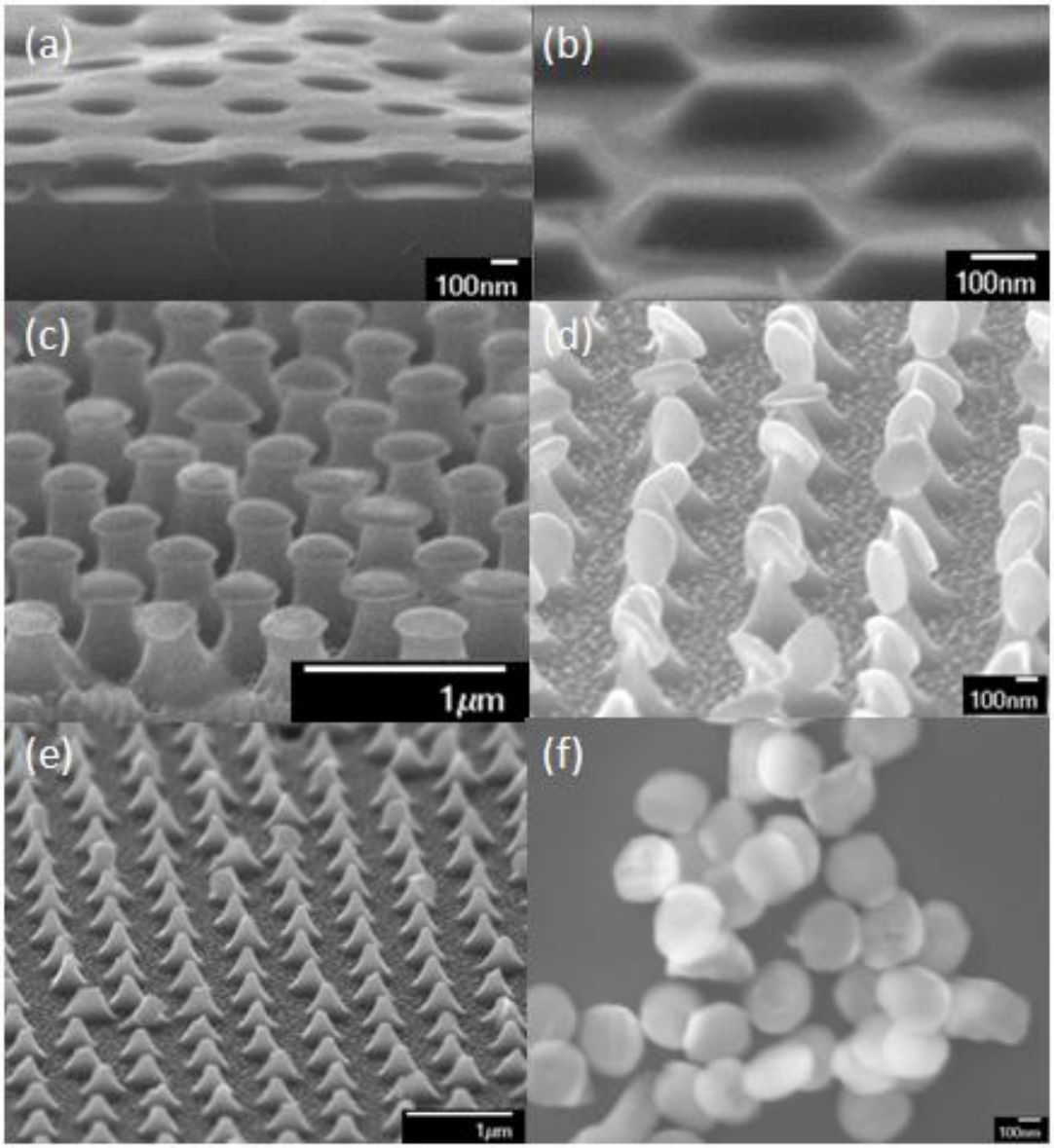


Figure 4.15: SEM images showing the steps of SAF fabrication.

For magnetic properties, we chose Fe/Ta multilayered SAF to demonstrate this fabrication process. A series of samples in the sequence of $Ta_{10nm}$/ $[Fe(t_{Fe})/Ta_{0.6nm}]_x$/ $Fe(t_{Fe})$/ $Ta_{10nm}$ were deposited by ion-beam sputtering with a deposition rate of less than 1Å/s, where *x* indicates the number of layer repeats. In these SAFs, there are even numbers of ferromagnetic layers therefore the magnetizations can cancel out in the absence of an external field [146,147]. The hysteresis loop of the as-fabricated SAF with $t_{Fe}$ = 5 nm and

different $x$ = 3,5,7 are shown in Fig. 4.17. The particle's behavior resembles a 'superparamagnetic' style with low remenance and coercivity. The number of repeats, $x$, leaves the majority of the loop unchanged, but slightly affects the behavior in the low field region, as demonstrated in Fig. 4.17. Specifically, as $x$ increases, the loop is slightly more difficult to reach saturation. This is likely due to the fact that there are more possible arrangements of the F layers for samples with higher $x$, therefore, it is harder to polarize all the F layers towards the external field direction. We also studied the magnetic properties of the SAFs after releasing in solution. As an example, we lifted off selectively the nanoparticles with $x$ = 5 and measured the hysteresis loop in water, as shown in Fig. 4.17(b). The saturation field is slightly increased as compared with the on-wafer loop (Fig. 4.17(a)). Since the particles are relatively free in solution, it is reasonable to see that a higher external field needs to be applied in order to polarize all of the NPs along the external field direction.

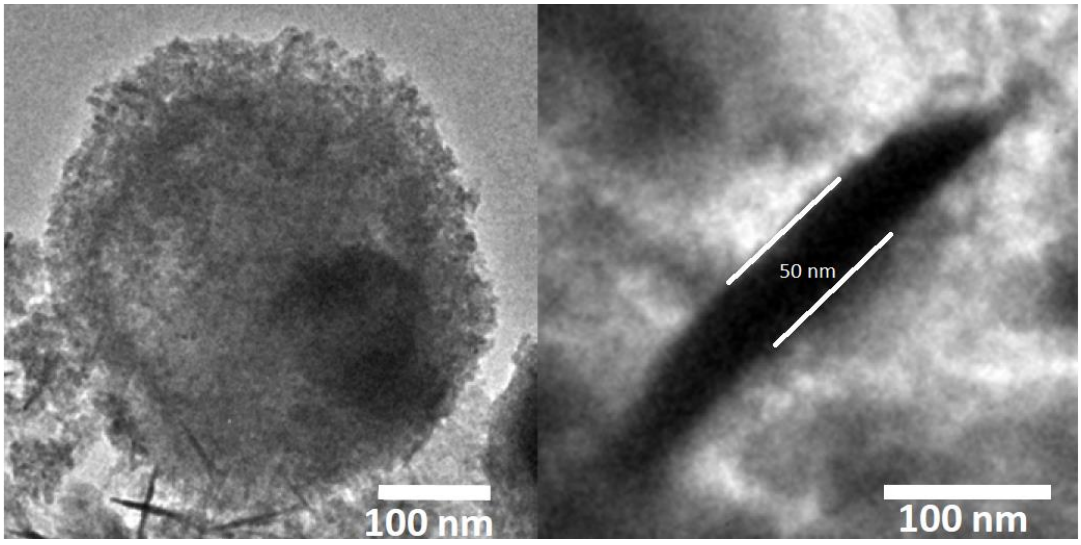


Figure 4.16: TEM images of the SAF after release in water (scale bar: 100 nm). The diameter and thickness of the wedge-shaped nanoparticle are ~300 nm and ~50 nm, indicating that the shape and dimension of the particle remains unchanged during processing.

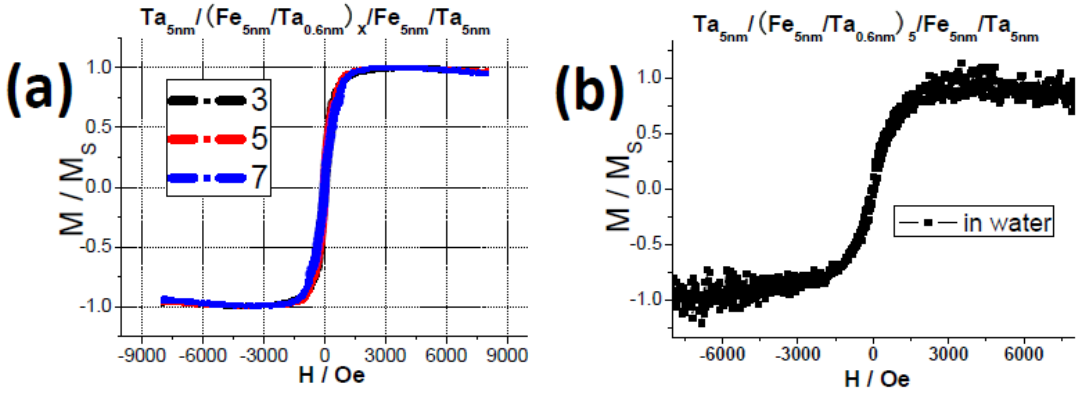


Figure 4.17: (a) Hysteresis loops of the SAF measured on wafer with different x = 3,5,7 ; (b) In-water hysteresis loop measured after release and centrifugation for nanoparticles with x = 5.

*4.1.5 Sub-100 nm nanoimprint process for magnetic patterning*

The above NIL processes (4.1.1-4.1.4), as they have been demonstrated, work well for mesoscale magnetic patterning. However, there are a number of important issues to be considered when scaling the process down to sub-100 nm according to our experiment. In this section, we describe the sub-100 nm NIL process independently.

*Master stamp fabrication*

In nanoimprint, a master stamp is the base of all subsequent processes. Commercial stamps with sub-100 nm features are usually quite expensive and the prices can go even higher for customized features. For lab research purposes, an alternative solution is to make such customized stamps by e-beam lithography using possible available resources such as public micro-fabrication user facilities (e.g. MFF and NTUF at UW). The steps of making a customized stamp using e-beam lithography are illustrated in

Fig. 4.18.

We have made a customized stamp using the e-beam writer at UW with an array of 30 nm × 90 nm hole pattern on a Si wafer (2 mm × 10 mm stamp area). The SEM image of the stamp is illustrated in Fig. 4.19. The motivation of fabricating such a stamp and the relevant application in magnetism will be discussed in the next chapter.

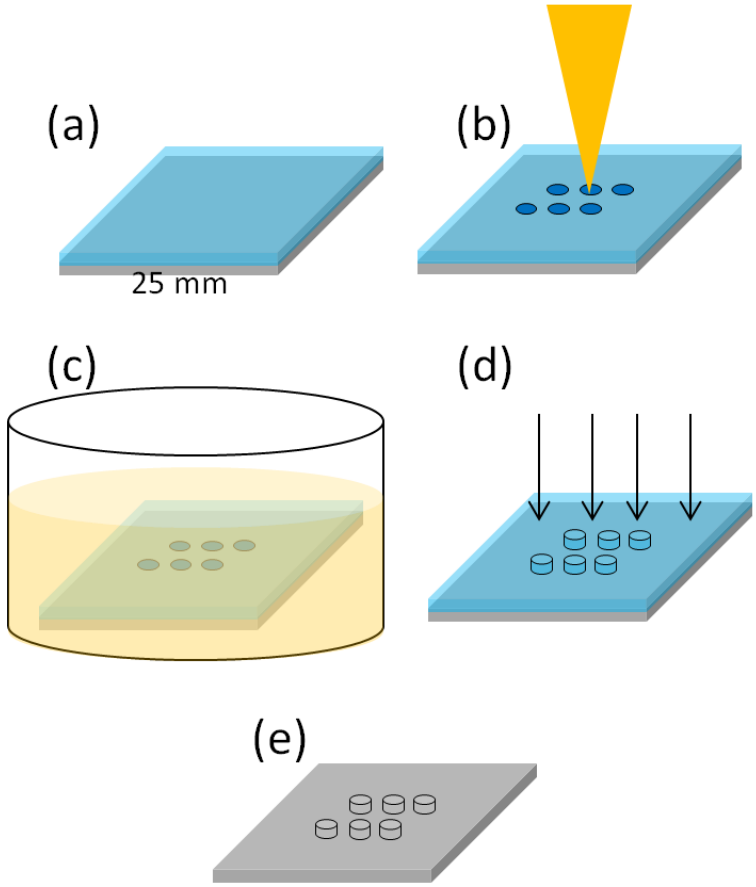


Figure 4.18: Process of making a NIL stamp. (a) spin-coating a 25 mm square piece of silicon wafer with a 60 nm thick film of resist, ZEP-520A (Nippon-Zeon Corporation). (b) The pattern was then exposed into the resist by direct-write electron beam lithography, using a JEOL JBX-6300FS e-beam lithography system (JEOL Ltd). The pattern of 30 × 90 nm rectangles was written using nanolithography mode, 100 kV, 500 pA electron beam, a placement grid of 2 nm, and a dose of 280 μC/cm$^2$. (c) The exposed resist was developed by immersion in n-amyl acetate for 45 seconds, then rinsed in isopropyl alcohol for 15 seconds, then dried with nitrogen. (d) The exposed pattern was transferred into the silicon wafer using inductively-coupled (ICP) etching in an Oxford PlasmaLab 100 system (Oxford Instruments, PLC), using sulfur hexafluoride and octafluorocyclobutane gasses. (e) Remaining resist was removed using an oxygen plasma.

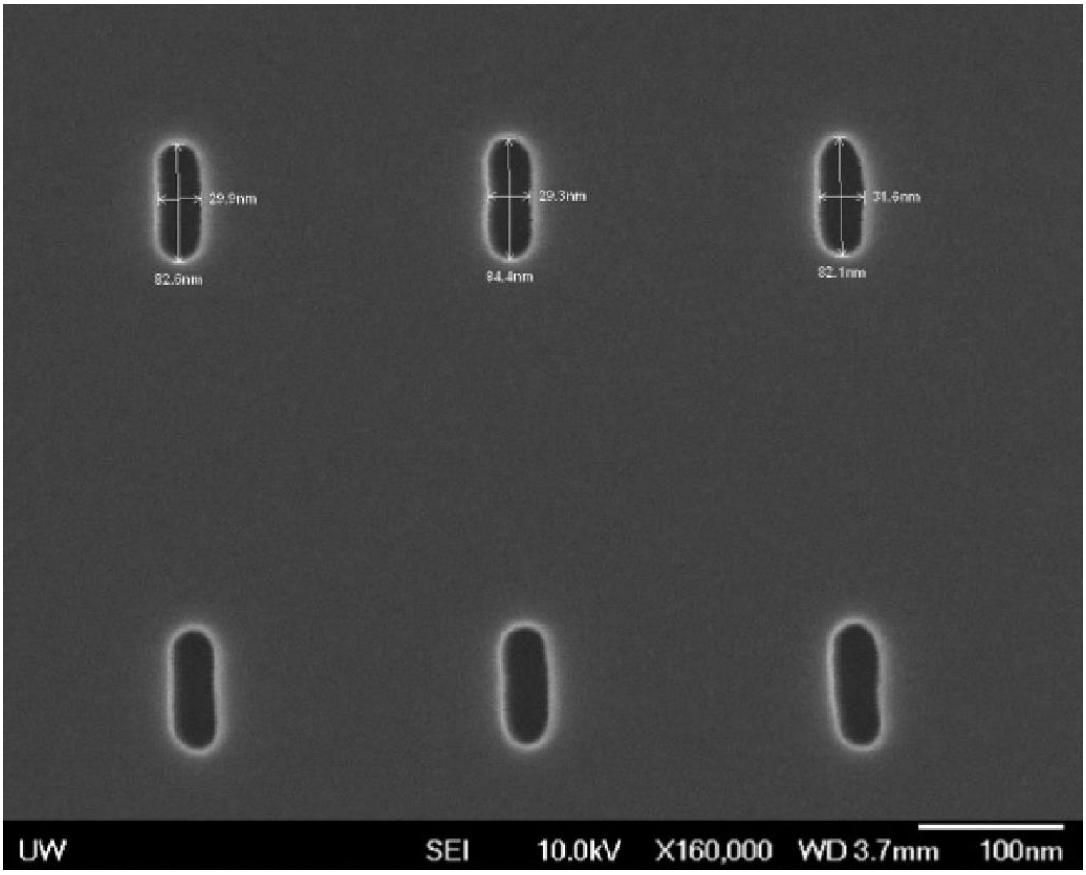


Figure 4.19: SEM image of our customized NIL stamp, consisting an array of 30 nm × 90 nm hole pattern on a Si chip (2 mm × 10 mm feature area).

*Ormostamp process*

At elevated temperatures, ETFE will crystallize into needle-like grains approximately 30 nm in length [143,148]. While not significant on the mesoscale range, the crystallized grains affect sub-100 nm particles created from an ETFE stamp as the ETFE will not faithfully replicate a Si master stamp with such small feature sizes. In order to make flexible copies of the imprinting stamps in this sub-100 nm size range, we chose to use a different polymer, commercial stamp material called Ormostamp, produced by Microresist Technology, GmbH.

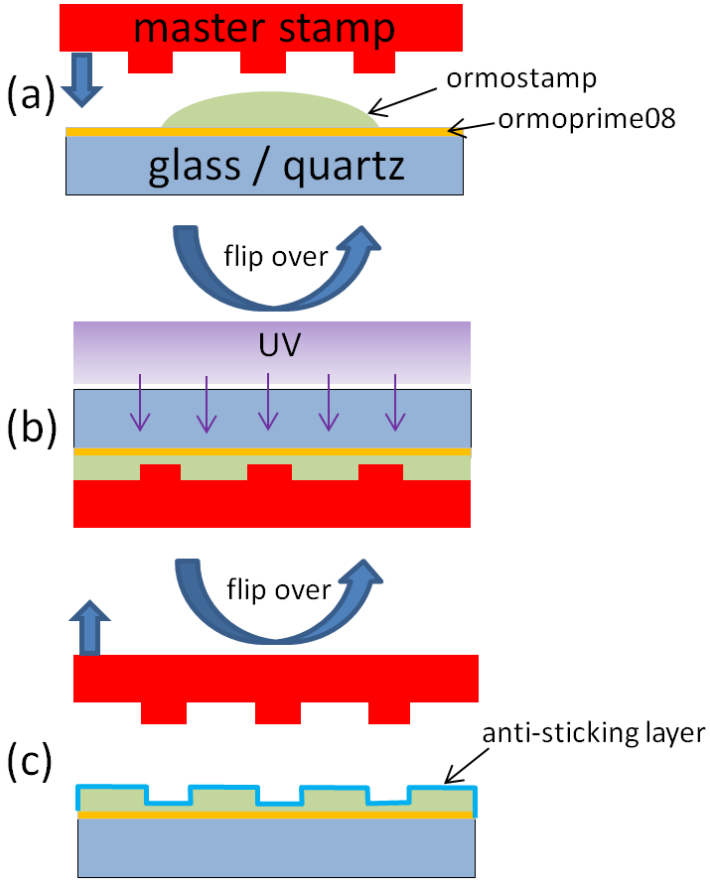


Figure 4.20: Illustration of the Ormostamp (working stamp) fabrication process. (a) stamp preparation: ormoprime08 is spin coated on substrate followed by the application of Ormostamp on top; (b) stamp curing: the sample stack is flipped over and cured under UV light; (c) stamp separation: the master stamp is carefully separated with the Ormostamp. Application of anti-sticking layer on the Ormostamp is required before use. [149]

The process to create an Ormostamp from a master stamp for general NIL purposes [149] is illustrated in Fig. 4.20. While the fabrication process is similar to creating an ETFE stamp, the process has been modified to accommodate the different stamp material. The master stamp is first cleaned with piranha for 1 hour and then barrel-etched with oxygen plasma at 150W and at 1 Torr for 5 min. Next, the release layer is coated by vacuum evaporation for 45 min, creating a hydrophobic surface. Separately, a small piece of substrate (Si, glass, or flexible PET) is cleaned in acetone and IPA with ultrasonication and dried in a stream of $N_2$. Barrel etch cleaning (hydrophilication) is also recommended, at 100W and 1Torr

for 2min. After cleaning, the substrate is spin coated with the primer 'Ormoprime08' (Microresist Technology, GmbH) at 3000 rpm for 60 s and post-baked on a hotplate at 150°C for 5min. The primer increases the adhesion between the substrate and the Ormostamp material.

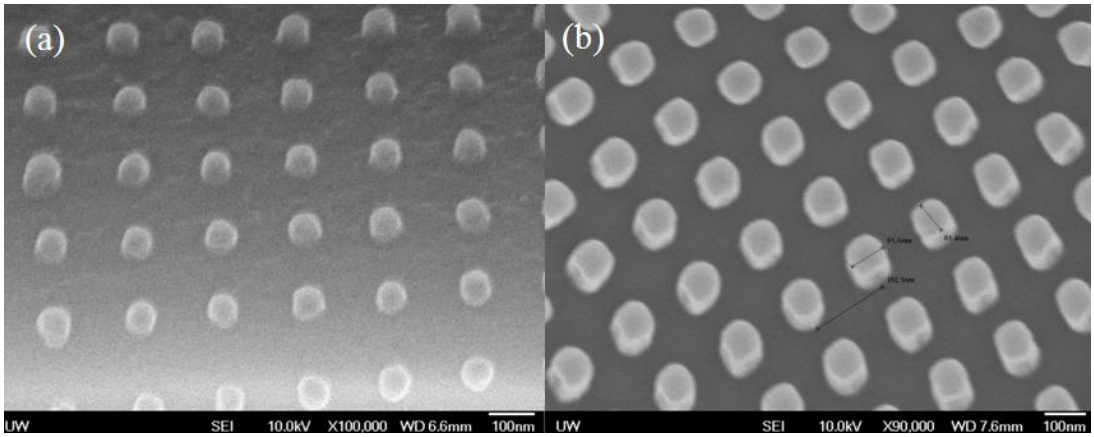


Figure 4.21: Ormostamp copies fabricated on (a) Si and (b) PET substrates. (scale bar: 100 nm)

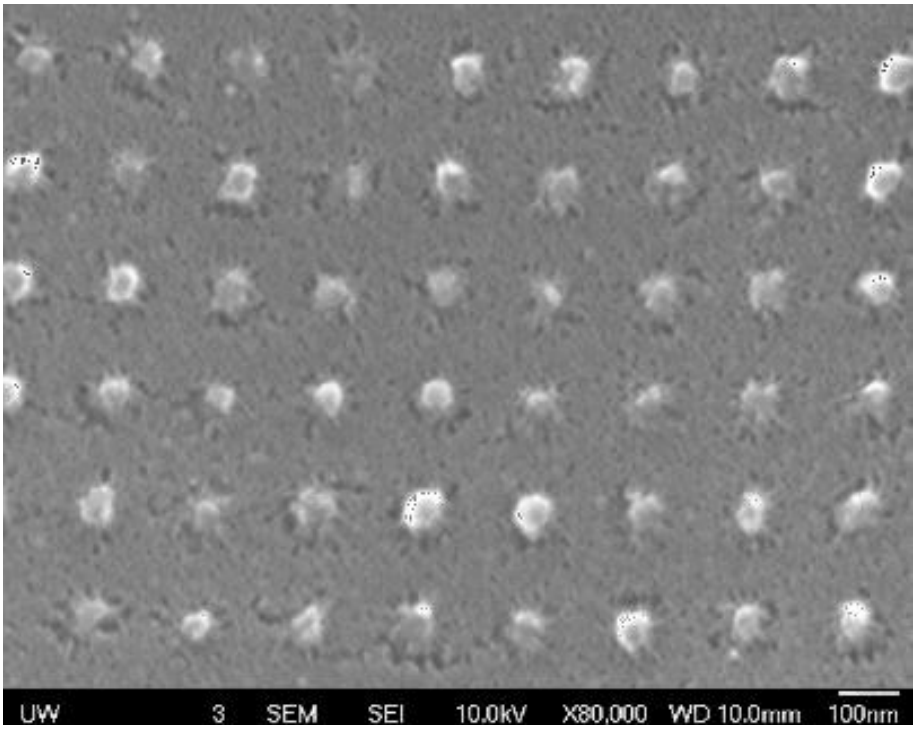


Figure 4.22: Ormostamp feature (pillars) on Si substrate after barrel etching with oxygen plasma (power used: 100W). (scale bar: 100 nm)

Following the primer application, a very small drop of gel-like Ormostamp is casted (dropped) on top of the substrate (Fig. 4.20(a)). The master stamp, with the feature side down, is pressed gently into the Ormostamp material until the master is immersed completely in Ormostamp. For optimal stamp fabrication, a soft bake at 100 $^{o}$C for 2 min is required to aid the Ormostamp flow around the master stamp. The Ormostamp material is then cured by UV light exposure. We used the Aligner with a light wavelength of 365 nm and for 2 min exposure time (Fig. 4.20(b)). Finally, the Ormostamp is baked on a hot plate at 150 °C for 10 min and then is carefully separated from the master with a razor blade. The final Ormostamp is imaged by SEM to check the quality of the replication (Fig. 4.21).

After release of the master stamp, the Ormostamp still needs an anti-stick coating before use in nanoimprint (Fig. 4.20(c)). To coat the stamp, the Ormostamp is treated under an oxygen-rich environment to active the surface (hydrophilication). This step ensures strong adhesion between the release layer and stamp surface. A UV ozone cleaning is recommended following surface activation, as it is a non-destructive process, or the stamp can be cleaned via barrel etching with oxygen plasma. However, we found that barrel etching will also etch the Ormostamp features on the substrate (Figure 4.22), and the feature size reduces with increasing etching power (Figure 4.23). In addition, the Ormostamp pillars become less robust as their dimension reduces. The imprints by Ormostamp etched at different intensities are shown in Fig. 4.23. The optimal etching power for obtaining efficient surface treatment is 25 W. If the stamp is not etched or is over-etched, the release layer will not be fabricated correctly, creating poor separation between the Ormostamp and the imprint resist during the de-molding process. These issues are illustrated in Fig. 4.24: either the resist peels off from its home wafer and sticks to the Ormostamp (Fig. 4.24(a)), or the Ormostamp detaches from its home wafer and sticks to the resist (Fig. 4.24(b)).

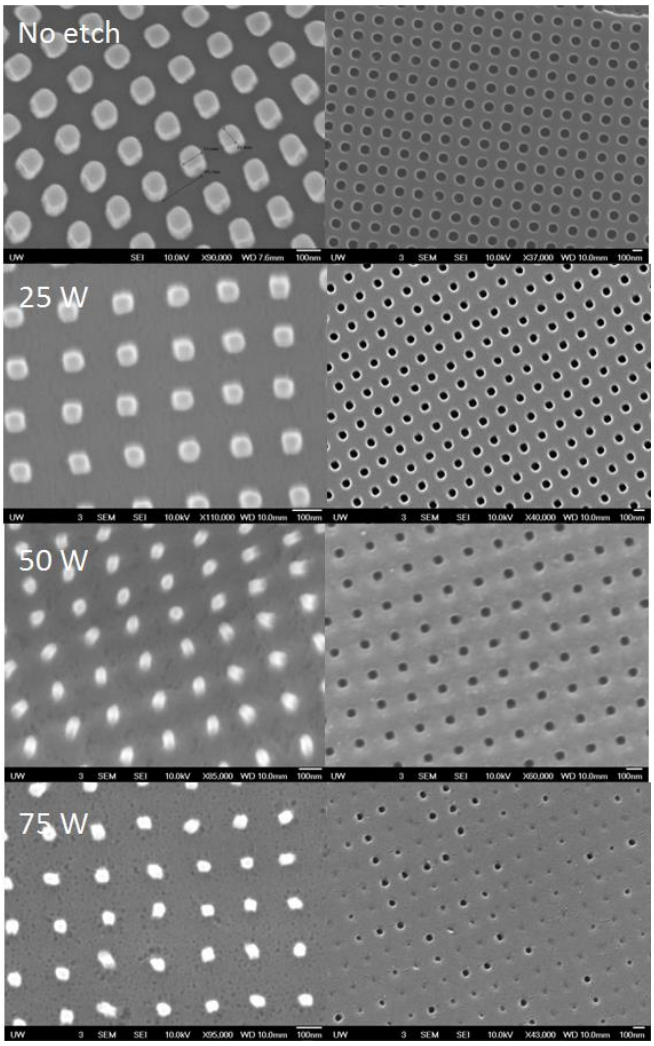


Figure 4.23: SEM images showing the etching effect of Ormostamp (pillar arrays) by oxygen plasma barrel etching (left column). Different powers are used for 1 min etching. The corresponding imprints (hole arrays) using the etched Ormostamp are indicated on the right column. (scale bar: 100 nm)

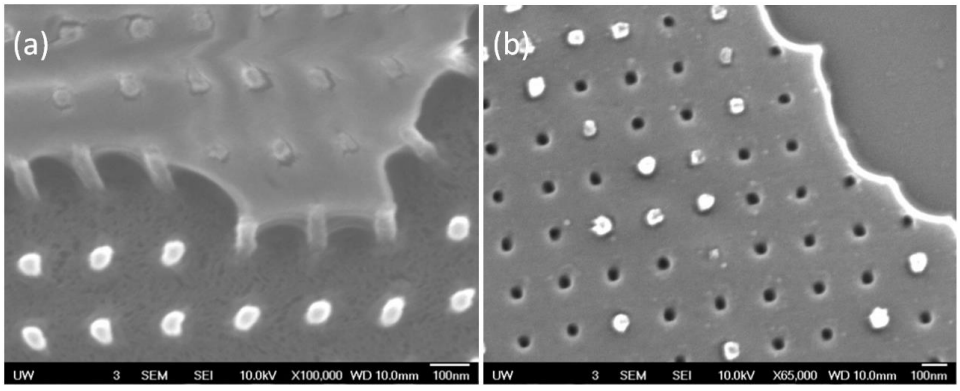


Figure 4.24: Effects due to poor release layer coating after de-molding. (a) Resist peels off and sticks to the Ormostamp features. (b) Ormostamp pillars detach from the stamp and stick to the resist. (scale bar : 100 nm)

*Nanoimprint with the Ormostamp*

With a successful release layer coating, the Ormostamp works as efficiently as the ETFE stamp in our bilayer-resist NIL process. Figure 4.25(a) shows the bilayer-resist undercut profile on Si wafer with sub-100 nm feature size imprinted with the Ormostamp (pillars). Here, the top, imprint resist is mr-I7010R from Microresist Technology, GmbH, which is a specifically-designed resist for sub-100 nm nanoimprint. The bottom undercut resist is the conventionally-used LOR 1A from MicroChem Corp. Such bilayer-resist enables the fabrication of high resolution sub-100 nm magnetic nanostructures (Figure 4.25(b)), and in the form of large-area arrays (Figure 4.26).

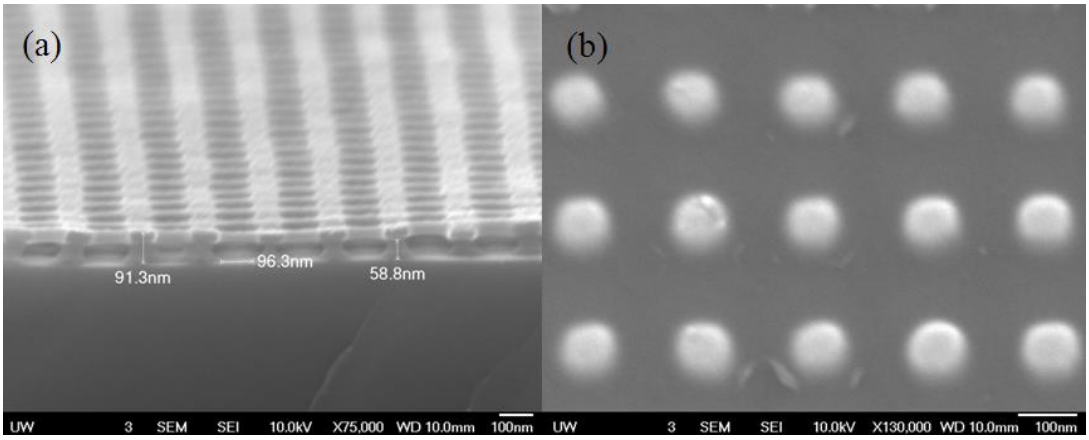


Figure 4.25: (a) Bilayer-resist profile on Si wafer. (b) High resolution sub-100 nm Fe/IrMn bilayer magnetic nanodot arrays. (scale bar: 100 nm)

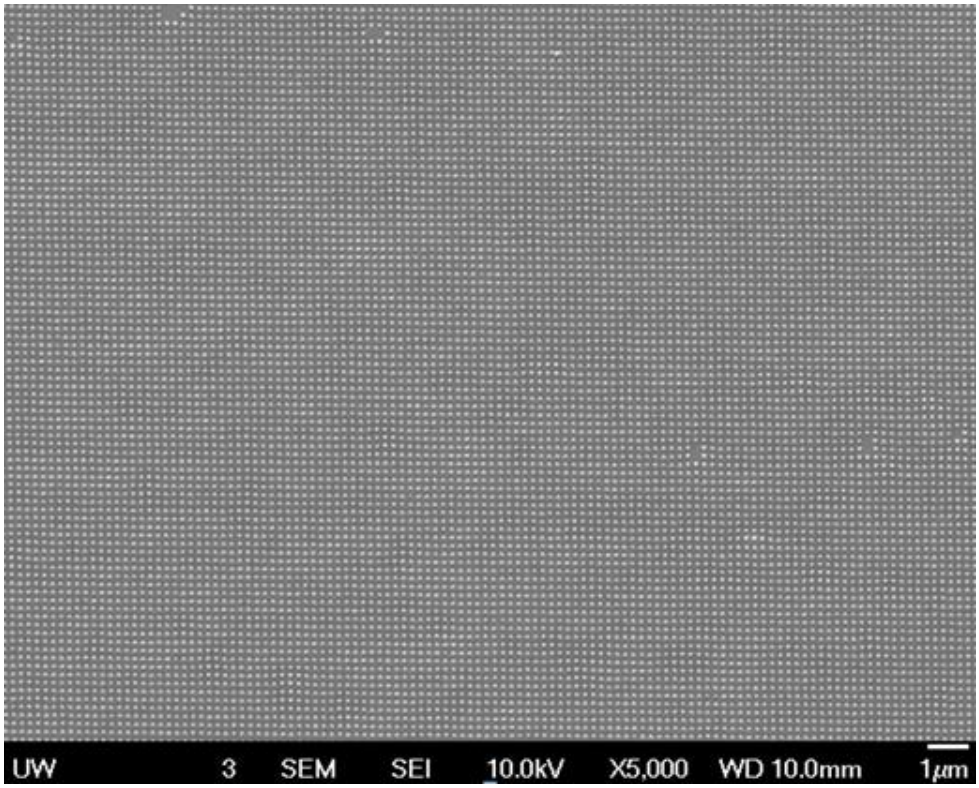


Figure 4.26: SEM image showing the large-area sub-100 nm Fe/IrMn bilayer magnetic nanodot arrays. (scale bar: 1 μm)

*4.1.6 Effect of nanofabrication process on the nanostructures*

*Poor contact of stamp and substrate*

During the imprint process, the stamp and the coated wafer must remain in close contact to ensure that the resist completely fills in the stamp trenches and copies the nanostructure features. If the contact is loose, the imprinted wafer does not adopt the features from the stamp and the imprints fails, as illustrated in Fig. 4.27. Bad contact is caused by a variety of sources, including low imprint pressure, low imprint temperature, defects (e.g. dust particles) between the stamp and resist, insufficient imprinting time, resist

sticking on stamp, and thin imprint resist thickness.

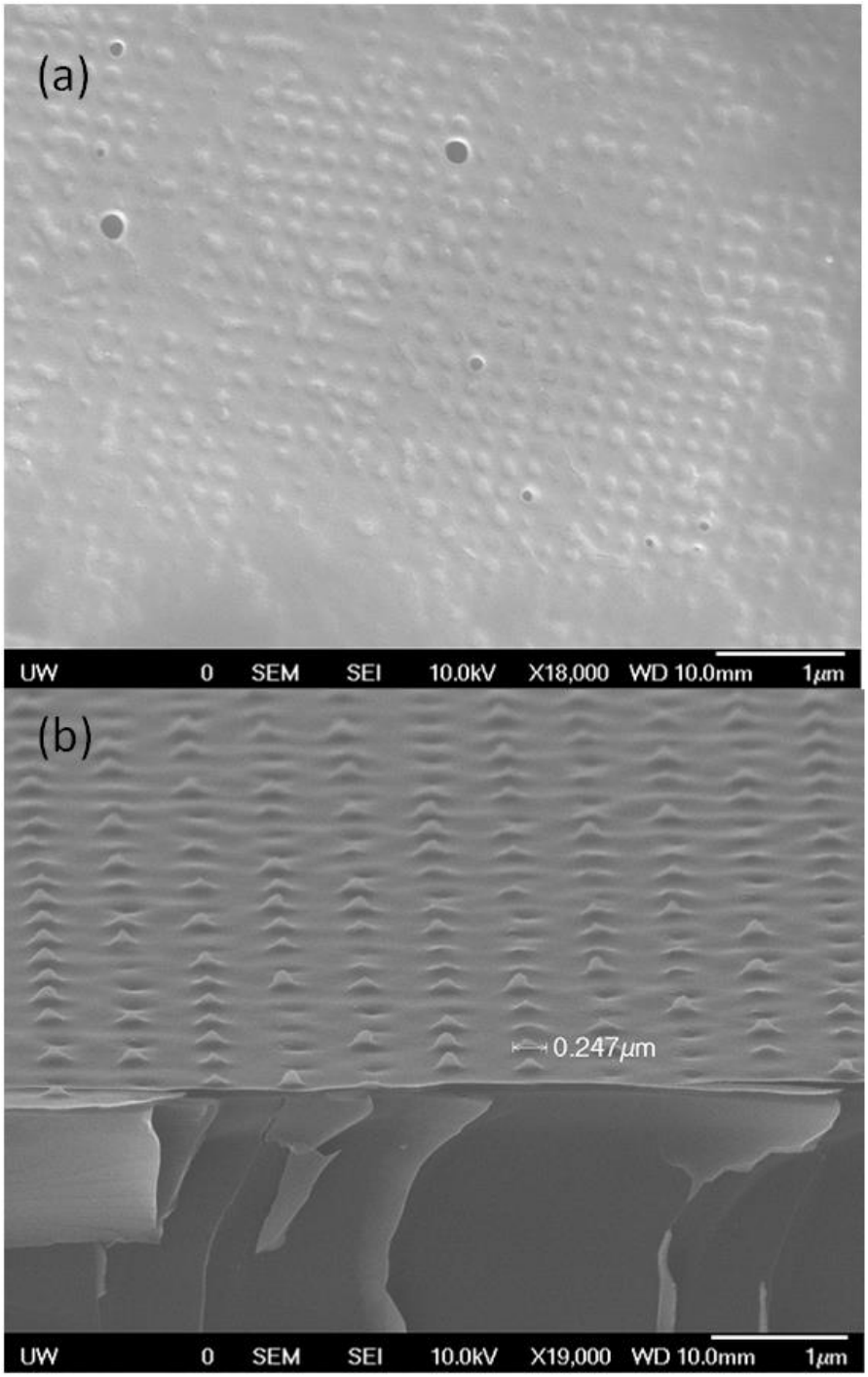


Figure 4.27: SEM (a) planar and (b) cross-section images showing the imperfect resist pillars on the substrates, as caused by bad contact between resist layer and stamp. . (scale bar: 1 μm)

*Insufficient reactive ion etching*

The aim of reactive ion etching is to remove the residue of the imprint resist (under the imprinted area) and a portion of undercut resist so that the desired lateral profile can be obtained. As discussed above, a longer etching time results in normal undercut profile while a shorter etching lead to the wedge shaped profile. Although a shorter etching profile is required in epitaxial patterning, the time must be long enough to remove the first imprint layer residue. The problem with a very short etching time is illustrated in Fig. 4.28, where the first layer residue was not completely removed but formed discontinuous 'networks'. Through the trenches and holes of networks in the imprint layer, the second resist layer can still be developed to form the wedge shaped profile, however, the deposited metals fail to reach the exposed substrate in the subsequent step.

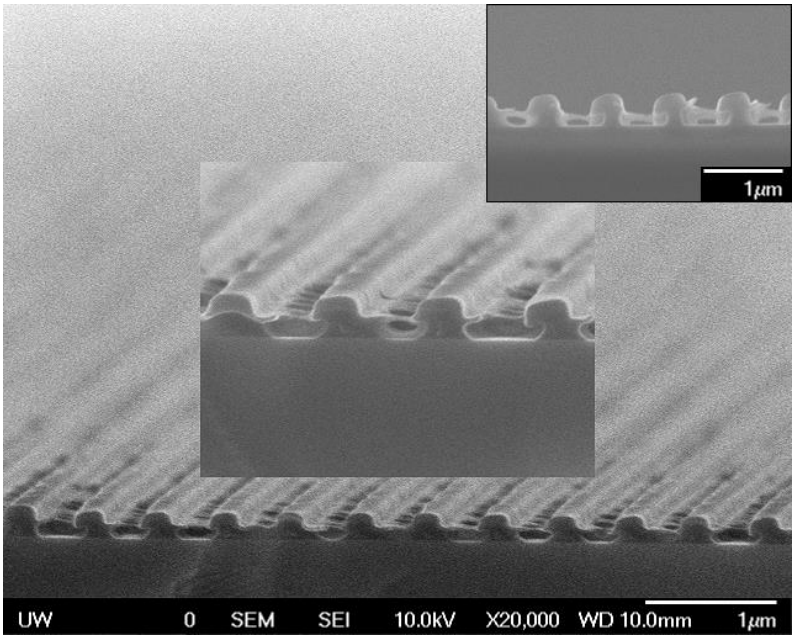


Figure 4.28: SEM images showing the effect from insufficient reactive ion etching, which leads to a failure of subsequent metallization. (scale bar: 1 μm)

*Off-axis reactive ion etching*

The ionized gas plasma generated in the reactive ion etcher has very good directionality, guaranteeing that the etch effect across the whole wafer is homogeneous. Ideally, the resist structural profile should always be symmetric before and after the etching is performed, and should be of the same thickness across the whole wafer. However, if the sample plane is tilted, either accidentally due to dust/defect underneath the wafer, or incorrect positioning of the sample in chamber, the reactive ion etching will occur off-axis and result in an asymmetric resist structural profiles (Fig. 4.29).

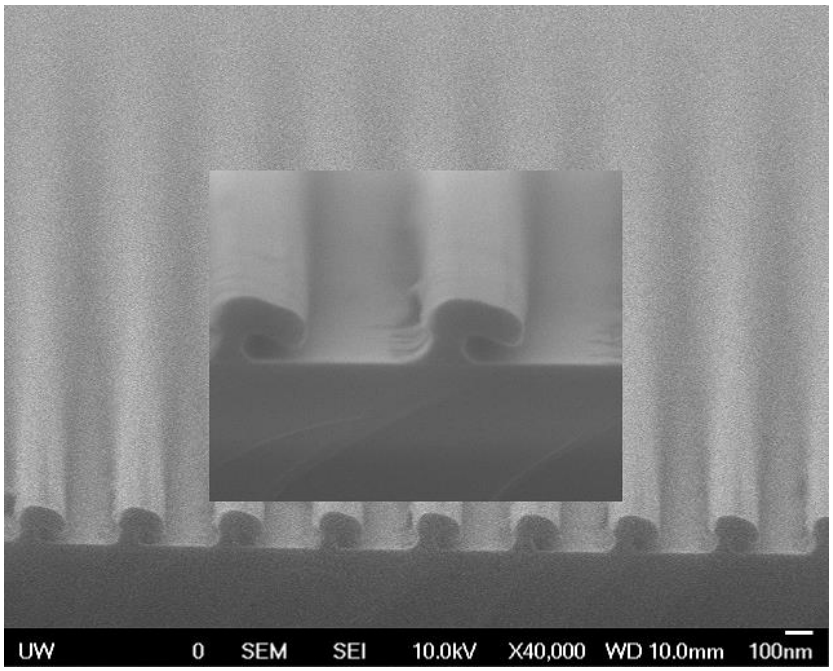


Figure 4.29: SEM images showing the effect of off-axis reactive ion etching, which leads to asymmetric resist structural profiles. (scale bar: 100 nm)

*Over- or under-development*

Wet-development of the undercut resist layer plays a critical role in obtaining good lateral resist profile. Over-development will result in a collapse of the resist nanostructure, as the lower undercut resist is not able to hold the weight of the top imprint layer (Fig. 4.30). Alternately, if the resist layer is under-developed, the substrate surface cannot be exposed for the subsequent metallization, as indicated in Fig. 4.31.

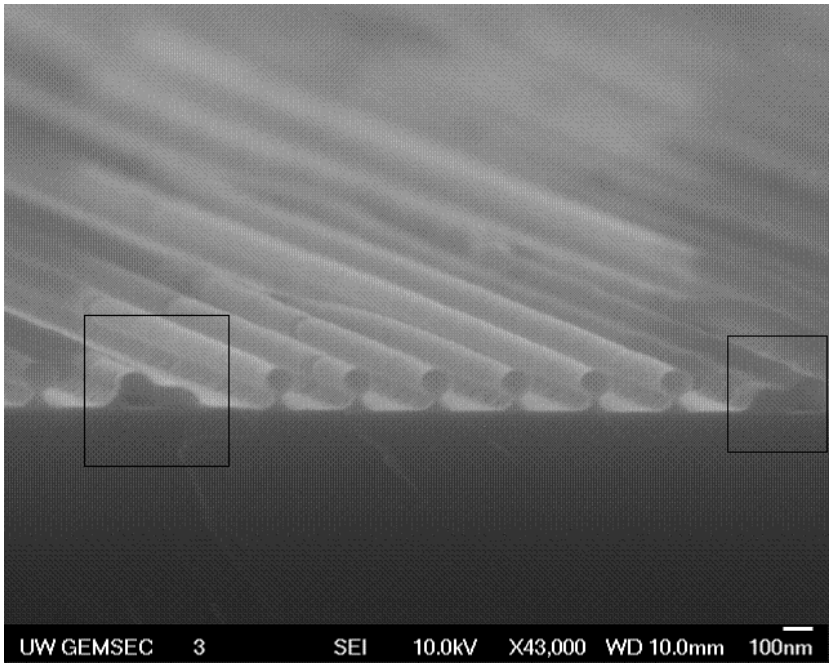


Figure 4.30: SEM images showing the effect of over-development, which leads to a collapse of the resist nanostructure. (scale bar: 100 nm)

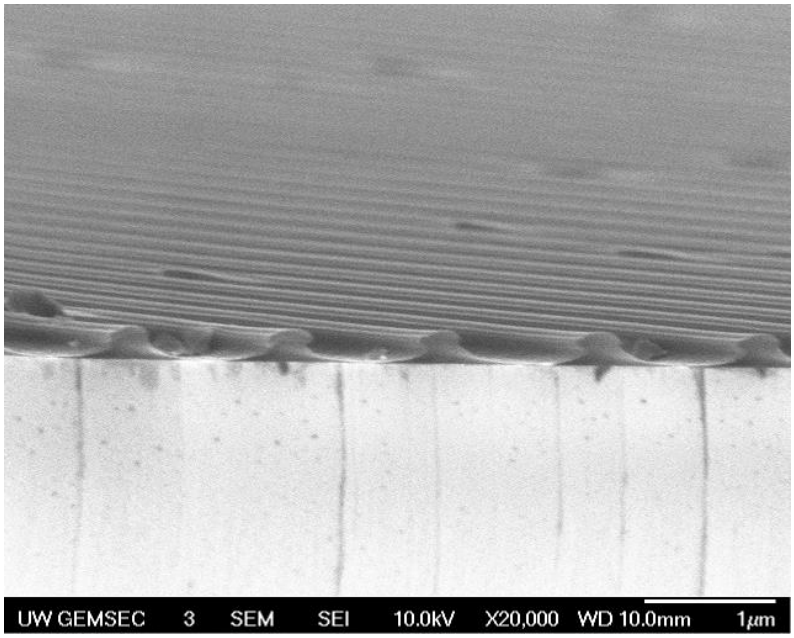


Figure 4.31: SEM images showing the effect of under-development, which leads to an incomplete exposure of the substrate. (scale bar: 1 μm)

*4.2 Epitaxial patterning via other approaches*

*4.2.1 Contact printing*

In the typical pattering techniques, all the processes (coating, imprinting, etching developing, and lift-off) are conducted on a single substrate, typically a Si wafer. However, when patterning on some special substrates, such as MgO, certain fabrication steps are not as easily accomplished. Photolithography on MgO substrate is complicated by the instrument expectations: the optical aligner in photolithography is designed for either 3 or 4 inch wafer, where a typical MgO substrate is only in the dimension of a 1 $cm^2$ square.

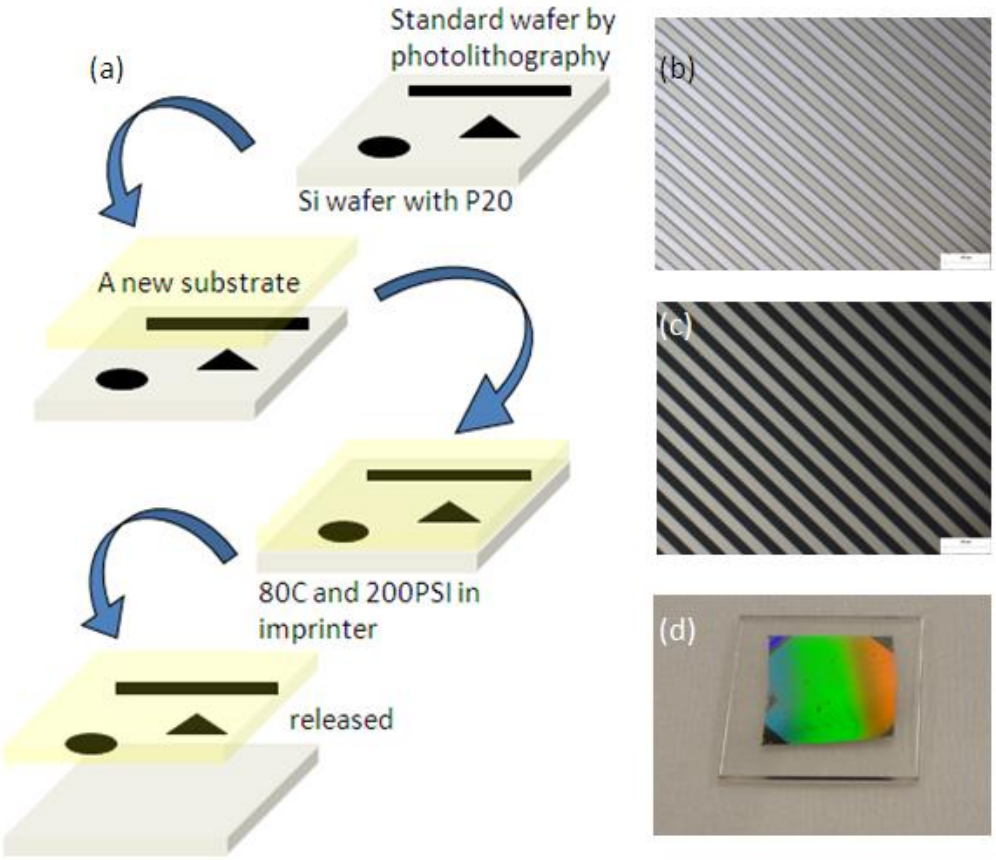


Figure 4.32: (a) Illustration of the contact transfer process. Optical microscopy images of (b) AZ1512 photoresist wire array transferred onto the MgO substrate. (c) Mo wire array after deposition and lift-off. (d) Photograph showing the complete, high-yield fabrication of epitaxial Fe/IrMn wire arrays on the transparent MgO substrate.

Alternatively, fabrication is achievable if the patterning is done in a conventional 3 or 4 inch wafer (donor wafer) and then transferred to a desirable substrate. Such a process is similar to the 'contact printing' used in the micro-electromechanics, where patterns are created on a Si wafer and then placed onto another pre-fabricated functional device [150]. One of the advantages of contact printing is the capability for creating three-dimensional micro- or nano-devices. Park *et al* has demonstrated a three-dimensional fabrication using a 'reverse-NIL' method [151].

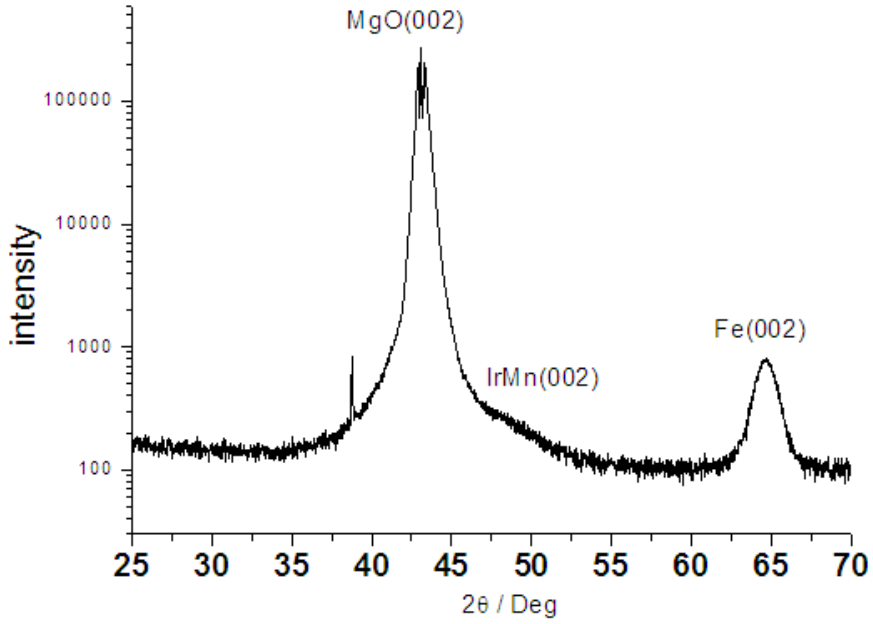


Figure 4.33: XRD *θ–2θ* scan of the epitaxial Fe/IrMn microwire array fabricated using the contact transfer recipe.

In a similar sense, we have developed a 'printing process' specifically for our application, i.e. epitaxial patterning, illustrated in Fig. 4.32. In our method, the patterned photoresist AZ1512 from a standard photolithography wafer is directly transferred on to single crystal MgO or pre-patterned substrate. We first pattern the desired structures in AZ1512 photoresist on a Si wafer using standard photolithography. Then we put the patterned Si wafer in close contact with a clean MgO substrate and imprint them with the nanoimprinter. It is worth noting that the nanoimprinter, which can be considered a 'pressure-temperature' tool, is ideal for such a purpose. Defect-free contract-transfer with nearly 100% yield can be obtained and very little resist residue remained on the original Si chip. Next, the AZ1512 template is transferred to a Mo mask, followed by the AZ1512 liftoff using acetone. The subsequent steps are similar to the epitaxial patterning introduced in Section 4.1: magnetic materials are deposited at elevated temperatures and the Mo mask is lifted-off by $H_2O_2$. The photograph in Fig. 4.32 shows the

complete high-yield fabrication of epitaxial Fe/IrMn wire arrays on the transparent MgO substrate. The structure of the epitaxial microwire arrays was checked by XRD, Fig. 4.33. Finally, as we are developing microscale patterns, the lateral resist profile (undercut) is not as critical here as on the nanoscale.

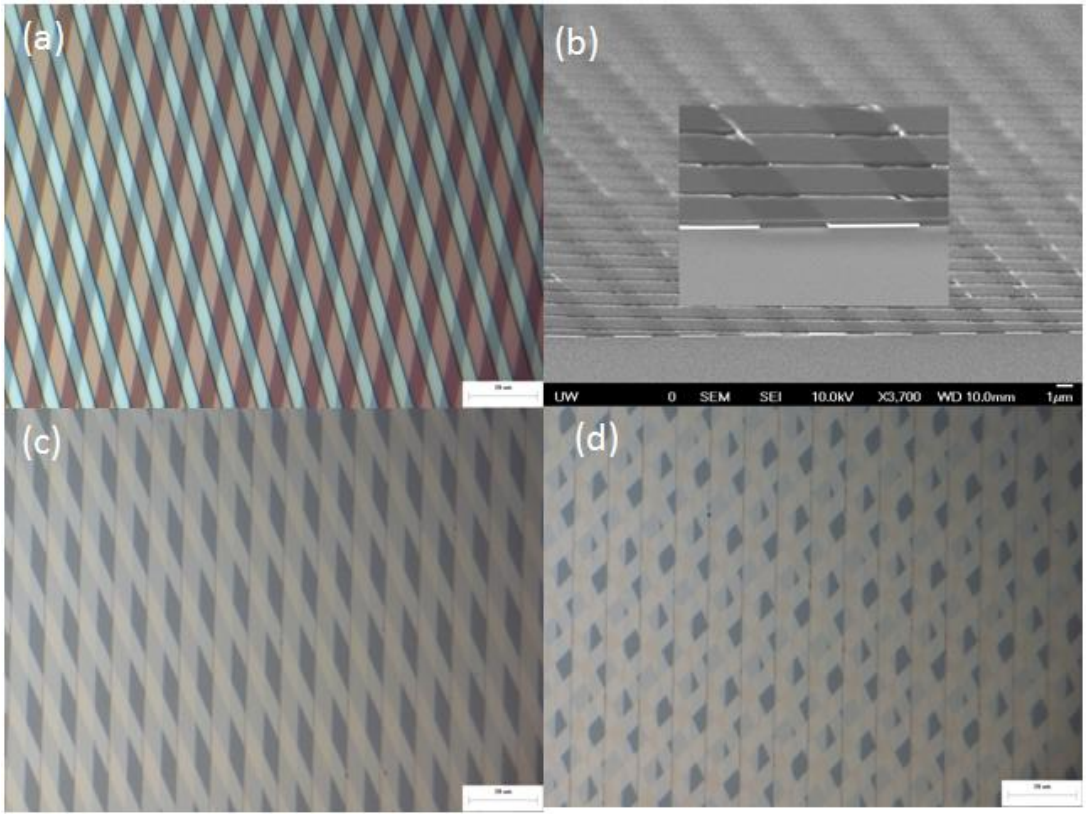


Figure 4.34: (a) Optical microscopy image showing the AZ1512 pattern transferred onto a pre-patterned Fe wire array. (b) SEM image of the cross-section view of AZ1512 attached on the Fe wires. Optical microscopy image of Fe networks consist (c) two layers of Fe wire arrays and (d) three layers of Fe wire arrays.

Similarly, we have demonstrated this contact transfer on to pre-patterned substrates. Magnetic Fe wire arrays on Si are first fabricated by standard photolithography (including metallization and lift-off), creating the pre-patterned substrate. Next, a small chip from the donor wafer is cut, brought into close contact with the pre-patterned substrate, and placed into the nanoimprinter. During the transfer, the AZ1512 wire arrays completely detach from the donor wafer and re-attach on the pre-patterned Fe wire arrays, Fig. 4.34(a) and (b). A second layer of Fe is then deposited, followed by AZ1512 lift-off, creating

a bilayer three-dimensional magnetic network (Fig. 4.34(c)). Repeating this process, we can continuously attach more layers and deposit Fe wire arrays (Fig. 4.34(d)) on to the network, fabricating complex magnetic multilayer microstructures.

### *4.2.2 Nanostencil lithography*

Nanostencil lithography is a novel method for fabricating nanometer scale patterns. It is a simple resistless parallel nanolithography process. The desired materials are directly deposited through the stencil on to the substrates. Various materials can be used as stencil membranes, including metals, Si, $Si_xN_y$, and polymers. These stencils are simultaneously robust and fragile. This method can be used for epitaxial patterning if the membrane is made from $Si_xN_y$ because the material can survive high deposition temperatures (> 800 $^oC$). However, $Si_xN_y$ membranes are mechanically fragile and require careful handling during sample preparation [152]. Figure 4.35 contains optical microscope images of a microdot array nanostencil made from $Si_xN_y$. Figure 4.36 displays the epitaxial magnetic microdot arrays fabricated by direct deposition through the stencil membranes.

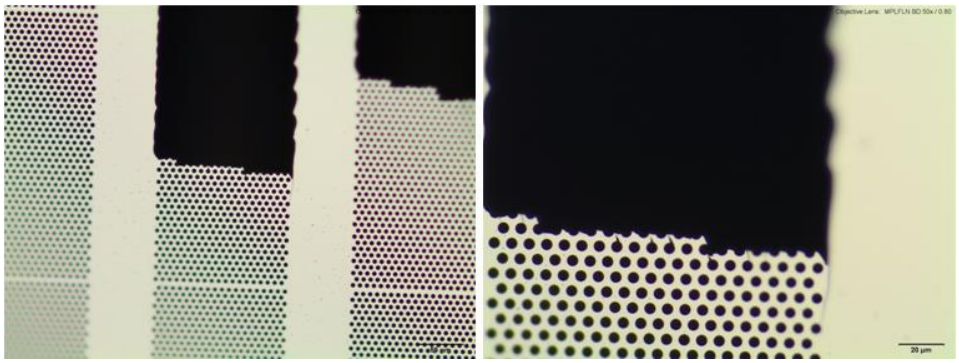

Figure 4.35: Optical microscopy images of a nanostencil using $Si_3N_4$ membrane and with microdot features.

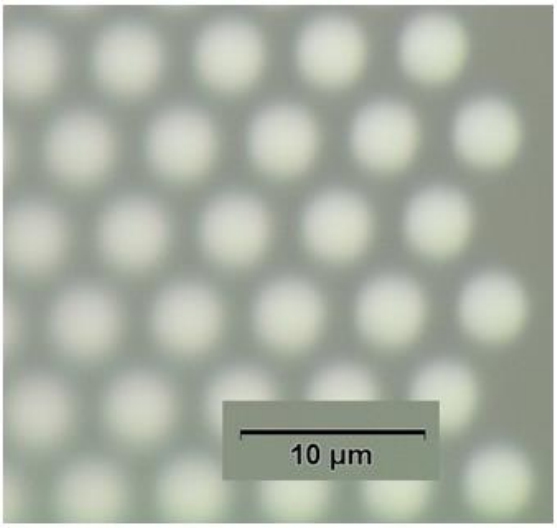


Figure 4.36: Optical microscopy image of epitaxial magnetic microdot arrays fabricated by direct deposition through the stencil membranes.

In summary, we focused on epitaxial patterning techniques using nanoimprint lithography, and also discussed other fabrication approaches including contact printing and nanostencil lithography. It should be noted that all these methods aim to enable epitaxial patterning via a direct deposition, which is advantageous over the 'Ar ion-milling' approach reported in the literature [137], where the epitaxial films are first deposited and then etched using high energy Ar plasma through the resist masks.

## *4.3 Typical magnetic characterizations of nanostructures*

### *4.3.1 Scanning probe microscopy*

Scanning probe microscopy (SPM) is a branch of microscopy that images a surface using a physical probe (tip) scanning the specimen. An image of the surface is constructed by mechanically scanning the probe on the sample and recording the probe-surface interaction as a function of position. There are many

kinds of interactions that can be probed, such as magnetic and electrostatic forces, van der Waals interactions, temperature variations, optical absorption, near-field optics, and acoustics. Common SPM includes scanning tunneling microscopy (STM) and atomic force microscopy (AFM). Only AFM and related techniques are discussed in this thesis.

*Atomic force microscopy*

The first AFM used a scanning tunneling microscope at the end of a cantilever to detect the bending of the lever, but now most AFMs employ an optical lever technique. The working principle for a typical AFM is indicated in Fig. 4.37. As the cantilever flexes, the light from the laser is reflected onto the split photo-diode. By measuring the difference signal, changes in the bending of the cantilever are measured. Since the cantilever obeys Hooke's Law for small displacements, the interaction force between the tip and the sample can be determined. Images are generated by scanning the tip across the surface, but rather than adjusting the height to maintain a constant current, the AFM measures the minute upward and downward deflections of the tip cantilever mechanism necessary to maintain a constant force of contact. As with the STM, these movements are used to build up an atomic-scale topographic map of the surface.

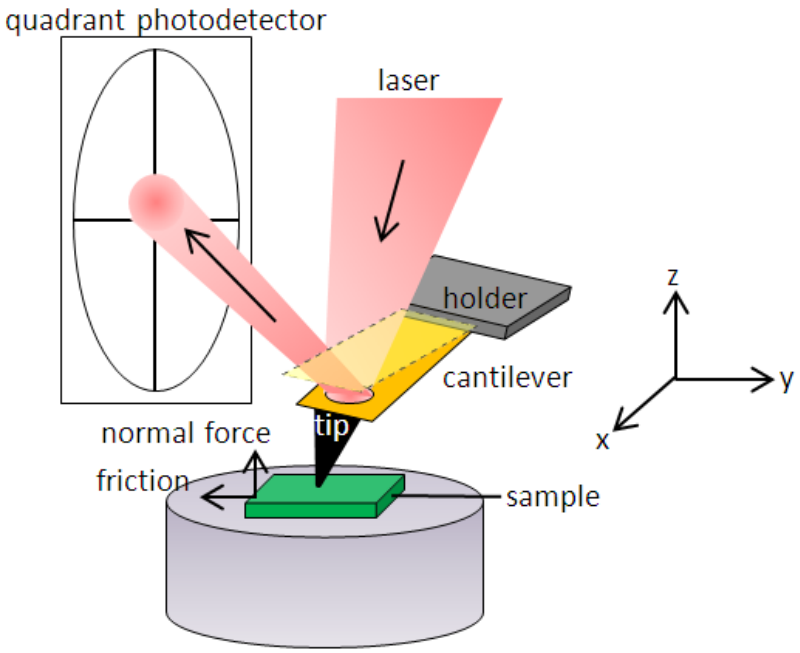


Figure 4.37: The working principle for a typical AFM.

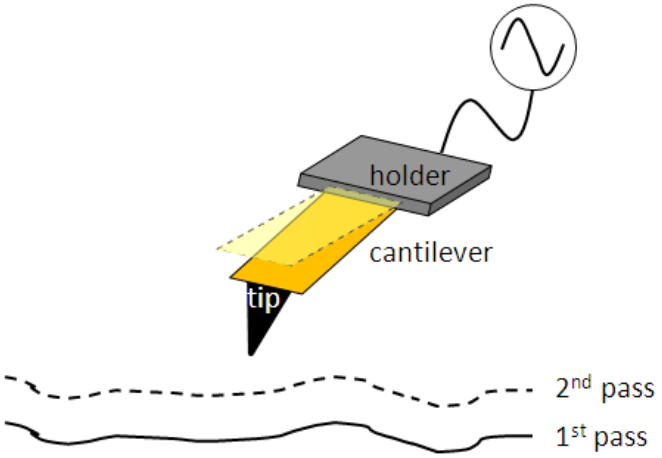


Figure 4.38: Working principle of a typical MFM under the 'Lift Mode'.

*Magnetic force microscopy*

The Magnetic Force Microscopy (MFM) is a type of SPM that uses the AFM equipped with a sharp magnetic probe that interacts with the sample's magnetic static fields. More specifically, the MFM is a

magnetic imaging technique sensitive to the spatial derivatives of the magnetic fields generated by a sample. These fields do not depend on the sample magnetization directly but result from the divergence of the magnetization. The MFM is a widespread, easy-to-use tool that provides high-resolution (sub-100 nm) images of the magnetic structures of a variety of materials. It is possible to image magnetic structures in air with this technique, giving the MFM a notable advantage over other high resolution techniques. In order to separate magnetic interactions from any other forces, such as van der Waal interactions, short-range repulsive, and capillary wetting interactions between the tip and sample, a 'Lift Mode' method is employed. Although the magnetic force is often weaker than other interactions when close to the surface, it is a long range force that falls off slowly and is present further from the surface. To separate the short range topographical interactions from the long range magnetic interactions, we make two separate measurements, or passes, over the same region of a specimen.

Figure 4.38 illustrates how the 'Lift Mode' works. The first pass is a measurement of the surface position (essentially the short range topographical forces). The data from this first pass provide a template to follow on a second pass with the tip held at a pre-defined distance given by the height information obtained from the first pass. This second pass is too far from the surface to analyze the stronger, non-magnetic, short-range interactions, but is close enough to measure the long range magnetic interactions. The MFM tip measures the gradient of the perpendicular magnetic field and generates a magnetic domain image. Figure 4.39 show examples of AFM and MFM images of lithographic wire and dot arrays. In the MFM images, the wires display a multi-domain state and the dot show a single domain state, as indicated by the white/black contrast.

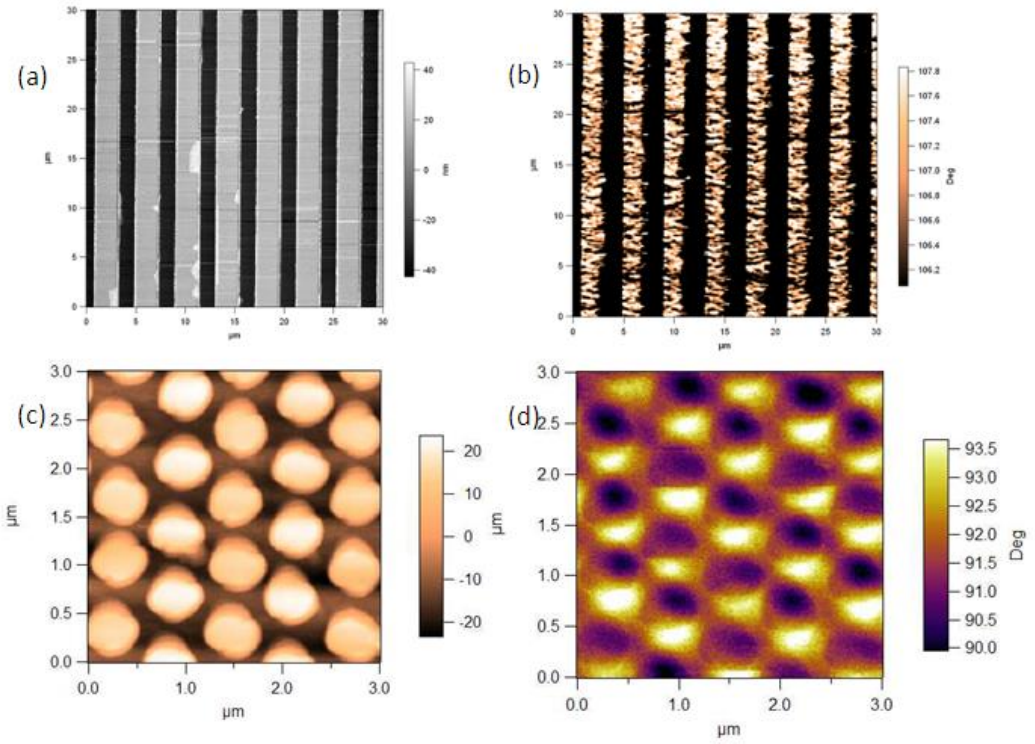


Figure 4.39: Lithographic Fe wire (3 µm) array probed by (a) AFM and (b) MFM. Lithographic Fe dot (300 nm) array probed by (a) AFM and (b) MFM. In the MFM images, the wire display a multi-domain state and the dot show a single domain state, as both can be recognized by the white/black contrast.

*4.3.2 Magnetotransport measurement*

We have shown in Chapter 2 that the anisotropic magnetoresistance (AMR) can be applied to study the magnetization reversal in epitaxial thin films. Specifically, high and low resistance values are observed when the current and magnetization aligned collinear and perpendicular, respectively. Here, we show that the AMR is also useful for characterization of nanostructures, particularly for nanowire arrays. Figure 4.40 illustrates the equipment setup for AMR measurements for nanowire arrays. Fe/IrMn bilayer nanowire array are fabricated using NIL on Si substrate. Four Au contact pads (I+, I-, V+, V-) are deposited across the wire array through a shadow mask. The chip is then mounted on the in-plane sample

holder (Quantum Design). The Au pads are wire bonded to the electrodes on the sample holder for connection. The current flows along the wire and the external field can be applied at different orientations with respect to the wire (current) direction by utilizing the in-plane sample rotator.

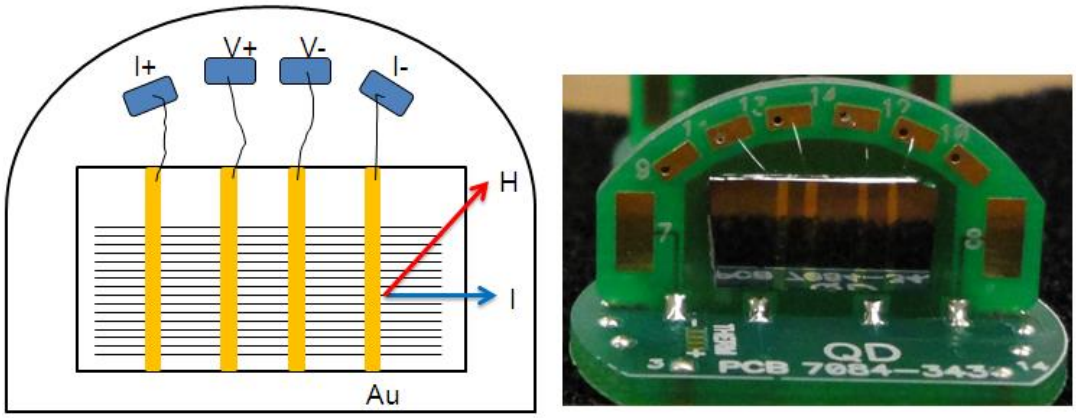


Figure 4.40: Illustration and photograph image of the AMR setup for measuring the magnetic nanowire arrays.

Figure 4.41 shows the AMR curves measured for the Fe/IrMn wire array at 20K, after field cooling (5 KOe) along the wire direction. When measured parallel to the wires, the resistance remains at a constant high value during the field sweeping. This indicates that the magnetization is either parallel or antiparallel along the wire direction, without any perpendicular component. In such a scenario, the

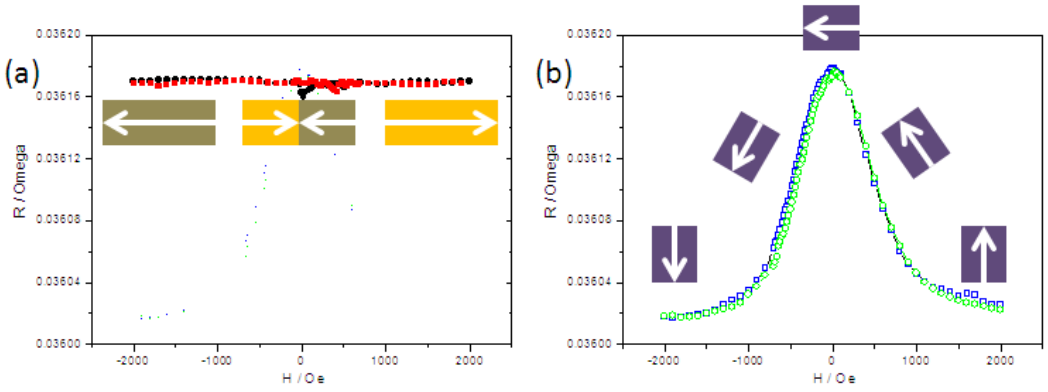


Figure 4.41: AMR curves measured for the Fe/IrMn wire array at 20K, after field cooling (5 KOe) along the wire direction, and for the external measuring field applied (a) parallel and (b) perpendicular to the wires. Magnetization direction is indicated by the arrow enclosed in a box.

magnetization reversal occurs via DW nucleation and propagation. This conclusion is physically reasonable, since the large shape anisotropy of the wire would favor a magnetization always parallel to the wire. When the resistance is measured perpendicular to the wire, a gradual change is observed, indicating the magnetization reversal mainly occurred by coherent rotation. Specifically, the magnetization is initially saturated perpendicular to the wire by the high field, giving rise to a low resistance state. The sample shows a high resistance state with rotation of magnetization to the wire direction. Such rotation behavior can be understood by the competing 'dragging force' on the magnetization from the two perpendicular torques caused by the external field and the shape anisotropy.

In summary, as introduced in this chapter, we have developed series of NIL processes for different applications in magnetism, including general NIL patterning, epitaxial patterning, nanoparticle release and sub-100 nm process. Such techniques can be applied for patterning magnetic structures over large area ($> 1 \times 1$ cm$^2$), and with nanostructure sizes ranging from several hundreds of nm to below 100 nm. From technology point of view, the NIL processes developed in this thesis can also have potential industrial impacts due to the various advantages of NIL itself (high-speed, high throughput, and cost-effective).

From a scientific point of view, the processes allow us to make relevant samples with competing magnetic anisotropies, including magnetocrystalline anisotropy, interface-induced anisotropies, and the shape anisotropy. Specifically, the shape anisotropy, usually in uniaxial symmetry, can be flexibly controlled by the lithography. Such competing anisotropies in one magnetic system can further give rise to different magnetic reversal properties compared to their thin-film counterparts, as will be discussed in the next chapter.

# Chapter 5

# MAGNETIZATION REVERSAL IN NANOSTRUCTURES

Contents of this chapter have been partially published in Ref.[154], [155], [157]

## *5.1 Confined domain wall structure in the nanowire*

In the epitaxial thin film samples, we have shown that the magnetization reversal occurs via domain wall nucleation and propagation along different easy axis of the cubic magnetocrystalline anisotropy. At certain external field, for example, we should be able to observe a magnetic domain point along a certain 'easy' direction, Fig. 5.1(a). However, in the nanowire samples, the magnetic domains are confined by the

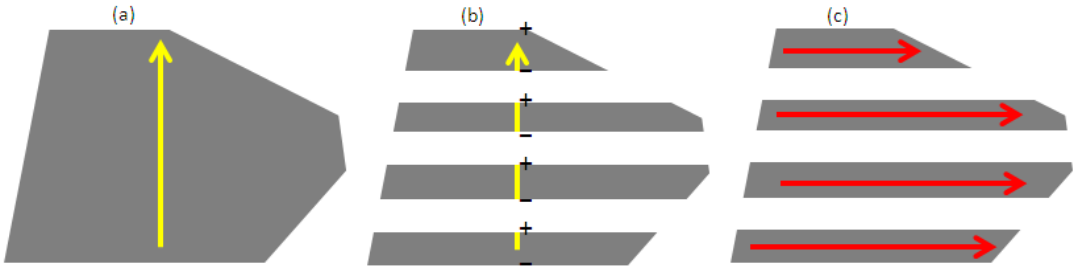


Figure 5.1: Illustration of (a) magnetic domain in a continuous film. (b) Patterned thin-film structure, showing the breaking of a domain by the discontinuous gratings along the perpendicular direction. If the magnetization aligns perpendicular to the wires, net magnetic 'charges' accumulates along the edges which is not energetically favorable. (c) Instead, magnetization prefers to align along the long axis of the wires to minimize the energy.

dimension of the wires (Fig. 5.1(b)). Specifically for a wire with a certain width, *d*, when the domain size, $\delta$, is greater than *d*, the magnetic domains would not be easily established along the perpendicular direction of the wires, but preferably form along the long axis of the wires. From the energy point of view, perpendicular magnetic domains will bring in positive and negative net 'magnetic charges' along each side of the wire, which are separated by a distance, *d*. Since *d* is smaller than $\delta$, such net 'charges' will bring about significant magnetostatic energy, which is not favorable. Therefore, the magnetization prefers to align along the wire direction so as to minimize the magnetostatic energy (Fig. 5.1(c)).

### *5.1.1 Evidence from direct imaging*

We performed magnetic domain imaging on continuous film sample by Kerr microscopy, and on lithographic wire samples by MFM. Figure 5.2 summarizes the experimental results for continuous film sample. Here, an epitaxial Fe film (with thickness of 15 nm) on MgO substrate was probed. As illustrated in Fig. 5.2, magnetic domains are expected to be observed along different easy axes (red, blue, yellow, green). In the real Kerr image, the Fe domains appear in a relatively large size (mm scale), reflecting the epitaxial growth. Magnetic domains pointing along different orientations are shown by the different color codes in the image. Black/white contrast showed magnetic domains aligned along opposite directions, i.e., black ($\rightarrow$) and white ($\leftarrow$). The gray color reflects the domains along the perpendicular direction ($\uparrow$ or $\downarrow$). A rather long (> 1 mm) $90^{o}$ domain wall can be found in the center of the image (enclosed by a dashed bar). Such long DW indicates the intrinsic DW structure, mediated by low defects concentration and weak structural confinement. Two representative regions were also identified and marked by A and B. The

zoom-in images for A and B are also shown (Fig. 5.2). In A, alternating (→) and (←) magnetic domains can be observed with alternating 180° DWs. In B, a coexistence of a 90° and a 180° DW was observed. These images confirm our predictions on the magnetic domain configurations, i.e., magnetic domains along different easy axes can be observed, whose structures are influenced by *very weak confinement or mediation from any extrinsic parameters* (defects or shape, etc), but rather by its *intrinsic preferences (magnetocrystalline anisotropy*).

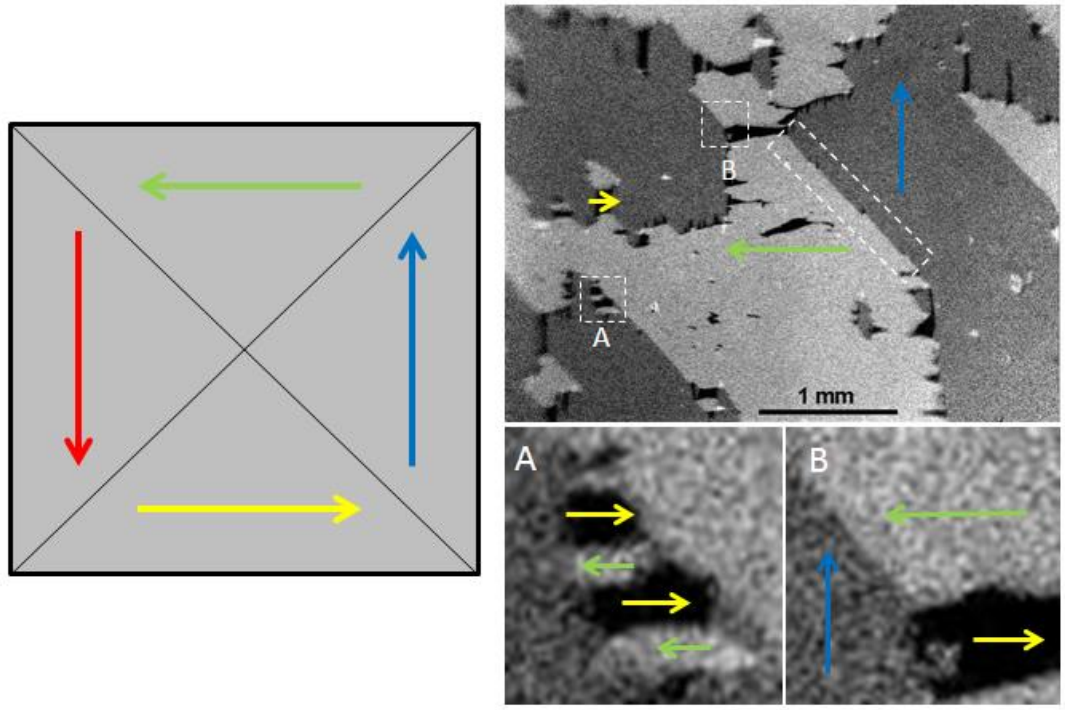


Figure 5.2: Schematic illustration and experimental Kerr images of magnetic domains in epitaxial Fe continuous film. Magnetic domains pointing along different orientations can be observed. (Kerr images were taken by our collaborator, by Dr. T. Eimüller at Bochum)

For lithographic wires, we probed two samples with different widths, 2 μm (Fig. 5.3(a)) and 300 nm (Fig. 5.3(b)), respectively. The 2 μm sample was 15 nm thick polycrystalline Fe wire arrays on Si wafer made by photolithography. The width of the wire is comparable to the domain size, i.e. $d \sim \delta$. In this case, the confinement of DWs from the wire shape is not so strong. DWs along different orientations are still

observed (Fig. 5.3(a)). On the other hand, the 300 nm wire sample is epitaxial Fe nanowire arrays (15 nm thick) on MgO made by NIL with the Mo lift-off technique. The domain size of epitaxial Fe films is estimated to be in the millimeter scale from the Kerr image of the continuous film sample (Fig. 5.2). As a result, the width of the wire, $d$ is far smaller than $\delta$, so a strong confinement of the domains (by the dimension of the wire) can be observed. In the MFM image, almost no color contrast is observed for such wires, indicating that the magnetization is homogenous along the wire direction. Any perpendicular domains are suppressed as well as relevant DWs. Along the wire long axis, however, magnetic domains and relevant DWs are not affected. For example, a transverse DW separating two antiparallel domains can be observed (Fig. 5.3(b)).

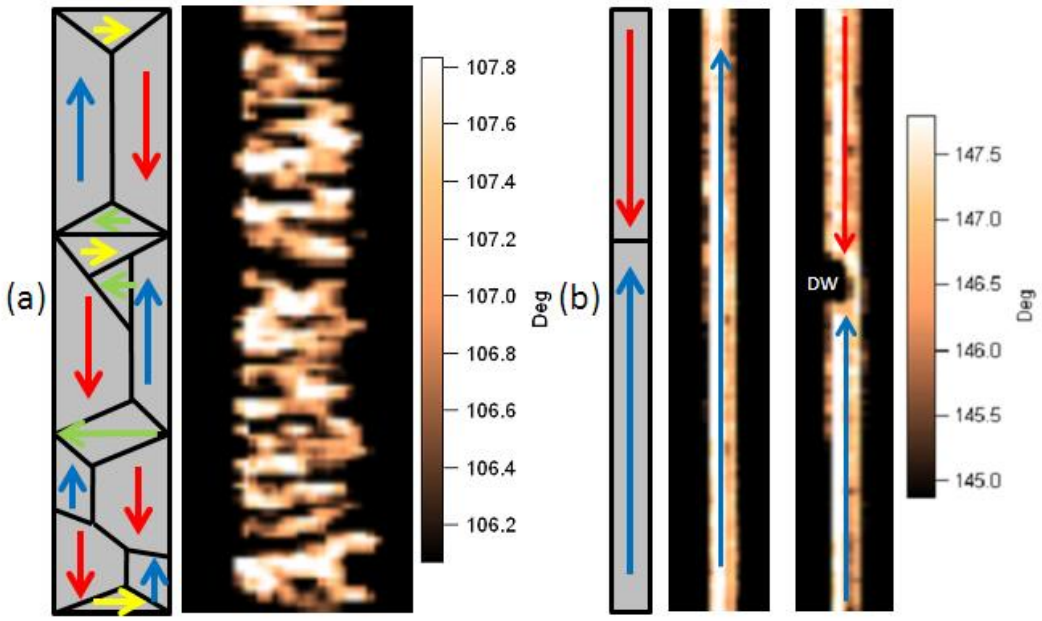


Figure 5.3: Schematic illustration and experimental MFM images of (a) 2 μm polycrystalline Fe wires, and (b) 300 nm epitaxial Fe wires.

*5.1.2 Magnetization reversal curves*

The magnetization reversal behaviors (hysteresis loops) are also influenced by the shape anisotropy of the wires. To show the effect of shape anisotropy, a polycrystalline Fe wire array (width ~ 300 nm, thickness ~ 15 nm) was first studied. Magneto-optic Kerr effect was applied to obtain the reversal curves at different orientations. When measured along the wire direction, a fat loop with large coercivity, ~ 250 Oe, was obtained. This is directly related to the suppressed paths for DW nucleation and propagation [153]. Specifically, DW nucleation and propagation along the perpendicular orientation is not an option anymore in the wire sample, since all the magnetization is confined along the wire axis. Most reversals occur via the nucleation of an opposite DW, and subsequent propagation of such DW along the wire axis (Fig. 5.4(a)). During the DW propagation, various defects, from both structure and shape, can also act as DW pinning centers and further hinder the reversal. In such a scenario, the DW has to either overcome the pinning force and continue the propagation, or find a new site to nucleate a new DW. In both cases, the result is an enhanced coercivity in the hysteresis loop. When measured perpendicular to the wires, the

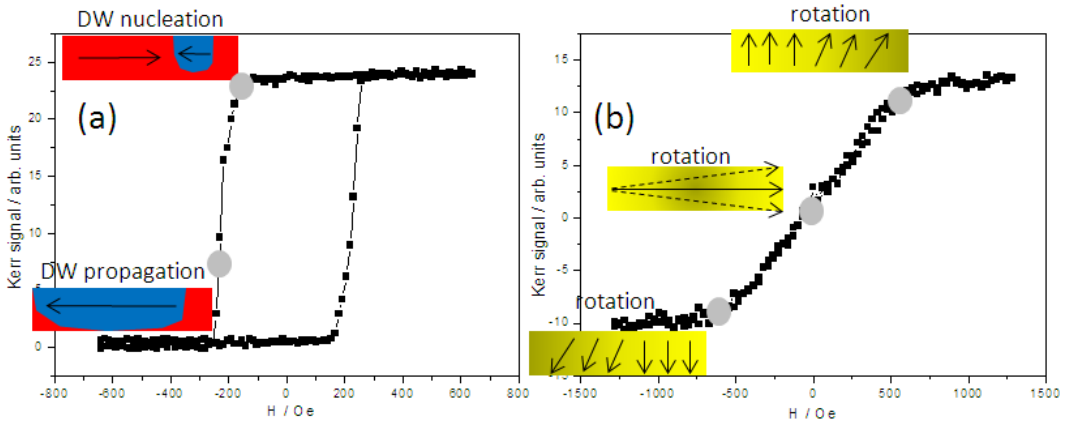


Figure 5.4: Magnetization reversal curves of the polycrystalline Fe nanowire array measured at room temperature (a) parallel to wire long axis; and (b) perpendicular to the wire axis.

magnetization is dragged to the hard axis by the strong external field, generating high magnetostatic energy. As the field decreases, the system wants to reduce the magnetostatic energy prior to any magnetization reversal behavior. The most effective way for reducing this energy is the coherent rotation of the magnetization to the wire direction (easy axis). Therefore, a gradual change of the magnetization vs. field was observed (Fig. 5.4(b)). At zero field, all the magnetization is aligned parallel to the wire, therefore a zero remanance was observed in the loop. Last but not least, the reversal curve displays very weak hysteresis behavior, confirming that the dominant mechanism for magnetization reversal is primarily reversible coherent rotation.

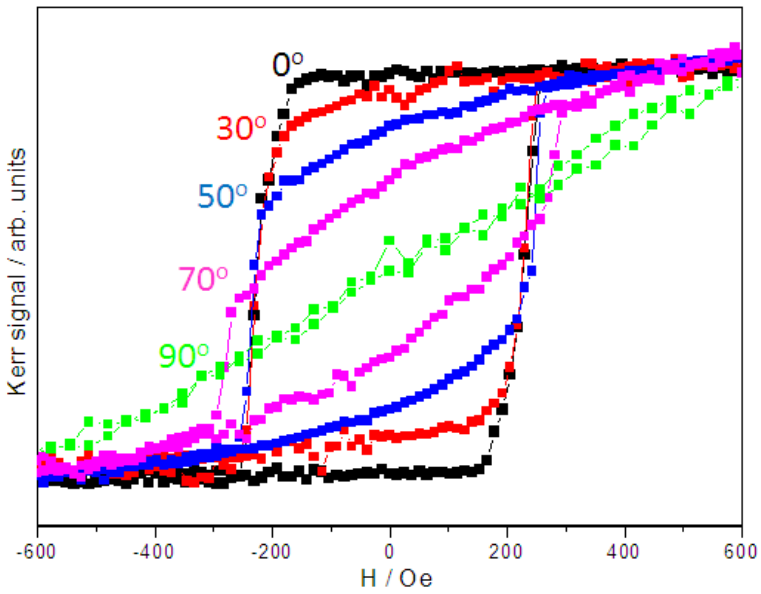


Figure 5.5: Hysteresis loops at other different field angles for the polycrystalline Fe nanowire array.

We also measured the hysteresis loops at other different field angles and the results are shown in Fig. 5.5. An evolution from the DW nucleation to the coherent rotation is clearly indicated by the transition from sharp switch (at $0^{o}$) to the gradual reversal (at $90^{o}$) of the magnetization. The coercivity is then summarized in the angular plot, Fig. 5.6. At parallel directions ($0^{o}$ and $180^{o}$), the coercivities are largest,

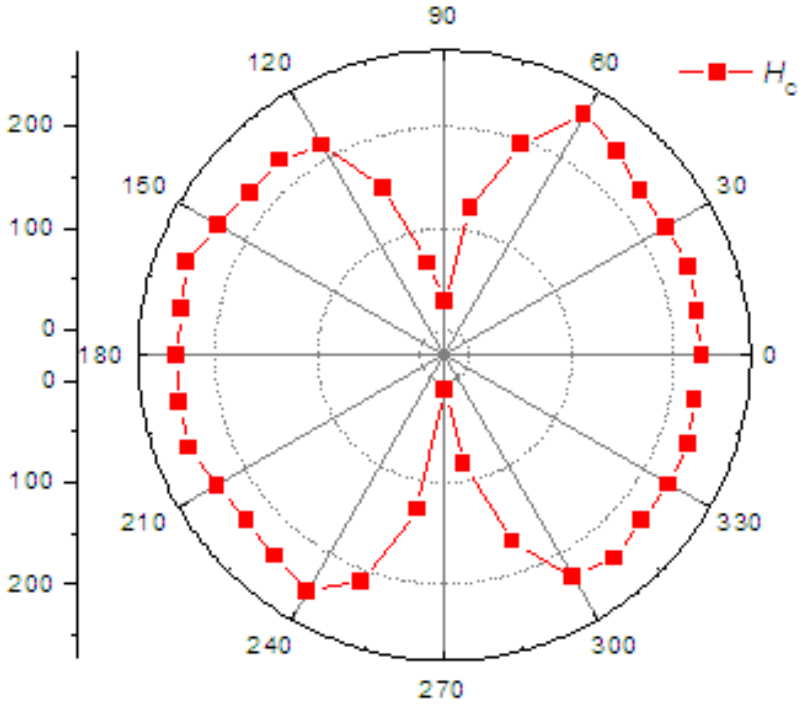


Figure 5.6: Polar plot of the coercivity obtained at each external field angle for the polycrystalline Fe nanowire array.

which is identified as a typical easy-axis behavior. Along the perpendicular directions (90$^o$ and 270$^o$), almost zero coercivities are obtained which correspond to the slim hysteresis loop. The plot also unambiguously reflects a 2-fold symmetry, which directly indicates the dominant uniaxial shape anisotropy.

## *5.2 Introducing magnetocrystalline and exchange anisotropy into the nanowire*

### *5.2.1 Magnetocrystalline anisotropy and irreversible jumps*

In epitaxial Fe nanowire arrays, the magnetocrystalline anisotropy also plays a role in the magnetic

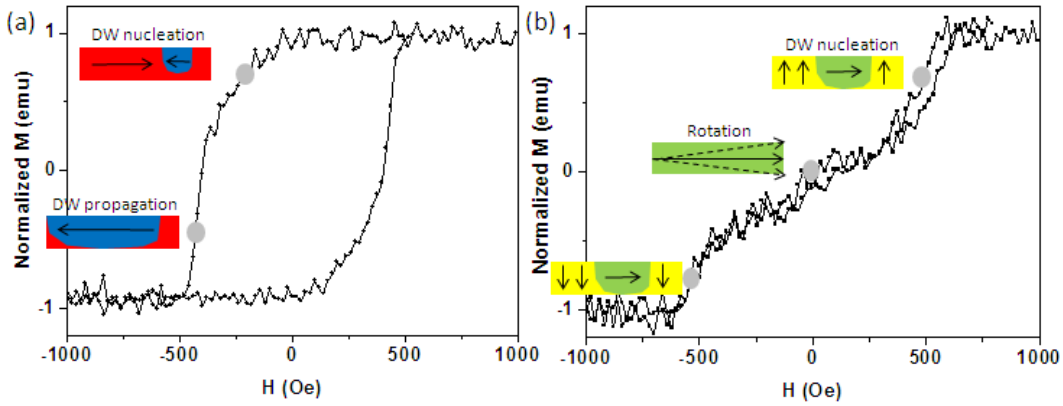


Figure 5.7: Magnetization reversal curves of the epitaxial Fe nanowire array measured at room temperature for (a) parallel to wire long axis; and (b) perpendicular to the wire axis.

reversal on top of the dominant shape anisotropy. We made a sample with the wire direction superimposed on one of the Fe cubic easy axis. Due to the 4-fold anisotropy of Fe, the perpendicular direction of the wire is another cubic easy axis. When measured along the wire, an even larger coercivity was observed, ~ 400 Oe, as compared with the polycrystalline wire, ~ 250 Oe. The reversal mechanism is still primarily DW nucleation and propagation along the wire. However, even less nucleation centers exist due to the smaller number of the defects in the epitaxial samples, which eventually results in a greater coercivity.

When measured perpendicular to the wire, the gradual reversal (coherent rotation) of magnetization is the dominant mechanism, however, little hysteresis behaviors were locally observed at high field, ~ ± 500 Oe, due to the superimposed anisotropy easy-axis. As the field decreases, significant magnetization, $M_{CR}$, still rotates gradually towards the wire axis in order to reduce the large magnetostatic energy. Nevertheless, magnetic reversal via DW movement becomes another option due to the superimposed magnetocrystalline anisotropy. Certain magnetization component, $M_{DW}$, that was strongly pinned along the cubic Fe easy axes, can go through a DW nucleation process and reverse from the perpendicular cubic

easy axis directly to the superimposed easy axis (wire axis), resulting in the local sharp reversal characteristic as well as the small hysteresis (signature for irreversible DW behaviors). The relative contribution of $M_{CR}$ and $M_{DW}$ to the reversal features depends on the competing strength of the magnetocrystalline and shape anisotropy. In systems with dominating magnetocrystalline anisotropy, such as an epitaxial Fe film with a small induced uniaxial anisotropy, the reversal is primarily controlled by $M_{DW}$ and displays sharp switching and substantial hysteresis behavior, as discussed in Chapters 1 and 3. In systems with dominating shape anisotropy, such as the nanowire samples we introduced here, the reversal is mainly manipulated by $M_{CR}$, with a gradual reversal but only local hysteresis. The separation of the two local hysteresis loops represents the strength of the uniaxial shape anisotropy.

*5.2.2 Exchange anisotropy and loop shift*

Unidirectional exchange anisotropy was further brought into the system by growing epitaxial Fe(10 nm)/MnPd(10 nm) bilayer nanowire arrays (line width ~ 300 nm) [154]. The EB direction was set along the wire direction that was also superimposed along Fe[100]. Hysteresis loop shift was observed as the resulting effect. For an example, we present the magnetic properties of *a*-axis Fe/MnPd wire arrays, probed by VSM, *M(H)*, and AMR, *R(H)*. The sample was first field-cooled under a magnetic field, $H_{cool}$=2 T, from 300 K to 10 K, below the blocking temperature, $T_B$ ~90 K of the *a*-axis Fe/MnPd. The field cooling process was performed in two different modes with $H_{cool}$ either parallel or perpendicular to the wire direction, respectively. Both the magnetization and resistance, versus field, i.e., $M(H)$ and $R(H)$, were measured at 10 K subsequent to each field-cooling process.

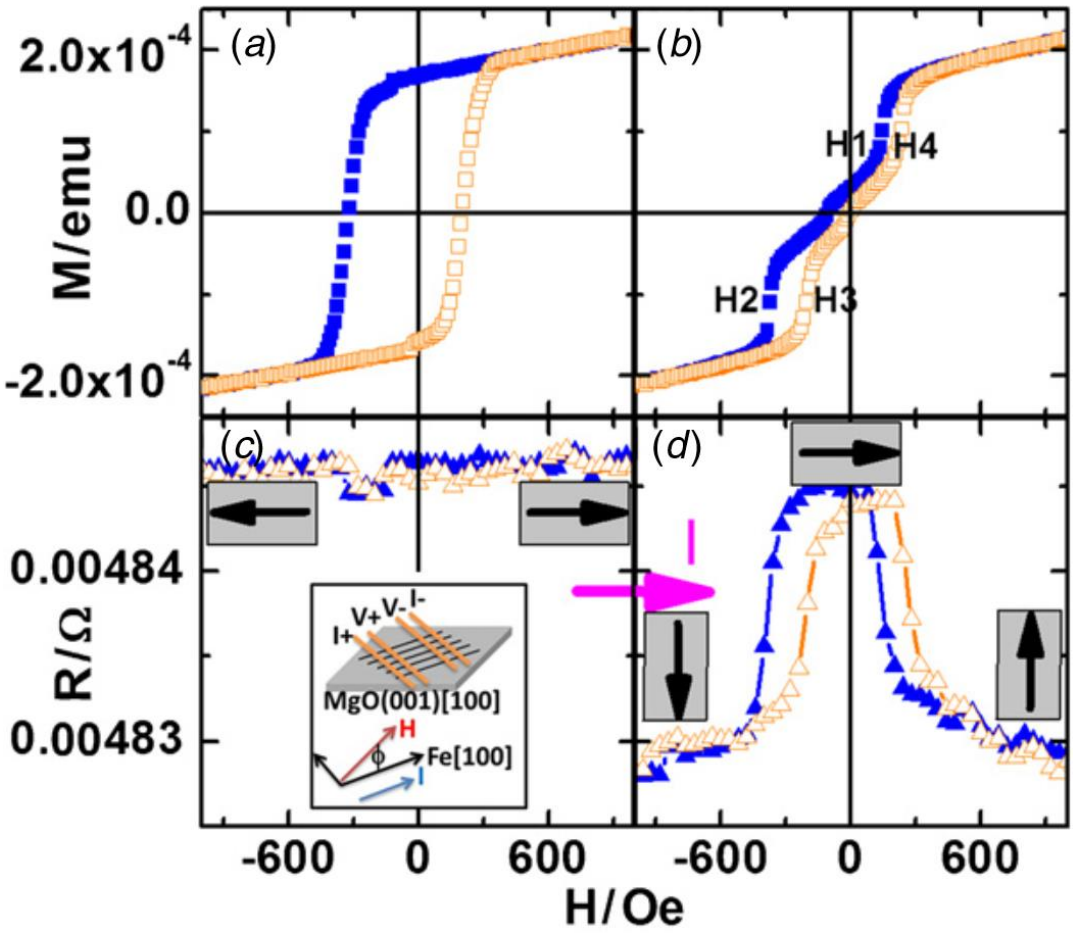


Figure 5.8: $M(H)$ curves measured at 10 K with (a) parallel and (b) perpendicular field cooling. $R(H)$ curves measured at 10 K with (c) parallel and (d) perpendicular field cooling. The magnetization orientation is represented by the black arrow enclosed in a box. The inset is a schematic illustration of the AMR measurement setup [154].

For parallel cooling and measurement, a broad hysteresis loop with one-step magnetic reversal was observed by VSM (Fig. 5.8(a)), showing that the magnetization reversal occurred by DW nucleation. An exchange bias field, $H_{eb}$, ~56 Oe was observed, which can be related to $K_{eb}$ through $K_{eb}=H_{eb}M_s$, where $M_s$ is the saturation magnetization per unit volume. The coercivity is ~265 Oe, more than one order of magnitude higher than that of the continuous films. For perpendicular cooling and measurement, the efficiency of the applied field to unpin a wall trapped in a pinning center decreases and the magnetization reversal via coherent rotation becomes more effective. This is evidenced by the gradual reversal behavior

of the $M(H)$ curve (Fig. 5.8(b)). Again, different from the polycrystalline nanowires, small magnetization jumps were observed in the epitaxial sample which took place at $H_1$ ~137 Oe, $H_2$ ~ -371 Oe for descending branch, and $H_3$ ~ -210 Oe, $H_4$ ~233 Oe for ascending branch, respectively. These jumps indicate the rapid relaxation of the magnetization along the wire direction, due to the collinear easy axes of the Fe magnetocrystalline anisotropy and the shape anisotropy. In other words, the magnetization relaxes more abruptly in our epitaxial nanowires than in the polycrystalline counterparts.

The AMR measurements were performed via the conventional 4-probe technique with the current flowing along the wire direction (also superimposed with the Fe [100] easy axis) (inset Fig. 5.8(c)). Four rectangular Au contact pads were deposited through a shadow mask across the nanowire arrays. The whole sample was mounted on an in-plane sample rotator to perform angular dependent $R(H)$ measurements. For parallel cooling and measurement, $R(H)$ stayed continuously at the high resistance level and showed no transitions during the whole magnetization reversal process, which indicates that the magnetization is either parallel or antiparallel to the direction of the current, (Fig. 5.8(c)), consistent with the $180^o$ DW nucleation and propagation of magnetization reversal. For perpendicular cooling and measurement, at the descending branch, the magnetization gradually rotates from the positive saturation (displaying low resistance), to the wire axis (displaying high resistance) as the field decreases, and finally rotates to the negative saturation (displaying low resistance), via coherent rotation (Fig. 5.8(d)). We also measured the angular dependent $R(H)$ signals at 10 K for each cooling mode, with the magnetic field applied at an angle $\phi$ with respect to the current direction. $\phi$ is varied from $0^o$ to $90^o$ in step of $10^o$. For both parallel cooling ($H_{cool}$ along $\phi = 0^o$) and perpendicular cooling ($H_{cool}$ along $\phi = 90^o$), $R(H)$ always stays at high resistance level for $\phi \leq 50^o$. Gradual changes of $R(H)$ signals can be only observed for $\phi > 50^o$, Fig.

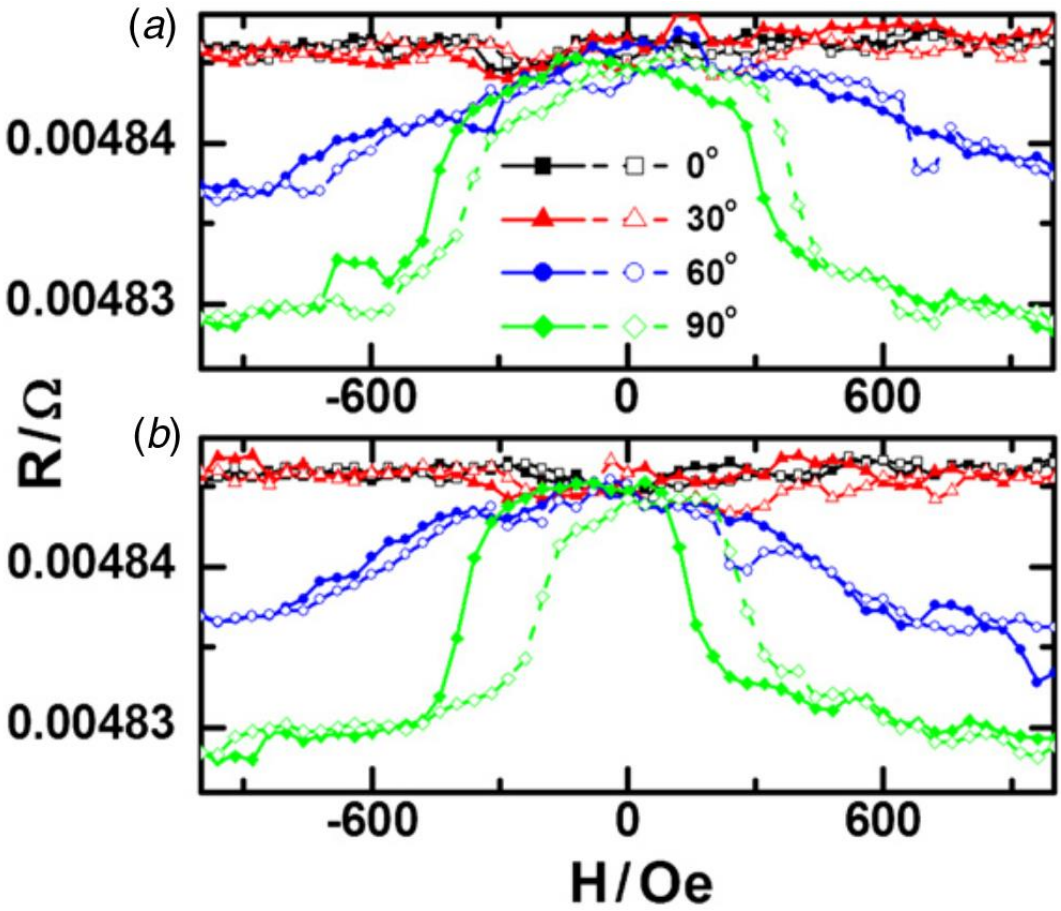


Figure 5.9: $R(H)$ curves measured at 10 K for the decreasing field (solid) and the increasing field (open) with parallel field cooling (a), and perpendicular field cooling (b), at selective angles, $\phi = 0^{\circ}$, $30^{\circ}$, $60^{\circ}$ and $90^{\circ}$, with respect to the wire axis [154].

5.9. This indicates that the magnetization reversal mechanism changes from DW nucleation to coherent rotation at approx. $\phi = 50^{o}$, which is consistent with the previous MOKE measurements.

*5.3 Misalignment of anisotropies in nanowires*

The above experiments have discussed the magnetic properties with collinear easy axis from the different anisotropies, i.e., magnetocrystalline, shape and exchange anisotropy. Actually, the competing effect can be more significant when these different easy axes are misaligned. The misalignment of the Fe

cubic anisotropy with the exchange anisotropy has been introduced in Chapter 3. Here we will discuss the other two combinations.

*5.3.1 Misaligned exchange and shape anisotropy*

We fabricated polycrystalline Co/IrMn nanowire arrays, $S_{WIRE}$, with the sequence of Cu(5nm)/Co(5nm)/IrMn(10nm)/Pt(2nm) and width of ~300 nm by nanoimprint lithography [155]. A permanent magnet with magnetization direction parallel to the metal lines was placed on the back of all the substrates, during thin film growth, to induce and control the EB direction. As a control, a Co/IrMn continuous film sample, $S_{FILM}$, was also grown with the same multilayer architecture. Each as-grown sample was cut into small pieces for selective post-growth treatment. Several film and wire pieces were

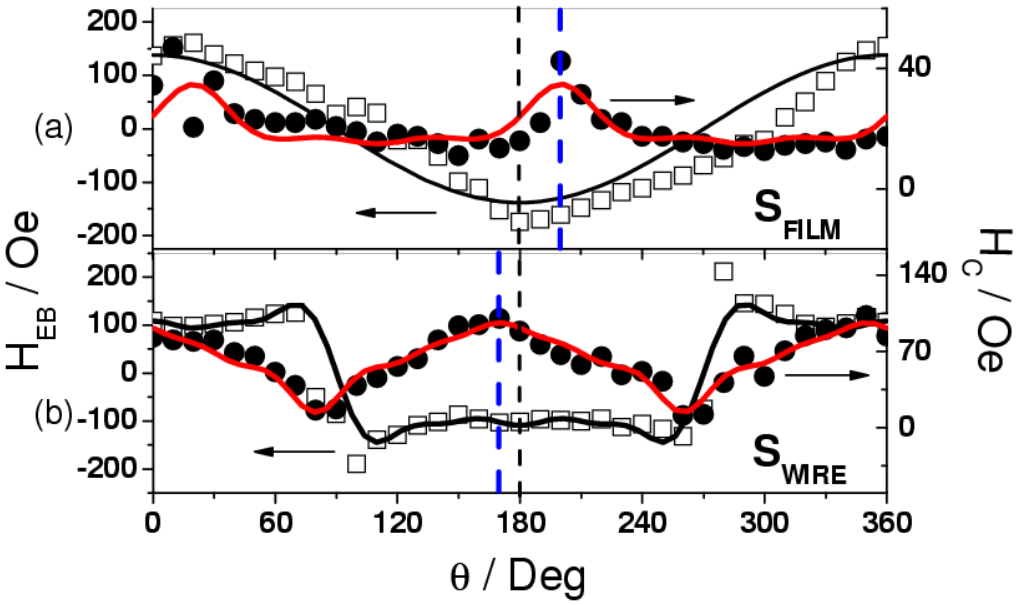


Figure 5.10: Angular dependence of coercivity and EB field of annealed sample (a) $S_{FILM}$ and (b) $S_{WIRE}$. All curves fitted to Ambrose model. Thin dashed line indicates the $K_{eb}$ direction, at 180°; thick dashed line indicates the coercivity peaks [155].

subsequently annealed in a vacuum chamber for 1h at 280°C, with a permanent magnet positioned along the same direction as the growth, and others kept in their as-grown state.

The angular dependence of the coercivity, $H_c(\theta)$, and the EB field, $H_{eb}(\theta)$, were measured by MOKE at room temperature for annealed samples, $S_{FILM}$ and $S_{WIRE}$ (Fig. 5.10). For a quantitative analysis, we applied the model of Ambrose *et al* [156], asserting that the unidirectional anisotropy has an inherent symmetry of $UD(\pi+\phi) = -UD(\phi)$ and uniaxial anisotropy has an inherent symmetry of $UA(\pi+\phi)=UA(\phi)$, resulting in the basic symmetry properties of $H_c$ and $H_{eb}$:

$$H_C(\theta) = H_C(0) \sum_{n=even} b_n \cos(n\theta), \tag{5.1}$$

$$H_{EB}(\theta) = H_{EB}(0) \sum_{n=odd} b_n \cos(n\theta), \tag{5.2}$$

where $\phi$ is the angle between the magnetization and exchange anisotropy axis, $\theta$ is the angle between the applied field and the EB direction and $\theta = 0^o$ represents the direction of $K_{eb}$. $H_{eb}$ for $S_{FILM}$ is reproduced by a single *cosine* term and expressed as $H_{eb}(\theta) = 138\text{Oe} \cos\theta$ (higher order terms are negligible). The angular dependence of coercivity, $H_c(\theta)$, displays two peaks; however, both are shifted to higher angles, by about 20°, with respect to 0° and 180°. The data points around $0^o$ have larger experimental errors due to the weak MOKE signals (around 0°) with the ensuing inaccurate reading of switching fields from hysteresis loops, but the 20° shift is clearly seen at $\theta$ = 200° (=180°+20°). This shift indicates the existence of a small uniaxial anisotropy at an angle of 20° from the direction of $K_{eb}$. This uniaxial anisotropy, termed as $K_{U\text{-}intrinsic}$, is very likely caused by the oblique growth condition during deposition, as the ion beam is directed from the target to the substrate at a small angle. Taking into account the misalignment of the $K_{U\text{-}intrinsic}$ and $K_{eb}$, the angular dependence of coercivity can be well-fitted, without including the noisy data around $0^\circ$, by even *cosine* terms expressed as: $H_c(\theta) = 20\text{Oe}$ (1+

0.34cos2($\theta$–20°) - 0.2cos4($\theta$–20°) + 0.14cos6($\theta$–20°) - 0.02cos8($\theta$–20°) + 0.01cos10($\theta$–20°)). Further, a small asymmetric behavior was observed for $H_{eb}$, which is also attributed to the misalignment of $K_{eb}$ and $K_{U\text{-}intrinsic}$.

For the $S_{WIRE}$ sample, due to the additional uniaxial shape anisotropy $K_{U\text{-}shape}$, arising from the wire morphology, the angular behavior of $H_{eb}$ and $H_c$ are both greatly modified. The coercivity was largely enhanced and clearly exhibited two maxima at ≈170° and ≈350° and two minima at ≈80° and ≈260°. The angular dependence of coercivity satisfies $H_c(\theta)$=63Oe (1+ 0.5cos2($\theta$+10°)- 0.07cos4($\theta$+10°)+ 0.1cos6($\theta$+10°)- 0.05cos8($\theta$+10°)+ 0.05cos 10($\theta$+10°)). The peaks of $H_c(\theta)$ are shifted to lower angles with respect to $K_{eb}$, by ~ -10°, indicating that the effective, $K_U$, combining $K_{U\text{-}intrinsic}$ and $K_{U\text{-}shape}$ , is non-collinear by about -10° with respect to $K_{eb}$. From these measurements, $K_{U\text{-}intrinsic}$ and $K_{U\text{-}shape}$ cannot be determined individually. For exchange bias, a single *cosine* term is no longer enough for fitting $H_{eb}(\theta)$; higher order *cosine* terms are required to obtain a good fitting, i.e., $H_{eb}(\theta)$ =136Oe (cos$\theta$- 0.42cos3$\theta$+ 0.28cos5$\theta$- 0.13cos7$\theta$+ 0.08cos9$\theta$). Besides, two asymmetric points are observed in $H_{eb}(\theta)$, at $\theta$=100° and $\theta$=280°. The higher order terms in the fitting and the asymmetric points in $H_{eb}(\theta)$ are both attributed to the wire-induced shape anisotropy along with the misalignment of $K_{eb}$ and effective $K_U$ in the $S_{WIRE}$ sample.

*5.3.2 Misaligned magnetocrystalline and shape anisotropy*

The effect of misaligned magnetocrystalline and shape anisotropies on the magnetic reversal was also studied [157]. Epitaxial Fe (15 nm thick) nanowire arrays were fabricated on MgO(001) using NIL

and the Mo lift-off technique. During imprint, the direction of the wires were purposely patterned at an angle, $\delta$ (~40°), with respect to the diagonal of the substrates (MgO(001)[110]) to induce an artificial misalignment, as shown in Fig. 5.11.

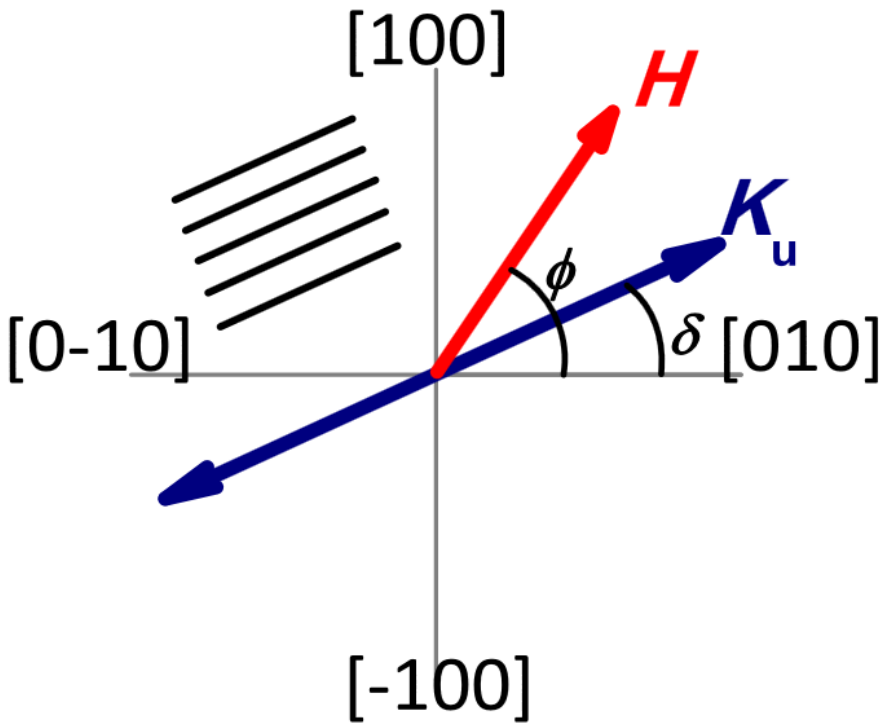


Figure 5.11: The relative orientations between the cubic Fe easy axes, the lithographic induced uniaxial anisotropy, $K_u$, and the external magnetic field. [157]

The large $K_u$ of the nanowires effectively induced an independent easy axis for the DW nucleation and propagation, which is verified by magneto-optic Kerr effect measurements using both longitudinal and transverse modes at various field orientations, $\phi$, defined as the angle between the external field and the Fe[010] axis (Fig. 5.11). For $\phi$ = 0°, sharp and two-step magnetization reversal was observed due to the breaking of the Fe cubic symmetry by the large, misaligned $K_u$ (Fig. 5.12(a)). The two-step switching route is: [010] → $K_u$ → [0-10], mediated by the nucleation and propagation of DWs along $K_u$ at $H_1$, and along [0-10] at $H_2$, respectively. For $\phi$ = 90°, far away from the $K_u$, a more complex three-step loop can

be observed (Fig. 5.12(b)). On the descending branch, the three steps correspond to the switching routes: [100] → [0-10] → $K_u$ → [-100]. The first switching is mediated by a 90° DW nucleation and the second one is attributed to the DW movements along $K_u$. The magnitude of the DW pinning energy, $\varepsilon_{90^\circ}$, and $K_u$ can be estimated by the switching fields as $\varepsilon_{90^\circ}/M$ = 51 Oe, $K_u cos\delta/M$ = 558 Oe (and therefore $K_u/M$ = 680 Oe), where $M$ is the total magnetization of the film. Such a large $K_u$, that is an order of magnitude higher than $\varepsilon_{90^\circ}$, effectively induced an independent easy axis for DW nucleation and propagation, which is difficult to be achieved in any continuous films. We also note that in the corresponding MOKE transverse signals, a 'flat basin' was observed around $H$ = 0 but with a small peak corresponding to the switching route [0-10] → $K_u$. Since the [010] axis is quite close to $K_u$, it is likely that the DW nucleation takes place simultaneously along both axes during the first reversal, i.e. [100] → [0-10], resulting in certain magnetization pinned along $K_u$ before the second switching. As a result, the small peak is observed when the rotating magnetization becomes collinear with the previously pinned magnetization.

Actually, the multi-step features can be observed at nearly all angles of the measurement. Close to [010] and [0-10], similar two-steps can be observed, for example, at $\phi$ = 340° (Fig. 5.12(c)). The only difference is an enhanced magnetization rotation behavior at higher field range, compared with the loop measured exactly at the easy axis (Fig. 5.12(a)). Physically, the magnetization would first rotate to a nearby easy axis just like a macrospin as the field decreases, before the nucleation of any new DWs. Another kind of two-step loop is shown in Fig. 5.12(d), for example, at $\phi$ = 120°, i.e., measured close to the Fe hard axis. Gradual magnetic reversal, rather than step switching was observed in the hysteresis curve, indicating that the magnetization reversal by coherent rotation is the dominant process.

Nevertheless, the two-step feature, indicating DW-type reversals, can still be clearly recognized in the transverse MOKE signals.

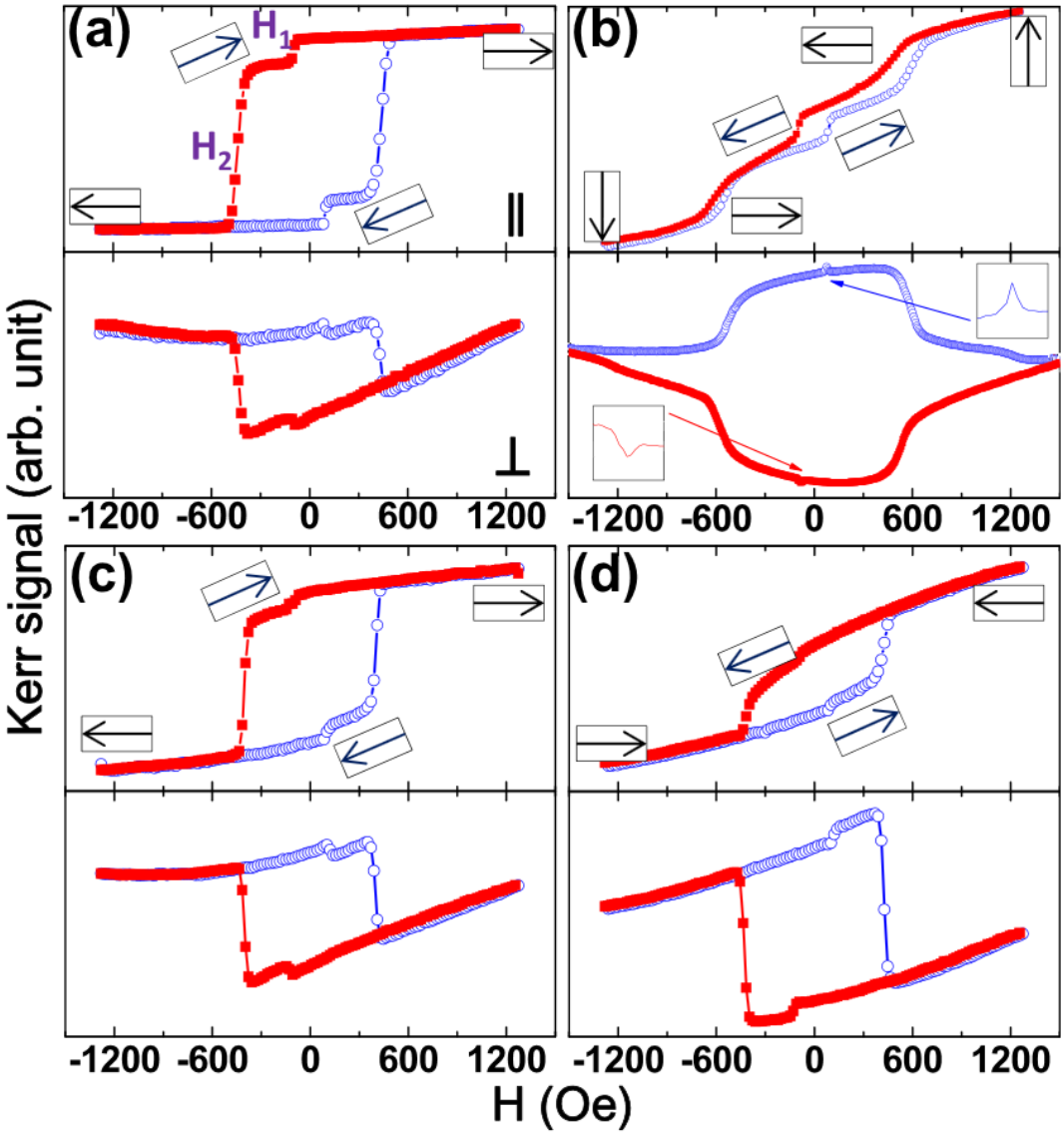


Figure 5.12: Longitudinal and transverse MOKE signals measured at (a) $\phi = 0°$, (b) $\phi = 90°$, (c) $\phi = 340°$, (d) $\phi = 120°$. Magnetization orientation at each step is illustrated by an arrow enclosed in a box. [157]

The $\phi$–dependence of the experimentally observed switching fields were summarized from the hysteresis loops of all $\phi$ from 0° to 360° in steps of 10° (Fig. 5.13). Two-step loops were observed at most $\phi$ and three-step ones were found at 90° and 270°. Specifically, $H_1$ was correlated to the magnetization

reversal from $K_u$ to the closest Fe easy axes, i.e. either Fe[010] or Fe[0-10]. Due to the uniaxial symmetry of $K_u$, the angular dependent behavior of $H_1$ shows a two-fold symmetry (Fig. 5.13(a)). On the other hand, $H_2$ indicates the magnetization reversal between the Fe cubic easy axes, and therefore, shows a fourfold-like symmetry with the four local maximums observed at $\phi = 0°$, $\phi = 90°$, $\phi = 180°$, and $\phi = 270°$ (Fig. 5.13(b)). In epitaxial Fe thin films, the induced uniaxial anisotropy and the intrinsic cubic magnetocrystalline anisotropy are superimposed on each other, resulting in new sets of non-orthogonal, bi-axial easy axes [16-19]. Here, in our epitaxial Fe nanowires, the significant uniaxial shape anisotropy effectively induces an independent easy axis for DW nucleation and propagation, while the intrinsic symmetry of the magnetocrystalline anisotropy was maintained.

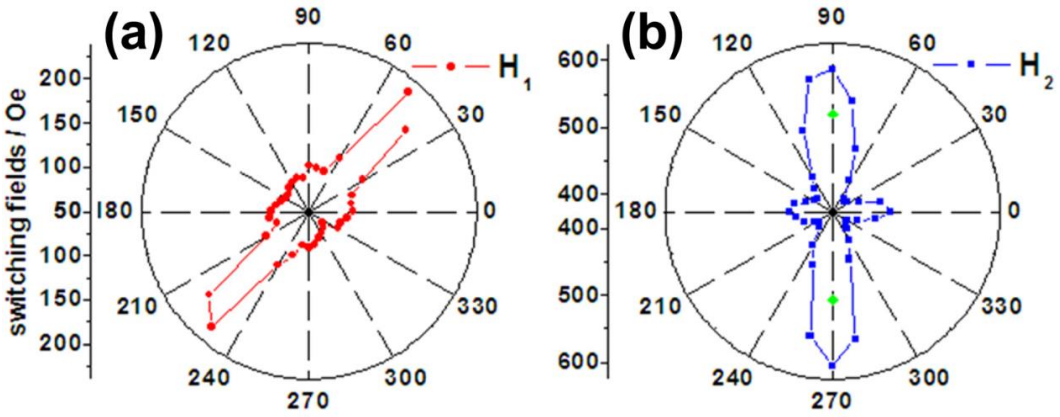


Figure 5.13: $\phi$-dependence of the experimentally observed switching fields for (a) $H_1$, displaying a twofold symmetry, and (b) $H_2$, showing a fourfold-like symmetry, respectively. Three-step loops were observed only at $\phi$=90° and 270° therefore an additional switching field was observed [157].

*5.4 Activated interfaces in exchange-biased nanodots*

In previous sections we have focused our discussions on the magnetic properties of nanowires. In this section, we will discuss the magnetic reversals in EB nanodots. Specifically, we will focus on the

activated/non-activated interfaces for exchange bias, which is one of the most important aspects in these nanodot structures. The motivation of such discussion is the 'always-confusing' effective interfaces of EB in these very small structures. In most analyses on EB nanostructures, the simple phenomenological equation:

$$\gamma A = \mu_0 M_s V H_{eb} \tag{5.3}$$

is still popularly used to determine the bias field of the sample, where γ is the interfacial exchange coupling, $A$ is interfacial surface area, $M_s$ is the F magnetization, and $V$ is the F volume. For one nanodot, the value of $A$ is usually given by the top surface area of such nanodot, independent of its thickness, since the AF layer is believed to be deposited 'on top of' the F layer. However, the possible contributions from the lateral surfaces of the nanodot to EB were not properly accounted in such an analysis. In a real sample fabrication, as illustrated in Fig. 5.14, the lateral surfaces of the F structure are likely also covered and thus biased by the AF material. For very small nanodots with large surface-to-volume ratio, the contribution from these additional interfaces to EB has to be taken into consideration for a more accurate analysis.

To account for the effect of the lateral EB interfaces, we propose a simple analytical model that considers the nanodot as a rectangle bar, made of Co, and with the dimension, L × W × H (Fig. 5.15). It should be noted that other EB systems (materials) can be also considered. Next, we assume the AF layer (e.g. CoO) is deposited so that the nanodot is covered by a thin CoO layer on all its surfaces except the bottom one (contacting with the substrate). For simplicity, the thickness of the AF layer, $t$, is homogeneous for all surfaces. As a result, there are totally five effective Co/CoO interfaces, named 'top', 'left', 'right', 'front' and 'back'. A 3D view and cross-section views for the Co rectangle bar are indicated

in Fig. 5.15. The interface area, $A$, of Eq. (5.3), can be written for each surface:

$$A_{left} = A_{right} = (L - 2t)(H - t)\,, \tag{5.4a}$$

$$A_{front} = A_{back} = (W - 2t)(H - t)\,, \tag{5.4b}$$

$$A_{top} = (L - 2t)(W - 2t), \tag{5.4c}$$

and the total F volume, $V$, is:

$$V = (L - 2t)(W - 2t)(H - t). \tag{5.5}$$

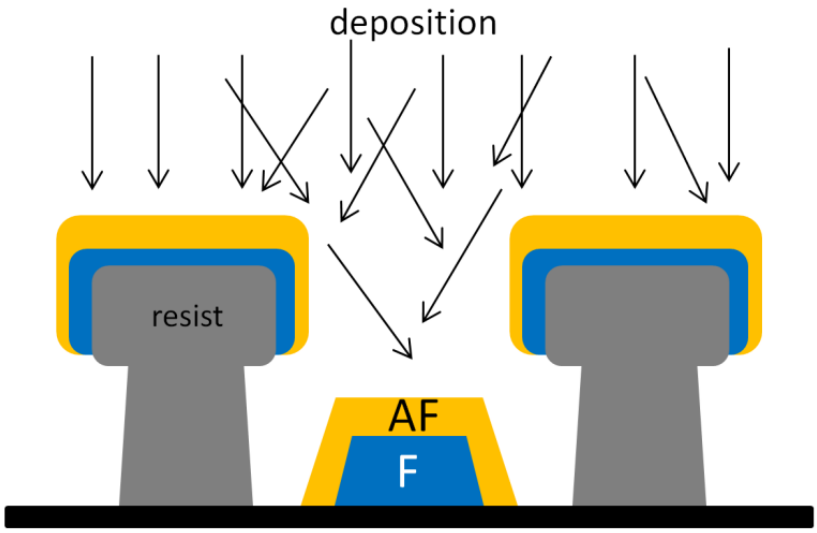


Figure 5.14: Illustration of a real sample fabrication by lithography-deposition-liftoff. The lateral surfaces of the F structure are likely also covered and thus biased by the AF material. The contribution from these additional interfaces to EB has to be taken into consideration for a more accurate analysis.

After field cooling to a temperature below the blocking temperature, the different interfaces, depending on the field cooling (FC) direction, are activated differently to induce the EB field. We consider three different FC scenarios. As shown in Fig. 5.16, FC along the long axis, L, will effectively activate the $A_{top}$, $A_{left}$, and $A_{right}$; FC along the short axis, W, will effectively activate the $A_{top}$, $A_{front}$, and $A_{back}$; FC along the normal axis, H, will effectively activate the $A_{left}$, $A_{right}$, $A_{front}$ and $A_{back}$. In each case, the interfaces normal to the FC direction would not be activated as effectively as the parallel ones. Here, we

use $\gamma_{para}$ and $\gamma_{perp}$ to denote the coupling energy of the parallel ( $\parallel$ ) and perpendicular ($\perp$) interfaces with respect to the FC direction.

The predicted EB field for each FC direction can be written is:

$$FC^{L}: \mu_0 H_{eb} = [\gamma_{para}(A_{top} + A_{left} + A_{right}) + \gamma_{perp}(A_{front} + A_{back})] / M_s V, \quad (5.6a)$$

$$FC^{W}: \mu_0 H_{eb} = [\gamma_{para}(A_{top} + A_{back} + A_{front}) + \gamma_{perp}(A_{left} + A_{right})] / M_s V, \quad (5.6b)$$

$$FC^{H}: \mu_0 H_{eb} = [\gamma_{para}(A_{front} + A_{back} + A_{left} + A_{right}) + \gamma_{perp}(A_{top})] / M_s V. \quad (5.6c)$$

The differences in $H_{eb}$ from different FC processes can be significant in very small structures.

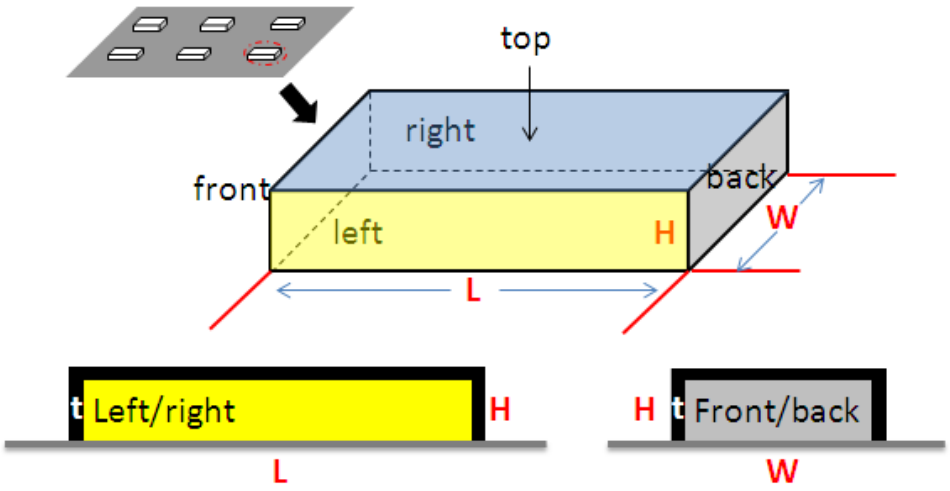


Figure 5.15: 3D view (top) and cross-section views (bottom) for the Co/CoO rectangle bar considered in our model.

As an example, we study a nanodot with the geometry of 30 nm × 90 nm (L = 3W). In our calculation, we used the spontaneous magnetization of Co, 1370 × $10^3$ A/m for the $M_s$, the value 0.3 mJ/$m^2$ for $\gamma_{para}$, and assumed a homogeneous CoO thickness, t =3 nm. All these values, including the nanodot dimension (L:W=3:1), are adopted from [158].

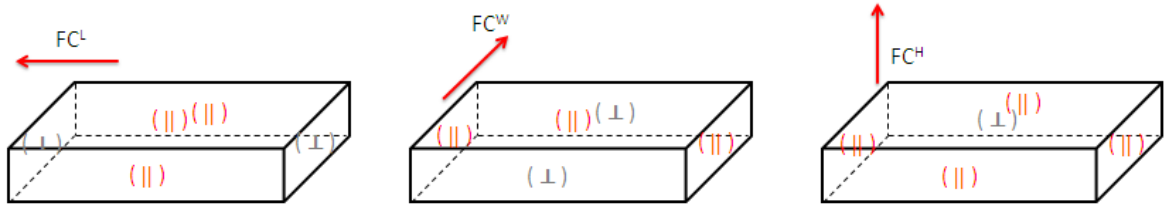


Figure 5.16: Illustration of the activated interfaces under different FC configurations. The interfacial coupling energy is different for parallel ( ∥ ) and perpendicular ( ⊥ ) interfaces with respect to the FC direction.

We first set H = 10 nm and varied the dimension, L and W. The calculated EB for the three FC cases are shown in Fig. 5.17. The value of $\gamma_{perp}$ is set equal to 82.8% × $\gamma_{para}$ = 0.25 mJ/m$^2$, derived from the bulk CoO structure [93]. The $H_{eb}$ values are different for the different FC conditions, and their differences decrease as the size of the nanodot increases. The difference between FC$^L$ and FC$^W$ is shown in Fig. 5.18. The two FC configurations give rise to ~20 Oe difference in $H_{eb}$ for a 10 nm × 30 nm nanodot, accounting for ~15% of its total $H_{eb}$. Next, we fixed the dimension, i.e. 90 nm × 30 nm, and varied H (Fig. 5.19). Similarly, the values of $H_{eb}$ rapidly decrease as H increases. In summary, for very small EB nanodots, different FC configurations give rise to quite significant differences in $H_{eb}$. Such differences decrease as the volume of the nanodot increases.

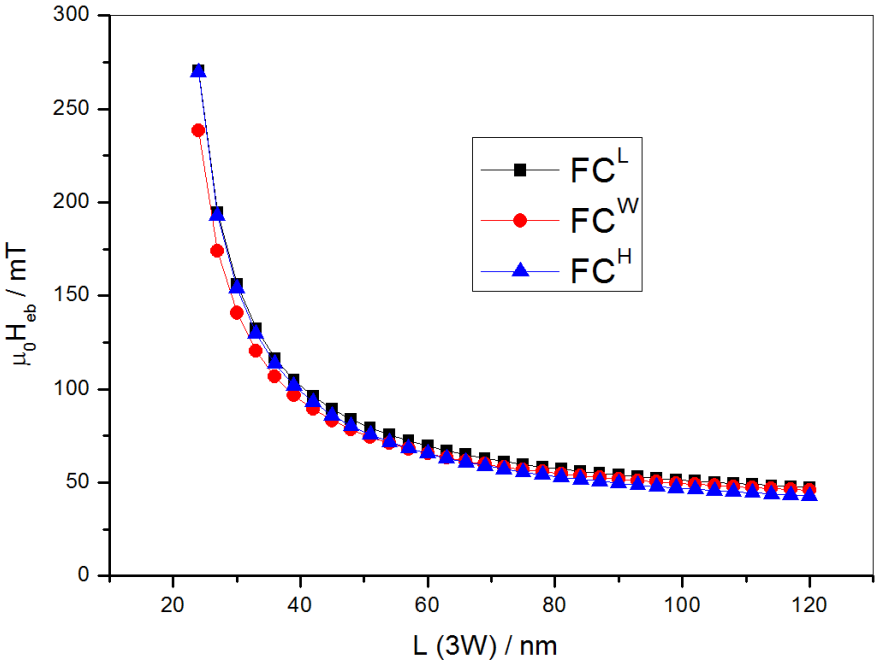


Figure 5.17: Calculated EB field vs. nanodot size for the different FC configurations. H is fixed to 10 nm.

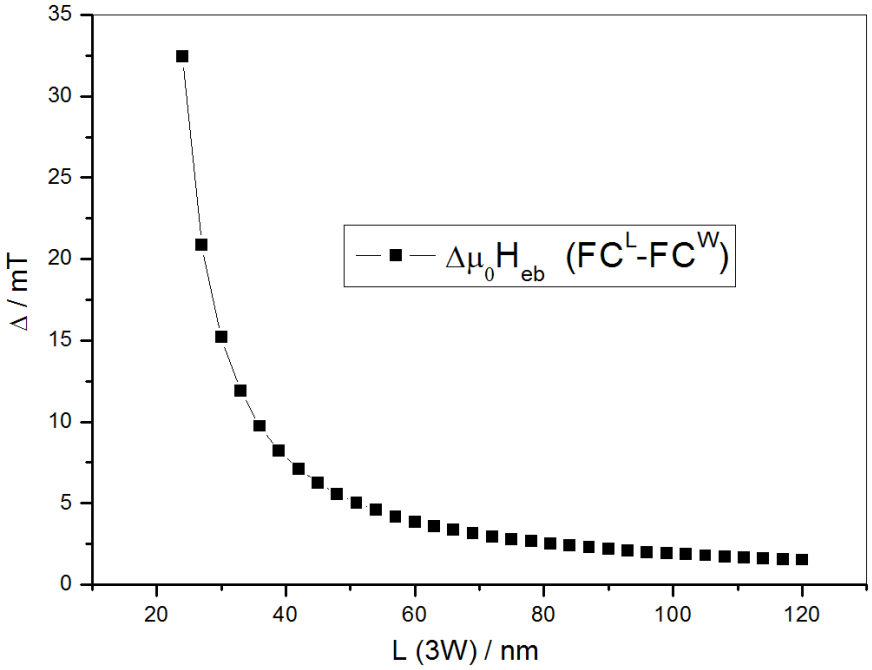


Figure 5.18: Calculated difference in EB field vs. nanodot size for $FC^L$ and $FC^W$ configurations. H is fixed to 10 nm.

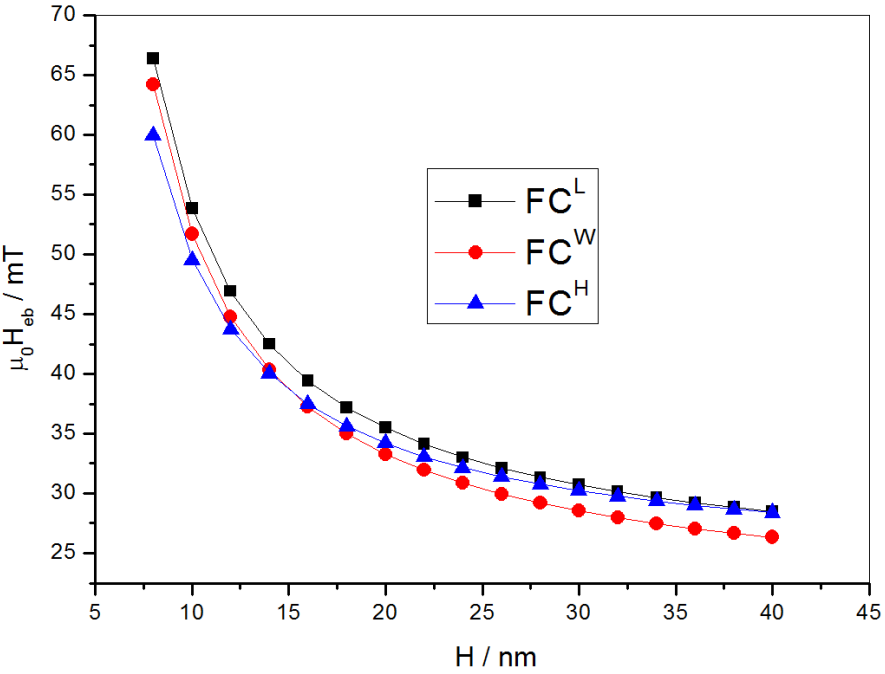


Figure 5.19: Calculated EB field vs. nanodot thickness for the different FC configurations. L is fixed to 90 nm.

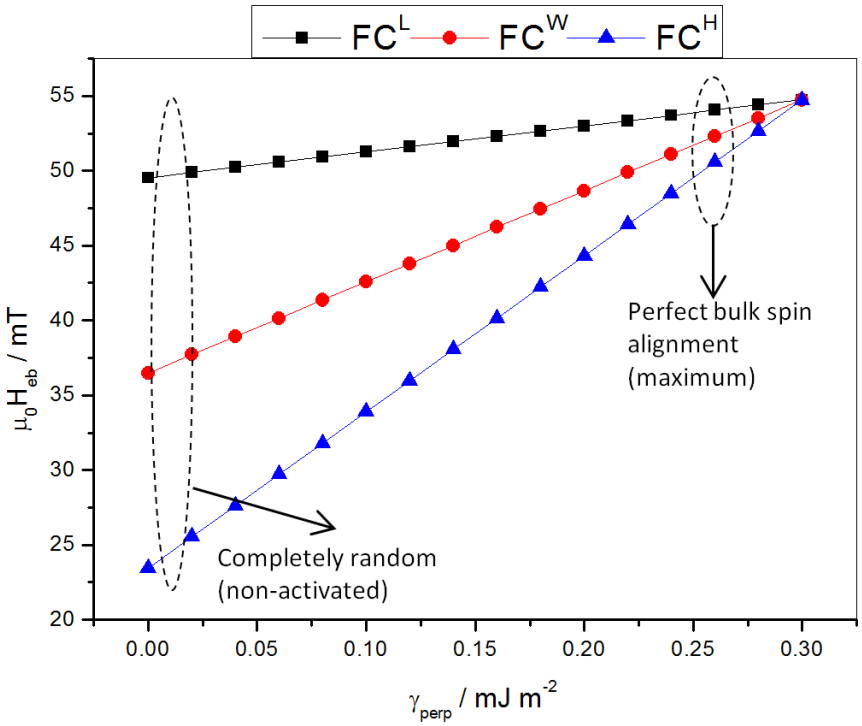


Figure 5.20: Calculated EB field vs. $\gamma_{perp}$ for the different FC configurations. L is fixed to 90 nm and $\gamma_{para}$ equals to 0.3 mJ/m$^2$.

Finally, for a fixed dimension of the nanodot, i.e. 90 nm(L) × 30 nm(W) × 10 nm(H), the EB value versus the perpendicular coupling strength, $\gamma_{perp}$, is also examined (Fig. 5.20). For real lab samples, the ratio, $\gamma_{perp}/\gamma_{para}$, lies in the range from 0 to 0.828, where 0 indicates a completely random/frustrated characteristic (not activated) of the perpendicular interface, while 0.828 (corresponding to $\gamma_{perp}$ = 0.25 $mJ/m^2$) is the maximum value for the perpendicular coupling energy derived from the bulk CoO structure [93].

In summary, by using a simple analytical model we have shown that the lateral interfaces of a nanodot contribute also to the EB field. Such contribution has been ignored for a long time, however, it can be quite significant in small structures (sub-50 nm). We propose, in our above calculations, that the effect of the lateral interfaces can be revealed by different FC and measuring configurations on a nanodot with certain aspect ratio. It would be very interesting to make the nanodots by lithography (e.g. NIL) and compare the experiments with our analytical model. In addition, the exchange coupling type and strength at the lateral interfaces under different FC processes worth to be investigated by advanced synchrotron techniques. In Chapter 4, we have shown that a NIL stamp can be made by e-beam lithography with similar features. Such experiments could be an interesting future work enlightened by this thesis.

# Chapter 6

# EXCHANGE BIAS USING A SPIN-GLASS

Contents of this chapter have been partially published in Ref.[182]

## *6.1 Thin-film/nanoparticle hybrid system*

The exchange-bias effect, as has already been introduced in previous chapters, is central to the design and operation of practical spin-electronic devices such as spin valves and magnetic tunnel junctions. Despite these successful applications, comprehensive understanding of EB has been elusive and remains a long-standing problem involving fundamental questions of surface and interface magnetism [36-41]. Phenomenologically, the EB effect manifests itself as a shift of the hysteresis loop along the field axis due to a unidirectional interface exchange coupling of a ferromagnet (F) and an antiferromagnet (AF). Typically, this shift of the hysteresis loop is in the negative field direction when cooled in a positive magnetic field and is usually referred to as negative EB. Such F/AF coupling has been widely studied in thin-film samples in which the F and AF phases, including their crystallography and interface spin-lattices, can be well-defined by controlling deposition conditions and studied with electrons and photons [159].

Recently, works on polycrystalline EB samples also showed that the AF layer is made of exchange-decoupled grains, whose size and size distribution play key roles to the EB effect. These AF grains, ~ 10 nm in size, essentially resemble small nanoparticles (NPs) [40]. Therefore, hybrid EB bilayers with the AF layer being chemically-synthesized NPs may bring pathways for tailoring their EB properties due to their controllable size, size distribution, morphology and crystallinity [160]. Such hybrid systems have not been reported so far. In addition, in nanostructured samples, such as NPs, a spin-glass (SG) state can be experimentally observed, particularly in metal-oxides [161] and –carbides [162], that show antiferromagnetic (AF) correlations. The SG state is a disordered magnetic state with frustrated interactions, augmented by stochastic positions of the spins, where conflicting interactions are randomly distributed. The term 'glass' is analogous to the positional disorder of a conventional, chemical glass. SG displays metastable structures leading to complex time scales which are difficult to explore. It is the unique time dependence which distinguishes SG from other magnetic systems. In most cases, such SG state arises from the random configuration of the surface magnetic moments and uncompensated surface spins with particularly enhanced contributions in NPs due to their large surface-to-volume ratio [163]. Further, such SG phases give rise to exotic properties when coupled with F phases. Recently, experiments on F/SG coupled bilayers showed EB related effects [164] that are typically observed in F/AF coupling. In particular, unusual positive EB, in addition to the conventional negative EB, have been discovered in the F/SG system and tentatively interpreted by an effective antiparallel coupling across the F/SG interface [165]. Further, temperature dependent measurements revealed subsequent decay of the positive EB after its establishment around blocking temperature, indicating that it may be a metastable state [166-168]. The disorder of the small AF grains or the grain boundaries have tentatively accounted for the above

experimental observations. However, particularly lacking in these models for such positive EB and the antiparallel coupling at the interface is a viable physical explanation for the origins of this phenomenon. Hybrid systems with the AF grains being replaced by NPs may provide a better route for revealing the important role of the AF grains to the EB effect.

We describe the discovery and investigation of a positive EB effect in a Fe-film/$CoO_x$-NP hybrid system. We reveal the co-existence of a positive EB with a SG magnetization, $M_{SG}$, which exhibit a strong relaxation effect depending on the magnetic cooling field and temperature. This SG magnetization is coupled antiparallel to the F magnetization upon field-cooling, as revealed by an *increase* in the field-free magnetization with time, i.e. a unique *upward* magnetization relaxation. This antiparallel coupling is further attributed to the antiferromagnetic superexchange interactions [169] of the local Fe-O-Co couples at the interface. Temperature dependent measurements show that the EB is determined by competing superexchange and conventional direct exchange interactions. Finally, our experimental results reveal the possibility of manipulating the EB effect via such an indirect exchange-coupling mechanism.

Bilayer samples were fabricated as follows: Co NPs (10 nm in diameter and with a narrow size distribution) were chemically synthesized by a thermal decomposition method [170,171]. Co-NP films, a few layers thick, were obtained by assembling these chemically synthesized Co NPs on clean Si substrates via a controlled solvent evaporation technique [172]. The films were annealed at 400$^{\circ}$C in a continuous $O_2$ flow furnace for 1.5 hours to convert the Co NPs to Co-oxide NPs.

*6.2 Surface analysis via the X-ray photoelectron spectroscopy*

Consistent with the O-rich annealing conditions, X-ray photoelectron spectroscopy (XPS) confirmed that the surface of $CoO_x$ is predominantly the thermodynamically stable $Co_3O_4$ with a CoO minor phase. The XPS was performed at 'National ESCA and Surface Analysis Center for Biomedical Problems (NESAC/BIO)' at the University of Washington through the external user program. All spectra were taken on a Surface Science Instruments S-probe spectrometer. This instrument has a monochromatized Al Kα X-ray source. X-ray spot size for these acquisitions was approximately 800 μm. Pressure in the analytical chamber during spectral acquisition was less than $5 \times 10^{-9}$ Torr. Pass energy for survey spectra (to calculate composition) was 150 eV and pass energy for high resolution scans was 50eV. The take-off angle (the angle between the sample normal and the input axis of the energy analyzer) was ~55° (55° take-off angle ≅ 50 Å sampling depth).

The Service Physics ESCA2000A Analysis Software was used to determine peak areas, to calculate the elemental compositions from peak areas above an inelastic (Shirley) background, and to peak fit the high resolution spectra. The binding energy scale of the high-resolution spectra was calibrated by assigning the most intense C1s high-resolution peak, a binding energy of 285.0 eV, i.e., hydrocarbon.

Two spots were analyzed. Analysis of the samples included survey spectra and high resolution spectra of C1s and Co2p peaks. A typical survey spectrum from the sample is shown in Fig. 6.1. C, O, and Co were detected on the sample surfaces. Surface compositions were calculated using the C1s, O1s, and Co3p peaks and collected in Table 6.1.

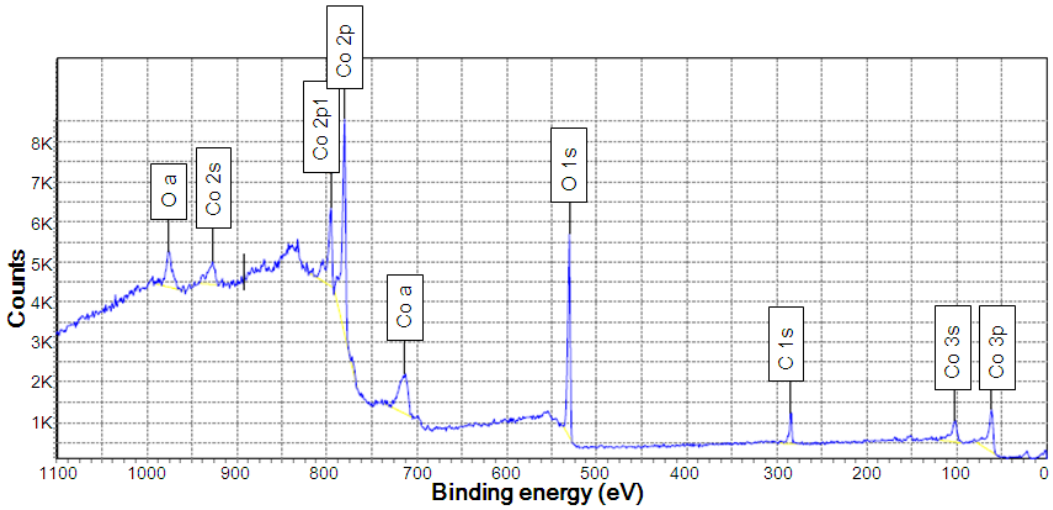


Figure 6.1: XPS survey from the $CoO_x$ sample.

| | XPS line | Atom % |
|---|---|---|
| Sample 1 | C1s | 20.8 |
| | O1s | 53.4 |
| | Co3p | 25.8 |
| Sample 2 | C1s | 20.9 |
| | O1s | 53.1 |
| | Co3p | 26.0 |

Table 6.1: $CoO_x$ Surface Composition.

Typical high resolution Co2p spectra from the sample were measured as shown in Fig. 6.2. Results from the Co peak fits were collected in Table 6.2.

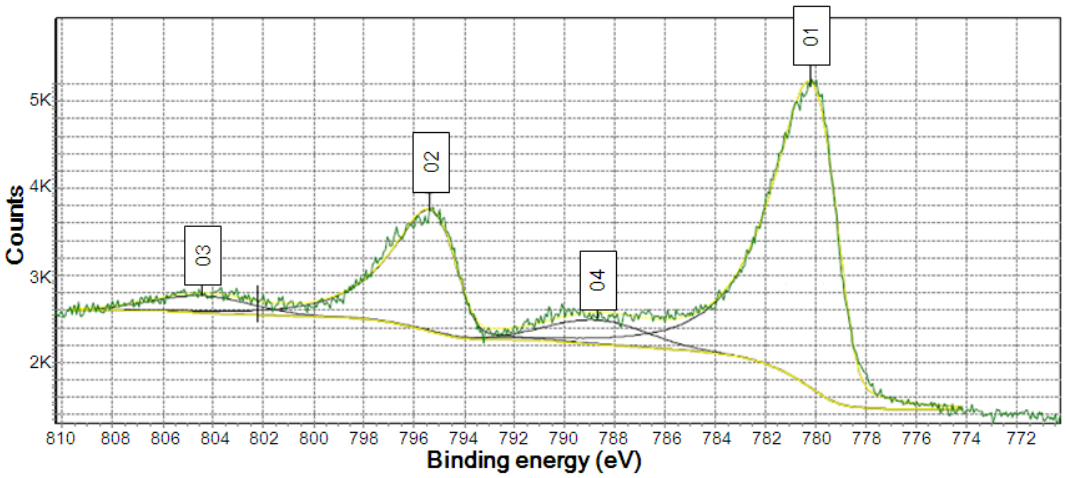


Figure 6.2: Co2p spectrum from the $CoO_x$ sample.

| | XPS line | Peak | Adjusted binding energy | Full width at half maximum |
|---|---|---|---|---|
| Sample 1 | Co 2p3/2 | 01 | 780.6 | 3.0 |
| | Co 2p1/2 | 02 | 795.8 | 3.0 |
| | * | 03 | 804.8 | 4.7 |
| | * | 04 | 789.1 | 4.7 |
| Sample 2 | Co 2p3/2 | 01 | 780.5 | 3.3 |
| | Co 2p1/2 | 02 | 795.8 | 3.3 |
| | * | 03 | 804.7 | 5.3 |
| | * | 04 | 788.7 | 5.3 |

Table 6.2: Co 2p peak fit results for the $CoO_x$ samples. (* = shake-up peaks)

The chemical bonding was identified by comparison of these values with values reported in the National Institute of Standards and Technology XPS database Version 3.5 and references therein. The

Co2p3/2 peak at 780.5-780.6 eV was consistent with those reported for $Co_3O_4$ (780.0 +/− 0.5) or CoO (780.5 +/− 0.3) or perhaps $Co_2O_3$ (780.4 +/− 0.8), though the values for the latter compound are sparse and variable. The difference in the 2p3/2 – 2p1/2 binding energies from the nanoparticle samples was 15.2 eV versus 15.2 for CoO and $Co_3O_4$ and 15.8 for $Co_2O_3$, so that the samples were primarily CoO and/or $Co_3O_4$. Finally, the weak intensity of the shake-up peaks at 789 and 805 eV indicated the surface was primarily $Co_3O_4$, as $Co_3O_4$ has weak shake-up peaks versus much stronger shake-up peaks for CoO. A collection of the standard spectra of Co-oxides can be found in [173]. Compared with Co-metal, CoO, $Co_3O_4$ and $Co(OH)_2$ all exhibit a shake-up peak around 805 eV. However, such shake-up peak is strong for both CoO and $Co(OH)_2$, while it is much weaker for $Co_3O_4$. This shake-up peak is important in identifying different valence states. Our XPS spectrum is very similar to the $Co_3O_4$ data reported in [173].

*6.3 Surface characterizations and magnetic measurements*

Scanning electron microscopy, Fig. 6.3(a), showed the particle size ~ 10nm dia. and atomic force microscopy (AFM), Fig. 6.3(b), confirmed a surface roughness < 4 nm. Next, we deposited a 30 nm Fe film followed by a 5 nm Ta cap, by ion beam sputtering at a base pressure ~$1 \times 10^{-7}$ Torr on top of the Co-oxide NP film. The magnetic properties were measured by a Quantum Design physical property measurement system over a wide range of temperatures and applied fields.

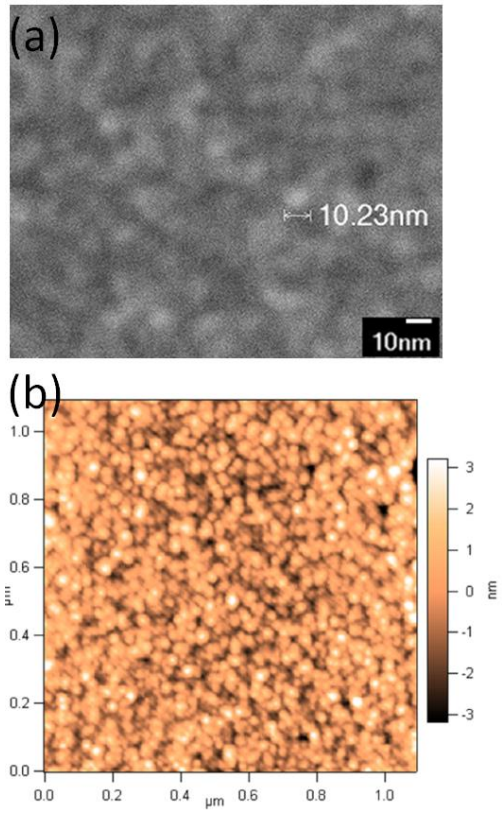


Figure 6.3: SEM (a) and AFM (b) images of the Co-oxide NP film.

Hysteresis loops of the sample at various temperatures from 10 to 300 K were measured (Fig.6.4(a)) and the temperature dependence of the coercivity, $H_c$ and the bias field, $H_{eb}$ are summarized in Fig. 6.4(b). The sample was initially cooled under a magnetic field, $H_{cool}$ = 10 kOe from 380 K down to 10 K and then measured on increasing temperature. For all $T$ < 200 K, the hysteresis loops exhibit a negative shift from the origin which is a signature of conventional EB. This EB is attributed to the exchange coupling between Fe and ordered CoO, below the blocking temperature ($T_B$, ~ 186 K) of the antiferromagnetic CoO phase [166]. When the sample is measured at temperatures higher than 200 K (CoO disordered), the loop-shift has switched to the same direction as $H_{cool}$, which indicates an unconventional positive EB and its magnitude, $H_{eb}$ ~9 Oe, remains roughly unchanged from 200 to 300 K. Careful calibrations and

repeated measurements were performed to ensure that the measured EB effect came from the sample and was not an artifact.

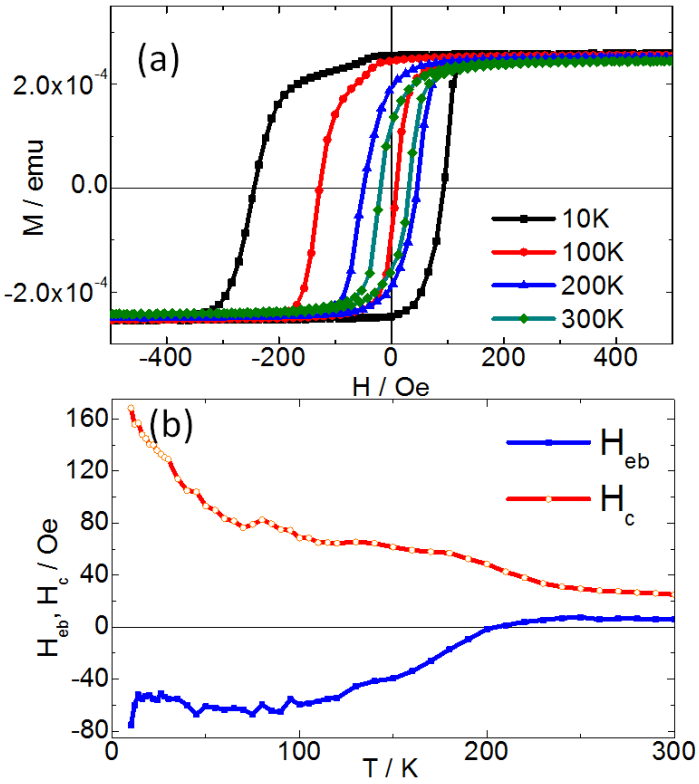


Figure 6.4: (a) Hysteresis loops of Fe/Co-oxide bilayers measured at selective temperatures upon field cooling. (b) Temperature dependence of the coercivity, $H_c$, and the exchange bias, $H_{eb}$.

The change in sign of EB points directly to a change in the nature of the *effective coupling* across the Fe/Co-oxide interface. As illustrated in Fig. 6.5(a), below 200 K, the CoO AF phase is well established thus the effective parallel ($J_1 > 0$) coupling between Fe ($S_{Fe}$) and Co ($S_{Co}$) spins, gives rise to the conventional negative EB [166]. Above 200 K, when the CoO loses its magnetic order, the result of the effective antiparallel coupling ($J_2 < 0$) between $S_{Fe}$ and the local SG magnetizations becomes visible (the origin of such coupling will be discussed later). To gain more insight into the physical mechanism of such coupling, we performed detailed field- and time-dependent measurements. Samples were initially cooled from 380 K to 300 K under various positive cooling fields, $H_{cool}$; after the temperature stabilized at 300 K,

the hysteresis loops were measured (Fig. 6.5(b)). Rounded hysteresis loops, rather than squared ones, were observed due to the imperfect Fe crystallinity of the particle film. Positive EB was observed and its value slightly increases with increasing $H_{cool}$ (= 0.5, 1, 2, 3, 5, 10 kOe). We then measured hysteresis loops after 24 hours and found the EB disappeared, regardless of the *magnitude* or *direction* of $H_{cool}$ (Fig. 6.5(b)). It also reconfirmed that the observed positive EB originated from the sample. These results together revealed two important characteristics of the antiparallel coupling that (1) it can be promoted by field cooling, but (2) it is only a metastable state.

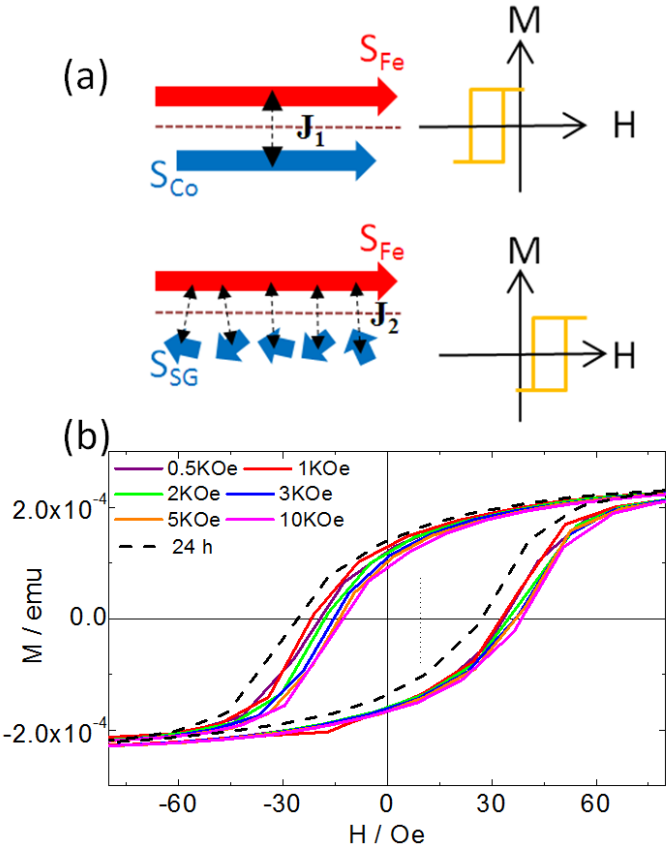


Figure 6.5: (a) Schematic illustration of the effective interface coupling that leads to negative or positive EB, i.e., parallel coupling ($J_1$>0) of $S_{Fe}$ and $S_{Co}$ at $T$ < 200 K, and antiparallel coupling ($J_2$<0) of $S_{Fe}$ and $S_{SG}$ at $T$ > 200 K. (b) Field cooling dependence of hysteresis loops at 300 K.

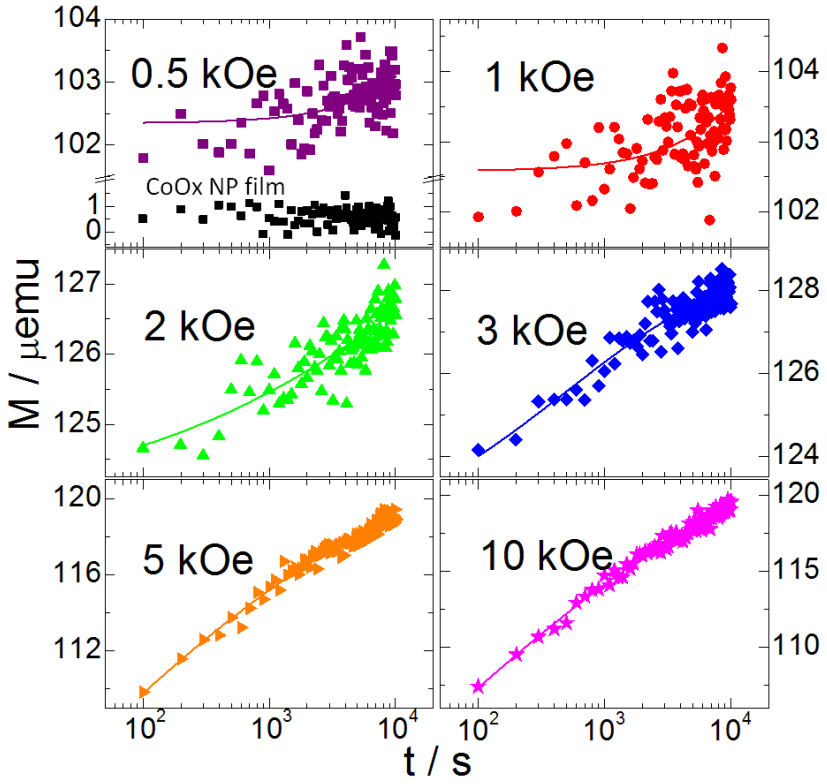


Figure 6.6: Cooling field dependence of the relaxation behavior, $M_{TRM}(t)$, measured at 300 K. Sample was cooled selectively under different fields, i.e. 0.5, 1, 2, 3, 5, 10 kOe. The curves are fitted by stretched exponential function (Eq. (6.1)) with fitting parameters listed in Table 6.3.

To characterize this metastable interfacial coupling, we further studied the time dependence by thermoremanent magnetization (TRM) measurement, $M_{TRM}(t)$ in a total time scale of $1.2 \times 10^{-4}$ s. For the measurements, the samples were initially cooled in positive $H_{cool}$ (= 0.5, 1, 2, 3, 5, 10 kOe) from 380 K to 300 K. After the temperature was stabilized at 300 K, with a fixed waiting time, $t_W$ = 200 s, $H_{cool}$ was reduced to zero and the magnetization was recorded at 300 K in zero field as a function of time. Fig. 6.6 showed the relaxation curve at each $H_{cool}$. The magnetization increases with time for all cooling fields. This increase, or 'upward' relaxation phenomenon, is inconsistent with the general expectation that the magnetization decrease with increasing time when measured in zero applied field. However, these results are consistent with an initial magnetization component pointing against the direction of $H_{cool}$ upon field

cooling which then diminishes on aging with time. This magnetization is also not due to unoxidized Co as the samples were annealed in a very O-rich environment. To further disprove this possibility, we measured a pure Co-oxide NP film and found no ferromagnetic response (hysteresis) or magnetization relaxation. Therefore, we attribute this behavior to the surface SG magnetization, $M_{SG}$, of the NPs [174] originating from the disordered AF phase. The effect of this SG component is more significant in NPs than in continuous films due to the local asymmetry of the NPs (reduced size, irregular shape, possible defects, etc). Each NP has a certain SG magnetization but they are disordered across the whole NP-film for temperatures greater than the glass transition temperature, $T_{SG}$. In our experiments, $H_{cool}$ aligns the magnetic moments of F (Fe) along the direction of the cooling field. When $H_{cool}$ is removed, the direction of the F magnetization, $M_F$, remains unchanged due to the large energy barriers and associated large relaxation time. The antiparallel interface coupling between F/SG switches the magnetization, $M_{SG}$, of the SG to a direction opposite to that of the cooling field, i.e., the effective F/SG coupling is antiferromagnetic ($J_2 < 0$). This antiferromagnetic coupling simultaneously gives rise to both positive EB and the upward relaxation. When the cooling field is turned off, $M_{SG}$ relaxes from the $-H_{cool}$ direction to random orientations arising from thermal activation. Therefore, the magnetization of the system relaxes (increases) from $M_F$-$M_{SG}$ to $M_F$. We further interpret the data by a stretched exponential function which is typically used in modeling magnetization relaxation behaviors [162]. The function expresses as:

$$M_{TRM}(t) = M_F^0 - M_{SG}^0 \exp[-(t/\tau)^{1-n}] \ , \tag{6.1}$$

where $M_F^0$ and $M_{SG}^0$ are time-independent, initial values for the F and SG components, respectively, that

are responsible for the observed relaxation behavior. The parameter $n$ and the time constant $\tau$ describe the relaxation rate of the SG component. The aging effect shows clear dependence with the magnitude of the cooling field; stronger $H_{cool}$ results in more significant relaxation behavior. The fitting parameters of the relaxation curves are summarized in Table 6.3. In general, $M_F^0$ is large (~$1 \times 10^{-4}$ emu) and almost unchanged; $M_{SG}^0$ increases with $H_{cool}$ and $\tau$ decreases with $H_{cool}$. Weak relaxation and small $M_{SG}^0$ (~$10^{-6}$ emu) were found for small $H_{cool}$ ( = 0.5, 1 kOe) that can hardly be modeled by the exponential function. It is noted that such small $M_{SG}^0$ is still above the sensitivity of our PPMS magnetometry (~$10^{-7}$ emu). On the other hand, much greater $M_{SG}^0$, as large as $6.0 \times 10^{-5}$ emu is activated at $H_{cool}$ = 10 kOe. Thus, larger cooling field can effectively activate more F/SG pairs at the interface, resulting in greater $M_{SG}^0$ and more significant relaxation (smaller $\tau$). For comparison, similar TRM measurement was also performed on pure Co-oxide NP film, Fig. 6.6. Negligibly small magnetization (< $10^{-6}$ emu) with almost no time dependence was observed. This indicates that without the FM/SG coupling, the external field can play no role on the SG magnetization. Finally, we measured relaxation curves at different temperatures from 10 K to 300 K upon field cooling from 380 K, using $H_{cool}$ = 10 kOe and $t_W$ = 200 s (Fig. 6.7). *Upward* relaxation was only observed for $T$ > 200 K, confirming that the positive EB is correlated to the surface SG behaviors. Below 200 K, normal downward relaxation was found and the time dependence is not substantial. For a complete discussion, we note that in some carefully-made planar films with large uncompensated AF magnetization, a random AF anisotropy can also lead to a sudden change in the EB sign but below the $T_B$. A vertical shift in the hysteresis loops was observed simultaneously as a signature of the uncompensated magnetization. In our particle films, the EB sign changed right above the $T_B$ where the AF phase already loses its magnetic order. No signature for the AF magnetization has been observed and the strong

relaxation behaviors confirmed the correlation of EB with the time-dependent SG magnetization.

| $H_{cool}$ (Oe) | $M_F^0$(emu) | $M_{SG}^0$(emu) | $\tau$ (s) | $n$ |
|---|---|---|---|---|
| 0.5 k | $1.1\times 10^{-4}$ | $7.7\times 10^{-6}$ | 100789 | 0.007 |
| 1 k | $1.1\times 10^{-4}$ | $7.4\times 10^{-6}$ | 75957 | 0.03 |
| 2 k | $1.3\times 10^{-4}$ | $6.3\times 10^{-6}$ | 55312 | 0.72 |
| 3 k | $1.3\times 10^{-4}$ | $7.3\times 10^{-6}$ | 522 | 0.62 |
| 5 k | $1.2\times 10^{-4}$ | $5.0\times 10^{-5}$ | 15 | 0.84 |
| 10 k | $1.2\times 10^{-4}$ | $6.0\times 10^{-5}$ | 20 | 0.85 |

Table 6.3: Summary of fitting parameters of the relaxation curve, using Eq. (6.1).

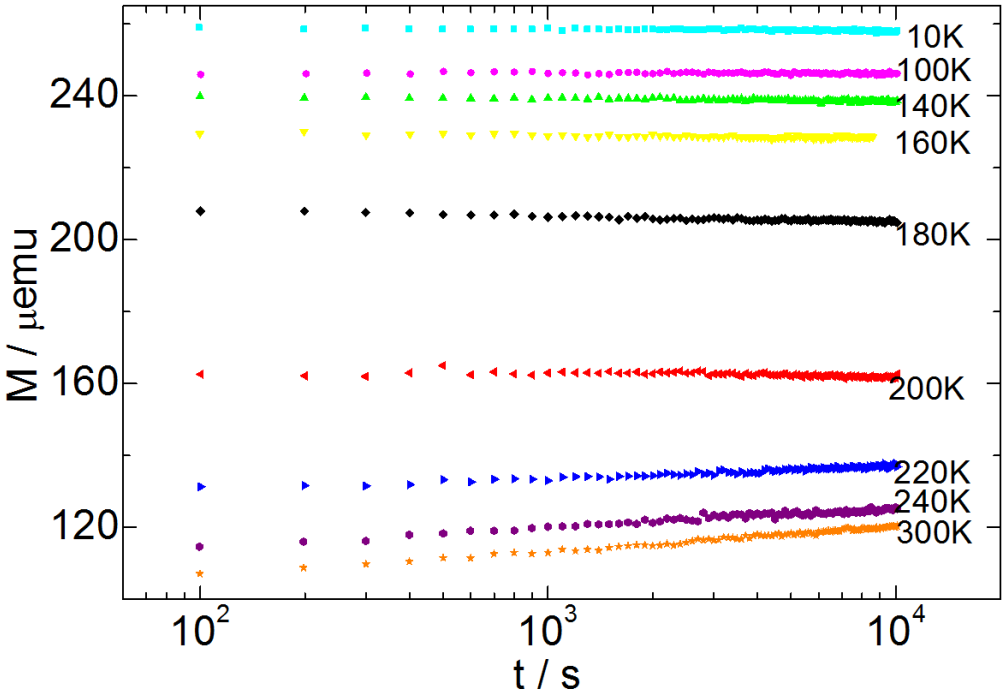


Figure 6.7: Relaxation behavior, $M_{TRM}(t)$, of Fe/Co-oxide measured at various temperatures from 10 – 300 K. Upward relaxation is only observed for $T > 200$ K, where the antiparallel coupling ($J_2<0$) dominates.

Earlier work has indicated that the superexchange effect might be responsible for the positive EB observed in Co/CoO bilayers [166]. Here, we carefully extend such interpretation and propose a model to explain the antiparallel coupling and the magnetization relaxation based on the interfacial superexchange

interaction [169]. Since the Co-oxide NP film was obtained from $O_2$ annealing of Co NPs, it is expected that large areas of the surface are oxygen terminated instead of metal (Co) terminated, which gives rise to surface oxygen dangling bonds [175]. After the Fe layer deposition, part of the interfacial Co spins may couple with Fe spins via superexchange mechanism mediated by the oxygen atom at the interface (Fig. 6.8(a)). Because Fe was deposited in a vacuum chamber, with an O-deficient environment, the Fe valence state is primarily $Fe^{2+}$ in the Fe-O-Co couple. The Co valence state is primarily $Co^{3+}$ as confirmed by XPS measurements. Figure 6.8(b) is a schematic illustration of such a $Fe^{2+}$-O-$Co^{3+}$ superexchange couple. Localized electrons in Fe and Co remain in their respective orbitals and transmit spin information via the O-bridge [176]. Antiferromagnetic superexchange coupling arises from the mediation of oxygen *p* electrons according to the so-called Goodenough-Kanamori-Anderson rules [177-179]. Such rules basically state that (1) the superexchange will be strongly anti-ferromagnetic between two magnetic ions with half-occupied orbitals which couple through an intermediary non-magnetic ion (e.g. $O^{2-}$), while (2) the coupling between an ion with a filled orbital and one with a half-filled orbital will be ferromagnetic. (3) The coupling between an ion with either a half-filled or filled orbital and one with a vacant orbital can be either antiferromagnetic or ferromagnetic, but generally favors ferromagnetic. (4) When multiple types of interactions are present simultaneously, the antiferromagnetic one is generally dominant since it is independent of the intra-atomic exchange term.

In certain localized O-rich area, small numbers of $Fe^{3+}$-O-$Co^{3+}$ superexchange couples with higher Fe valence state ($Fe^{3+}$) may also exist, however, the nature of such coupling is still antiferromagnetic [180] and thus will not affect our conclusion. These Fe-O-Co couples further lead to antiparallel configuration of the F and SG magnetization upon field cooling. Once the cooling field is cut off, each local SG

magnetization relaxes to a random orientation and reduces the total $M_{SG}$ finally to zero. It is worth noting that recently in the Fe/Fe-oxide NP system [165], similar positive EB was also reported with an O-deficient interface at $T > T_{SG}$. Their results can also be explained within our model by considering either $Fe^{2+}$-O-$Fe^{2+}$ (similar to $Fe^{2+}$-O-$Co^{3+}$ couple) or $Fe^{3+}$-O-$Fe^{3+}$ superexchange couple which are both antiferromagnetic [180,181].

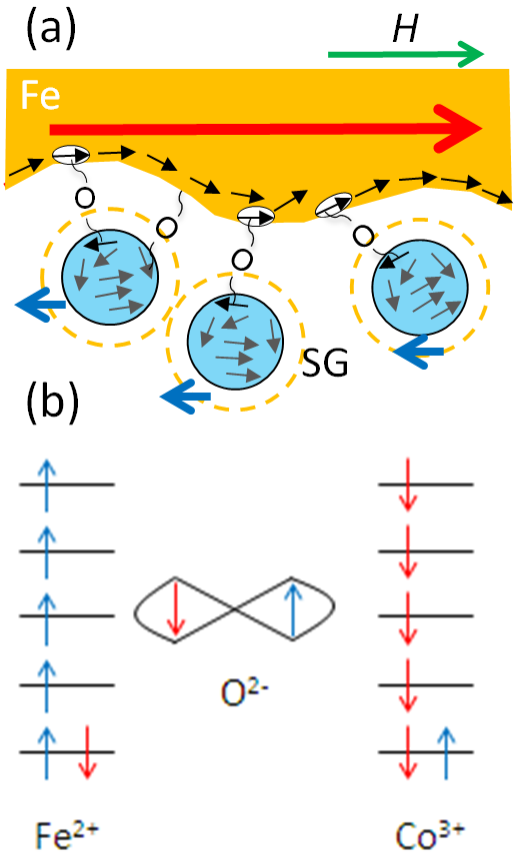


Figure 6.8: Schematic illustration of (a) the antiparallel coupled $M_F$ and $M_{SG}$ due to interface superexchange coupling; and (b) antiferromagnetic superexchange interaction between $Fe^{2+}$-O-$Co^{3+}$ couple.

In summary, in the hybrid Fe-film/Co-oxide NP systems, we have shown that the relaxation behavior of a spin-glass magnetization is responsible for the unconventional positive EB effect. This is due to the indirect superexchange coupling across the F/SG interface, where Fe moments are coupled antiparallel with the spin-glass in the Co-oxides. Such SG moments do not themselves respond to the external field;

however, they can show strong cooling field dependence mediated by the F/SG coupling. The key results of this chapter have been published in [182]. Our proposed scenario of the interface also provides insight to the positive exchange bias and related properties in other metal/metal-oxide EB systems.

# Chapter 7

# CONCLUSIONS AND FUTURE WORK

We have:

1) Developed epitaxial growth recipes for exchange-biased ferromagnetic/antiferromagnetic bilayers (Fe/IrMn, Fe/MnPd), and demonstrated the control of the magnetocrystalline anisotropy via such epitaxial growth.

2) studied the magnetization reversal properties of the epitaxial exchange-biased bilayers using magneto-optic Kerr effect and anisotropic magnetoresistance, and developed a quantitative model that well explains the domain wall nucleation and propagation behavior in these bilayers.

3) investigated systematically the dependence of magnetic anisotropies on the various sample parameters (layer thicknesses, temperature, relative orientations, interface spin behaviors, and the antiferromagnetic bulk structure).

4) developed large-area, high-speed, efficient epitaxial patterning process using nanoimprint lithography with a bilayer-resist template for improved lift-off, and demonstrated the fabrication of epitaxial magnetic

hetero-nanostructures (Fe/IrMn, Fe/MnPd) with different sizes from sub-100 nanometer to micrometer.

5) demonstrated a simplified approach for the release of synthetic antiferromagnetic nanoparticles into aqueous solution by a direct substrate etching.

6) studied the magnetization reversal and domain wall movement in epitaxial exchange-biased nanowire arrays under competing magnetocrystalline, exchange, and shape anisotropies.

7) investigated the interface coupling and positive exchange bias in a Fe-film/CoO-nanoparticles hybrid systems, and correlated the exchange bias to a unique interfacial superexchange effect for the first time.

This thesis provides a systematic understanding on the magnetization reversal under competing magnetic anisotropies and the spin behaviors both at the interface and in the bulk of epitaxial exchange bias systems. However, many of the unique reversal properties, such as the spin-reorientation-transition and multi-step domain-wall nucleation, require further investigations by advanced characterization techniques. For example, data on the temperature dependent thermal expansion of MnPd lattices might be needed to explain the spin-reorientation transition in Fe/MnPd bilayers; also the time-resolved magnetic imaging technique might be useful to provide insight on the successive domain-wall nucleation.

To better understand the magnetic reversal and interface coupling at small length scale, high-quality, epitaxial magnetic nanostructures are greatly desired, which involves further developing on the sub-100 nm nanoimprint lithography and related processes. The use of Ormostamp (Microresist Technology), combined with the Mo liftoff process, is very promising. From a physics point of view, exchange spring effect at the interface of the hard/soft magnets (such as FePd/FeNi) is also an interesting topic, in addition to the exchange bias effect studied in this thesis.

For the lithographic particle release, use of plastic stamps and substrates will help to simplify the

process and enhance the throughput of products. In addition, non-toxic Fe3O4 is a promising material for any future applications in the emerging field of bio-nanomagnetism. Additional investigations on the functional coatings of such magnetic nano-carriers are also greatly encouraged.

# BIBLIOGRAPHY


[1] M. T. Johnson, P. J. H. Bloemen, F. J. A. den Broeder, and J. J. de Vries, 'Magnetic anisotropy in metallic multilayers', *Rep. Prog. Phys.* 59, 1409, (1996). doi:10.1088/0034-4885/59/11/002

[2] S. Chikazumi, '*Physics of Ferromagnetism*', Oxford University Press. (1997). R. C. O'Handley, '*Modern Magnetic Materials, Principles and Applications*', John Wiley & Sons, Inc. (2000). A. Aharoni, '*Introduction to the Theory of Ferromagnetism*', Clarendon Press. (1996).

[3] C. Martnez-Boubeta, J. L. Costa-Kramer, and A. Cebollada, 'Epitaxy, magnetic and tunnel properties of transition metal/MgO(001) heterostructures', *J. Phys.: Condens. Matter*. 15, R1123, (2003). doi:10.1088/0953-8984/15/25/202

[4] G. Wastlbauer, and J. A. C. Bland, 'Structural and magnetic properties of ultrathin epitaxial Fe films on GaAs(001) and related semiconductor substrates', *Advances in Physics*. 54:2, 137-219, (2005). doi:10.1080/00018730500112000

[5] W. H. Butler, X.-G. Zhang, and T. C. Schulthess, and J. M. MacLaren, 'Spin-dependent tunneling conductance of Fe|MgO|Fe sandwiches', *Phys. Rev. B* 63, 054416, (2001). doi:10.1103/PhysRevB.63.054416

[6] C. M. Boubeta, C. Clavero, J. M. Garcia-Martin, G. Armelles, A. Cebollada, L. Balcells, J. L. Menendez, F. Peiro, A. Cornet, and M. F. Toney, 'Coverage effects on the magnetism of Fe/MgO(001) ultrathin films', *Phys. Rev. B* 71, 014407, (2005). doi:10.1103/PhysRevB.71.014407

[7] Yu. V. Goryunov, N. N. Garif'yanov, G. G. Khallinlin, I. A. Garfullin, L. R. Targirov, F. Schreiner, Th. Muhge, and H. Zabel, 'Magnetic anisotropies of sputtered Fe films on MgO substrates', *Phys. Rev. B* 52, 13450, (1995). doi:10.1103/PhysRevB.52.13450

[8] R. M. Bozorth, '*Ferromagnetism*', D. Van Nostrand Company, Inc., New York. (1951).

[9] C. D. Graham Jr., 'Magnetocrystalline Anisotropy Constants of Iron at Room Temperature and Below', *Phys. Rev*. 112, 1117, (1958). doi:10.1103/PhysRev.112.1117

[10] E. C. Stoner, and E. P. Wohlfarth, 'A mechanism of magnetic hysteresis in heterogeneous alloys', *Philosophical Transactions of the Royal Society A: Physical, Mathematical and Engineering Sciences* 240, (826): 599–642, (1948). doi:10.1098/rsta.1948.0007

[11] R. P. Cowburn, S. J. Gray, and J. A. C. Bland, 'Multijump magnetic switching in in-plane magnetized ultrathin epitaxial Ag/Fe/Ag(001) films', *Phys. Rev. Lett.* 79, 4018, (1997). doi:10.1103/PhysRevLett.79.4018

[12] R. P. Cowburn, S. J. Gray, J. Ferre, J. A. C. Bland, and J. Miltat, 'Magnetic switching and in-plane uniaxial anisotropy in ultrathin Ag/Fe/Ag(100) epitaxial films', *J. Appl. Phys.* 78, 7210, (1995). doi:10.1063/1.360431

[13] C. Daboo, R. J. Hicken, E. Gu, M. Gester, S. J. Gray, D. E. P. Eley, E. Ahmad, J. A. C. Bland, R. Ploessl, and J. N. Chapman, 'Anisotropy and orientational dependence of magnetization reversal processes in epitaxial ferromagnetic thin films', *Phys. Rev. B* 51, 15964, (1995). doi:10.1103/PhysRevB.51.15964

[14] J. Chen and J. L. Erskine, 'Surface-step-induced magnetic anisotropy in thin epitaxial Fe films on W(001)', *Phys. Rev. Lett*. 68, 1212, (1992). doi:10.1103/PhysRevLett.68.1212

[15] Y. Park, E. E. Fullerton, and S. D. Bader, 'Growth-induced uniaxial in-plane magnetic anisotropy for ultrathin Fe deposited on MgO(001) by oblique-incidence molecular beam epitaxy', *Appl. Phys. Lett.* 66, 2140, (1995). doi:10.1063/1.113929

[16] Qing-feng Zhan, Stijn Vandezande, Chris Van Haesendonck, and Kristiaan Temst, 'Manipulation of in-plane uniaxial anisotropy in Fe/MgO(001) films by ion sputtering', *Appl. Phys. Lett.* 91, 122510, (2007). doi:10.1063/1.2789396

[17] Qing-feng Zhan, Chris Van Haesendonck, Stijn Vandezande, and Kristiaan Temst, 'Surface morphology and magnetic anisotropy of Fe/MgO(001) films deposited at oblique incidence', *Appl. Phys. Lett*. 94, 042504, (2009). doi:10.1063/1.3075847

[18] Qing-feng Zhan, Stijn Vandezande, Kristiaan Temst, and Chris Van Haesendonck, 'Magnetic anisotropies of epitaxial Fe/MgO(001) films with varying thickness and grown under different conditions', *New J. Phys.* 11, 063003, (2009). doi:10.1088/1367-2630/11/6/063003

[19] Qing-feng Zhan, Stijn Vandezande, Kristiaan Temst, and Chris Van Haesendonck, 'Magnetic anisotropy and reversal in epitaxial Fe/MgO(001) films', *Phys. Rev. B* 80, 094416, (2009). doi:10.1103/PhysRevB.80.094416

[20] Wolfgang Kuch, 'Magnetic imaging', *Letc. Notes Phys.* 697, 275, (2006). doi:10.1007/b11594864

[21] Peter M. Levy and Shufeng Zhang, 'Resistivity due to Domain Wall Scattering', *Phys. Rev. Lett.* 79, 5110, (1997). doi:10.1103/PhysRevLett.79.5110

[22] K. Kondou, N. Ohshima, S. Kasai, Y. Nakatani, and T. Ono, 'Single shot detection of the magnetic domain wall motion by using tunnel magnetoresistance effect', *Appl. Phys. Express*. 1, 061302, (2008). doi:10.1143/APEX.1.061302

[23] T. Ono, H. Miyajima, K. Shigeto, K. Mibu, N. Hosoito, and T. Shinjo, 'Propagation of a magnetic domain wall in a submicrometer magnetic wire', *Science* 284, 468, (1999). doi:10.1126/science.284.5413.468

[24] M. Klaui, C. A. F. Vaz, J. Rothman, J. A. C. Bland, W. Wernsdorfer, G. Faini, and E. Cambril, 'Domain wall pinning in narrow ferromagnetic ring structures probed by magnetoresistance measurements', *Phys. Rev. Lett.* 90, 097202, (2003). doi:10.1103/PhysRevLett.90.097202

[25] T. Koyama, D. Chiba, K. Ueda, K. Kondou, H. Tanigawa, S. Fukami, T. Suzuki, N. Ohshima, N. Ishiwata, Y. Nakatani, K. Kobayashi, and T. Ono, 'Observation of the intrinsic pinning of a magnetic domain wall in a ferromagnetic nanowire', *Nat. Mat.* 10, 194, (2011). doi:10.1038/nmat2961

[26] V. D. Nguyen, L. Vila, P. Laczkowski, A. Marty, T. Faivre, and J. P. Attane, 'Detection of domain-

wall position and magnetization reversal in nanostructures using the magnon contribution to the resistivity', *Phys. Rev. Lett.* 107, 136605, (2011). doi:10.1103/PhysRevLett.107.136605

[27] Y. Kasatani, A. Yamaguchi, H. Yamamoto, and H. Miyajima, 'Magnetization reversal and wall propagation velocity in single-crystalline and polycrystalline Fe wires', *Phys. Rev. B* 81, 224425, (2010). doi:10.1103/PhysRevB.81.224425

[28] H. Yamamoto, Y. Kasatani, A. Yamaguchi, and H. Miyajima, 'Giant magnetoresistance effect detection of magnetization reversal in single crystalline nanowires', *J. Phys.: Conf. Ser.* 200, 042028, (2010). doi:10.1088/1742-6596/200/4/042028

[29] M. T. Bryan, S. Bance, J. Dean, T. Schrefl, and D. A. Allwood, 'Transverse and vortex domain wall structure in magnetic nanowires with uniaxial in-plane anisotropy', *J. Phys.: Condens. Matter.* 24, 024205, (2012). doi:10.1088/0953-8984/24/2/024205

[30] M. Hayashi, L. Thomas, C. Rettner, R. Moriya, X. Jiang, and Stuart S. P. Parkin, 'Dependence of current and field driven depinning of domain walls on their structure and chirality in permalloy nanowires', *Phys. Rev. Lett.* 97, 207205, (2006). doi:10.1103/PhysRevLett.97.207205

[31] M.-Y. Im, L. Bocklage, P. Fischer, and G. Meier, 'Direct observation of stochastic domain-wall depinning in magnetic nanowires', *Phys. Rev. Lett.* 102, 147204, (2009). doi:10.1103/PhysRevLett.102.147204

[32] L. O'Brien, D. Petit, E. R. Lewis, R. P. Cowburn, D. E. Read, J. Sampaio, H. T. Zeng, and A.-V. Jausovec, 'Tunable remote pinning of domain walls in magnetic nanowires', *Phys. Rev. Lett.* 106, 087204, (2011). doi:10.1103/PhysRevLett.106.087204

[33] G. Beach, 'Spintronics: Beyond the speed limit', *Nature Mater*. 9, 959, (2010). doi:10.1038/nmat2909

[34] A. Yamaguchi, T. Ono, S. Nasu, K. Miyake, K. Mibu, and T. Shinjo, 'Real-space observation of current-driven domain wall motion in submicron magnetic wires', *Phys. Rev. Lett.* 92, 077205, (2004). doi:10.1103/PhysRevLett.92.077205

[35] W. H. Meiklejohn and C. P. Bean, 'New magnetic anisotropy', *Phys. Rev.* 102, 1413, (1956). doi:10.1103/PhysRev.102.1413

[36] J. Nogues and I. K. Schuller, 'Exchange bias', *J. Magn. Magn. Mater.* 192, 203, (1999). doi:10.1016/S0304-8853(98)00266-2

[37] A. E. Berkowitz and K. Takano, 'Exchange anisotropy - a review', *J. Magn. Magn. Mater.* 200, 552, (1999). doi:10.1016/S0304-8853(99)00453-9

[38] R. L. Stamps, 'Mechanisms for exchange bias', *J. Phys. D: Appl. Phys.* 33, R247, (2000). doi:10.1088/0022-3727/33/23/201

[39] M. Kiwi, 'Exchange bias theory', *J. Magn. Magn. Mater.* 234, 584, (2001). doi:10.1016/S0304-8853(01)00421-8

[40] K. O'Grady, L.E. Fernandez-Outon, G. Vallejo-Fernandez, 'A new paradigm for exchange bias in polycrystalline thin films', *J. Magn. Magn. Mater.* 322, 883, (2010).

doi:10.1016/j.jmmm.2009.12.011

[41] H. Zabel and S. D. Bader, '*Magnetic heterostructures*', Springer, Berlin Heidelberg. (2008).

[42] D. Mauri, H. C. Siegmann, P. S. Bagus, and E. Kay, 'Simple model for thin ferromagnetic films exchange coupled to an antiferromagnetic substrate', *J. Appl. Phys.* 62, 3047, (1987). doi:10.1063/1.339367

[43] A. P. Malozemoff, 'Random-field model of exchange anisotropy at rough ferromagnetic-antiferromagnetic interfaces', *Phys. Rev. B* 35, 3679, (1987). doi:10.1103/PhysRevB.35.3679

[44] A. P. Malozemoff, 'Mechanisms of exchange anisotropy (invited)', *J. Appl. Phys.* 63, 3874, (1988). doi:10.1063/1.340591

[45] A. P. Malozemoff, 'Heisenberg-to-Ising crossover in a random-field model with uniaxial anisotropy', *Phys. Rev. B* 37, 7673, (1988). doi:10.1103/PhysRevB.37.7673

[46] U. Nowak, K. D. Usadel, J. Keller, P. Miltényi, B. Beschoten, and G. Güntherodt, 'Domain state model for exchange bias. I. Theory', *Phys. Rev. B* 66, 014430, (2002). doi:10.1103/PhysRevB.66.014430

[47] J. Keller, P. Miltényi, B. Beschoten, G. Güntherodt, U. Nowak, and K. D. Usadel, 'Domain state model for exchange bias. II. Experiments', *Phys. Rev. B* 66, 014431, (2002). doi:10.1103/PhysRevB.66.014431

[48] P. Miltényi, M. Gierlings, J. Keller, B. Beschoten, B. Güntherodt, U. Nowak, and K. Usadel, 'Diluted Antiferromagnets in Exchange Bias: Proof of the Domain State Model', *Phys. Rev. Lett.* 84, 4224, (2000). doi:10.1103/PhysRevLett.84.4224

[49] J. I. Hong, T. Leo, D. J. Smith, and A. E. Berkowitz, 'Enhancing Exchange Bias with Diluted Antiferromagnets', *Phys. Rev. Lett.* 96, 117204, (2006). doi:10.1103/PhysRevLett.96.117204

[50] Joo-Von Kim and R. L. Stamps, 'Hysteresis from antiferromagnet domain-wall processes in exchange-biased systems: Magnetic defects and thermal effects', *Phys. Rev. B* 71, 094405, (2005). doi:10.1103/PhysRevB.71.094405

[51] Joo-Von Kim and R. L. Stamps, 'Defect-modified exchange bias', *Appl. Phys. Lett.* 79, 2785, (2001). doi:10.1063/1.1413731

[52] F. Radu, A. Westphalen, K. Theis-Brohl, and H. Zabel, 'Quantitative description of the azimuthal dependence of the exchange bias effect', *J. Phys. Condens. Matter* 18, L29, (2006). doi:10.1088/0953-8984/18/3/L01

[53] H. Ohldag, T. J. Regan, J. Stöhr, A. Scholl, F. Nolting, J. Lüninhg, C. Stamm, S. Anders, and R. L. White, 'Spectroscopic identification and direct imaging of interfacial magnetic spins', *Phys. Rev. Lett.* 87, 247201, (2001). doi:10.1103/PhysRevLett.87.247201

[54] H. Ohldag, A. Scholl, F. Nolting, E. Arenholz, S. Maat, A. T. Young, M. Carey, and J. Stohr, 'Correlation between exchange bias and pinned interfacial spins', *Phys. Rev. Lett.* 91, 017203, (2003). doi:10.1103/PhysRevLett.91.017203

[55] Y. Shiratsuchi, H. Noutomi, H. Oikawa, T. Nakamura, M. Suzuki, T. Fujita, K. Arakawa, Y. Takechi, H. Mori, T. Kinoshita, M. Yamamoto, and R. Nakatani, 'Detection and In Situ Switching of Unreversed Interfacial Antiferromagnetic Spins in a Perpendicular-Exchange-Biased System', *Phys. Rev. Lett.* 109, 077202, (2012). doi:10.1103/PhysRevLett.109.077202

[56] S. Roy, M. R. Fitzsimmons, S. Park, M. Dorn, O. Petracic, Igor V. Roshchin, Zhi-Pan Li, X. Batlle, R. Morales, A. Misra, X. Zhang, K. Chesnel, J. B. Kortright, S. K. Sinha, and Ivan K. Schuller, 'Depth Profile of Uncompensated Spins in an Exchange Bias System', *Phys. Rev. Lett.* 95, 047201, (2005). doi:10.1103/PhysRevLett.95.047201

[57] S. Bruck, G. Schutz, E. Goering, X. Ji, and K. M. Krishnan, 'Uncompensated moments in the MnPd/Fe exchange bias system', *Phys. Rev. Lett*. 101, 126402, (2008). doi:10.1103/PhysRevLett.101.126402

[58] J. Wu, J. S. Park, W. Kim, E. Arenholz, M. Liberati, A. Scholl, Y. Z. Wu, Chanyong Hwang, and Z. Q. Qiu, 'Direct Measurement of Rotatable and Frozen CoO Spins in Exchange Bias System of CoO/Fe/Ag(001)', *Phys. Rev. Lett.* 104, 217204, (2010). doi:10.1103/PhysRevLett.104.217204

[59] N. C. Koon, 'Calculations of exchange bias in thin films with ferromagnetic / antiferromagnetic interfaces', *Phys. Rev. Lett.* 78, 4865, (1997). doi:10.1103/PhysRevLett.78.4865

[60] T. C. Schulthess and W. H. Butler, 'Consequences of Spin-Flop Coupling in Exchange Biased Films', *Phys. Rev. Lett.* 81, 4516, (1998). doi:10.1103/PhysRevLett.81.4516

[61] C.-H. Lai, H. Matsuyama, R. L. White, T. C. Anthony, and G. G. Bush, 'Exploration of magnetization reversal and coercivity of epitaxial NiO{111}/NiFe film', *J. Appl. Phys.* 79, 6389, (1996). doi:10.1063/1.362007

[62] J. Geshev, L. G. Pereira, and J. E. Schmidt, 'Angular dependence of the exchange bias obtained from magnetization and ferromagnetic resonance measurements in exchange-coupled bilayers', *Phys. Rev. B* 64, 184411, (2001). doi:10.1103/PhysRevB.64.184411

[63] M. R. Fitzsimmons, P. Yashar, C. Leighton, I. K. Schuller, J. Nogues, C. F. Majkrzak, and J. A. Dura, 'Asymmetric magnetization reversal in exchange-biased hysteresis loops', *Phys. Rev. Lett.* 84, 3986, (2000). doi:10.1103/PhysRevLett.84.3986

[64] P. Kappenberger, I. Schmid, H. J. Hug, 'Investigation of the exchange bias effect by quantitative magnetic force microscopy', *Adv. Eng. Mater.* 7, 332, (2005). doi:10.1002/adem.200500088

[65] F. Romanens, S. Pizzini, F. Yokaichiya, M. Bonfim, Y. Pennec, J. Camarero, J. Vogel, J. Sort, F. Garcia, B. Rodmacq, and B. Dieny, 'Magnetic relaxation of exchange biased Pt/Co multilayers studied by time-resolved Kerr microscopy', *Phys. Rev. B* 72, 134410, (2005). doi:10.1103/PhysRevB.72.134410

[66] C. Mathieu, M. Bauer, B. Hillebrands, J. Fassbender, G. Güntherodt, R. Jungblut, J. Kohlhepp, and A. Reiders, 'Brillouin light scattering investigations of exchange biased (110)-oriented NiFe/FeMn bilayers', *J. Appl. Phys*. 83, 2863, (1998). doi:10.1063/1.367049

[67] P. Blomqvist, K. M. Krishnan, and H. Ohldag, 'Direct imaging of asymmetric magnetization reversal in exchange-biased Fe/MnPd bilayers by x-ray photoemission electron microscopy', *Phys. Rev. Lett.* 94, 107203, (2005). doi:10.1103/PhysRevLett.94.107203

[68] W. Keune, V. E. Kuncser, M. Doi, M. Askin, H. Spies, B. Sahoo, E. Duman, M. Acet, J. S. Jiang, A. Inomata, and S. D. Bader, 'Mössbauer effect study of the Fe spin structure in exchange-bias and exchange-spring systems', *J. Phys. D: Appl. Phys.* 35, 2352, (2002). doi:10.1088/0022-3727/35/19/305

[69] Ivan K. Schuller, 'Unusual phenomena in exchange-biased nanostructures', *Mat. Res. Soc. Bull.* 29, 642, (2004). doi:10.1557/mrs2004.184

[70] A. Mougin, S. Mangin, J. F. Bobo, and A. Loidl, 'New trends in magnetic exchange bias', *Eur. Phys. J. B* 45, 155, (2005). doi:10.1140/epjb/e2005-00184-5

[71] Mark Blamire and Bryan Hickey, 'Magnetic materials: Compensating for bias', *Nature Mater.* 5, 87, (2006). doi:10.1038/nmat1561

[72] N. Cheng, J. P. Ahn, and K. M. Krishnan, 'Epitaxial growth and exchange biasing of PdMn/Fe bilayers grown by ion-beam sputtering', *J. Appl. Phys.* 89, 6597, (2001). doi:10.1063/1.1360677

[73] P. Blomqvist, K. M. Krishnan, and D. E. McCready, 'Growth of exchange-biased MnPd/Fe bilayers', *J. Appl. Phys*. 95, 8019, (2004). doi:10.1063/1.1713023

[74] P. Blomqvist, K. M. Krishnan, and Er. Girt, 'Magnetization process in exchange-biased MnPd/Fe bilayers', *J. Appl. Phys*. 95, 8487, (2004). doi:10.1063/1.1751230

[75] P. Blomqvist, K. M. Krishnan, S. Srinath, and S. G. E. te Velthuis, 'Magnetization processes in exchange-biased MnPd/Fe bilayers studied by polarized neutron reflectivity', *J. Appl. Phys.* 96, 6523, (2004). doi:10.1063/1.1806257

[76] T. J. Moran, J. Nogués, D. Lederman, and Ivan K. Schuller, 'Perpendicular coupling at Fe–FeF2 interfaces', *Appl. Phys. Lett.* 72, 617, (1998). doi:10.1063/1.120823

[77] Y. Ijiri, J. A. Borchers, R. W. Erwin, and S. –H. Lee, P. J. van der Zaag, and R. M. Wolf, 'Perpendicular Coupling in Exchange-Biased Fe3O4/CoO Superlattices', *Phys. Rev. Lett.* 80, 608, (1998). doi:10.1103/PhysRevLett.80.608

[78] Y. Ijiri, T. C. Schulthess, J. A. Borchers, P. J. van der Zaag, and R. W. Erwin, 'Link between Perpendicular Coupling and Exchange Biasing in Fe3O4/CoO Multilayers', *Phys. Rev. Lett.* 99, 147201, (2007). doi:10.1103/PhysRevLett.99.147201

[79] Qing-feng Zhan and K. M. Krishnan, 'In-plane reorientation of magnetization in epitaxial exchange biased Fe/MnPd bilayers', *Appl. Phys. Lett.* 96, 112506, (2010). doi:10.1063/1.3367705

[80] B. Y. Wang, C. H. Chuang, S. S. Wong, J. J. Chiou, W. C. Lin, Y. L. Chan, D. H. Wei, and Minn-Tsong Lin, 'Flipping magnetization induced by noncollinear ferromagnetic - antiferromagnetic exchange coupling', *Phys. Rev. B* 85, 094412, (2012). doi:10.1103/PhysRevB.85.094412

[81] C. Leighton, M. R. Fitzsimmons, P. Yashar, A. Hoffmann, J. Nogués, J. Dura, C. F. Majkrzak, and I. K. Schuller, 'Two-Stage Magnetization Reversal in Exchange Biased Bilayers', *Phys. Rev. Lett*. 86, 4394, (2001). doi:10.1103/PhysRevLett.86.4394

[82] S. G. Wang, A. Kohn, C. Wang, A. K. Petford-Long, S. Lee, R. Fan, J. P. Goff, L. J. Singh, Z. H.

Barber, and R. C. C. Ward, 'Exchange bias in epitaxial Fe/$Ir_{0.2}Mn_{0.8}$ bilayers grown on MgO(001)', *J. Phys. D: Appl. Phys.* 42, 225001, (2009). doi:10.1088/0022-3727/42/22/225001

[83] S. Chung, A. Hoffmann, and M. Grimsditch, 'Interplay between exchange bias and uniaxial anisotropy in a ferromagnetic/antiferromagnetic exchange-coupled system', *Phys. Rev. B* 71, 214430, (2005). doi:10.1103/PhysRevB.71.214430

[84] B. Lewis and J. C. Anderson, '*Nucleation and Growth of Thin Films*', Academic Press, New York. (1978).

[85] B. A. Joyce, 'Molecular beam epitaxy', *Rep. Prog. Phys.* 48, 1637, (1985). doi:10.1088/0034-4885/48/12/002

[86] L.W. Martin, Y.-H. Chu, and R. Ramesh, 'Advances in the growth and characterization of magnetic, ferroelectric, and multiferroic oxide thin films', *Mater. Sci. Eng. R* 68, 89 (2010). doi:10.1016/j.mser.2010.03.001

[87] J. Shen, Z. Gai, and J. Kirschner, 'Growth and magnetism of metallic thin films and multilayers by pulsed-laser deposition', *Surf. Sci. Reports* 52, 163, (2004). doi:10.1016/j.surfrep.2003.10.001

[88] D. L. Smith, '*Thin film deposition, principles & practice*', McGraw-Hill, INC, (1995).

[89] J. J. Cuomo, S. M. Rossnagel, and H. R. Kaufman, '*Handbook of Ion Beam Processing Technology, Principles, Deposition, Film Modification and Synthesis*', Noyes Publications, (1989).

[90] W. Zhang, M. E. Bowden, and K. M. Krishnan, 'Competing effect of magnetocrystalline anisotropy and exchange bias in epitaxial Fe/IrMn bilayers', *Appl. Phys. Lett*. 98, 092503, (2011). doi:10.1063/1.3561516

[91] Z. Q. Qiu and S. D. Bader, 'Surface magneto-optic Kerr effect (SMOKE)', *J. Magn. Magn. Mater.* 200, 664, (1999). doi:10.1016/S0304-8853(99)00311-X

[92] M. Cormier, J. Ferre, A. Mougin, J.-P. Cromieres, and V. Klein, 'High resolution polar Kerr magnetometer for nanomagnetism and nanospintronics', *Rev. Sci. Instrum*. 79, 033706, (2008). doi:10.1063/1.2890839

[93] S. Maat, K. Takano, S. S. P. Parkin, and Eric E. Fullerton, 'Perpendicular Exchange Bias of Co/Pt Multilayers', *Phys. Rev. Lett.* 87, 087202, (2001). doi:10.1103/PhysRevLett.87.087202

[94] C-R. Chang, 'A hysteresis model for planar Hall effect in thin films', *IEEE Trans. Magn.* 36, 1214, (2000). doi:10.1109/20.877658

[95] E. Arenholz and K. Liu, 'Angular dependence of the magnetization reversal in exchange-biased Fe / $MnF_2$', *Appl. Phys. Lett*. 87, 132501, (2005). doi:10.1063/1.2058207

[96] W. Zhang, Q. F. Zhan, and K. M. Krishnan, 'Angular dependent magnetization reversal in exchange biased bilayers under a modified 'effective field model'', arXiv:1102.5387.

[97] Qing-feng Zhan and Kannan M. Krishnan, 'Angular dependence of magnetization reversal process in exchange biased epitaxial MnPd/Fe bilayers', *J. Appl. Phys*. 107, 09D703, (2010).

doi:10.1063/1.3340449

[98] Q. F. Zhan, W. Zhang, and K. M. Krishnan, 'Antiferromagnetic layer thickness dependence of the magnetization reversal in the epitaxial MnPd/Fe exchange bias system', *Phys. Rev. B*. 83 094404, (2011). doi:10.1103/PhysRevB.83.094404

[99] S. Brück, S. Macke, E. Goering, X. Ji, Q. Zhan, and K. M. Krishnan, 'Coupling of Fe and uncompensated Mn moments in exchange-biased Fe/MnPd', *Phys. Rev. B* 81, 134414, (2010). doi:10.1103/PhysRevB.81.134414

[100] C. Binek, A. Hochstrat, and W. Kleemann, 'Exchange bias in a generalized Meiklejohn –Bean approach', *J. Magn. Magn. Mater.* 234, 353, (2001). doi:10.1016/S0304-8853(01)00390-0

[101] W. Zhang and K. M. Krishnan, 'Probing the magnetization reversal in epitaxial Fe/IrMn exchange biased bilayers using angle-dependent anisotropic magnetoresistance', *J. Appl. Phys*. 111, 07D712, (2012). doi:10.1063/1.3675179

[102] M. Klaui, C. A. F. Vaz, J. Rothman, J. A. C. Bland, W. Wernsdorfer, G. Faini, and E. Cambril, 'Domain Wall Pinning in Narrow Ferromagnetic Ring Structures Probed by Magnetoresistance Measurements', *Phys. Rev. Lett*. 90, 097202, (2003). doi:10.1103/PhysRevLett.90.097202

[103] S. Brems, K. Temst, and C. Van Haesendonck, 'Origin of the Training Effect and Asymmetry of the Magnetization in Polycrystalline Exchange Bias Systems', *Phys. Rev. Lett*. 99, 067201, (2007). doi:10.1103/PhysRevLett.99.067201

[104] J. Camarero, J. Sort, A. Hoffmann, J. M. García-Martín, B. Dieny, R. Miranda, J. Nogués, 'Origin of the Asymmetric Magnetization Reversal Behavior in Exchange-Biased Systems: Competing Anisotropies', *Phys. Rev. Lett*. 95, 057204, (2005). doi:10.1103/PhysRevLett.95.057204

[105] E. Jiménez, J. Camarero, J. Sort, J. Nogués, A. Hoffmann, F. J. Teran, P. Perna, J. M. García-Martín, B. Dieny, and R. Miranda, 'Highly asymmetric magnetic behavior in exchange biased systems induced by noncollinear field cooling', *Appl. Phys. Lett.* 95, 122508, (2009). doi:10.1063/1.3236768

[106] E. Jiménez, J. Camarero, J. Sort, J. Nogués, A. Hoffmann, N. Mikuszeit, J. M. García-Martín, B. Dieny, and R. Miranda, 'Emergence of noncollinear anisotropies from interfacial magnetic frustration in exchange-bias systems', *Phys. Rev. B* 80, 014415, (2009). doi:10.1103/PhysRevB.80.014415

[107] J. Nogues, D. Lederman, T. J. Moran, and I. K. Schuller, 'Positive Exchange Bias in $FeF_2$-Fe Bilayers', *Phys. Rev. Lett*. 76, 4624, (1996). doi:10.1103/PhysRevLett.76.4624

[108] W. Zhang and K. M. Krishnan, 'Domain wall nucleation in epitaxial exchange biased Fe/IrMn bilayers with highly misaligned anisotropies', *J. Magn. Magn. Mater.* 324, 3129, (2012). doi:10.1016/j.jmmm.2012.05.016

[109] P. J. Jensen and H. Dreyssé, 'In-plane magnetic reorientation in coupled ferro- and antiferromagnetic thin films', *Phys. Rev. B* 66, 220407(R), (2002). doi:10.1103/PhysRevB.66.220407

[110] M. L. Silva, A. L. Dantas, and A. S. Carriço, 'Threshold for reorientation of the magnetization in F/AF bilayers', *J. Magn. Magn. Mater.* 292, 453, (2005). doi:10.1016/j.jmmm.2004.11.315

[111] J. H. Seok, H. Y. Kwon, S. S. Hong, Y. Z. Wu, Z. Q. Qiu, and C. Won, 'In-plane spin reorientation transition in a two-dimensional ferromagnetic/antiferromagnetic system studied using Monte Carlo simulations', *Phys. Rev. B* 80, 174407, (2009). doi:10.1103/PhysRevB.80.174407

[112] K. Zhang, T. Zhao, and H. Fujiwara, 'Training effect of exchange biased iron–oxide/ferromagnet systems', *J. Appl. Phys.* 89,6910, (2001). doi:10.1063/1.1360682

[113] C. Binek, 'Training of the exchange-bias effect: A simple analytic approach', *Phys. Rev. B* 70, 014421, (2004). doi:10.1103/PhysRevB.70.014421

[114] A. Hoffmann, 'Symmetry Driven Irreversibilities at Ferromagnetic-Antiferromagnetic Interfaces', *Phys. Rev. Lett.* 93, 097203, (2004). doi:10.1103/PhysRevLett.93.097203

[115] N. J. Gökemeijer, R. L. Penn, D. R. Veblen, and C. L. Chien, 'Exchange coupling in epitaxial CoO/NiFe bilayers with compensated and uncompensated interfacial spin structures', *Phys. Rev. B* 63, 174422, (2001). doi:10.1103/PhysRevB.63.174422

[116] P. J. van der Zaag, Y. Ijiri, J. A. Borchers, L. F. Feiner, R. M. Wolf, J. M. Gaines, R. W. Erwin, and M. A. Verheijen, 'Difference between Blocking and Néel Temperatures in the Exchange Biased Fe3O4/CoO System' *Phys. Rev. Lett.* 84, 6102, (2000). doi:10.1103/PhysRevLett.84.6102

[117] H. Ohldag, H. Shi, E. Arenholz, J. Stöhr, and D. Lederman, 'Parallel versus Antiparallel Interfacial Coupling in Exchange Biased Co/FeF2', *Phys. Rev. Lett.* 96, 027203, (2006). doi:10.1103/PhysRevLett.96.027203

[118] F. I. F. Nascimento, A. L. Dantas, L. L. Oliveira, V. D. Mello, R. E. Camley, and A. S. Carriço, 'Thermal hysteresis of ferromagnetic/antiferromagnetic compensated bilayers', *Phys. Rev. B* 80, 144407, (2009). doi:10.1103/PhysRevB.80.144407

[119] A. Barbier, C. Mocuta, W. Neubeck, M. Mulazzi, F. Yakhou, K. Chesnel, A. Sollier, C. Vettier, and F. de Bergevin, 'Surface and Bulk Spin Ordering of Antiferromagnetic Materials: NiO(111)', *Phys. Rev. Lett.* 93, 257208, (2004). doi:10.1103/PhysRevLett.93.257208

[120] R. Morales, Z. P. Li, J. Olamit, K. Liu, J. M. Alameda, and I. K. Schuller, 'Role of the Antiferromagnetic Bulk Spin Structure on Exchange Bias', *Phys. Rev. Lett.* 102, 097201, (2009). doi:10.1103/PhysRevLett.102.097201

[121] F. Y. Yang and C. L. Chien, 'Spiraling Spin Structure in an Exchange-Coupled Antiferromagnetic Layer', *Phys. Rev. Lett.* 85, 2597, (2000). doi:10.1103/PhysRevLett.85.2597

[122] M. G. Blamire, M. Ali, C. W. Leung, C. H. Marrows, and B. J. Hickey, 'Exchange Bias and Blocking Temperature in Co/FeMn/CuNi Trilayers', *Phys. Rev. Lett.* 98, 217202, (2007). doi:10.1103/PhysRevLett.98.217202

[123] Y. Xu, Q. Ma, J. W. Cai, and L. Sun, 'Evidence of bulk antiferromagnet spin rearrangement during ferromagnetic layer reversal in a double exchange bias sandwich', *Phys. Rev. B* 84, 054453, (2011). doi:10.1103/PhysRevB.84.054453

[124] W. Zhang and K. M. Krishnan, 'Spin-flop coupling and rearrangement of bulk antiferromagnetic spins in epitaxial exchange-biased Fe/MnPd/Fe/IrMn multilayers', *Phys. Rev. B* 86, 054415, (2012).

doi:10.1103/PhysRevB.86.054415

[125] Stuart S. P. Parkin, Masamitsu Hayashi, and Luc Thomas, 'Magnetic Domain-Wall Racetrack Memory', *Science* 320, 190, (2008). doi:10.1126/science.1145799

[126] R. C. Jaeger, 'Lithography'. *Introduction to Microelectronic Fabrication*. Upper Saddle River: Prentice Hall. (2002).

[127] M. A. McCord and M. J. Rooks, *SPIE Handbook of Microlithography, Micromachining and Microfabrication*. (2000).

[128] Stephen Y. Chou, Peter R. Krauss, and Preston J. Renstrom, 'Imprint Lithography with 25-Nanometer Resolution', *Science* 272, 85, (1996). doi:10.1126/science.272.5258.85

[129] L Jay Guo, 'Recent progress in nanoimprint technology and its applications', *J. Phys. D: Appl. Phys*. 37, R123, (2004). doi:10.1088/0022-3727/37/11/R01

[130] L. J. Guo, 'Nanoimprint Lithography: Methods and Material Requirements', *Adv. Mater.* 19, 495, (2007). doi:10.1002/adma.200600882

[131] Y. Liu, D. N. Weiss, and J. Li, 'Rapid Nanoimprinting and Excellent Piezoresponse of Polymeric Ferroelectric Nanostructures', *ACS Nano* 4, 83, (2010). doi:10.1021/nn901397r

[132] Chia-Ching Chang, Kien Wen Sun, Shang-Fan Lee, and Lou-Sing Kan, 'Self-assembled molecular magnets on patterned silicon substrates: Bridging bio-molecules with nanoelectronics', *Biomaterials* 28, 1941, (2007). doi:10.1016/j.biomaterials.2006.11.048

[133] J. I. Martín, J. Nogués, K. Liu, J. L. Vicent, and I. K. Schuller, 'Ordered magnetic nanostructures: fabrication and properties', *J. Magn. Magn. Mater.* 256, 449, (2003). doi:10.1016/S0304-8853(02)00898-3

[134] J. Nogués, J. Sort, V. Langlais, V. Skumryev, S. Suriñach, J.S. Muñoz, and M.D. Baró, 'Exchange bias in nanostructures', *Phys. Rep.* 422, 65, (2005). doi:10.1016/j.physrep.2005.08.004

[135] A. O. Adeyeye and N. Singh, 'Large area patterned magnetic nanostructures', *J. Phys. D: Appl. Phys.* 41, 153001, (2008). doi:10.1088/0022-3727/41/15/153001

[136] J. W. Lau and J. M. Shaw, 'Magnetic nanostructures for advanced technologies: fabrication, metrology and challenges', *J. Phys. D: Appl. Phys.* 44, 303001, (2011). doi:10.1088/0022-3727/44/30/303001

[137] E. Paz, F. Cebollada, F. J. Palomares, F. García-Sánchez, and J. M. González, 'Control of magnetization reversal by combining shape and magnetocrystalline anisotropy in epitaxial Fe planar nanowires', *Nanotehnology* 21, 255301, (2010). doi:10.1088/0957-4484/21/25/255301

[138] M. Ciria, F. J. Castaño, J. L. Diez-Ferrer, J. I. Arnaudas, B. G. Ng, R. C. O'Handley, and C. A. Ross, 'Origin of transverse magnetization in epitaxial Cu/Ni/Cu nanowire arrays', *Phys. Rev. B* 80, 094417, (2009). doi:10.1103/PhysRevB.80.094417

[139] A. Hoffmann, M. Grimsditch, J. E. Pearson, J. Nogués, W. A. A. Macedo, and I. K. Schuller, 'Tailoring the exchange bias via shape anisotropy in ferromagnetic/antiferromagnetic exchange-

coupled systems', *Phys. Rev. B* 67, 220406(R), (2003). doi:10.1103/PhysRevB.67.220406

[140] B. J. McMorran, A. C. Cochran, R. K. Dumas, Kai Liu, P. Morrow, D. T. Pierce, and J. Unguris, 'Measuring the effects of low energy ion milling on the magnetization of Co/Pd multilayers using scanning electron microscopy with polarization analysis', *J. Appl. Phys.* 107, 09D305, (2010). doi:10.1063/1.3358218

[141] O. D. Roshchupkina, J. Grenzer, T. Strache, J. McCord, M. Fritzsche, A. Muecklich, C. Baehtz, and J. Fassbender, 'Focused ion beam induced structural modifications in thin magnetic films', *J. Appl. Phys.* 112, 033901, (2012). doi:10.1063/1.4739302

[142] D. R. Barbero, M. S. M. Saifullah, P. Hoffmann, H. J. Mathieu, D. Anderson, G. A. C. Jones, M. E. Welland, and U. Steiner, 'High-Resolution Nanoimprinting with a Robust and Reusable Polymer Mold', *Adv. Funct. Mater.* 17, 2419, (2007). doi:10.1002/adfm.200600710

[143] D. N. Weiss, S. T. Meyers, and D. A. Keszler, 'All-inorganic thermal nanoimprint process', *J. Vac. Sci. Technol. B* 28, 823, (2010). doi:10.1116/1.3463454

[144] N. Suzuki, H. Tanaka, S. Yamanaka, M. Kanai, B. K. Lee, H. Y. Lee, and T. Kawai, 'Epitaxial Nanodot Arrays of Transition-Metal Oxides Fabricated by Dry Deposition Combined with a Nanoimprint-Lithography-Based Molybdenum Lift-Off Technique', *Small* 4, 1661, (2008). doi:10.1002/smll.200800734

[145] K. M. Krishnan, 'Biomedical Nanomagnetics: A Spin Through Possibilities in Imaging, Diagnostics, and Therapy', *IEEE Trans. Magn.* 46, 2523, (2010). doi:10.1109/TMAG.2010.2046907

[146] W. Hu, R. J. Wilson, A. Koh, A. Fu, A. Z. Faranesh, C. M. Earhart, S. J. Osterfeld, S -J. Han, L. Xu, S. Guccione, R. Sinclair, and S. X. Wang, 'High-Moment Antiferromagnetic Nanoparticles with Tunable Magnetic Properties', *Adv. Mater.* 20, 1479, (2008). doi:10.1002/adma.200703077

[147] W. Zhang and K. M. Krishnan, 'Direct release of synthetic antiferromagnetic nanoparticles by defect free thermal imprinting', *J. Appl. Phys.* 111, 07B509, (2012). doi:10.1063/1.3673405

[148] D. N. Weiss, H-C. Yuan, B. G. Lee, H. M. Branz, S. T. Meyers, A. Grenville, and D. A. Keszler, 'Nanoimprinting for diffractive light trapping in solar cells', *J. Vac. Sci. Technol. B* 28, C6M98, (2010). doi:10.1116/1.3498754

[149] Microresist Technology, GmbH (http://www.microresist.de/).

[150] Corinne E. Packard, Apoorva Murarka, Eric W. Lam, Martin A. Schmidt, and Vladimir Bulović, 'Contact-Printed Microelectromechanical Systems', *Adv. Mater.* 22, 1840, (2010). doi:10.1002/adma.200903034

[151] Hyunsoo Park, Huifeng Li, and Xing Cheng, 'Optimizing nanoimprint and transfer-bonding techniques for three-dimensional polymer microstructures', *J. Vac. Sci. Technol. B* 25, 2325, (2007). doi:10.1116/1.2804518

[152] Riad Nechache, Cristian Victor Cojocaru, Catalin Harnagea, Christian Nauenheim, Mischa Nicklaus, Andreas Ruediger, Federico Rosei, and Alain Pignolet, 'Epitaxial Patterning of $Bi_2FeCrO_6$ Double Perovskite Nanostructures: Multiferroic at Room Temperature', *Adv. Mater.* 23,

1724, (2011). doi:10.1002/adma.201004405

[153] J. P. Attané, D. Ravelosona, A. Marty, V. D. Nguyen, and L. Vila, 'Coercivity enhancement in FePt nanowires due to the suppression of available paths for domain wall propagation', *Phys. Rev. B* 84, 144418, (2011). doi:10.1103/PhysRevB.84.144418

[154] W. Zhang, D. N. Weiss, and K. M. Krishnan, 'Thermal nanoimprint process for high-temperature fabrication of mesoscale epitaxial exchange-biased metallic wire arrays', *J. Micromech. Microeng.* 21, 045024, (2011). doi:10.1088/0960-1317/21/4/045024

[155] W. Zhang, D. N. Weiss, and K. M. Krishnan, 'Competing anisotropies and temperature dependence of exchange bias in Co|IrMn metallic wire arrays fabricated by nanoimprint lithography', *J. Appl. Phys.* 107, 09D724, (2010). doi:10.1063/1.3367959

[156] T. Ambrose, R. L. Sommer, and C. L. Chien, 'Angular dependence of exchange coupling in ferromagnet/antiferromagnet bilayers', *Phys. Rev. B* 56, 83, (1997). doi:10.1103/PhysRevB.56.83

[157] W. Zhang, M. E. Bowden, and K. M. Krishnan, 'Nanoimprint-lithography patterned epitaxial Fe nanowire arrays with misaligned magnetocrystalline and shape anisotropies', *J. Appl. Phys.* 113, 17B502, (2013). doi:10.1063/1.4794358

[158] S. Laureti, S. Y. Suck, H. Haas, E. Prestat, O. Bourgeois, and D. Givord, 'Size Dependence of Exchange Bias in Co/CoO Nanostructures', *Phys. Rev. Lett.* 108, 077205, (2012). doi:10.1103/PhysRevLett.108.077205

[159] G. Srajer, L. H. Lewis, S. D. Bader, A. J. Epstein, C. S. Fadley, E. E. Fullerton, A. Hoffmann, J. B. Kortright, K. M. Krishnan, S. A. Majetich, T. S. Rahman, C. A. Ross, M. B. Salamon, I. K. Schuller, T. C. Schulthess, and J. Z. Sun, 'Advances in nanomagnetism via X-ray techniques', *J. Magn. Magn. Mater*. 307, 1, (2006). doi:10.1016/j.jmmm.2006.06.033

[160] T. Wen and K. M. Krishnan, 'Cobalt-based magnetic nanocomposites: fabrication, fundamentals and applications', *J. Phys. D: Appl. Phys.* 44, 393001, (2011). doi:10.1088/0022-3727/44/39/393001

[161] H. Wang, T. Zhu, K. Zhao, W. N. Wang, C. S. Wang, Y. J. Wang, and W. S. Zhan, 'Surface spin glass and exchange bias in Fe3O4 nanoparticles compacted under high pressure', *Phys. Rev. B* 70, 092409, (2004). doi:10.1103/PhysRevB.70.092409

[162] C.-P. Chen, L. He, Y. Leng, and X. Li, 'Weak ferromagnetism and spin-glass state with nanosized nickel carbide', *J. Appl. Phys.* 105, 123923, (2009). doi:10.1063/1.3155997

[163] V. Baltz, G. Gaudin, P. Somani, and B. Dieny, 'Influence of edges on the exchange bias properties of ferromagnetic/antiferromagnetic nanodots', *Appl. Phys. Lett*. 96, 262505, (2010). doi:10.1063/1.3449123

[164] M. Ali, P. Adie, C. H. Marrows, D. Greig, B. J. Hickey, and R. L. Stamps, 'Exchange bias using a spin glass', *Nat. Mater.* 6, 70, (2007). doi:10.1038/nmat1809

[165] W. Wang, F. Takano, M. Takenaka, H. Akinaga, and H. Ofuchi, 'Anomalous temperature-dependent exchange bias in Fe films deposited on Si substrates with the native oxide layer', *J. Appl. Phys.* 103, 093914, (2008). doi:10.1063/1.2917087

[166] F. Radu, M. Etzkorn, R. Siebrecht, T. Schmitte, K. Westerholt, and H. Zabel, 'Interfacial domain formation during magnetization reversal in exchange-biased CoO/Co bilayers', *Phys. Rev. B* 67, 134409, (2003). doi:10.1103/PhysRevB.67.134409

[167] C. Prados, E. Pina, A. Hernando, and A. Montone, 'Reversal of exchange bias in nanocrystalline antiferromagnetic–ferromagnetic bilayers', *J. Phys.: Condens. Matter.* 14, 10063, (2002). doi:10.1088/0953-8984/14/43/305

[168] T. Gredig, I. N. Krivorotov, P. Eames, and E. D. Dahlberg, 'Unidirectional coercivity enhancement in exchange-biased Co/CoO', *Appl. Phys. Lett.* 81, 1270, (2002). doi:10.1063/1.1498505

[169] P. W. Anderson, 'Antiferromagnetism. Theory of Superexchange Interaction', *Phys. Rev.* 79, 350, (1950). doi:10.1103/PhysRev.79.350

[170] V. F. Puntes, K. M. Krishnan, and P. A. Alivisatos, 'Colloidal Nanocrystal Shape and Size Control: The Case of Cobalt', *Science* 291, 2115, (2001). doi:10.1126/science.1058495

[171] Y. Bao, M. Beerman, A. B. Pakhomov, and K. M. Krishnan, 'Controlled Crystalline Structure and Surface Stability of Cobalt Nanocrystals', *J. Phys. Chem. B*. 109, 7220, (2005). doi:10.1021/jp044363n

[172] T. L. Wen and S. A. Majetich, 'Ultra-Large-Area Self-Assembled Monolayers of Nanoparticles', *ACS Nano* 22, 8868, (2011). doi:10.1021/nn2037048

[173] M. C. Biesinger, B. P. Payne, A. P. Grosvenor, L. W. M. Lau, A. R. Gerson, R. St. C. Smart, 'Resolving surface chemical states in XPS analysis of first row transition metals, oxides and hydroxides: Cr, Mn, Fe, Co and Ni', *Appl. Surf. Sci.* 257, 2717, (2011). doi:10.1016/j.apsusc.2010.10.051

[174] L. He, 'Parallel versus antiparallel interfacial exchange coupling in ferromagnet/spin-glasses', *J. Appl. Phys*. 109, 123915, (2011). doi:10.1063/1.3597786

[175] M. De Santis, A. Buchsbaum, P. Varga, and M. Schmid, 'Growth of ultrathin cobalt oxide films on Pt(111)', *Phys. Rev. B* 84, 125430, (2011). doi:10.1103/PhysRevB.84.125430

[176] L. He and L. Guo, 'Competition of the antiferromagnetic superexchange with the ferromagnetic double exchange in dicobalt complexes', *Appl. Phys. Lett*. 97, 182509, (2010). doi:10.1063/1.3514583

[177] J. Kanamori, 'Superexchange interaction and symmetry properties of electron orbitals', *J. Phys. Chem. Solid* 10, 87, (1959). doi:10.1016/0022-3697(59)90061-7

[178] P. W. Anderson, '*Magnetism*', edited by G. T. Rado and H. Suhl (Academic, New York, 1963).

[179] J. B. Goodenough, '*Magnetism and the Chemical Bond*' (Interscience, New York, 1963).

[180] X. Luo, W. Xing, Z. Li, G. Wu, and X. Chen, 'Impact of the Fe doping on magnetism in perovskite cobaltites', *Phys. Rev. B* 75, 054413, (2007). doi:10.1103/PhysRevB.75.054413

[181] M.-H. Phan, T.-L. Phan, T.-N. Huynh, S.-C. Yu, J. R. Rhee, N. V. Khiem, and N. X. Phuc, 'Spin dynamics and spin-glass state in Fe-doped cobaltites', *J. Appl. Phys*. 95, 7531, (2004).

doi:10.1063/1.1667442

[182] W. Zhang, T. L. Wen, and K. M. Krishnan, 'Positive exchange bias and upward magnetic relaxation in a Fe-film/CoO-nanoparticle hybrid system', *Appl. Phys. Lett.* 101, 132401, (2012). doi:10.1063/1.4754610

APPENDIX A

CGS unit and SI unit

**CGS unit to SI unit:**

Length, position (L, x): 1 cm = $10^{-2}$ m

Mass (m): 1 g = $10^{-3}$ kg

Time (t): 1 s = 1 s

Velocity (v): cm/s = $10^{-2}$ m/s

Acceleration (a): 1 Gal = 1 cm/$s^2$ = $10^{-2}$ m/$s^2$

Force (F): 1 dyne = 1 g·cm/$s^2$ = $10^{-5}$ N

Energy (E): 1 erg = 1 g·$cm^2$/$s^2$ = $10^{-7}$ J

Power (P): 1 erg/s = 1 g·$cm^2$/$s^3$ = $10^{-7}$ W

Pressure (p): 1 barye = 1 g/(cm·$s^2$) = $10^{-1}$ Pa

[Source: Wikipedia]

APPENDIX B

Procedures of operating NX-B100 Nanoimprinter

**Procedure:**

1) Enable the 'Nanoimprint' in the Coral system.

2) If the computer is not on (no screen display), open the cover at the left side of the Nanoimprinter and boot the connected PC.

3) After booting completed, click USER icon to start the Windows.


4) On the Windows desktop, double-click the Nx-B200 v3.65 icon and start the software program.

5) Login with your ID and password to start the program. To do this, pull down the menu, click user login

**Theses ID and password are NOT the same with the Coral system.

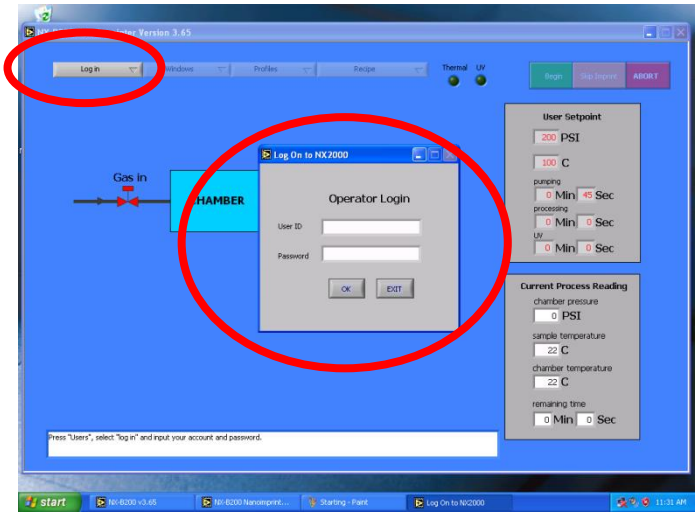


6) Go to recipe (Very right tab)

If you already have recipe then press load recipe then move to 9)

If you don't have recipe to work with then press user set then continue 7)

7) Input desired parameters.

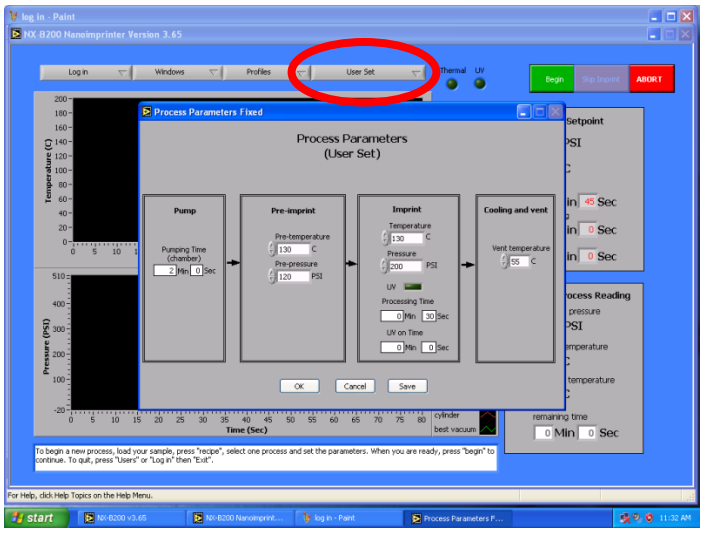


**[Some standard parameters:**

**Eg**. **Pump time:** 2 minutes

**Preimprint temperature:** Conventionally same temperature as imprint temperature.

**Pre Pressure < Imprint Pressure<500psi,**

**Vent temperature:** 45~65C (Don't make it below room temperature)]

8) Save your recipe to → C:\NIL recipes**.txt (contact staff for setting your own folder)

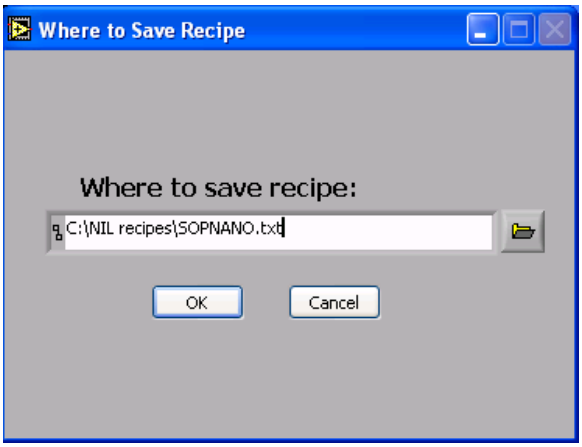


9) Load your recipe and double-check whether your parameters are all correct, click OK

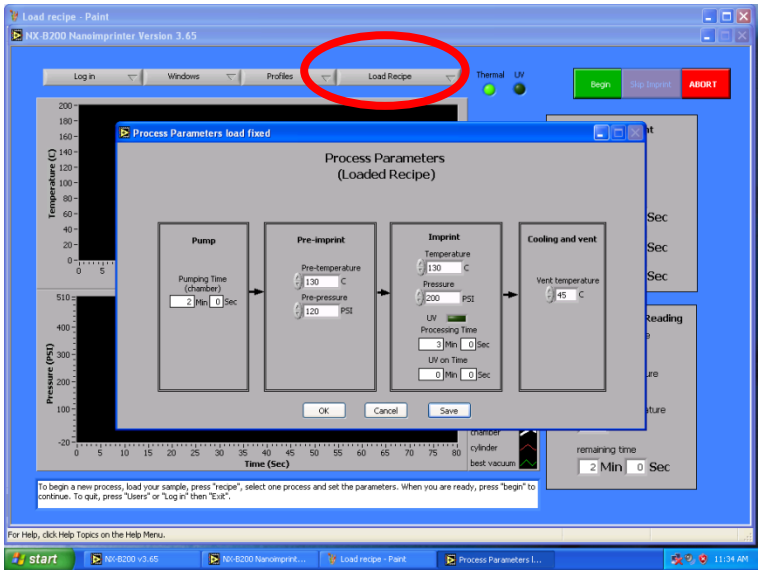


10) Gently pull out the NIL stage, take out the metal frame, flip over and sit it well on the table with a cleanroom napkin at the bottom. Gently separate the top silicone film, and put your stamp-wafer stack on the bottom silicone film. Cover the stack with the top silicone film.

11) Put back the metal plates, and make sure all the springs are in place. ** This is very important!

12) Fully close the stage.

13) Start the imprinting by clicking Begin (Green Button)

14) When the warning window pop up, click ‘OK’.

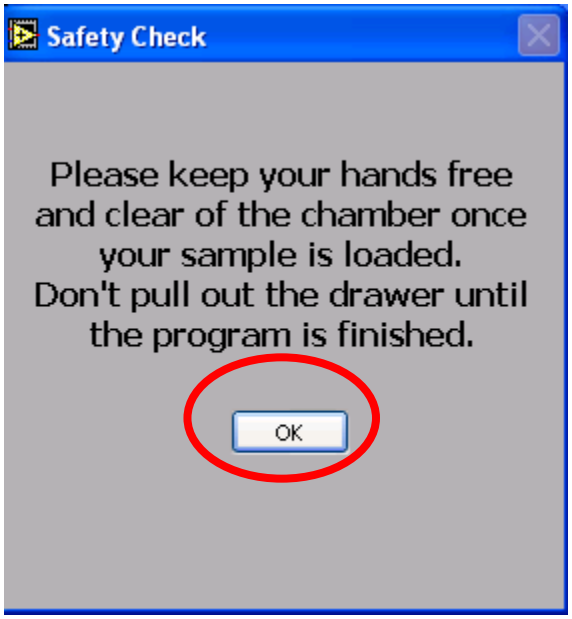


15) Wait until the process finishes. It usually takes about 3-4 min in total. The NIL process has four steps, i.e. pumping, pre-imprint, imprint, and cooling/venting.

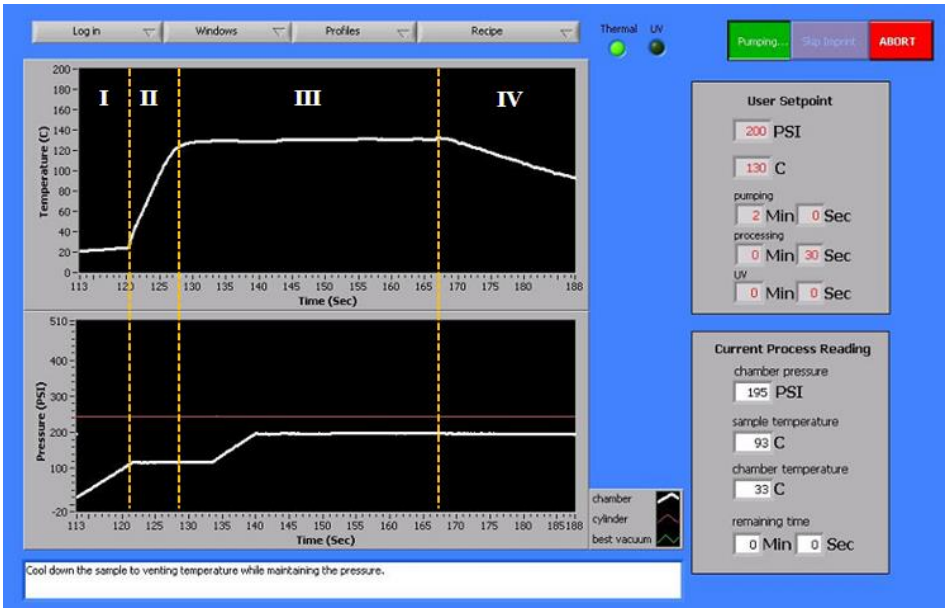


Specifically, in step I (pumping), the imprinter chamber is pressurized at an intermediate level by a mechanical pump, which brings the mold and substrate into close contact; in step II (pre-imprinting), the temperature ramps up rapidly to the imprint temperature (~120$^{o}$C) and the pressure is kept unchanged. This step pre-melts the coated resist. After the temperature stabilizes, in step III (imprinting), the pressure

increases to the desired imprint pressure (200 psi) and is kept for several minutes for imprinting. The imprint time is normally 2 – 5 min. Finally, in step IV (cooling/releasing), the temperature decreases rapidly to room temperature, followed by the chamber venting using $N_2$ supply.

**Wait until it is completely vented** and all the programs are finished, gently open the NIL stage, and take out the metal frame, flip over, gently separate the top silicone film, and take out your sample stack.

16) Cover back the top silicone plates, return the frame to chamber, and make sure all the springs are in place.

17) Fully close the stage.

18) Close the software program by click Login menu, → exit.

19) Log off Windows but you don't have to shut off the PC.

20) Log off Coral.

**Cleaning procedure for Silicone plates:**

When silicone plates are used repeatedly without cleaning, silicone films lose adhesiveness from dirt. This lack of adhesiveness can cause damage in the process. To prevent this, please follow this cleaning process:

1) The bottom silicone film is held by small magnets onto the metal frame. The film can be taken out for cleaning by removing those small magnets.

2) Put Acetone into chemical wipe, and scrub silicone films inside and outside.

3) put IPA into chemical wipe, and scrub silicone films inside and outside.

4) Blow dry with Nitrogen nozzle to dry off remaining chemicals.

5) This should remove all the dirt from silicone films

**Trouble shooting/Common problems:**

**1) Computer is not responsive even after successful booting:**

Make sure you have logged into the Coral System and you are an authorized user

**2) Cannot log into the program with Coral ID and password:**

Make sure you set up new ID and password for the program. Coral ID and password DON'T work for this particular program.

**3) The pressure does not increase even though pump is working:**

Check with staff to see if the house Nitrogen is low, this do happen once in a while. If the house nitrogen is OK, abort the program, and open the chamber and make sure all the springs are in place. [Actually, one is not expected to abort the program during NIL, one should let it finish]

**4) There was a air venting noise, but I cannot open the chamber:**

Please wait few seconds until the program is finished (Wait until following notice to come up).

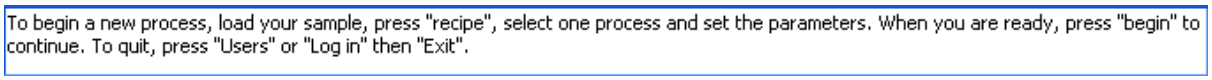


There is a few seconds gap between the air venting noise, and the end of the program.

**5) The recipe that I set worked for the first time, so I pressed BEGIN, but it is using different recipe:**

You have to load the recipe every time you operate since the program automatically reload the default recipe from Nanonex folder which is a test recipe that essentially do nothing.

Finally, we show below some examples of the imprinted resist with this NX-B100 NIL tool.

Nanowire

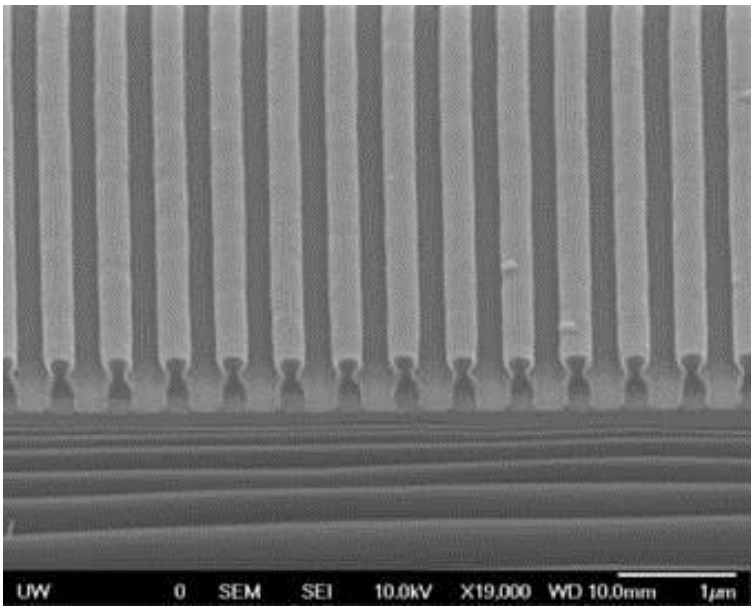


Nanopillar

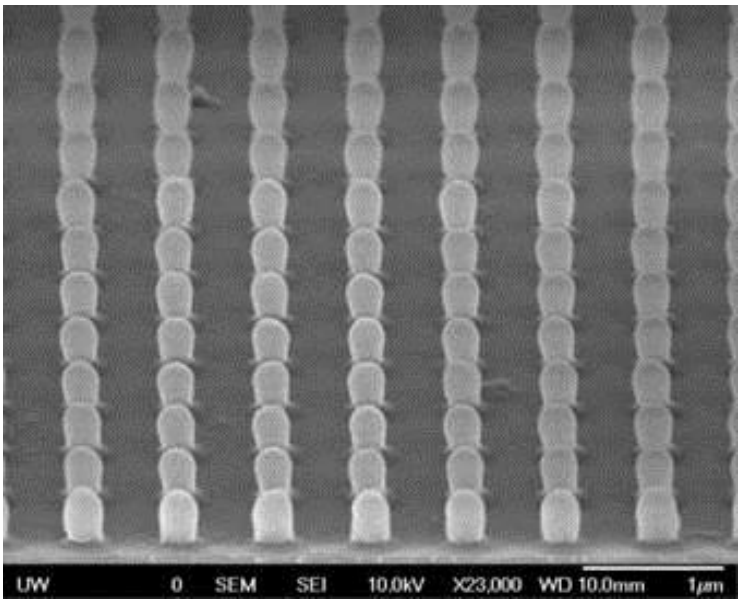

Nanohole

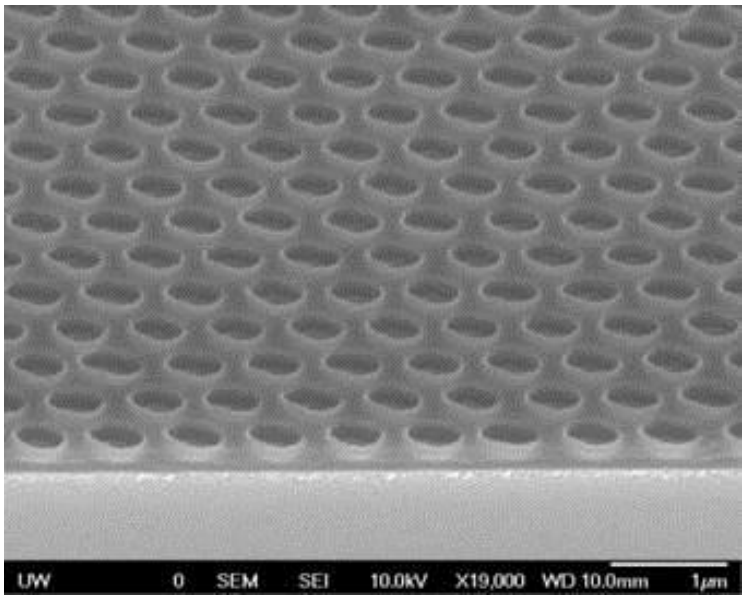

APPENDIX C

Nanoimprint recipes

## A. Bilayer NIL and liftoff (general NIL process)

Procedure:

(1) Clean the substrate (e.g. 3 inch Si wafer) by oxygen plasma using the Barrel Etcher, at 150 W for 1 - 5 min. If using MgO as substrate, this step should be skipped since the oxygen plasma could roughen the well-polished surface of MgO.

(2) Place the substrate on a hot plate (200°C) for 5 - 10 min to remove any moisture.

(3) Rinse the substrate under Acetone and IPA, then blow dry using N2 gun.

(4) Spin coat the undercut resist by Headway spinner. For resist dispensing, use of filter and syringe can remove the unwanted particles in the resist solvent, but not necessary. The dispense recipes are as follows:

PMGI[1]: 1000 rpm, 500 rpm/s, 40 s. (Pre-spin: 500 rpm, 300 rpm/s, 3 s)

LOR 1A[1] (preferred): 3000 rpm, 1000 rpm/s, 40 s. (Pre-spin: 500 rpm, 300 rpm/s, 3 s)

When working on small size substrates, the substrate should be sticked onto a larger wafer using a small

[1] MicroChem Technologies Inc.

piece of double-side tape. Carbon tape usually works quite well.

(5) Soft bake the coated wafer on a hot plate (200°C) for 10 min. (Temperature and baking time is VERY critical for consistent results)

(6) Spin coat the imprint resist by Headway spinner on top of the undercut layer. Recipes are as follows:

NXR 7%[2] (mesoscale): 4000 rpm, 1000 rpm/s, 40 s. (Pre-spin: 500 rpm, 300 rpm/s, 3 s)

7010R[3] (sub-100 nm): 2000 rpm, 1000 rpm/s, 40 s. (Pre-spin: 500 rpm, 300 rpm/s, 3 s)

(7) Soft bake the coated wafer on a hot plate; recipe for NXR 7% is 150°C and 1.5 min; recipe for 7010R is 100°C and 1 min.

(8) Sample loading for NIL: gently pull out the NIL stage; take out the silicone plates, flip over; separate the top silicone film; put the coated substrate on top of the bottom silicone film, facing up; put the NIL stamp on top of the substrate, facing down (if using plastic working stamps such as ETFE, an additional empty Si wafer should be placed subsequently on top of the working stamp, so as to improve the thermal conduction during NIL); cover the top silicone film; make sure there are almost no bubbles in between the two silicone films; put the NIL stage back into the chamber.

(9) Imprinting: set the program in the software and it will run automatically. The imprint recipe is as follows:

Standard thermal: pre-imprint at 120 psi and 120°C for 5 s; imprint at 200 psi and 120°C for 30 - 60 s. Note that there is a standard 2 min pumping before the pre-imprint, as well as a 45 s venting/cooling after the imprint.

---

[2] Nanonex Corporation.

[3] Microresist Technology, GmBH.

(10) Demolding: take out the NIL stage; separate the two silicone films and take out the stamp/substrate combination; carefully separate the stamp and the substrate using a razor blade (if using plastic working stamps, just peel off the stamp from the corner).

(11) Use reactive ion etching (RIE) to remove the imprint layer residue. The purpose of this step is to expose the second undercut layer for further wet development. The RIE recipe is Descum (oxygen plasma) at 25 W and 25 s using Trion. The etch time depends on the resist thickness, imprint stamp, and feature size, therefore is subjected to change. (However, if everything was done right, 25 s developing for nanodots, and 20 s developing for nanowires work consistently). 15 - 30 s is a good range of time for developing NXR 7% resist at the mesoscale sizes.

(12) Develop the undercut resist layer using TMAH[1]: put the imprinted chip into TMAH solution and monitor the developing time using a timer; when reaching the desired time, take out the chip quickly and immerse it into DI water; gently shake the chip in the DI water; then blow dry using N2 gun. The idea of this step is to obtain the resist undercut profile.

(13) Metallization with desired materials.

(14) Liftoff: put the deposited chip into Remover PG[1] solution and apply ultrasonication for 3 - 5 min; put the chip into IPA solution and shake the chip gently to remove the Remover PG residue; then put the chip into DI water and shake the chip gently to remove the IPA residue; blow dry using N2 gun.

(15) Sample is ready for subsequent measurements and tests.

**B. Bilayer NIL and Mo transfer (epitaxial NIL process)**

Procedure:

Go through step (1) to (11) in Sec. A.

(12) Develop the undercut resist layer using TMAH. The process is similar to step (12) in Sec. A. However, a wedge-shaped resist profile is desired instead of a normal undercut.

(13) Deposit Mo layer using either evaporation or sputtering. Typical thickness of Mo is 70 - 100 nm.

(14) Liftoff. The process is similar to step 14 in Sec. A.

(15) Metallization, with desired materials, and at elevated temperatures for epitaxial growth.

(16) Mo liftoff: put the deposited chip into 30% H2O2 solution and apply ultrasonication for 3 - 5 min; put the chip into DI water and shake the chip gently; blow dry using N2 gun.

(17) Sample is ready for subsequent measurements and tests.

**C. Release of nanoparticles using SF6+O2 RIE etching**

Procedure:

Go through step (1) to (14) in Sec. A.

(15) After the desired measurement and characterization has been done, use RIE etching for release of the nanoparticles. Use Si Recipe in Trion (SF6+O2 mix) but adjust the power and time to 50 W of power for 3 minutes in order to etch the silicon substrate.

(16) After the complete etching, silicon substrate should look like cone that has nanoparticles loosely attached on top.

(17) BECAREFUL not to shake or give external force to the substrate since external force will detach the

nanoparticles from the Si substrate.

(18) Put the chip into the solution and ultra-sonicate for 3 minutes in order to detach all the nanoparticles from Si Substrate.

(19) Sample is ready in solution for measurements and tests.

**D. Salinization process of NIL stamps**

Procedure:

(1) Clean the stamp (e.g. Si or Quartz master stamps) by oxygen plasma using the Barrel Etcher, at 150 W for 3 - 5 min. If doing reclaim on used stamps, one should apply a longer etching time such as 5 - 10 min. This step also makes the surface of the stamp hydrophilic.

(2) Find the plastic vacuum desiccator (located beneath the hangers for the HF-suits) which we use for vacuum evaporation.

(3) Remove the top part of the vacuum desiccator; put the stamp on the porous, plastic tray in the vacuum desiccator, facing up; make sure that there is a small plastic lid at the bottom center of the vacuum desiccator; then put just 1-2 small drops of the trichloro(1H,1H,2H,2H-perfluorooctyl)silane[4] through the center hole of the tray into the small plastic lid at the bottom (please be very careful with the trichloro(1H,1H,2H,2H-perfluorooctyl)silane as it is very toxic); put back the top part of the vacuum desiccator, check the seal of the O-ring.

(4) Connect the vacuum desiccator to the pumping line on the wall and make it a vacuum system. Double

[4] Sigma-Aldrich.

check the vacuum and the seal.

(5) Wait for 45 min.

(6) Release the vacuum very slowly and carefully by disconnecting the pumping line.

(7) Take out the stamp. Put back the vacuum desiccator for next use.

(8) The stamp is ready to use. The surface should be hydrophobic after the salinization.

**E. ETFE process (mesoscale NIL)**

Procedure:

(1) Cut a small piece of ETFE sheet (10 mils = 0.254 mm thickness, DuPont "Tefzel" Type LZ general-purpose film); the size of the piece should be slightly larger than that of the master stamp.

(2) Ultrasonication of the ETFE in Acetone and IPA for 5 min, respectively.

(3) Rinse the ETFE with Acetone and IPA again, using the squeeze bottle.

(4) Blow dry using N2 gun.

(5) Sample loading: gently pull out the NIL stage; take out the silicone plates, flip over; separate the top silicone film; put an empty Si wafer on top of the bottom silicone film; put the clean ETFE piece on top of the Si wafer, facing up; put the master stamp (Si or quartz stamps, salinized) on top of the ETFE, facing down; cover the top silicone film; make sure there are almost no bubbles in between the two silicone films; put the NIL stage back into the chamber.

(6) Hot embossing with the imprinter: set the program in the software and it will run automatically. The embossing recipe is as follows:

ETFE1: pre-imprint at 200 psi and 250°C for 10 s; imprint at 450 psi and 250°C for 1 - 3 min. Note that there is a standard 2 min pumping before the pre-imprint, as well as a 45 s venting/cooling after the imprint.

(7) Separation: take out the NIL stage; separate the two silicone films and take out the stamp/ETFE combination; carefully separate the stamp and the ETFE by peeling off the ETFE from the corner).

(8) The ETFE working stamp is ready to use. Salinization is not necessary.

**F. Ormostamp process (sub-100 nm NIL)**

Procedure:

(1) Cut a small piece of Si (if copying from transparent, quartz master stamp) or glass (if copying from non-transparent, Si master stamp).

(2) Clean it with Acetone and IPA; ultrasonication is recommended.

(3) Bake the piece on a hot plate (200°C) for 10 min.

(4) Clean it by oxygen plasma using the Barrel Etcher at 150 W for 5 min. This step makes the surface of the substrate hydrophilic.

(5) Spin coat 'ormoprime08[3]' by the Headway spinner, at 3000 rpm, 1000 rpm/s and 60 s.

(6) Hard bake on a hot plate (150°C) for 5 min.

(7) Cast a very small drop of the gel-like Ormostamp[3] onto the substrate.

(8) Place the master stamp (salinized) on top of the Ormostamp gel, facing down.

(9) Gently press the master stamp against the substrate; make sure the Ormostamp gel cover the whole

master stamp area.

(10) Soft bake on a hot plate (85°C) for 2 min.

(11) Expose the master-stamp/Ormostamp combination under the UV light (365 nm wavelength) for 2 min using the ABM-aligner. Note that either the substrate or the master stamp needs to be transparent.

(12) Hard bake the master-stamp/Ormostamp combination on a hot plate (135°C) for 10 min.

(13) Demolding: carefully separate the master stamp and the Ormostamp with a razor blade.

(14) Treat the Ormostamp with oxygen plasma by the Barrel Etcher, at 25 W and 1 min. Higher power is not recommended as it will hurt the Ormostamp. This step makes the Ormostamp surface hydrophilic.

(15) The Ormostamp needs to be salinized before it can be used for NIL.